TOWARDS PROGRAMMABLE NEUTRAL ATOM ARRAYS WITH ALKALINE-EARTH-LIKE YTTERBIUM FOR QUANTUM COMPUTING AND SIMULATION

Dissertation
zur Erlangung des Doktorgrades
an der Fakultät für Mathematik, Informatik und Naturwissenschaften
Fachbereich Physik
der Universität Hamburg

vorgelegt von

Nejira Pintul

Hamburg

2025

Gutachter/innen der Dissertation:	Prof. Dr. Klaus Sengstock Prof. Dr. Henning Moritz
Zusammensetzung der Prüfungskommission:	Prof. Dr. Klaus Sengstock Prof. Dr. Henning Moritz Prof. Dr. Ludwig Mathey Dr. Juliette Simonet Prof. Dr. Roman Schnabel
Vorsitzende/r der Prüfungskommission:	Prof. Dr. Roman Schnabel
Datum der Disputation:	14.10.2025
Vorsitzender des Fach-Promotionsausschusses PHYSIK:	Prof. Dr. Wolfgang J. Parak
Leiter des Fachbereichs PHYSIK:	Prof. Dr. Markus Drescher
Dekan der Fakultät MIN:	Prof. Dr.-Ing. Norbert Ritter

Abstract

Neutral atoms trapped in optical tweezer arrays open new frontiers for building controllable and scalable quantum systems. Owing to their excellent coherence properties and controllability, alkaline-earth(-like) atoms such as ytterbium (Yb) and strontium (Sr) have emerged as leading candidates for quantum computing and simulation.

This thesis reports on the design and implementation of a new experimental apparatus for generating optically-controlled Yb atom arrays. Key capabilities include laser-cooling, high resolution imaging, magnetic field control and dynamically reconfigurable optical tweezers. Tailored to the *omg* qubit architecture utilizing the nuclear spin-1/2 states in ^{171}Yb, the system allows for excitation to clock and Rydberg states, as well as single-qubit control via Raman transitions.

We demonstrate trapping of individual Yb atoms in programmable two-dimensional optical tweezer arrays generated by a spatial light modulator. Using a narrow-line cooling and imaging transition, we achieve high-fidelity site-resolved fluorescence imaging of single atoms trapped at the magic wavelength. To characterize the platform, we measure the lifetime, atomic temperature in tweezers and trap frequencies. Furthermore, we present the implementation of a Rydberg laser system for excitation and detection of Yb Rydberg atoms.

The work in this thesis provides a solid foundation for future quantum computing and simulation experiments with individually controlled Yb atoms featuring Rydberg-mediated interactions.

Zusammenfassung

Neutrale Atome in geometrisch angeordneten optischen Mikrofallen bieten neue Möglichkeiten für die Realisierung kontrollierbarer und skalierbarer Quantensysteme. Aufgrund ihrer hervorragenden Kohärenzeigenschaften haben sich Experimente mit Erdalkali-und Erdalkali-ähnlichen Atomen wie Ytterbium (Yb) und Strontium (Sr) als ein vielversprechendes Forschungsfeld für Quantencomputing- und simulation etabliert.

Im Rahmen der vorliegenden Arbeit wurde ein neuer experimenteller Aufbau entwickelt und realisiert, der zur Erzeugung einzelner optisch-kontrollierbarer Yb-Atome in Mikrofallen dient. Das System ermöglicht Laserkühlung, die Erstellung hochaufgelöster Abbildungen mit einem Mikroskopobjektiv, die Erzeugung von Magnetfeldern sowie dynamisch rekonfigurierbare Mikrofallenpotentiale. Der Aufbau ist speziell auf die *omg* Qubit-Architektur zugeschnitten, welche auf dem $I = 1/2$ Kernspin von ^{171}Yb beruht und erlaubt sowohl Uhrenzustands- und Rydberganregungen als auch Raman-Übergänge zwischen zwei Qubit-Zuständen.

Ein zentrales Ergebnis dieser Arbeit ist das Einfangen einzelner Yb-Atome in programmierbaren zweidimensionalen Mikrofallenanordnungen, die mit einem örtlichen Lichtmodulator erzeugt werden. Mithilfe des schmalen Kühl-und Abbildungsübergangs in Yb, gelang es im Rahmen dieser Arbeit ortsaufgelöste Fluoreszenzabbildungen einzelner Yb Atome bei der magischen Wellenlänge aufzunehmen. Zur Charakterisierung des experimentellen Aufbaus wurden die Lebensdauer, die Atomtemperatur und die Fallenfrequenzen bestimmt. Darüber hinaus wurde ein Lasersystems zur Anregung und Detektion von Yb Rydberg-Atomen implementiert.

Die Ergebnisse dieser Arbeit bilden die Grundlage für die zukünftige Durchführung von Quantencomputing- und Quantensimulationsexperimenten mit individuell-kontrollierbaren Yb Atomen mit Rydberwechselwirkungen.

Contents

Chapter 1

Introduction

The past decades have seen remarkable technological progress in engineering controllable quantum systems. In pursuit of harnessing the quantum mechanical properties of such systems to provide enhanced capabilities over their classical counterparts, a multitude of hardware platforms emerged. These range from artificial atoms such as superconducting circuits, semiconductor quantum dots and nitrogen-vacancy centers in diamond to trapped ions, photonic circuits and cold atom systems.

In recent years, interest intensified and shifted more from fundamental physics towards real-world applications of quantum technologies [1–4], extending over a wide range of research areas including quantum metrology [5, 6], sensing [7, 8], communication [9, 10], information processing [11–14], computation [15–17] and simulation [18–21]. Most notably, the prospect of quantum computers [22] is one of the main driving forces governing today's quantum technology landscape and has unleashed a global race for the first useful realization of such a device. With its paradigm-shifting potential, quantum computing offers a pathway to address challenging computational problems considered intractable by classical means [23–26]. Such problems are highly-relevant in quantum cryptography [27, 28], high-energy physics [29, 30], material science [31] or quantum chemistry [32, 33] and could play a pivotal role in future drug discovery [34, 35] as well as in solving combinatorial optimization problems with applications in logistics [36] or finance [37–40]. Quantum-based processors promise to deliver critical speedup over classical devices by employing tailored algorithms [41] that operate according to the laws of quantum mechanics, making use of phenomena such as superposition or entanglement to store information into quantum bits (qubits) and execute quantum logical circuits. They are especially well suited for certain problem classes, with prominent examples including factoring of integers via Shor's algorithm [42] or unstructured search problems via Grover's algorithm [43].

The foundational ideas for universal quantum computing were first introduced in the early 1980s by Paul Benioff [44, 45], spurring further contributions in the years ahead [46–48]. Shortly thereafter, the idea of using artificial quantum systems to simulate the behavior of complex quantum systems appearing in nature was put forth [49, 50]. It later laid the groundwork for the research field of quantum simulation [51–53] as a way to overcome the exponential scaling when studying quantum many-body systems. Despite intense efforts ever since, building an adequate fault-tolerant quantum computing platform remains an exceptionally challenging undertaking due to the fragile nature of quantum systems. On the one hand, qubits must be well isolated from external perturbations to maintain high degrees of coherence, on the other hand, they must allow for precise control and be able to interact with each other when required.

Among the various research frontiers focusing on quantum computing, neutral atom arrays with Rydberg-mediated interactions [54–58] have lately attracted significant interest, offering compelling new capabilities in terms of scalability, error correction and qubit encoding architectures for both analog and digital quantum computing. This thesis focuses on experimentally exploring neutral atom arrays in optical tweezers as a versatile platform for quantum computation and simulation.

Over the past decade quantum information processing with neutral atoms has evolved into a competitive platform that is becoming on par with leading technologies such as trapped ions [59] and superconducting qubits [60], both of which surpassed two-qubit gate fidelities of 99.9 % [61, 62] and recently claimed to have demonstrated quantum supremacy [16, 63]. The neutral atom approach relies on individual atoms held in tightly-focused optical tweezers which can be geometrically arranged into a programmable quantum register. Qubits encoded in the electronic states of individual atoms are manipulated by laser light or microwaves, while interactions are mediated by long-range Rydberg interactions.

Neutral atom trapping technology was pioneered in the 1990s and early 2000s, alongside technological innovations in laser cooling techniques. This led to the first observation of a single cesium atom in a magneto-optical trap in 1994 [64], followed by the first demonstrations of single atom trapping using optical tweezers in 2001 [65, 66]. Several milestones followed in the subsequent years, including the generation of *arrays* of optical tweezers, the preparation of individual atoms via collisional blockade [65] and the advent of quantum gas microscopy [67, 68], which enabled single-site-resolved imaging of large-scale systems. With the availability of spatial light modulators and acousto-optical deflectors in the mid 2010s, fully programmable multi-spot tweezer geometries [69–71] and dynamic control became widely accessible, allowing for atom-by-atom assembly through rearrangement to produce defect-free arrays [72–75]. State-of-the-art capabilities now include trapping of up to 6100 individual neutral atoms [76], single-site addressability [77] and mid-sequence atom replacement from a reservoir [78, 79].

In parallel with advances in atom trapping, the exploration of highly-excited Rydberg atoms in cold atom systems gained significant interest, leading to the realization of frozen Rydberg gases at the end of the 1990s [80, 81]. A seminal proposal in 2001 by Jaksch et al. [54, 82, 83] introduced the idea of employing neutral atoms for quantum information science and utilizing Rydberg interactions for generating entangling quantum gates. Experimental efforts resulted in the first demonstration of the previously predicted Rydberg blockade between two individual atoms in 2009 [84–86]. This opened the way for utilizing individually-controlled neutral atoms with Rydberg interactions as a tunable quantum simulator [87–89] for studying various model Hamiltonians, particularly spin models [90–93], and enabled the exploration of phenomena such as quantum magnetism [94], exotic phases of matter [95, 96] and non-equilibrium many-body dynamics [97, 98] in a controlled environment. Meanwhile, the implementation of the first Rydberg-mediated two-qubit gate in 2010 [99] marked an important breakthrough and a significant step towards quantum information processing with neutral atoms [89, 100]. Since then, the field of neutral atom quantum computing has advanced rapidly, resulting in a series of key milestones. Neutral atom quantum processors [101, 102] have scaled to hundreds and even thousands of qubits [76, 94, 103–106], demonstrating two-qubit gate fidelities of 99.5 % on up to 60 atoms in parallel [107] and solving optimization problems such as finding the maximum independent set (MIS) on unit disc graphs [108].

Despite these remarkable achievements, fault-tolerant operation remains a long-standing goal, as current neutral atom experiments still suffer from limited coherence times, considerable atom loss, system size constraints and lack sufficient error mitigation. To overcome these challenges, current research is directed towards developing new strategies, including the exploration of utilizing more complex atomic species [109], circular Rydberg states [110, 111], tweezer arrays coupled to optical cavities [112–114] or even dual-species architectures [115, 116]. Alkaline-earth(-like) atoms such as strontium (Sr) or ytterbium (Yb) trapped in optical tweezers [117–120] have gained significant interest due to their divalent electronic structure and long-lived metastable 'clock' state, which are commonly utilized in optical lattice clocks [121]. Among them, ^{171}Yb has emerged as a leading candidate for quantum information science and plays a central role in this thesis. Leveraging its unique electronic structure allows quantum information to be encoded in highly coherent and controllable nuclear spin-1/2 qubits, featured in both the electronic ground and metastable state, which are connected via the ultra-narrow optical clock transition [122–124]. Recent tweezer experiments with ^{171}Yb successfully demonstrated outstanding capabilities including efficient preparation of large-scale arrays via enhanced loading schemes [125, 126], motional ground state cooling [125, 127] and fast and high-fidelity single-qubit gate operations [128, 129]. Enabled by non-destructive state detection [126, 130], mid-circuit readout [126, 131], continuous replenishment of lost atoms [78] and tailored error correction schemes via erasure conversion [132–135], experiments with ^{171}Yb successfully executed logical quantum circuits in a zone-based architecture and enabled two-qubit entangling gate fidelities of 99.72(3) % [135], marking the current state-of-art for neutral atom based platforms.

This thesis presents efforts towards building quantum systems with individual ytterbium atoms and aims at providing a research platform for quantum information science and quantum simulation. In the context of this thesis, a new experimental apparatus for trapping, imaging and manipulating single alkaline-earth-like ytterbium atoms has been designed and constructed. An outline of this work is provided in the following.

Outline of this thesis

Chapter 2 aims at providing basic information on the atomic properties of Yb relevant for this experiment. Chapter 3 details the generation of uniform optical tweezer arrays by employing computer-generated holography. Chapter 4 describes the experimental setup and provides a detailed description of the laser systems for cooling, trapping, fluorescence imaging and optical addressing. Chapter 5 presents the main experimental results, including first measurements characterizing cooling and single-atom trapping performances. Chapter 6 outlines progress toward enabling excitation to Rydberg states. A summary of each chapter is provided below.

Chapter 2 - Introduction to Neutral Atom Arrays with Ytterbium

This chapter reviews the key atomic properties of ytterbium (Yb) relevant for applications in quantum computation and simulation and gives an overview of the electronic structure of Yb. It provides the foundation for understanding how to encode quantum information into neutral ^{171}Yb atoms within the *omg* qubit architecture and motivates the experimental work presented in the remainder of this thesis.

Chapter 3 - Arbitrary 2D Tweezer Array Generation

This chapter presents an approach for generating arrays of tightly-focused optical tweezers using a holographic technique based on manipulating the phase of the wavefront. Arbitrary tweezer patterns are created with a spatial-light-modulator (SLM), enabling flexible and programmable control over the trap geometry. The first part of the chapter briefly reviews the operating principle of SLMs and introduces a variant of the Gerchberg–Saxton algorithm that is utilized to attain uniform trap intensities. The second part describes the experimental implementation of optical tweezer arrays and investigates the optical quality and the resulting trap uniformity after iterative optimization.

Chapter 4 - Experimental Platform

This chapter gives a detailed description of the experimental apparatus for cooling, trapping and manipulating individual Yb atoms. The first part provides an overview of the key components - this includes the science cell, magnetic field generation and high-resolution imaging system. The second part presents the overall optical and mechanical layout of the experiment, followed by a detailed description of the individual laser systems.

Chapter 5 - Trapping and Imaging Individual ^{171}Yb Atoms in Optical Tweezers

This chapter demonstrates the core capabilities of our optical tweezer platform utilizing alkaline-earth-like ytterbium. It provides a detailed description of the experimental procedures employed for cooling, trapping and preparing individual ^{171}Yb atoms in an optical tweezer array operated at a magic wavelength (759 nm).

First, a series of basic characterization measurements of the first stage cooling in a 3D magneto optical trap is performed. This includes measurements of the atomic temperature and lifetime. The second part focuses on measurements with ^{171}Yb atoms in optical tweezers. First, the process of obtaining individually-trapped atoms via light-assisted collisions is studied in detail. A high-fidelity fluorescence imaging protocol for single atom detection is presented, followed by an in-depth analysis. The chapter concludes with measurements of the lifetime, temperature and trap frequency of optically trapped ^{171}Yb atoms.

Chapter 6 - Towards Ytterbium Rydberg Atoms

This chapter describes the implementation of a Rydberg laser system, designed to overcome some of the current technical challenges, including beam intensity uniformity, precise control over frequency, amplitude, phase and beam pointing stability. The chapter begins by reviewing the fundamental properties of Rydberg atoms in the context of quantum computing with neutral alkaline-earth atoms in programmable tweezer arrays. Then, the laser system for providing strong, high-fidelity Rydberg interactions is presented, followed by the design and implementation of a laser system for detecting Rydberg atoms via autoionization.

Chapter 2

Introduction to Neutral Atom Arrays with Ytterbium

This chapter provides a concise review of the atomic properties of ytterbium (Yb) most relevant for trapped neutral atom experiments with interactions mediated by highly excited Rydberg states. Such experiments have applications in quantum computing, quantum simulation and precision metrology.

We begin with an overview of optical trapping of alkaline-earth(-like) atoms and review their key atomic features, including their divalent electronic structure, the presence of metastable states and the existence of nuclear spin states in fermionic species.

In the second part, we discuss the most relevant transitions in ytterbium and highlight their role and advantages for optical tweezer experiments. We further motivate the choice of the fermionic isotope ^{171}Yb for the experiments presented in this work. We then give a brief introduction to neutral atom quantum computing with ytterbium and review the *omg architecture*, which provides a tailored qubit encoding scheme for ^{171}Yb. We conclude the chapter with an overview of our experimental apparatus for neutral atom tweezer experiments using ytterbium atoms.

2.1 Properties of Alkaline Earth(-like) Atoms

Optical trapping of alkaline-earth(-like) elements became accessible only recently. Its unique atomic properties allow more flexibility for experiments compared to alkali atoms such as potassium or rubidium. Most notably known for their divalent electronic level structure and the presence of metastable states, these atoms can be leveraged for enhanced optical control and manipulation in optical tweezer experiments.

In the following, we briefly discuss optical trapping of individual alkaline-earth(-like) atoms and review the most fundamental properties of alkaline-earth(-like) atoms such as strontium (Sr) or ytterbium (Yb).

Optical trapping of alkaline-earth(-like) atoms

Optical tweezers are tightly focused laser beams that are far-detuned from an atomic resonance, allowing to trap individual atoms and confine their position in all three spatial dimensions. Trapping of microscopic particles using laser beams has been first demonstrated by Arthur Ashkin in the 1970s [136]. Further advances [137] have resulted in the development of modern optical tweezer techniques, for which Ashkin has been awarded the 2018 Nobel prize in Physics.

Trapping single atoms in optical tweezers relies on the optical dipole force, which arises from the interaction of the light field with the atom. This effect is governed by the AC Stark shift, in which shifts the presence of a far off-resonant light field shifts the atomic energy levels. For red-detuned light, this creates an attractive potential, pulling atoms toward regions of highest intensity. A tightly focused red-detuned laser beam thus provides a spatially varying energy shift, allowing to confine single atom within a small volume at the beam focus. A schematic illustration is shown in Fig. 2.1a. The tight focus is achieved using a high-numerical aperture microscope objective. A more detailed discussion of the optical tweezers implementation is provided in Chapter 3.

While trapping of individual atoms in optical tweezer potentials was already demonstrated in the early 2000s [65, 66], the first arrays of individually trapped alkaline-earth atoms followed much later in 2018 with strontium at Caltech [118] and subsequently at JILA [117]. Optical trapping of single ytterbium atoms was reported for the first time in 2019 at Princeton [138].

Two-Electron Structure

The defining feature of alkaline-earth atoms such as strontium (Sr) is their divalent electronic structure, which contributes to their distinct atomic properties. Although ytterbium (Yb) is not an alkaline-earth atom, it exhibits similar properties as it features two valence electrons as well and is therefore commonly referred to as an alkaline-earth-like element.

Much like helium, the two outer electrons can be arranged into a spin singlet where the total electronic spin is $S = 1$ (as in the ground state ${}^1\mathrm{S}_0$) or into a spin triplet ($S = 0$). It is therefore convenient to divide electronic states into two manifolds corresponding to the singlet or triplet manifold. Electric-dipole transitions between these two manifolds are forbidden by dipole selection rules, i.e. $\Delta S = 0$. However, mixing between singlet and triplet states arising from spin-orbit coupling and (in odd isotopes) hyperfine interactions, makes these transitions weakly-allowed and results in narrow linewidths. Narrow-line transitions the ${}^3\mathrm{P}_J$ states are also referred to as *intercombination lines*, which can be utilized for various tasks including narrow-line cooling or high-fidelity imaging among many other things. Figure 2.1b shows a simplified schematic of the electronic structure of ^{171}Yb.

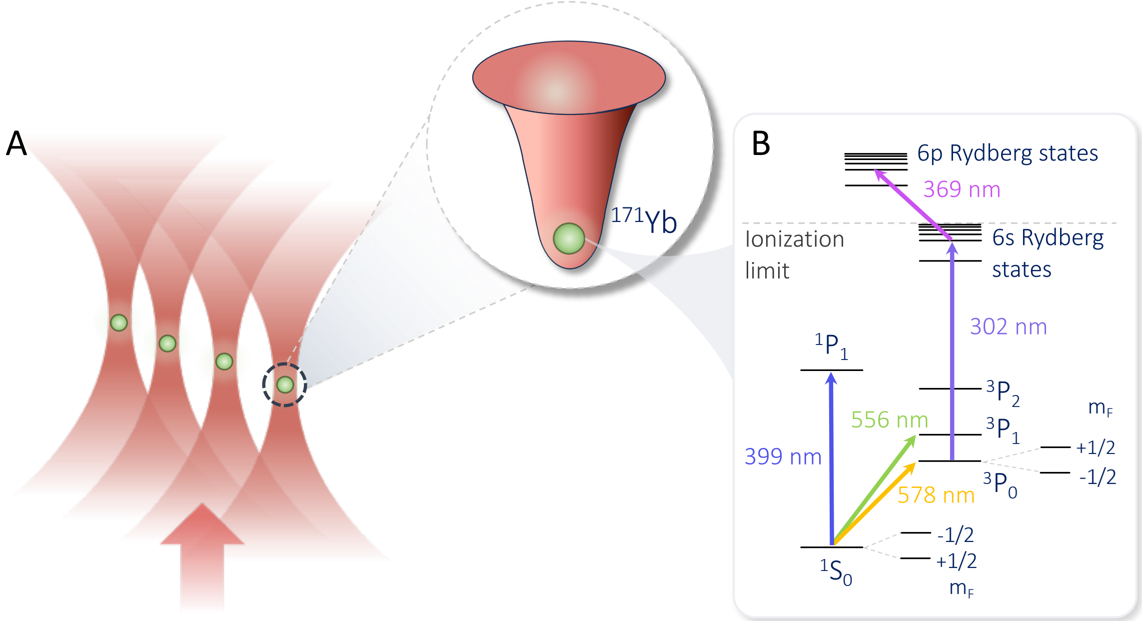

Figure 2.1 | Alkaline-earth-like ytterbium in optical tweezers. **(A)** Tightly-focused laser beams (optical tweezers) can be used to trap individual atoms at the intensity maximum. Inset: Illustration showing the resulting trapping potential in which Yb atoms can be captured. **(B)** Simplified level scheme of ^{171}Yb. Characteristic for divalent atoms, the electronic structure of Yb features a ^{3}P triplet manifold with metastable states $^3\mathrm{P}_0$, $^3\mathrm{P}_2$ and a broad singlet transition to $^1\mathrm{P}_1$ from the ground state. Rydberg states can be accessed via a single photon transition from $^3\mathrm{P}_0$ from which auto-ionizing states can be reached. The hyperfine structure in the ground and $^3\mathrm{P}_0$ gives rise to nuclear spin states $|m_F = \pm 1/2\rangle$ in the presence of a magnetic field.

Metastable states

Another remarkable feature of alkaline-earth(-like) atoms is the existence of two long-lived, metastable excited states ($^3\mathrm{P}_0$ and $^3\mathrm{P}_2$) in the triplet manifold. Transitions from the ground state to the $^3\mathrm{P}_0$ state are ultranarrow because they are doubly-forbidden by electric dipole selection rules, i.e. $\Delta J = 0$. In ytterbium, this so-called clock state state has a lifetime of 20 s for ^{171}Yb [139] and is utilized in optical lattice atomic clocks for its extraordinary coherence properties [121, 140]. In quantum computation and simulation applications, this metastable state is a powerful resource as it effectively serves as a second ground state, opening up new possibilities for highly-coherent control.

Nuclear spin and angular momentum decoupling

In alkaline-earth-(like) atoms both the ground and clock states have a total angular momentum of $J = 0$, resulting in strong decoupling between the nuclear spin I and electronic angular momentum. Because of the lacking electronic angular momentum, the nuclear spin states of fermionic alkaline-earth isotopes such as ^{87}Sr or ^{171}Yb have a vanishing linear Zeeman shift, making them especially robust against magnetic field fluctuations. An additional feature of nuclear spin states is that they experience a vanishing light shift, which is especially relevant in the presence of optical tweezers and further improves the coherence properties of these states.

In the next section, we further elaborate on some specific properties of ytterbium and which advantages its electronic structure provides for optical tweezer experiments.

2.2 Ytterbium in Optical Tweezers

The unique electronic and nuclear properties of ytterbium offer a variety of attractive capabilities compared to optical tweezer platforms employing alkali atoms. Ytterbium is especially well suited for applications in quantum information science, primarily because of the presence of long-lived metastable states, single-photon Rydberg transitions and highly-coherent nuclear spin states. Here we provide an overview of all transitions in ytterbium relevant to the experiment described in this work.

2.2.1 Atomic Properties of Ytterbium

Ytterbium is a rare earth element belonging to the group of lanthanides (atomic number 70) and has seven stable isotopes. The electronic configuration of ytterbium in the ground state is $[\mathrm{Xe}]4f^{14}6s^2$, featuring a filled 4f- and 6s-shell. The divalent electronic structure gives ytterbium similar atomic properties as alkaline earth elements (see Sec. 2.1). While the bosonic isotopes (such as ^{174}Yb) all have zero nuclear spin ($I = 0$), the fermionic isotopes such as ^{171}Yb or ^{173}Yb posses non-zero nuclear spins $I = 1/2$ and $I = 5/2$, respectively. A detailed electronic level structure showing the relevant transitions is illustrated in Fig. 2.2.

In this thesis, we perform all work with the odd isotope ^{171}Yb because of its attractive electronic structure for applications in quantum information science. Its nuclear spin $I = 1/2$ and vanishing electronic angular momentum $J = 0$ result in nuclear spin states in both the ground and excited clock state, which are well suited for encoding qubits in each of these two manifolds. A more detailed discussion on the possibilities of utilizing ^{171}Yb for quantum computing will be given in Sec. 2.2.2.

We now discuss all transitions relevant for optical addressing and trapping, while highlighting possible applications and advantages that the level structure of ^{171}Yb offers for optical tweezer experiments.

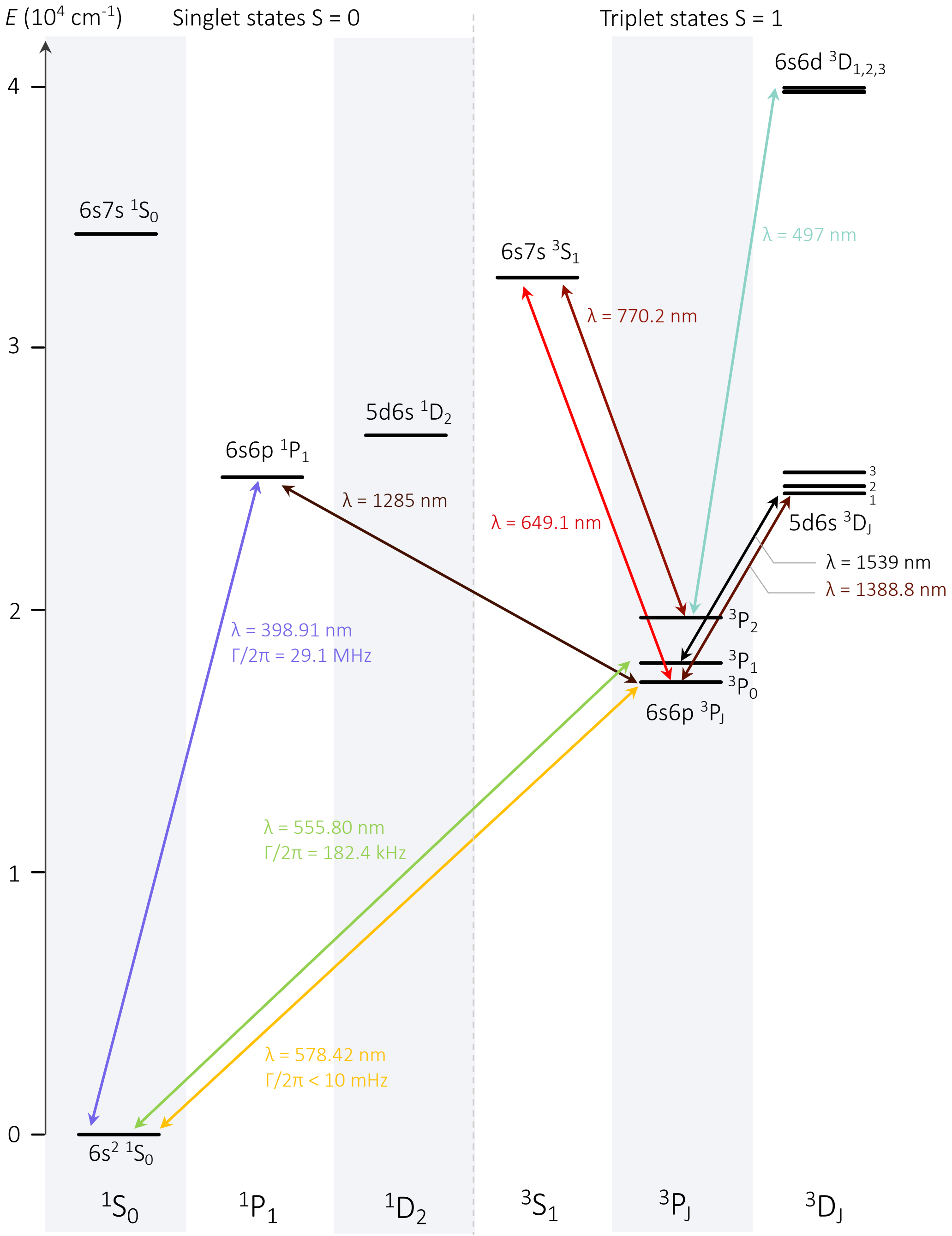

Figure 2.2 | Level diagram for ^{171}Yb. Schematic of the electronic structure of ytterbium with the most relevant low-lying energy levels. The level diagram is separated into singlet (left) and triplet (right) manifolds. Transitions between these two manifolds are weakly allowed, whereas transitions within the manifolds are strong. Applications for each transition are discussed in the main text.

399 nm - Transition
$^1\mathrm{S}_0 \leftrightarrow {}^1\mathrm{P}_1 \mid \Gamma = 2\pi \times 29\,\mathrm{MHz}$

In this experiment, the dipole-allowed, broad 399 nm "blue" $^1\mathrm{S}_0 \leftrightarrow {}^1\mathrm{P}_1$ transition in Yb and is primarily used for 2D MOT first-stage laser cooling. It provides a strong cycling transition with a Doppler temperature of about 700 µK, that allows for fast initial cooling of the hot atomic vapor released by the dispenser. Further, this transition offers the possibility of performing fast fluorescence imaging of individually-trapped atoms [120, 125].

556 nm - Intercombination Transition
$^1\mathrm{S}_0 \leftrightarrow {}^3\mathrm{P}_1 \mid \Gamma = 2\pi \times 182\,\mathrm{kHz}$

The (green) intercombination transition is forbidden under *LS* coupling but due to spin-orbit coupling, the $^3\mathrm{P}_1$ state gains a small admixture of the $^1\mathrm{P}_1$ singlet state, resulting in a weakly dipole allowed transition with a narrow linewidth. The green intercombination transition is useful for various tasks. This transition is most commonly employed for second-stage laser cooling of Yb in a 3D magneto-optical trap (MOT). The narrow linewidth of this transition allows for low Doppler temperatures of 5 µK. Further, this transition is used for high-fidelity fluorescence imaging in this experiment as it simultaneously provides Doppler cooling while scattering photons for single-atom detection. The intercombination line can be used for Raman sideband cooling schemes to reach the motional ground state of the optical tweezer potential, as well as gray-molasses [126] and EIT cooling [141]. The $^3\mathrm{P}_1$ state can also be utilized as an intermediate state for a two-photon transition to a Rydberg state. Single-qubit gates can be realized by driving the nuclear spins in the $^1\mathrm{S}_0$ ground state in fermionic Yb species via Raman transitions on the intercombination line.

578 nm - Ultra-narrow 'Clock' Transition
$^1\mathrm{S}_0 \leftrightarrow {}^3\mathrm{P}_0 \mid \Gamma < 2\pi \times 10\,\mathrm{mHz}$

This transition is doubly forbidden by electric dipole selection rules because it requires both $\Delta S = 0$ and $J = 0 \rightarrow J' = 0$, giving rise to an ultra-narrow transition. Because the only lower-lying state is the $^1\mathrm{S}_0$ ground state, $^3\mathrm{P}_0$ is metastable with a lifetime of 20 s in ^{171}Yb [139]. This state is therefore commonly referred to as the clock state due to its application in optical lattice clock experiments and as a frequency standard. Further, the lack of electronic angular momentum $J = 0$ in both the ground and clock state leads to a vanishing differential light shift in the presence of optical tweezer light. In odd isotopes, the zero electronic angular momentum also results in an exceedingly small linear Zeeman shift and therefore makes the nuclear spins insensitive to magnetic field fluctuations, adding to its excellent coherence properties. The clock state opens up interesting possibilities for applications for fault-tolerant quantum computing, due to its highly-coherent properties. In ^{171}Yb, the long-lived clock state serve as an effective second ground state and the nuclear spins in both the ground and excited state can be used to encode spin-1/2 qubits, which we will discuss further in Sec. 2.2.2. Lastly, excitation from the $^3\mathrm{P}_0$ to a Rydberg state can accomplished with a single-photon transition in the optical range, avoiding the need for an intermediate state as required in alkali atoms, which adds another source of decoherence.

649 nm - Qubit Control
$^3\mathrm{P}_0 \leftrightarrow 6s7s^3\mathrm{S}_1$

The 649 nm transition can be used to implement rotations of the nuclear qubit. This is accomplished by coherently driving Raman transitions between the two nuclear spins $|^3\mathrm{P}_0, m_F = \pm 1/2\rangle$ of the clock state via $6s7s^3\mathrm{S}_1$. In combination with a 770 nm laser beam, the 649 nm transition can also be used for non-destructive spin-selective qubit state readout. This involves coherently driving a two-photon Raman transitions on a nuclear qubit state $|^3\mathrm{P}_0, m_F = \pm 1/2\rangle$ in ^{171}Yb, using $6s7s^3\mathrm{S}_1$ as an intermediate state, followed by sequential transfer to the metastable $^3\mathrm{P}_2$ state and depumping via the state $6s6d^3\mathrm{D}_2$ to the ground state.

770 nm - Qubit Control
$^3\mathrm{P}_2 \leftrightarrow 6s7s^3\mathrm{S}_1$

The 770 nm transition can be used in conjunction with a 649 nm laser beam to realize coherent Raman transitions between the metastable $^3\mathrm{P}_0$ and $^3\mathrm{P}_2$ state via $6s7s^3\mathrm{S}_1$ for a non-destructive qubit detection scheme (see description of 649 nm). This transition can also be used to repump any population in $^3\mathrm{P}_2$, as this state is anti-trapped at the trapping wavelengths employed in this thesis.

Repump Transitions
$^3\mathrm{P}_2 \leftrightarrow 6s6d^3\mathrm{D}_2$ | 497 nm
$^3\mathrm{P}_0 \leftrightarrow 6s6p^1\mathrm{P}_1$ | 1285 nm
$^3\mathrm{P}_0 \leftrightarrow 5d6s^3\mathrm{D}_1$ | 1388 nm

The 497 nm transition connecting the metastable $^3\mathrm{P}_2$ state with $6s6d^3\mathrm{D}_2$ can be used as part of a repump scheme (see 649 nm), over which atoms can be transfer back to the ground state via radiative decay and then imaged either on the green $^3\mathrm{P}_1$ or blue $^1\mathrm{P}_1$ transition.

Another possibility for repumping of the states in $^3\mathrm{P}_0$, is by using the 1285 nm transition to $^1\mathrm{P}_1$.

The 1388 nm repump transition to the $5d6s^3\mathrm{D}_1$ state can be used as an alternative intermediate state to $6s7s^3\mathrm{S}_1$ with 649 nm to drive Raman transitions between the nuclear spin states in $^3\mathrm{P}_0$. This wavelength can also be used for quantum network applications.

1539 nm - Optical Pumping
$^3\mathrm{P}_1 \leftrightarrow 5d6s^3\mathrm{D}_1$ | 1539 nm

The $^3\mathrm{P}_0$ state can populated by optical pumping involving a two-photon process via $^1\mathrm{S}_0 \leftrightarrow ^3\mathrm{P}_1$ and $^3\mathrm{P}_1 \leftrightarrow 5d6s^3\mathrm{D}_1$. Upon decay from $5d6s^3\mathrm{D}_1$ into $^3\mathrm{P}_0$, initialization into the clock state can be achieved.

UV wavelengths - Rydberg excitation and detection

$^3\mathrm{P}_0 \leftrightarrow 6s75s\,^3\mathrm{S}_1$ | 302 nm
$6s75s\,^3\mathrm{S}_1 \leftrightarrow 6s^2\mathrm{S}_{1/2}$ | 369 nm

Rydberg states with principle numbers $n \approx 75$ can be reached directly from the $^3\mathrm{P}_0$ clock state via a single-photon transition at 302 nm. This eliminates the need for two-photon excitation schemes required in alkali atoms, thereby avoiding losses through intermediate states and enabling higher Rabi frequencies. Owning to the divalent structure of Yb, the remaining Yb^+ion core has significant polarizability which allows Rydberg atoms with sufficiently large n to generate an attractive force and be trapped in red-detuned tweezers [142]. A more detailed discussion of Rydberg excitations is provided in Chapter 6. Further, the remaining ion core of the Yb Rydberg atom has a strong optical transition at 369 nm driving the $6sns \rightarrow 6p_{1/2}ns$ transition, resulting in rapid autoionization loss, which can be utilized for high fidelity Rydberg detection [143, 144]. It is further possible to use this transition to locally tune Rydberg states out of resonance with global Rydberg beams, albeit this requires local control of the 369 nm beam [145].

532 nm - Green Trapping Wavelength

Optical tweezers at 532 nm offers magic trapping conditions for the $^1\mathrm{S}_0 \leftrightarrow ^3\mathrm{P}_1, m_J = 0$ transition in ^{174}Yb [146]. Moreover, this wavelength has been employed for applying local light-shifting operations to site-selectively tune the clock state out of resonance [126]. This trapping wavelength is well-suited for implementing dynamic atom rearrangement protocols with ^{171}Yb atoms [147], facilitated by the large polarizability of Yb at 532 nm. A drawback, however, is the possibility of atom loss through a two-photon ionization process from $^3\mathrm{P}_1$ involving two 532 nm photons, carrying sufficient energy to exceed the ionization threshold.

759 nm - Red Trapping Wavelength

Tweezers operated at 759 nm provides magic trapping condition for the clock transition $^1\mathrm{S}_0 \leftrightarrow ^3\mathrm{P}_0$ in ^{171}Yb. By tuning the polarization angle of the tweezer beam[1], it is possible to simultaneously attain magic trapping conditions for the green cooling and imaging transition $^1\mathrm{S}_0 \leftrightarrow ^3\mathrm{P}_1, m_F = \pm 1/2$. This trapping wavelength will be the central for the work performed throughout this thesis. The future goal of the experiment is to combine 759 nm tweezers with movable tweezers at 532 nm, enabling dynamic atom rearrangement.

460 nm, 483 nm, 487 nm - Alternative Trapping Wavelengths

Shorter-wavelength optical tweezers have the advantage of tighter focusing but also makes atoms susceptible to atom loss via two-photon ionization out of $^3\mathrm{P}_1$, since two trapping photons are sufficient to reach the ionization limit. In our experiment we do not employ any of the following trapping wavelengths but these are commonly used in the community.

---

[1] The concept of *magic angle trapping* is discussed in Ch. 5.2.1.

Optical tweezers operated at 460 nm offer magic trapping conditions for the clock transition [148] and provide a deep trapping potential due to enhanced polarizability at this wavelength.

The trapping wavelength 483 nm [131] allow magic trapping of the $^1\mathrm{S}_0 \leftrightarrow {}^3\mathrm{P}_1, m_F = \pm 3/2$ transition in ^{171}Yb, while 487 nm [133] tweezers allow the $m_F = \pm 1/2$ states to be trapped magically.

2.2.2 Quantum Computing with Ytterbium

Quantum computing is based on storing quantum information is units of quantum bits (qubits), represented by two orthonormal states typically denoted by $|0\rangle$ and $|1\rangle$ and referred to as the computational basis. Unlike in classical binary bits, these two states represent a quantum mechanical two-level system, allowing $|0\rangle$ and $|1\rangle$ to be in a coherent quantum superposition.

In neutral atoms, qubits can be encoded into the electronic and nuclear degrees of freedom of individual atoms. An ensemble of individually-controlled atoms can be arranged into two-dimensional arrays, forming a quantum register. In digital quantum computing[2], quantum algorithms are executed on the quantum register through a sequence of quantum logic gates applied to the qubits. To perform arbitrary computations, a universal gate set is required, consisting of arbitrary single-qubit rotations and at least one entangling two-qubit gate [149].

Arbitrary rotations on the qubit state are achieved by coherently driving qubit transitions on the Bloch sphere with an external field and adjusting the pule duration as well as the relative phase of the driving field.

Two-qubit gates are realized by interactions between the qubits and are most commonly achieved by Rydberg-mediated interactions in the neutral atom platform to implement quantum logic, where the excitation of one atom conditions the excitation of a second atom. We return to the topic of Rydberg excitations in Chapter 6, where we discuss the implementation of two-qubit gates in greater detail.

However, achieving high-fidelity single and two-qubit gate operations in the presence of technical noise, still remains a key challenge and further improvements in decoherence suppression and error correction protocols are required. The physical implementation of qubits plays a crucial role in mitigating these challenges. A particularly promising qubit encoding scheme takes advantage of the unique level structure of ^{171}Yb, particularly the $I = 1/2$ nuclear spin. In the so-called optical-metastable-ground-state (*omg*) qubit architecture proposed in Ref. [124], three separate qubit manifolds are encoded in a

---

[2] In contrast to digital quantum computing, where discrete gates operations are applied sequentially, the neutral atom platform also supports an analog computing mode, in which the quantum system naturally evolves under a carefully engineered Hamiltonian, producing a solution to a given computational problem. Examples of analog quantum computing applications are quantum simulation and quantum annealing.

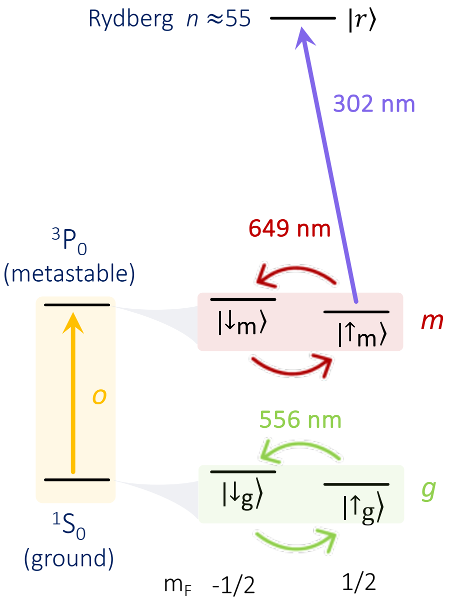

Figure 2.3 | Qubit encoding scheme in ^{171}Yb (*omg* architecture). Level structure illustrating the metastable (m) and ground (g) state qubit [124], encoded in the nuclear 1/2-spins of ^{171}Yb. The qubit basis is formed by $|0\rangle \equiv |m_F = +1/2\rangle$ and $|1\rangle \equiv |m_F = -1/2\rangle$. The two qubit manifolds are connected by an optical (o) qubit, represented by the clock transition $^1S_0 \leftrightarrow {}^3P_0$. Single-qubit rotations between the nuclear spins in the metastable (ground) qubit are performed by coherently driving Raman transitions via $^3S_1$ ($^3P_1$) using 649 nm (556 nm). Rydberg states ($|r\rangle$) can be accessed from the $^3P_0$ state via a single-photon transition to implement entangling two-qubit gates.

single ^{171}Yb atom, as illustrated in Fig. 2.3. Our experiment is designed to provide all the necessary technical capabilities required for implementing the *omg* qubit encoding. This qubit architecture was originally proposed in the context of trapped ion systems [150, 151] and later adapted to the neutral atom platform for ^{171}Yb. Here, the ground state (g) qubit is encoded in the $^1S_0$ ground state nuclear 1/2-spins $\{\downarrow_g, \uparrow_g\}$, while the metastable (m) qubit $\{\downarrow_m, \uparrow_m\}$ is encoded in the $^3P_0$ clock state. The Zeeman states in each manifold form the qubit basis $|0\rangle \equiv |m_F = +1/2\rangle$ and $|1\rangle \equiv |m_F = -1/2\rangle$. The two qubit manifolds are connected by the optical (o) qubit, represented by the clock transition. Encoding qubits in the nuclear spin states of ^{171}Yb, provides several advantages that leverage the coherence properties of this atom.

Due to the metastable nature of the $^3P_0$ clock state, it can be regarded as an effective second ground state, providing ^{171}Yb with the capability to hist two qubits simultaneously within one atom. Single-qubit rotations between the qubit states within each manifold can be accomplished by optical Raman transitions via an intermediate state. Rotations on the nuclear spins in the metastable level can be performed with 649 nm via the $^3S_1$ state. Ground state qubit rotations can be implemented with a 556 nm beam via $^3P_1$.

Rydberg states can be accessed from the metastable states in a single-photon transition at 302 nm in contrast to two-photon transitions which suffer from off-resonant scattering from an intermediate state. This allows to implement fast, high-fidelity two-qubit entangling gates.

Further, the m qubit is well-suited for shelving operations, in which qubits can can be selectively transferred from g into m to perform readout of the remaining g spins. Meanwhile the shelved population is m is dark to imaging light, allowing for non-destructive spin readout and mid-circuit measurements [126].

Lastly, the omg architecture supports error correction schemes based on *erasure conversions*, which rely on detecting leakage out of the metastable computational subspace via fluorescence, thereby converting physical errors into erasures, i.e. errors in known locations [132]. In practice, this is achieved by monitoring decay events to the ground state by imaging the population on the ${}^1\mathrm{S}_0 \leftrightarrow {}^1\mathrm{P}_1$ transition. Erasure conversion is particularly useful for error correction protocols, since atom loss and radiative decay are dominant error sources. The implementation of mid-circuit erasure checks has recently been demonstrated experimentally [133, 134], marking an important step toward fault-tolerant neutral atom computing.

2.3 Overview of the experiment

We now give a general overview of our ytterbium-based optical tweezer apparatus.

Figure 2.4 shows a simplified schematic of the key components, while a complete description of the experimental apparatus is given in Chapter 4.

All experiments are carried-out in an ultra-high vacuum glass cell. Ytterbium atoms are first cooled in a two-dimensional magneto optical trap (MOT) and subsequently transferred to a three-dimensional MOT (not shown) using three pairs of counter-propagating 556 nm beams, which are also used for fluoresence imaging.

Optical tweezers are generated by a high-numerical-aperture (NA) microscope objective to produce near-diffraction-limited traps. Ytterbium-171 atoms are trapped in a tweezer array operated at the magic wavelength of 759 nm (see inset). The tweezer patterns are generated with a spatial-light-modulator (SLM) (see Chapter 3). After passing through the glass cell, the trapping light is re-collimated by a second, identical microscope objective and imaged onto a diagnostics camera.

The setup also supports trapping of ^{174}Yb in 532 nm tweezer arrays created by a pair of crossed acousto-optic deflectors (AODs). The 532 nm and 759 nm beams are combined on a dichroic mirror, enabling hybrid operation of both trapping wavelengths. This enables trapping of ^{171}Yb in static 759 nm tweezers and dynamic rearrangement of atoms using 532 nm AOD-generated tweezers. Single-atom detection is achieved by collecting fluorescence through the same high-NA objective and imaging onto a camera. Additionally, a global clock and Rydberg beam will allow to excite Yb atoms to the metastable clock state or to Rydberg states (see Chapter 6) in the future.

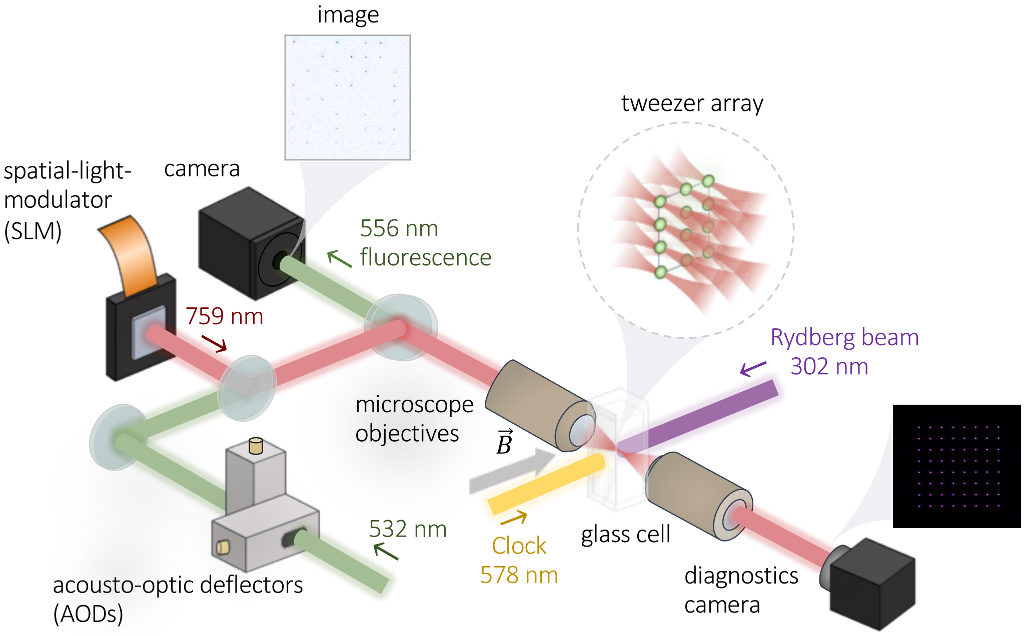

Figure 2.4 | Schematic overview over the Yb tweezer experiment. Ytterbium atoms isolated and laser cooled in an ultra-high vacuum glass cell. Optical tweezers are generated with a high numerical aperture microscope objective. A spatial-light-modulator produces a static tweezer arrays at 759 nm. A pair of crossed acousto-optic deflectors is used to generate tweezer arrays at 532 nm for atom reconfiguration. The trapping light can be imaged on a camera for diagnostics purposes. Fluorescence is collected on a camera to detect single atoms (see inset). For clarity, the imaging beams are not shown. A pair of magnetic coils (not shown here) is used to generate a magnetic field B. A global 578 nm and Rydberg beam (302 nm) will allow excitation to the metastable $^3\mathrm{P}_0$ state or to Rydberg states.

Chapter 3

Arbitrary 2D Tweezer Array Generation

Optical tweezers have become an indispensable tool in cold atom experiments. By focusing a far off-resonant laser beam to a tight spot with beam waists of typically below 1 µm, individual atoms can be isolated at the local intensity maximum of what is known as an optical tweezer.

Continued advances in optical trapping techniques have enabled the assembly of atoms into large-scale arrays of optical tweezers, forming the backbone of quantum information processing and simulation with neutral atoms.

In this chapter, we present our approach for generating arrays of tightly-focused optical tweezers using a holographic technique which manipulates the phase of the optical wavefront. Arbitrary tweezer patterns are created with a spatial-light-modulator (SLM), which allows flexible and programmable control over the trap geometry.

First, we give a brief description of the working principle of spatial light modulators. We discuss the calculation of computer-generated holograms to create arrays of optical tweezers using an SLM. We then outline a Gerchberg-Saxton algorithm for achieving uniform trap intensities. The second part of this chapter is dedicated to the experimental implementation of SLM-generated tweezer arrays. Here we characterize the optical quality of the resulting tweezer spots and the trap uniformity across a rectangular 64-site array.

The optical tweezer generation methods presented in this chapter have been developed by Jonas Rauchfuß under co-supervision of the author. An extensive characterization of the SLM employed in this experiment, as well as a detailed description of the tweezer generation and uniformity-optimization procedure can be found in the Master thesis of Jonas Rauchfuß [152]. The experimental results presented in this chapter have been conducted together with Tobias Petersen.

3.1 Holographic optical tweezer generation

There are several technologies currently available to create *arrays* of optical tweezer traps. While using acousto-optic modulators (AODs) is a well-established technique that enabled the creation of large-scale tweezer arrays, allowing dynamic operation on a ms timescale, the generation of multiple spots in parallel is limited to row and column operations. To overcome this drawback, we combine two technologies to produce precisely controlled and reconfigurable tweezer arrays in this experiment: Liquid Crystal on Silicon (LCoS) spatial light modulators (SLMs) [69, 70] and a pair of crossed AODs [72, 153]. An SLM is used for generating a static array of tweezers, while superimposing them with AOD-generated tweezers allows atom rearrangement through dynamic movement of the tweezers to produce deterministically loaded arrays. The hybrid approach has enabled several recent breakthroughs in the field of neutral atom trapping [88, 102].

This thesis focuses on holographic tweezer generation using SLMs, which works by manipulating the phase of the laser beam. A detailed description of the implementation of AOD-based tweezer arrays at our experiment can be found in the thesis of Tobias Petersen [154] and is not further discussed here.

Other techniques used for 2D tweezer array generation rely on digital mirror devices (DMDs) [155] or microlens arrays (MLAs) [156]. Compared to other devices, SLMs offer the highest degree of flexibility in the achievable tweezer geometry, while maintaining high degrees of stability in intensity as well as shape. Platforms based on SLMs provide a promising path towards generating larger system sizes, a key challenge in enabling large-scale quantum computing, with current experiments capable of producing 12100 sites and readily trapping up to 6100 atoms [76].

3.1.1 Hologram generation using a spatial light modulator

In this section, we first outline the experimental setup used to create holographically generated tweezer arrays implemented at our experiment, followed by a brief review of the working principle of the utilized spatial light modulator. We then describe how spatial phase modulation enables the tailored shaping of illumination patterns.

Overview of the experimental platform

Figure 3.1 shows a simplified schematic of our experimental platform for generating SLM-based optical tweezers used to trap ^{171}Yb atoms. The optical tweezers operate at a wavelength $\lambda = 759\,\mathrm{nm}$. The high-numerical aperture (NA $= 0.5$) microscope objective (Special Optics), focuses the beam to create tightly-focused microtraps. To monitor the resulting light pattern, the trapping beam propagates through a second objective and is imaged onto a diagnostics camera (Basler acA3088-57um). Part of the light is picked off and sent to a Shack-Hartman sensor (Imagine Optic,

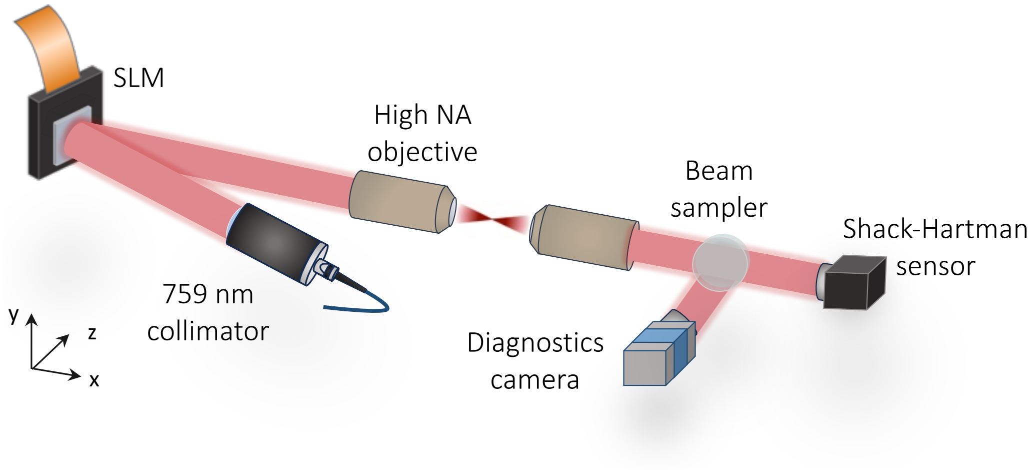

Figure 3.1 | SLM tweezer generation. Schematic illustration of the setup for SLM-based optical tweezer generation. Laser light at 759 nm is incident on a spatial-light-modulator (SLM) at an angle of 6 °. A phase pattern is imprinted onto the SLM to generate optical tweezer spots in the image plane. Note, that a telescope (not depicted here) is employed to expand the beam and conjugate the Fourier planes. Optical tweezers are focused down with a high-NA microscope objective onto the atoms. Trapping light is re-collimated with a second objective and imaged with a CMOS camera. The wavefront is analyzed with a Shack-Hartmann sensor.

HASO4 broadband) to directly measure the wavefront of the beam. This allows us to analyze the resulting trapping potential and to implement direct feedback to the SLM (X15213-02, Hamamatsu-Photonics). For clarity, the relay optics used for image conjugation are omitted in this schematic. A detailed description of this setup can be found in Ch. 4.2.1.

In the following, we give a brief technical overview of LCOS-SLMs in the context of optical trapping techniques utilized within this thesis. We base our description on the X15213-SLM series from Hamamatsu, as employed through this thesis. For more comprehensive reviews, the reader is referred to Refs. [157–159].

LCOS spatial light modulators

Spatial light modulators have gained significant interest across a multitude of research disciplines due to their ability to dynamically shape light fields. This includes diverse applications in microscopy, imaging or quantum optics [65]. In particular, phase-only Liquid Crystal on Silicon (LCOS) SLMs are a versatile tool for generating arbitrary optical tweezer patterns for atom trapping [160]. These optical devices modulate the phase of the incident laser light by digitally displaying a phase pattern on the SLM which modulates the local refractive index for each pixel accordingly, effectively controlling the optical wavefront. Hologram-based light shaping even enables assembly of atoms in 3D configurations [161].

A schematic diagram of the working principle of a typical LCOS-SLM is shown in Figure 3.2. These devices consist of an array of individually addressable liquid crystal

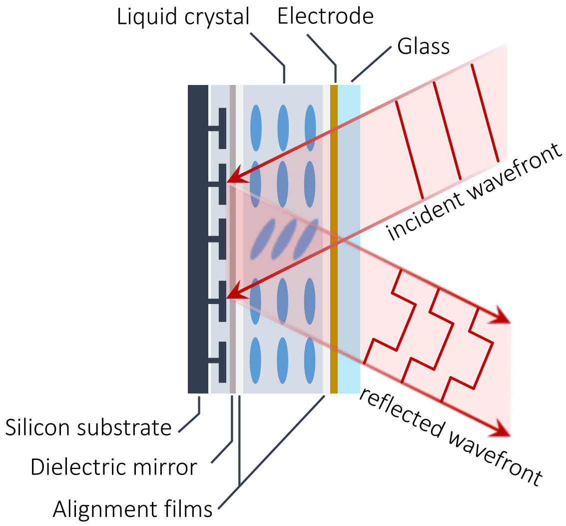

Figure 3.2 | Liquid Crystal on Silicon (LCOS) spatial light modulator. Schematic illustration of the working principle of an LCOS-SLM (based on the X15213 series from Hamamatsu). By applying a voltage, the orientation of the liquid crystal layer can be controlled for each individual SLM pixel. This induces a change in the refractive index of the material, resulting in a spatial modulation of the phase of the reflected light field. A dielectric mirror, ensures high reflectivity.

pixels that modulate the phase of the light. Note, that our description is based on the X15213 series from Hamamatsu.

An LCOS-SLM is comprised by several different layers as illustrated in Fig. 3.2a. It consists of a silicon substrate, a dielectric mirror, alignment films, a bi-refringent liquid crystal layer, an electrode and a glass substrate. The silicon substrate enables voltage control of each individual pixel, which modifies the orientation of the liquid crystals accordingly. This changes the index of refraction, thus introducing a spatially varying phase modulation across the beam. Precise spatial control of the phase can only be obtained for linearly polarized light, as the phase delay induced by the bi-refringent material is polarization-dependent. Further, the input polarization must match the liquid crystal alignment to ensure correct operation.

The resulting modulation is non-linear with respect to the applied voltage, therefore a pre-defined look-up-table is used to achieve the desired modulation amount. A dielectric mirror layer ensures high reflectivity of the reflected beam.

While LCOS-SLMs offer the greatest spatial flexibility when it comes to creating large-scale light patterns, most commercial options operate at a relatively low refresh rates of about 60 Hz to a few hundreds of Hz. However, advances in SLM technology have led to devices achieving refresh rates of over 1 kHz albeit with some trade-offs such as a reduced active aperture or lower phase resolution [159].

In our experiment, the SLM-generated optical tweezer array is operated in a static manner, since the 60 Hz SLM refresh rate is much slower than the relevant atomic timescales.

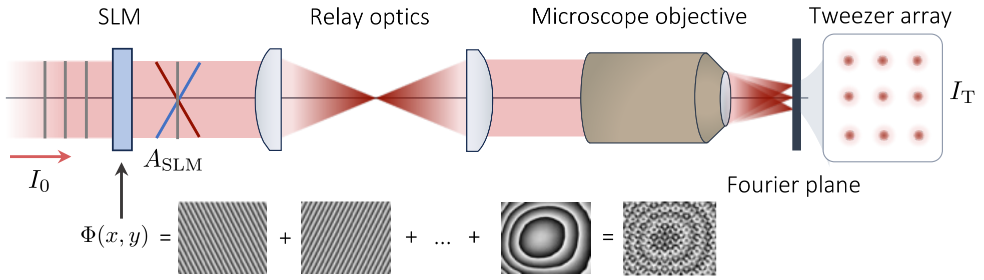

Figure 3.3 | Holographic optical tweezer array generation. Schematic of the optical tweezer generation with an SLM. The phase of the incident light field is modulated by the SLM according to the 2D phase mask $\Phi(x_s, y_s)$, consisting of composite phase masks for generating a single tweezer spot m displaced by an amount (x_m, y_m) in the image plane of the optical system. The targeted illumination pattern is described by the intensity distribution I_{T}. The resulting complex amplitude after the SLM is denoted by A_{SLM}. The wavefront tilt resulting from the elementary phase masks is illustrated by the blue, red and grey lines. A relay telescope in $4f$ configuration is used to adapt the beam size to the back focal plane of the microscope objective.

Spatial phase modulation

We now look at how the spatial phase pattern imprinted on the light field by the SLM is transformed into a corresponding intensity distribution in the image plane of an optical system, as schematically shown in Fig. 3.3. The following description is based on Refs. [162, 163]. The targeted intensity distribution I_{T} in the focal plane of the imaging system is given by

$$I_{\mathrm{T}} = |\mathscr{F}(A_{\mathrm{SLM}})|^2, \tag{3.1}$$

where $\mathscr{F}$ refers to the two-dimensional Fourier transform and A_{SLM} the complex amplitude distribution of the laser light field after the SLM, which we define as

$$A_{\mathrm{SLM}}(x, y) = \sqrt{I_0}\, e^{i\Phi(x_s, y_s)}. \tag{3.2}$$

Here, I_0 is the intensity distribution of the incident beam and $\Phi(x_s, y_s)$ is the two-dimensional phase mask imprinted by the SLM. The phase can take values from 0 to 2π.

From eqs. 3.1 and 3.4 we see that the intensity pattern I_{T} can be altered by manipulation of the phase $\Phi(x_s, y_s)$. Therefore, to obtain the desired intensity distribution, our task consists of finding a corresponding phase pattern $\Phi(x_s, y_s)$ to display on the SLM. An intuitive assumption would be to take the inverse Fourier transform of eq. 3.1 to extract the amplitude of the laser light field. However, to modulate the light field accordingly we would require to alter both the phase and intensity of the incoming beam, which cannot be accomplished using a phase-only SLM. Calculating a corresponding phase for a targeted intensity pattern I_{T} is a well-known problem and is referred to as a phase-retrieval [164], which can be solved algorithmically.

Up to some trivial cases, there do not exist exact solutions for Φ for a given target distribution I_{T}. To approximate a phase mask corresponding to a tweezer array pattern I_{T}, we implement a Gerchberg-Saxton (GS) algorithm, which belongs to the class of iterative Fourier transform algorithms. The implementation of a GS algorithm is outlined in Sec. 3.1.2.

To generate an array of microtraps, we add up all individual phase patterns for producing a *single* microtrap at the desired position to obtain a hologram for the targeted intensity distribution. Additionally, we apply a correction phase pattern provided by the manufacturer to offset the bending of the SLM screen. Because the relative intensities will be non-uniform at the begining, we optimize the parameters for the phase pattern with the GS algorithm.

In the next section, we discuss how we obtain a phase pattern and improve the uniformity of the tweezers using a Gerchberg-Saxton algorithm by using feedback from a camera.

3.1.2 Implementation of the Gerchberg-Saxton algorithm

To calculate the correspond phase Φ_{SLM} for a targeted intensity pattern in the image plane of an optical system, we employ a Gerchberg-Saxton algorithm. In general, this algorithm usually involves iteratively propagating between the SLM and focal plane by performing Fourier and inverse Fourier operations of the calculated light field until the phase eventually converges. By following this procedure, the intensity distribution in the image plane can be shaped into arbitrary light patterns [70, 165].

However, our goal consists of producing individual light spots, that can be arranged into tailored geometries, which is a much more straightforward undertaking. This objective can be attained by utilizing a simplified version of the GS algorithm, thereby alleviating the need for time-consuming computation of the Fourier transform. This variant of the GS algorithm relies on the summation of elementary phase patterns Δ_m, each generating a single optical tweezer spot m at a defined location in the focal plane (x_m, y_m) . The idea of elementary phase patterns is illustrated in Fig. 3.3 and has been developed previously in Refs. [163, 166, 167].

Designing computer-generated holograms

We can think of displacing a Gaussian beam in the focal plane of a lens by tilting the incoming wavefront. This can be achieved by imprinting a linear ramp onto the SLM. The elementary phase pattern Δ_m for generating tweezer m at position (x_m, y_m) in the focal plane then takes the form

$$\Delta_m(x_s, y_s) = \frac{2\pi}{\lambda f}(x_m x_s + y_m y_s), \tag{3.3}$$

where x_s, y_s are the coordinates in the SLM plane, λ is the wavelength, f the focal length of the lens and $(x_m, y_m) = (0, 0)$ denotes the focal plane of the lens.

The complex amplitude of the light field in the SLM plane can then be written as

$$A_{\mathrm{SLM}}(x_s, y_s) = \sum_m w_m \, e^{i(\Delta_m(x_s, y_s) + \theta_m)}, \tag{3.4}$$

where $e^{i\theta_m}$ is the relative phase between the elementary tweezer phase patterns Δ_m and w_m is a weight factor, which will become relevant for achieving uniformly bright later on.

Following the argumentation from Ref. [167], an intuitive way to view this is in a picture where the light is propagating backwards through the optical system. The light spots in the focal plane, can then be considered as N point-like light sources. After propagation through the lens, the light from each spot would form an interference pattern in the plane of the SLM according to its relative phase and amplitudes.

Because we can only control the phase and not the amplitude with the SLM, a good starting point is to imprint only the phase of the above expression onto the SLM given by

$$\Phi(x_s, y_s) = \arg(A_{\mathrm{SLM}}(x_s, y_s)), \tag{3.5}$$

which we calculate using equations (3.3), (3.4). A good initial guess is obtained by using random phases θ_m and $w_m = 1$ for all m. The real amplitudes, phases, trap weights w_m and phase offsets θ_m will be iteratively determined by the GS algorithm.

Further, we define the complex amplitude V_m of the $m-$th light spot using the expressions for the phase mask ϕ_{SLM} imprinted on the SLM and the elementary phase pattern Δ_m as

$$V_m = \iint e^{i[\Phi(x_s, y_s) - \Delta_m(x_s, y_s)]} dx_s dy_s. \tag{3.6}$$

Relevant for the assessment of the trap quality is the intensity of the individual traps, given by $I_m = |V_m|^2$. Achieving uniform trap depths becomes especially important in future tweezer experiments where precise control of atomic states is required, particularly when addressing the clock transition or performing Raman cooling schemes. To quantify the trap intensity uniformity, we define the relative tweezer intensity standard deviation as [166]

$$\sigma_I = 100 \cdot \sqrt{\frac{\langle (I_m - \langle I \rangle)^2 \rangle_m}{\langle I \rangle}}, \tag{3.7}$$

where $\langle \cdot \rangle_m$ denotes the average over the trap with index m and $\langle I \rangle$ the mean intensity across the array.

Iterative intensity correction

To generate highly uniform holograms tailored to our target intensity distribution, we employ a Gerchgberg-Saxton algorithm optimizing the parameters (w_m, θ_m) with respect to σ_I. The algorithm involves following steps:

1. Define the positions of each trap m by determining a set of coordinates (x_m, y_m). Assign a random relative phase θ_m^0 to each trap and set the initial trap weight w_m^0 to 1.
2. Calculate a composite phase mask Φ^n using equations (3.4) and (3.5).
3. Calculate the trap amplitudes V_m^n with the diffraction formula given by eq. (3.6).
4. Calculate the new hologram with updated values for the phase offset and amplitude:

$$\theta_m^n = \arg[V_m^n], \tag{3.8}$$

$$w_m^n = w_m^{n-1} \frac{\langle |V_m^n| \rangle_m}{|V_m^n|}. \tag{3.9}$$

5. Insert the new values for θ_m^n and w_m^n and repeat the steps (3) and (4) until the relative standard deviation σ_I^n has reached a threshold (usually a few percent) or until a predefined number of iterations n has passed.

The algorithm iteratively adjusts the trap weights to better approximate the target intensity distribution. This means systematically decreasing (or increasing) the trap weight w_m^n when the trap amplitude $|V_m^n|$ is higher (or lower) than the average trap amplitude $\langle |V_m^n| \rangle_m$.

To optimize the *actual* intensity distribution of the optical tweezers employed in the experiment, we incorporate camera feedback into the GS algorithm using a diagnostics camera. The simplified beam layout is illustrated in Fig. 3.1.

The implementation of the camera feedback procedure is documented in the Master thesis of Jonas Rauchfuß [152] and is briefly outlined here. The protocol for camera feedback requires accurately identifying the positions of the individual traps in the camera image. To accomplish this, we calibrate the mapping from the coordinates of the target image (x_m, y_m) to the corresponding camera coordinates by consecutively generating a spot at three distinct positions, taking an image each time and extracting the transformation factors. This allows us to accurately determine the conversion factor between the pixels on the camera image and the actual positions (x_m, y_m) of the tweezers despite possible rotations of the camera image due to misalignment.

The second step consists of defining a region of interest containing each trap and performing a two-dimensional Gaussian fit to the signal to extract all beam parameters, including the peak intensity, which is used for intensity correction in the GS algorithm. However, this approach does not take experimental imperfections into account, which distort the signal obtained by the camera. A more accurate result can be achieved by using a in-situ trap depth measurements obtained from an atomic signal for a more accurate feedback signal [163].

3.2 High-resolution imaging of SLM tweezer arrays

We now turn to the experimental implementation of SLM-generated tweezer arrays into our apparatus, where we evaluate the optical quality and intensity uniformity of the produced traps. As already discussed, obtaining uniform trap intensities across the array is crucial for providing equal trapping potentials. Light shifts arising because of non-uniform tweezer intensities are detrimental for experiments as it can lead to insufficient photon scattering during detection or could lead to excess heating in the traps. Further, the achievable beam waist of the optical tweezers and thus the trapping depth depends on the optical quality of the microtraps.

In this section, we first apply the previously described Gerchberg-Saxton alogrithm for a 8×8 rectangular array at 759 nm and investigate its performance. We assess the optical quality of the traps by imaging the trapping beam along its optical axis and performing a wavefront analysis using a Shack-Hartman sensor. We conclude the chapter by demonstrating various trapping geometries.

3.2.1 Characterization of in-situ SLM-generated trap potentials

For our characterization measurements of the optical tweezers, we record the resulting intensity distribution after transmission through the science cell using a CMOS camera. The optical layout is illustrated schematically in Fig. 3.1. Note, that we use additional optics for expanding or reducing the beam size, which are not included in the schematics for visual clarity.

Optimizing trap intensities

We start by calculating a computer-generated hologram (CGH) using the composite phase mask approach, where we input random starting phases and uniform amplitudes. Our target image is a rectangular 8×8 - array. The resulting trap intensities after displaying the CGH onto the SLM are shown in Fig. 3.4a. The initial standard deviation σ_I for this set of tweezer spots is 16 %, where the darkest spot is 65 % as bright as the mean tweezer intensity, whereas this value is 170 % for the brightest trap.

After obtaining the initial intensity distribution, we now run the GS algorithm. In each iteration n of the algorithm, the relative trap intensities I_m^n of each trap m are extracted from the camera image and used as feedback for adjusting the weighting factors of each elementary phase mask. Figure 3.4b shows the trap intensities across the array after 19 iterations of the GS algorithm, achieving a relative tweezer intensity standard deviation of 1.8 %.

Figure 3.4c shows the intensity non-uniformity across the array as a function of the GS iteration index. To further reduce system-induced inhomogeneities[1], we modify the algorithm described in Sec. 3.1.2 by incorporating a phase-fixed technique [165]. In this approach, the phase θ_m is held constant beyond iteration n of the GS algorithm. In our case, the phase is fixed from iteration 14, indicated by the orange line in Fig. 3.4c. This constraint helps to reduce system-induced non-uniformities more efficiently by avoiding additional phase rotations, resulting in faster convergence compared to the traditional GS algorithm and enabling higher degrees of uniformity.

In a separate test setup, we achieved standard deviations of below 0.5 % across rectangular tweezer arrays as large as 9×11 using the phase-fixed approach. A description of the optimized algorithm and its implementation can be found in the Master thesis of Carina Hansen [168]. The measurements further indicate that the performance of the GS algorithm is ultimately constrained by the camera's noise floor. Improving the imaging conditions could therefore yield even more homogeneous tweezer arrays.

A caveat to the direct measurement of light potential via a camera in a dedicated optical analysis setup is that the algorithm only takes the intensities into account that are measured by the camera. Therefore, any optical elements located between the optical tweezers generated by the microscope objective and the diagnostics camera can introduce aberrations that distort the recorded image of the traps.

By analyzing the wavefront of each of the employed optical surfaces, the SLM can be utilized to compensate for any distortions that might impair the actual intensity uniformity and the optical quality of the trap. Aberration correction is performed by adding phase patterns of the corresponding Zernike polynomials to the existing holograms [70]. However, an unknown component is introduced by the optical surfaces of the glass cell because we can only measure the wavefront after transmission through *both* optical windows[2]. A more promising and accurate approach relies on probing an atomic signal to infer the light shifts induced by the trapping light, as has been successfully demonstrated in Ref. [163]. This technique was not integrated into the experimental setup during the course of this thesis but is planned for future work.

Imaging of a single SLM-generated optical tweezer

We now analyze a single optical tweezer generated by our SLM Setup. Figure 3.5 shows the results of an axial scan, where we have recorded images of the tweezer at different positions along the optical axis using our diagnostics camera.

---

[1] We further noticed intensity variations on our camera images arising from interference effects caused by the camera's cover glass, which distorted the results obtained using the GS algorithm. To eliminate this issue, we removed the cover glass and no longer have this problem.

[2] We have measured the wavefront after transmission through the glass cell and have observed minimal wavefront errors with a wavefront rms of 0.9 % λ, which is a promising result.

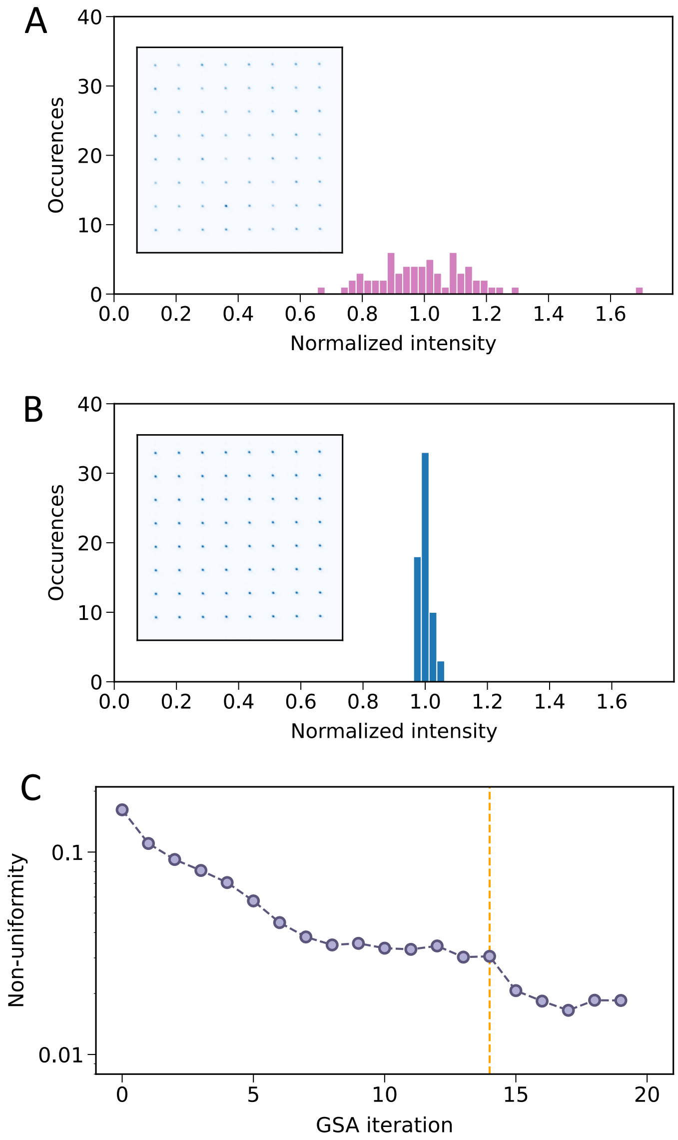

Figure 3.4 | Trap uniformity of a 8×8 array. Improvement of the trap intensity uniformity across a 64-site array using a Gerchberg-Saxton (GS) algorithm. **(A)** Histogram of the relative intensity levels in the initial tweezer array with a standard deviation σ_I of 16 %. The array is obtained by displaying an initial CGH of the target intensity pattern onto the SLM. The inset shows the intensity distribution recorded with the diagnostics camera. **(B)** Histogram of the intensity levels and image (inset) of the same array after performing 19 GS iterations, yielding a relative tweezer intensity standard deviation of 1.8 %. **(C)** Intensity non-uniformity across the tweezer array as a function GS iteration index. Using a fixed-phase approach, the phase is kept constant from iteration 14 onward, indicated by the orange line (see main text for more information).

When moving away from the focal plane, we observe faint concentric rings around the center of the beam. This effect is caused by diffraction of the Gaussian input beam caused by clipping of the beam at the entrance of the microscope objective. As a result, the beam shows characteristics of an Airy disk intensity profile. In the limit of an input beam with plane wavefronts, the microscope objective will produce the smallest possible spot, which is then referred to as *diffraction-limited*.

In reality, the objective is not illuminated uniformly since the input laser beam has a Gaussian intensity profile and the beam is clipped by an aperture[3]. The produced tweezer will therefore be obtained by convolution of the Gaussian beam with the corresponding point spread function of the imaging system.

At each position, we extract the peak intensity and plot this value against the axial position, shown at the bottom of Fig. 3.5. We fit the data using the following function

$$\sigma(z) = \sigma_0 \cdot \mathrm{sinc}\left(\frac{\pi(z - z_0)}{2\delta_z}\right)^2, \tag{3.10}$$

where z is the axial position, z_0 the location of the focal plane and δ_z characterizes the width of the curve. We find that the data is well described by the model. We extract a width of $\delta_z = 4.7 \pm 0.2\,\mu\mathrm{m}$, which quantifies how tightly focused the beam is and is relevant for the ability to trap atoms.

In the focal plane, the optical tweezer is well-approximated by a Gaussian intensity profile. We extract beam waists $w_{0,x} = 766 \pm 9\,\mathrm{nm}$ and $w_{0,y} = 695 \pm 8\,\mathrm{nm}$ for the horizontal and vertical directions, respectively. The diffraction limited spot size (at the $1/e^2$ level) is given by

$$w_{\mathrm{diff}} = 0.41 \frac{\lambda}{\mathrm{NA}}, \tag{3.11}$$

where λ is the wavelength of the trapping light and NA the numerical aperture of the microscope objective, which is 0.5 in our case. Similarly, we can determine the length scale along the propagation axis at which the peak intensity has dropped to the $1/e^2$-level

$$\delta_{\mathrm{z}} = 1.4 \frac{\lambda}{\mathrm{NA}^2} \tag{3.12}$$

For a trapping wavelength of 759 nm, the smallest achievable spot size according to eq. 3.11 is 622 nm in our setup. For δ_z we expect a minimal value of about $4.3\,\mu\mathrm{m}$, which is in accordance to the measured value of $\delta_z = 4.7 \pm 0.2\,\mu\mathrm{m}$.

However, there is a trade-off between achievable spot size and transmitted optical trapping power: If we want to uniformly illuminate the objective to achieve small spot sizes, a large portion of the Gaussian input beam will be blocked at the entrance of the objective. To quantify the relationship between the Gaussian input beam w_0

---

[3] In the experiment, the beam passes a circular aperture to reduce unnecessary illumination of the microscope objective, which can cause fluorescence emitted by the housing material. This effect is particularly detrimental when using 532 nm tweezers since this is the same wavelength that is used for fluorescence imaging, resulting in a significant increase in background noise in the atomic signal

and the radius of the input aperture r, i.e. the clear aperture of the objective, we define the fill fraction given by $F = w_0/r$. In the limit, where the Gaussian input beam w_0 is much smaller than the clear aperture of the objective r, most of the power will be transmitted through the objective but the spot size produced by the objective will be larger than the diffraction-limited tweezer size. Conversely, in the limit of a uniformly-illuminated input beam, that is $F \to \infty$, we expect to achieve a diffraction-limited spot size.

Assuming a fill fraction of $F = 1$, i.e. the beam is cut off at the waist of the Gaussian input beam, we can calculate an expected a spot size that is about $10.5\,\%$ larger than the diffraction limit given by eq. 3.11. Following the argumentation in Ref. [169], a good compromise is to choose $F = 0.9$, where the trapping depth has its optimum. Using standard Fourier optics, we estimate that at this filling fraction, the resulting spot size is approximately $11.8\,\%$ larger than the diffraction-limited value. This suggests that an additional $5\,\%$ reduction in tweezer size would yield the optimal spot size and thus optimize the trap depth.

Wavefront analysis

Optical aberrations can lead to a decreased peak intensity and can introduce shape non-uniformities across the array, leading to reduced trapping capabilities.

Here, we directly probe the wavefront of an SLM-generated optical tweezer produced by our apparatus. For this measurement we use a Shack-Hartman sensor (Imagine Optics, HASO4 Broadband) and the beam geometry depicted in Fig. 3.1, allowing us to detect deviations from an ideal, plane wavefront. Such devices consist of a microlens array and a camera sensor located in the focal plane of the microlenses. Tilts in the incoming wavefront produce displacements in the individual focal spots from which the wavefront errors can be reconstructed. The resulting optical aberrations are described in terms of Zernike polynomials, which are a set of orthogonal functions [170].

Figure 3.6 shows the results from the wavefront measurement of a single trapping beam. The RMS wavefront error across the entire beam is $0.107\,\lambda$ with a peak-to-valley error of $0.516\,\lambda$. Figure 3.6a shows the extracted Zernike coefficients in units of the trapping wavelength. Here, we have omitted the first three terms corresponding to tilt and focus, which are solely determined by the positioning of the sensor relative to the beam. Figure 3.6b shows the corresponding wavefront, which is reconstructed using the Zernike coefficients on the left.

The beam introduces moderate wavefront errors, with the most prominent aberration being oblique astigmatism, which can be further reduced by improving the alignment of the optical elements. Higher order terms most likely arise from manufacturing imperfections of the utilized optical elements. In principle, the remaining aberrations could be compensated by the imprinting the appropriate phase pattern onto the SLM to cancel the present wavefront distortions, however subsequent optics after the science

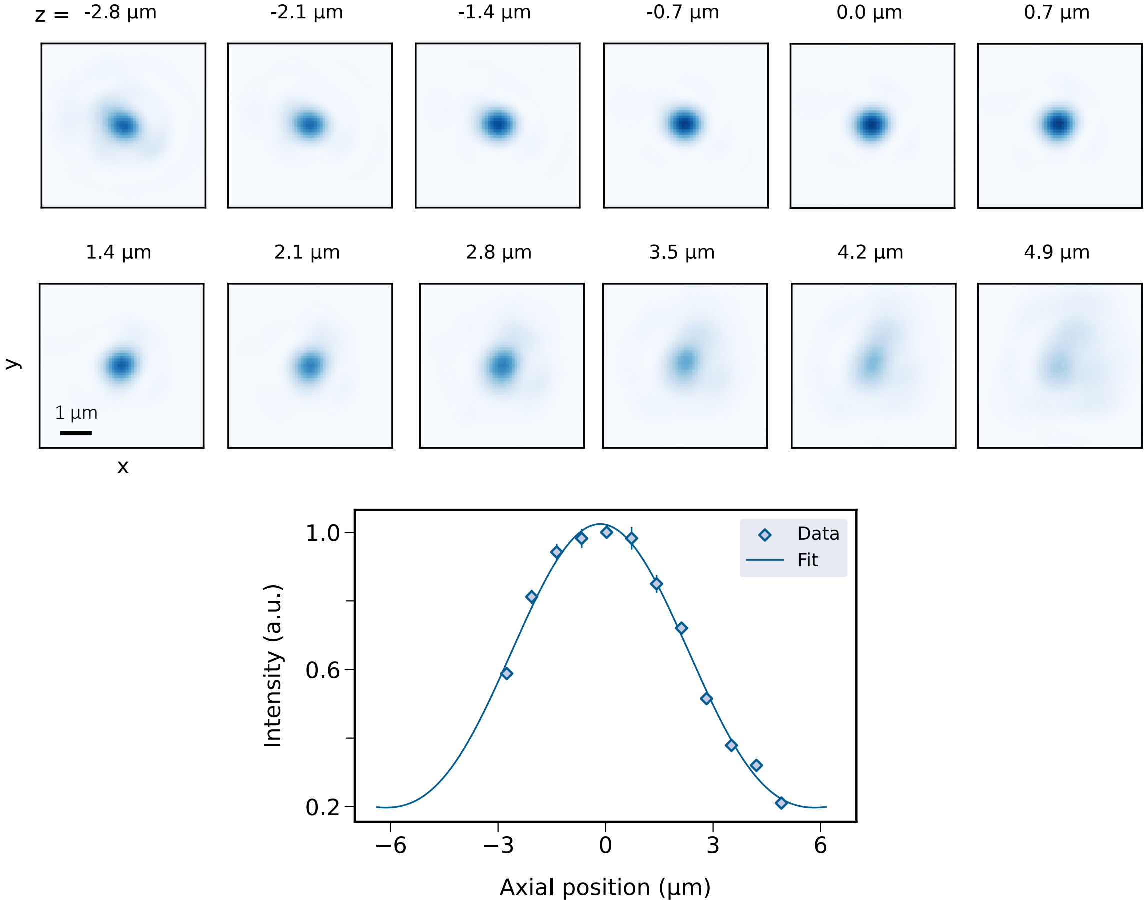

Figure 3.5 | Axial scan of a single SLM-generated optical tweezer. (Top) Images of a single SLM tweezer from an array at different positions z along the optical axis. (Bottom) Normalized peak intensity as a function of the axial position z. The intensity of each tweezer image is computed by averaging over a center region of 4x4 pixels. See main text for the fit function. The width is characterized by $\delta_z = 4.7 \pm 0.2\,\mu\mathrm{m}$.

cell affects the wavefront measurement. A more reliable method would be to use an in-situ atomic signal as feedback.

Gallery of array geometries

Figure 3.7 shows a selection of tweezer geometries we have implemented, demonstrating the versatility of SLMs. For each configuration, we show the target intensity distribution recorded with the diagnostics camera (left), the corresponding phase pattern (middle) and an averaged fluorescence image (right) obtained by loading single ^{171}Yb atoms into the traps and averaging over 60 images.

Of particular interest for quantum information applications are dimer systems. Fig 3.7a shows a two-dimensional array composed of pairs of atoms. By allowing the dimers to interact controllably, it allows for the implementation of two-qubit gate-based

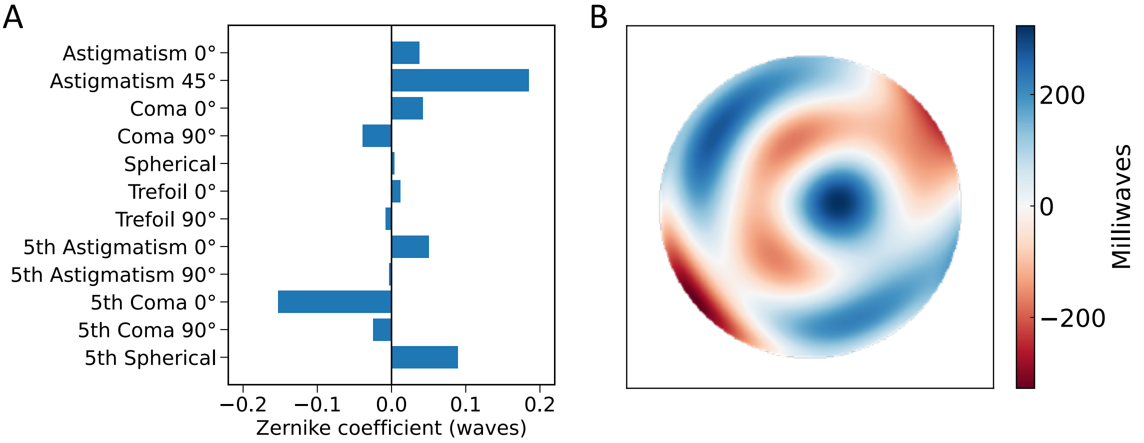

Figure 3.6 | Wavefront analysis using a Shack-Hartman sensor. Measurement of the wavefront of an SLM-generated tweezer trap after transmission through the science cell and optical system. **(A)** Extracted Zernike coefficients of the wavefront, each representing a type of optical aberration. **(B)** Reconstructed wavefront in units of the trapping wavelength (759 nm), with an RMS wavefront error of 0.107 λ and a peak-to-valley error of 0.516 λ.

operations. In our setup we achieve a minimal tweezer spacing of about 3.5 µm at which the spots are well-separated with negligible interference between them [152].

One-dimensional systems with boundary conditions can be realized, as shown in Fig. 3.7. Octogonal ring arrays can be implemented to study phenomena such as transport, thermalization or phase transitions [171].

We also demonstrate the ability to create different non-trivial lattice geometries, which can be useful to explore various phenomena in 2D. Most notably this includes honeycomb (Fig. 3.7c), triangular (Fig. 3.7d) [94, 172] or Kagome lattices [96], allowing the study of Graphene, frustration or topological spin liquids.

The ability to create arbitrary tweezer geometries opens up the possibility of encoding and solving graph-theoretical problems by employing quantum annealing protocols.

3.3 Summary and outlook

In this chapter we presented the successful generation of uniformly illuminated arrays of optical tweezers using a spatial light modulator (SLM).

We first discussed the design of computer-generated holograms to produce arbitrary two-dimensional target intensity trap patterns of up to 64 sites. We proceeded with the implementation of a modified Gerchberg-Saxton algorithm with camera feedback to optimize the trap intensity uniformity across an array, thereby reducing the standard deviation across an 8×8 array from 16 % to 1.8 %. Substantial improvements to the intensity uniformity can be made by directly probing an atomic signal to infer the light shifts induced by the trapping light as demonstrated in Ref. [163]: This approach

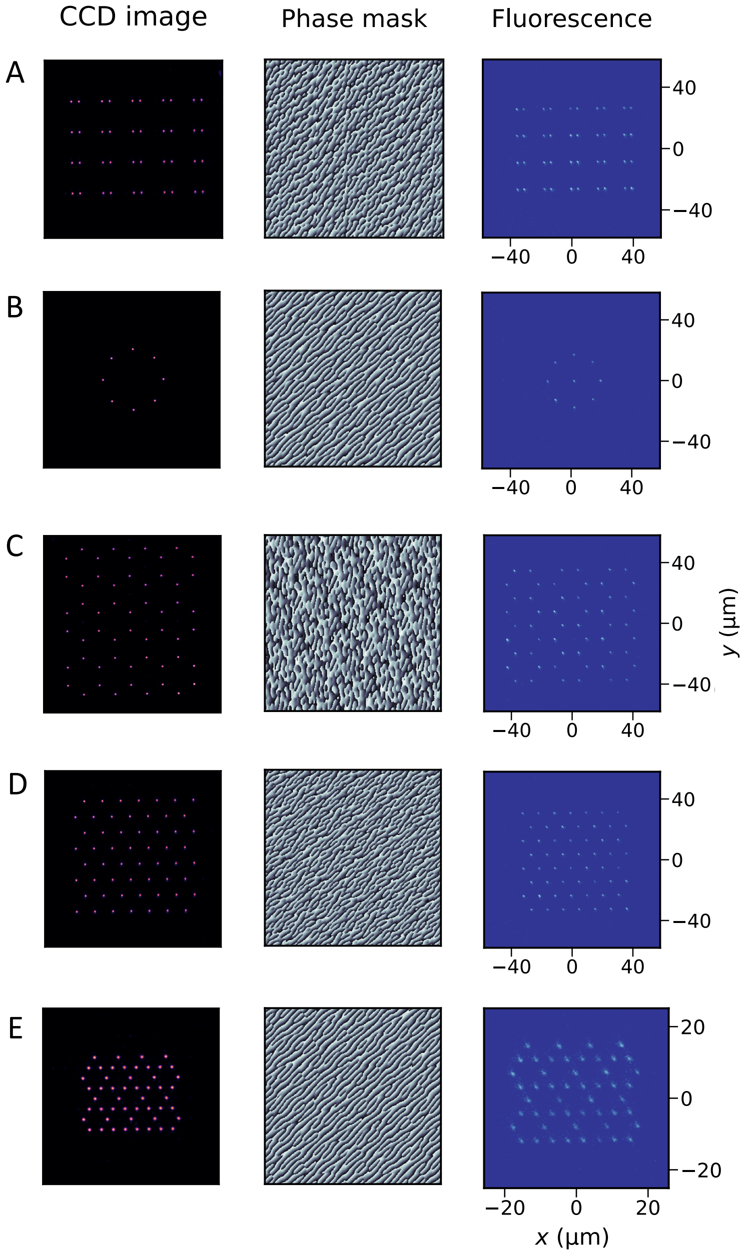

Figure 3.7 | Tweezer geometry gallery. A selection of tweezer geometries generated by an SLM. The right images show the intensity pattern measured on a diagnostics camera after running a GS algorithm to produce uniform trap intensities. The images in the middle show the corresponding phase pattern displayed in the SLM. The images on the right are averaged fluorescence images obtained by loading single ^{171}Yb atoms into the traps. The images are averaged 60 times. The depicted geometries include **A** dimers on a 2D grid, **(B)** a ring with 8 atoms, **(C)** a honeycomb lattice, **(D)** a triangular lattice and **(E)** a Kagome lattice.

eliminates errors arising from distortions of the camera image used for feedback caused by optical elements between the science cell and the diagnostics camera.

To assess the optical quality of the SLM-generated traps, we analyzed the intensity distribution along the axial direction of the trapping beam, suggesting near diffraction-limited performance of our system. We measured a spot size of $w_0 = 731\,\mathrm{nm}$, which is only about $17\,\%$ larger than the theoretical diffraction limit for our system. We also performed a wavefront analysis of a single tweezer beam, obtaining a wavefront RMS deviation of $\delta_{\mathrm{rms}} = 0.11\,\lambda$ after propagation through the entire optical system. Further improvements can be achieved by optimizing the alignment of the optical system and using the SLM as a corrective element to compensate for the measured wavefront distortions by imprinting an appropriate phase pattern [70]. With appropriate improvements, such as optimized imaging conditions, an intensity uniformity of $< 0.5\,\%$ is in reach, as demonstrated in one of our test setups [168].

Finally, we demonstrated the loading of single ^{171}Yb atoms into different tweezer geometries, showcasing the flexibility of this approach.

The next viable step consists of combining this SLM-based approach with the already implemented AOD-generated tweezer setup in order to add the capability of atom-by-atom reconfiguration to produce near-deterministically loaded arrays.

Other future improvements include the upgrade to a high-speed SLM, which could be utilized for parallel atom rearrangement or site-specific excitation [173], thus overcoming the limitations that experiments face, when employing AODs for these tasks.

Chapter 4

Experimental Platform

Optical tweezer experiments combine laser-cooling techniques with single-atom control to provide a versatile platform ideally suited for engineering isolated and well-controlled programmable quantum systems. This chapter describes an apparatus for cooling, trapping and manipulating individual Yb atoms. We present a new tweezer experiment based on a previous machine, originally designed for studies of ultracold quantum gases of ytterbium, as described in [174].

In the first part, we discuss the key components of our optical tweezer experiment, including the science cell, generation of magnetic fields and high resolution imaging.

The second part of this chapter provides an overview of the experimental apparatus where we present the layout of the main experiment. We give a detailed description of the individual laser systems, prior to being guided to the main experiment. These include the laser setups for operating a 2D/3D magneto-optical trap (MOT), high-fidelity single-atom imaging and optical tweezer generation.

The newly built experimental tweezer platform described here serves as a foundation for future explorations of quantum model systems or quantum information processing with alkaline-earth neutral atom arrays.

The design of the experiment has been conceptualized by the entire team. The main experiment has been built by T. Petersen and the author. The individual laser systems were built in a team effort.

4.1 Tweezer experiment components

Here, we discuss the core components that form the backbone of our optical tweezer experiment with Yb atoms. We summarize key features of the ultra-high vacuum (UHV) glass cell, in-house built magnetic field coils and a set of custom-designed high numerical aperture microscope objectives.
Figure 4.1 shows a model of the experimental apparatus. The optics is located on multiple bread boards, extending over several levels. We distinguish between the optical table, the main breadboard on the level of the science cell and two upper

breadboards located above the science cell. The inset showcases the core of the experiment. This includes the UHV science chamber in the center, the main magnetic coils as well as compensation coils and two microscope objectives.

4.1.1 Science cell

The central element of the apparatus is a fused silica science glass cell cuvette from Hellma with dimensions 26 mm × 36 mm × 80 mm and a window thickness of 3 mm. The glass cuvette has been manufactured by optically contacting the surfaces instead of using glue, which allows higher baking temperatures and an improved vacuum quality. The tweezer experiments are conducted in an ultra-high vacuum environment to reduce atoms loss due to background collisions. The rectangular design of the glass cell allows for excellent optical-access. The exterior surfaces of the glass cuvette are coated with a broadband anti-reflection (AR) coating (390 nm - 950 nm). The top facet of the fused silica cuvette remains uncoated, offering a broad transmission range for UV to IR wavelengths. Thus we let the UV beams at 302 nm and 369 nm propagate through this surface.

The science cell is part of a 2D/3D MOT system, comprised by a 2D-MOT glass cell and the 3D-MOT science cell, connected via a differential pumping tube to decouple the vacuum present in each glass cell. Ytterbium atoms in form of vapor are emitted from a dispenser (Alvatec, AS-4-Yb-500-S) in the 2D-MOT chamber. Hot Yb atoms are released through a slit to prevent the ytterbium vapor from depositing on the inside surfaces of the 2D-MOT glass cell.

The vertical arrangement of the 2D-/3D-MOT system allows for efficient transfer of pre-cooled atoms generated in the 2D-MOT which fall under gravity through the transfer stage and into the 3D-MOT science chamber for further laser cooling and for performing experiments. The 3D-MOT cell is connected to a CF flange by a glass-to-metal transition and attached to the main chamber.

The vacuum system remains unchanged to the first-generation setup and a detailed description of the assembly can be found in Refs. [175] and [174].

Since our cuvette's windows are rather thin (3 mm) compared to typical glass cells employed in tweezer experiments (∼5 mm), the effect of glass cell deformation under vacuum conditions is more pronounced. For a finite element analysis of our glass cell and further characterization measurements, see Ref. [154]. Wavefront measurements of the evacuated glass cell reveal a RMS wavefront error of $< \lambda/100$ across the entire smaller (26 × 80) mm facet of the cuvette, suggesting sufficiently high surface flatness for enabling diffraction-limited performance of the microscope objective. Conversely, the larger (36 × 80) mm facets show a larger RMS wavefront error of $\sim \lambda/4$ across the entire window. Thus, we perform high-resolution imaging through the smaller facets of the glass cell.

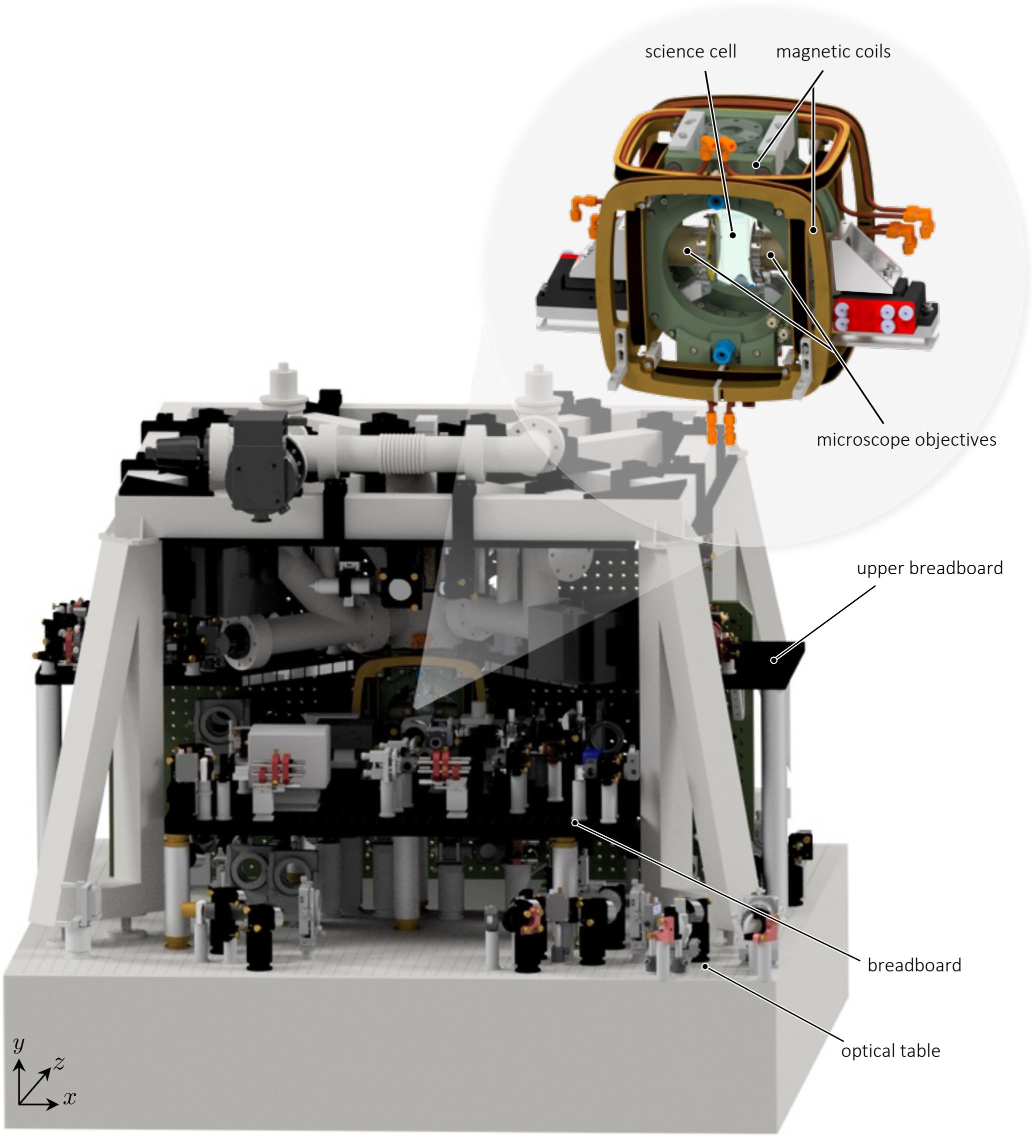

Figure 4.1 | **Experimental apparatus.** Model of the main experimental apparatus with a detailed view of the science chamber. The optics is located across several levels of the experiment - the optical table, a breadboard and two upper breadboards. The inset shows the ultra-high-vacuum glass cell, two microscope objectives and magnetic field coils. For details on the components, see main text.

A widely used alternative to our glass cell design is the use of octagonal glass cells from e.g. Precision Glassblowing with nano-textured AR coated windows, which allows for broadband applications.

4.1.2 Magnetic field

Magneto-optical trapping and manipulation of atomic states requires a DC magnetic field. We use a pair of 'primary coils' arranged in Helmholtz configuration to apply a magnetic field gradient and for defining a quantization axis. The primary coils are manufactured from ULTEM, which is non-magnetic and known for its mechanical stability. To account for stray fields, we use three pairs of compensation coils arranged around the glass cell.

The coils are designed with the consideration to produce a uniform magnetic field on relevant length scales which is on the order of a few 100 µm. Here we show magnetic field simulations for both the primary and compensation magnetic coils utilized for the designing process. Since the objectives need to fit in between the primary magnetic coils, the distance between them are constrained by the diameter of the objectives.

Primary Coils

Depending on the application, the primary coils are operated in Anti-Helmholtz configuration to provide a magnetic field gradient for trapping and laser-cooling atoms in a 3D magneto-optical trap or in Helmholtz to generate a strong magnetic field of up to 500 G. To handle large thermal loads, the primary coils feature water-cooling. The mechanical design of the primary magnetic field coils is shown in Fig. 4.2a. The coils consist of cooper diameters with 2.1 mm diameter thickness spaced by 0.5 mm and are looped in a 8×6 configuration (see Fig. 4.2b). The magnetic field strength at current I along the axial direction z of a pair of coils $i = (1, 2)$ separated by distance D with N axial layers each and radii R_i is given by

$$B(z) = \frac{\mu_0 N I}{2}\left(\frac{R_1^2}{(R_1^2 + (D/2 - z)^2)^{3/2}} + \frac{R_2^2}{(R_2^2 + (D/2 - z)^2)^{3/2}}\right), \tag{4.1}$$

where μ_0 is the permeability of free space. To achieve a uniform field, coils are operated at in Helmholtz configuration where $R_i = D$. Because our goal is to generate a strong magnetic field, the wires are looped in radial and axial layers and the Helmholtz condition is modified slightly. To ensure a uniform magnetic field over a sufficient volume ($\sim (100\,\mu\text{m})^3$) at the center of the coils where experiments will take place, we perform simulations to determine optimal coil radii R at given distance D for the coil design based on Ref. [174].

Figure 4.2c shows the magnetic field along the axial direction x at current $I = 1$ A for different radii R using eq. 4.1. The distance is kept constant at 77 mm. Note, that here R is defined as the radius of the inner most loop. Shown is the magnetic field generated by the individual coils and the total magnetic field. Because we want to optimize the uniformity, we compute the slope of the B field at the center as a function of R. The curvature is determined by a quadratic fit. In our setup, the uniformity is maximized at $R = 97$ mm. Figure 4.1e shows the deviation of B from the center value within an 8 mm interval for $R = 79$ mm, confirming that the choice of coil parameters should offer sufficient uniformity on length scales of our experiments. The final design and implementation of the primary coils as well as measurement of the resulting magnetic field can be found in Ref. [154].

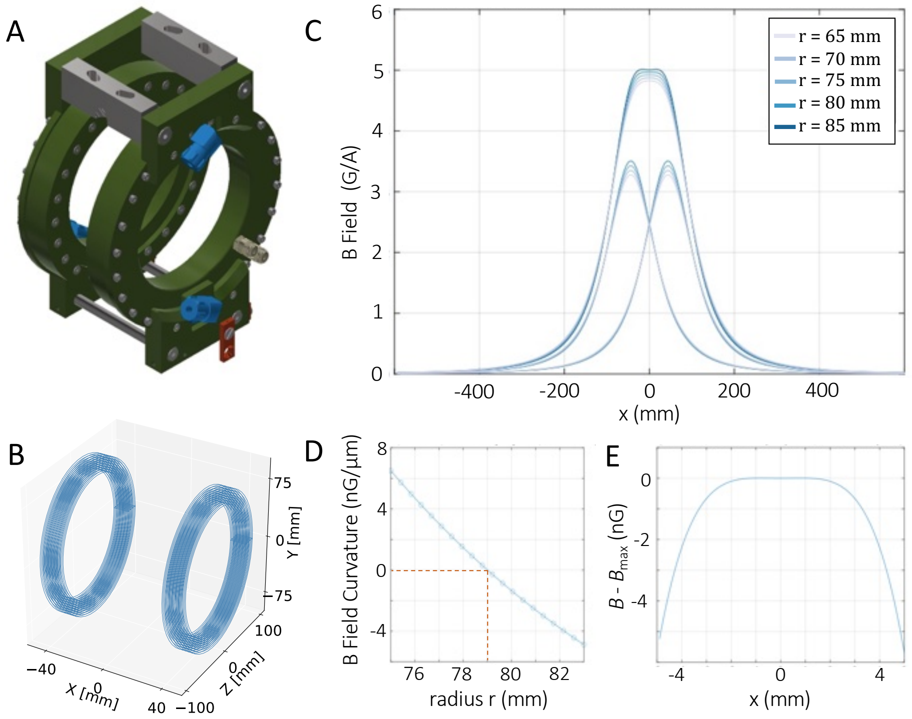

Figure 4.2 | Primary magnetic field. Simulations of the magnetic field to determine the optimal parameters for the coil pair. **(A)** Mechanical design of the resulting primary coils made from ULTEM and featuring water cooling. **(B)** Model of the wire loops arranged in 8 radial and 6 axial layers. **(C)** Simulated magnetic field generated by the individual coils (left and right) and the resulting magnetic field along the axial direction for different loop radii R at current $I = 1\,A$. The distance between the coils is fixed as it is constrained by our mechanical setup. **(D)** Slope of the magnetic field at $x = 0$ approximated by a parabola as a function of coil radius R. **(E)** Magnetic field along x in an 8 mm interval for R = 79 mm.

Compensation Coils

To compensate stray fields and produce an offset field, we utilize three orthogonal pairs of coils, referred to as X, Y, Z compensation coils corresponding to the coordinate system for our experiment (see Fig. 4.1). The mechanical design of the compensation coil cage is presented in Fig. 4.3a. Each compensation coil consists of three cooper wire layers. A description of the design and engineering process can be found in [154]. The design of the coils was primarily determined by the tight space constraints at the experiment. A computation of the axial magnetic field generated by each compensation coil is shown in Fig. 4.3b-d.

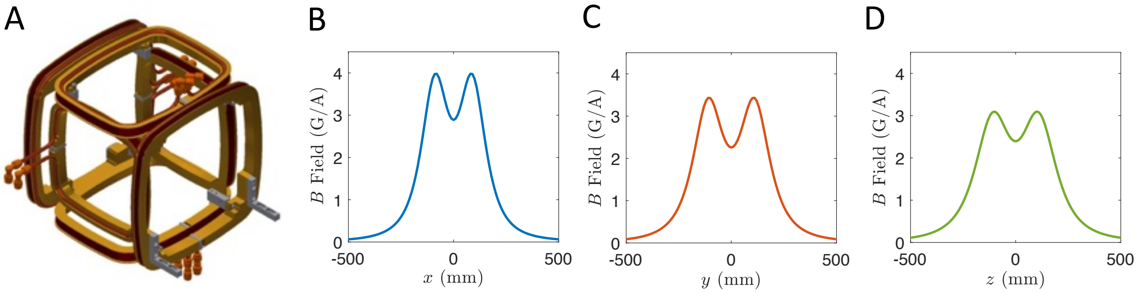

Figure 4.3 | Compensation coils. (A) Mechanical design of the compensation coils for generating offset fields. **(B-D)** Simulated axial magnetic field generated by the X, Y and Z compensation coil pair, respectively.

4.1.3 Microscope objectives

We use a custom-designed microscope objective from Special Optics to generate tightly focused spots and image single atoms. For re-collimation and imaging of the trapping beam we use a second objective, with identical imaging properties. Here, we summarize some of the most important characteristic of our high resolution imaging objectives.

The numerical aperture (NA) of our objectives is specified as 0.5, allowing us to achieve tightly confined trapping potentials and sufficient resolution for single-atom imaging. It allows for diffraction-limited operation within a field of view of 282 µm.

Given the geometric restrictions at our experiment, the objectives are designed with a working distance of 20 mm. At given NA, the longer working distance results in a larger entrance pupil of 28 mm, which requires us to use 2-inch diameter optics upstream the laser system to adapt the beam size to the aperture. The effective focal length is 28 mm. Further, the objectives are corrected for a fused silica glass window thickness of 3 mm.

The use of a wide range of wavelengths in the context of the experiments, requires sufficient transmission for 399-759 nm through the objective, while also maintaining diffraction-limited performance at these wavelengths. We achieve transmission efficiencies of above 91 % for 556-759 nm and 71 % for 399 nm. The chromatic focal shift is specified as 6 µm across the entire wavelength range, however measurements suggest a focal shift of 15 µm between 399 nm and 759 nm.

The objectives are manufactures from ULTEM, which is a non-magnetic material. This is important, as the objectives are located in between the primary magnetic coils, which produce high magnetic fields. The housing diameter of 45 mm imposed restrictions on the design of the magnetic coil.

Measurements of the numerical aperture, transmission characteristics and the chromatic focal shifts were performed in a test setup after receiving the objectives and are presented in Ref. [176]. Direct measurements of the point-spread function for 556 nm and 759 nm tweezers are shown in Ref. [154].

We use a second objective to image the resulting tweezer beams. It has identical imaging specification, however it has a hole of 3 nm diameter drilled along its optical axis. The reason behind this is that it can be potentially used for guiding a global UV-beam (or other beams for global addressing) through the objective, while protecting the objective's lenses from UV-induced damage.

4.2 Laser systems

Here we describe the laser setup of the Yb tweezer experiment. We first present the design of main experiment, which comprises the optical setup centered around the science cell. We then give a detailed description of the individual laser systems, in particular for providing light to the 2D and 3D MOT, the imaging and tweezer generation of both AOD and SLM-based setups.

4.2.1 Optical design of the main experiment

In this section we present the optical layout of the main experiment centered around the science chamber. In order to fully utilize the optical access surrounding the glass cell, the experiment extends over multiple levels.

Optical table

We first discuss the laser setup on the optical table, which includes laser systems for tweezer generation. It features both SLM- and AOD-based setups for generating tweezer trapping potentials. Figure 4.4 shows a schematic of the optical setup. In this work, we primarily focus on SLM-generated tweezers and only briefly outline the AOD-based setup. For a detailed description on the AOD-based optical tweezer system, see Ref. [154]. The SLM-setup is operated with 759 nm laser light. The light is guided to the main experiment via a PM fiber and exits the fiber using a collimator (Schäfter+Kirchhoff 60FC-L-4-M75-02). A built-in circular aperture allows us to clip the beam at 12 mm to adapt the beam size to the SLM chip. We use a Hamamatsu liquid crystal on silicon SLM (X15213-02). For optimal operation, the SLM requires incident light with horizontal polarization which is parallel to the plane of incidence. We therefore tune the polarization state of the beam appropriately using

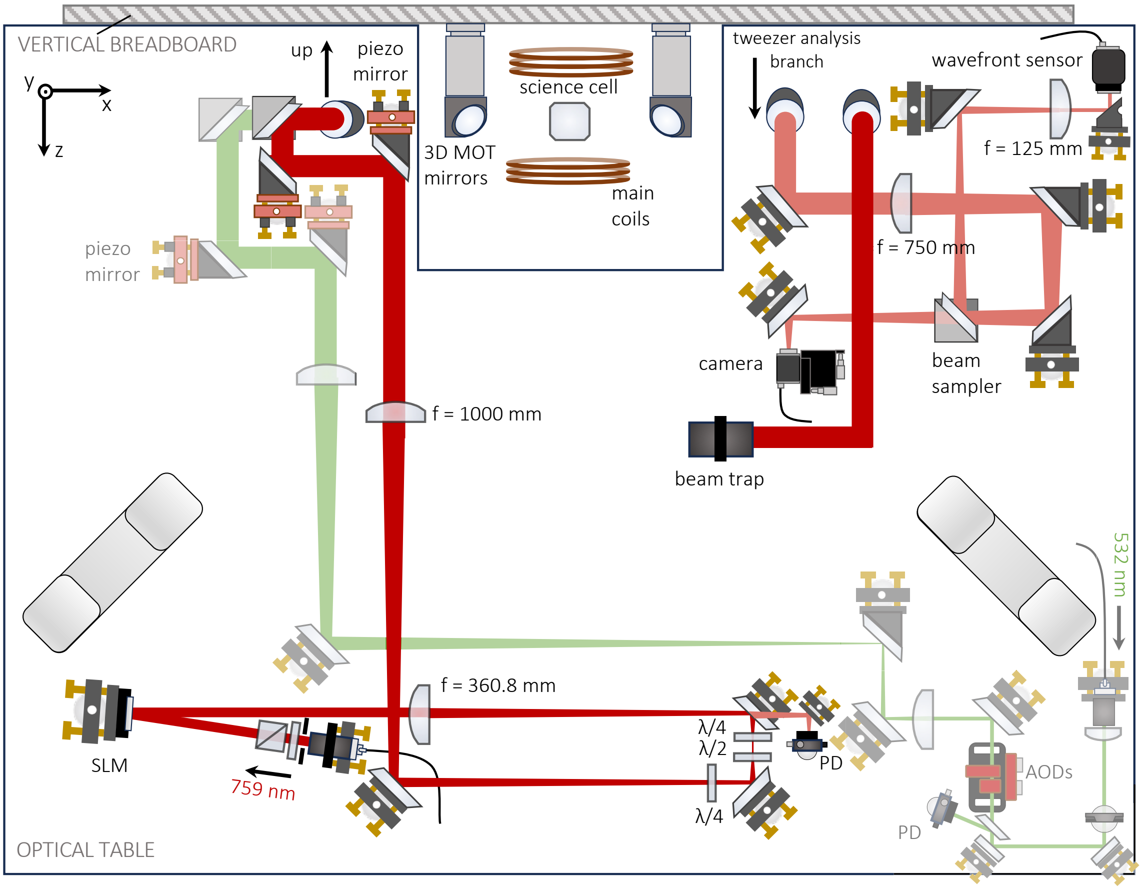

Figure 4.4 | Main experiment beam layout (optical table). Schematic of the main experiment located on the first (bottom) level. The setup includes laser systems for both SLM- and AOD-based tweezer arrays. SLM-tweezers are generated with laser light at 759 nm exiting a fiber (red). The beam diameter is reduced to 12 mm using an aperture. The polarization is tuned using a half-wave plate and polarizing beam splitter. The incidence angle on the SLM is 6°. The beam is expanded with a $1:2.8$ telescope. Transmission through a mirror is used for power monitoring. The polarization state is tuned with half- and quarter waveplates. Fine-alignment is accomplished with piezo actuated mirror mounts. The beam is reflected at a dichroic mirror, sent to the upper level (along $y-$axis). After passing the science cell (not shown here), some light is picked off for imaging and wavefront-measurements. Remaining light is redirected to a beam trap. The AOD laser system (green) is shown with reduced opacity.

a polarizing-beam-splitter (PBS) and a half-wave plate. The beam is directed onto the SLM at an incidence angle of 5 °, as specified by the manufacturer. The SLM head is mounted on a kinematic mirror mount baseplate and offers tip and tilt adjustments using precision adjustment screws. After reflection off of the SLM, we adapt the beam size to the aperture of the microscope objective using a 1:2.8 telescope.

We expand the beam from 12 mm to 28 mm using plano-convex lenses with focal lengths $f_1 = 360\,\mathrm{mm}$ and $f_2 = 1000\,\mathrm{mm}$, respectively. We opt for lenses with excellent surface quality ($\lambda/10$) from CVI Laser Optics and large focal lengths to mitigate aberrations. As optimal alignment of all optical components is critical for producing high-quality optical tweezers, the telescope lenses are mounted in precision multi-axis lens positioners (LP-2A, Newport). We place the first lens of the telescope at a distance $d = f_1$ after the SLM to make sure that the SLM plane and back focal plane of the objective are conjugate. To avoid clipping and the need for large polarization optics, we place two quarter-wave plates a a half-wave plate near the focal point of the telescope. This allows us to tune the polarization to achieve a first-order magic trapping condition for the $^1\mathrm{S}_0 \leftrightarrow {}^3\mathrm{P}_1, F' = 3/2, m_F = -1/2$ transition in ^{171}Yb. We orient the tweezer polarization at the magic angle of 17 ° with respect to the magnetic field B, which is consistent with Ref. [126]. After the beam expander, we use two piezo-actuated mirror mounts (8821, New Focus) for increased alignment precision and the possibility of remote operation. The SLM-beam is combined with the AOD laser setup (shown in reduced opacity) at a custom dichroic mirror from Laseroptik that reflects 740-800 nm and transmits 500-650 nm. The combined beams are redirected along the y-axis to a breadboard on an upper level of the experiment. After propagating through the glass cell, the tweezer beam is reflected back to the optical table where we perform measurements of the tweezer array to assess the optical quality. For this analysis a small portion of the beam is picked off by a nano-textured beam sampler. The remaining light is redirected to a beam trap. The beam is split once again in two optical paths. A portion of the light is used to image the optical tweezers on a CMOS camera (acA3088-57um, Basler) using a $f = 750\,\mathrm{mm}$ achromatic lens, shared by both optical paths. We removed the sensor's cover glass that the camera came with because it caused Newton's rings on the images. The second optical path is redirected to a Shack-Hartman sensor (HASO4 BroadBand, Imagine Optic), which measures the wavefront of the beam. This allows us to directly identify aberrations present in the optical tweezer beam as well as to aid the alignment process of the microscope objective. As the wavefront sensor operates with collimated light, we use a $f = 125\,\mathrm{mm}$ achromatic lens for re-collimation and in order to adapt the beam diameter to the sensor's size. We now proceed with the optical layout on the second level of the experiment.

Optical breadboard

Figure 4.5 shows the laser setup on the main breadboard located in the horizontal plane containing the science cell. Here, the microscope objectives are located, all beams are combined and MOT as well as single-atom imaging is performed.

First, we continue the description of the optical path for SLM-based optical tweezer potentials. After the laser beam is launched from the optical table onto the breadboard, it is reflected by a dichroic mirror that reflects 532+759 m and transmits 399+556. The beam is then focused down into the glass cell by a high NA microscope objective. A second, identical microscope objective is used for re-collimation [1]. Both objectives are mounted on a multi-axis piezo-actuated stage (8081, Newport) to allow for precise optical alignment, which is imperative for achieving diffraction-limited spots. The objectives are located between the two primary magnetic coils, which generate a DC magnetic field and provide a quantization axis. The three pairs of compensation coils are arranged around the glass cell along all three dimensions.

We use a nano-textured beam sampler to pick off a small portion of the light after propagation through the science cell to image the resulting optical tweezers (see Fig. 4.4). Light transmitted through the beam sampler is guided to the optical table as well, where the optical power is safely dumped in a beam trap.

The two counter-propagating 556 nm beams for 3D MOT laser-cooling exit optical fibers using collimators with built-in circular apertures (Schäfter+Kirchhoff, -M60-33) and travel along the z-axis of the experiment. A pair of counter-propagating 3D-MOT beams travel diagonally in the xy plane but are not shown here for simplicity but is discussed in the next section.

The 3D-MOT cloud is imaged via absorption imaging using a 399 nm laser beam, traveling along the z-axis. The fiber collimator (Schäfter+Kirchhoff, 60-FC-4-M100) is located on the back breadboard of the experiment and is combined with one of the 3D-MOT beams on a dichroic mirror. The shadow that is cast from the atomic cloud is imaged after propagation through the science cell on a CCD camera (pco.pixelfly USB, Excelitas) using a telescope resulting in a magnification of $M = 0.3$.

Single-atom imaging is performed by collecting fluorescence at 556 nm which is emitted by individual atoms trapped in optical tweezers. Photons scattered from the atoms propagate back through the microscope objective and the light can be separated from the incoming tweezer light at the dichroic mirror, where it can be imaged in a spatially-resolved manner on a CMOS camera (ORCA-Quest 2, Hamamatsu) using a $f = 500\,\mathrm{mm}$ lens. The resulting magnification of the fluorescence imaging system amounts to $M = 17.6$.

---

[1] The two objectives have identical optical specifications, however the objective used for re-collimation has a hole drilled with a diameter of 3 mm along its optical axis. The reason behind this is that it can be potentially used for guiding a global UV-beam (or other beams for global addressing) through the objective, while protecting the objective's lenses from UV-induced damage.

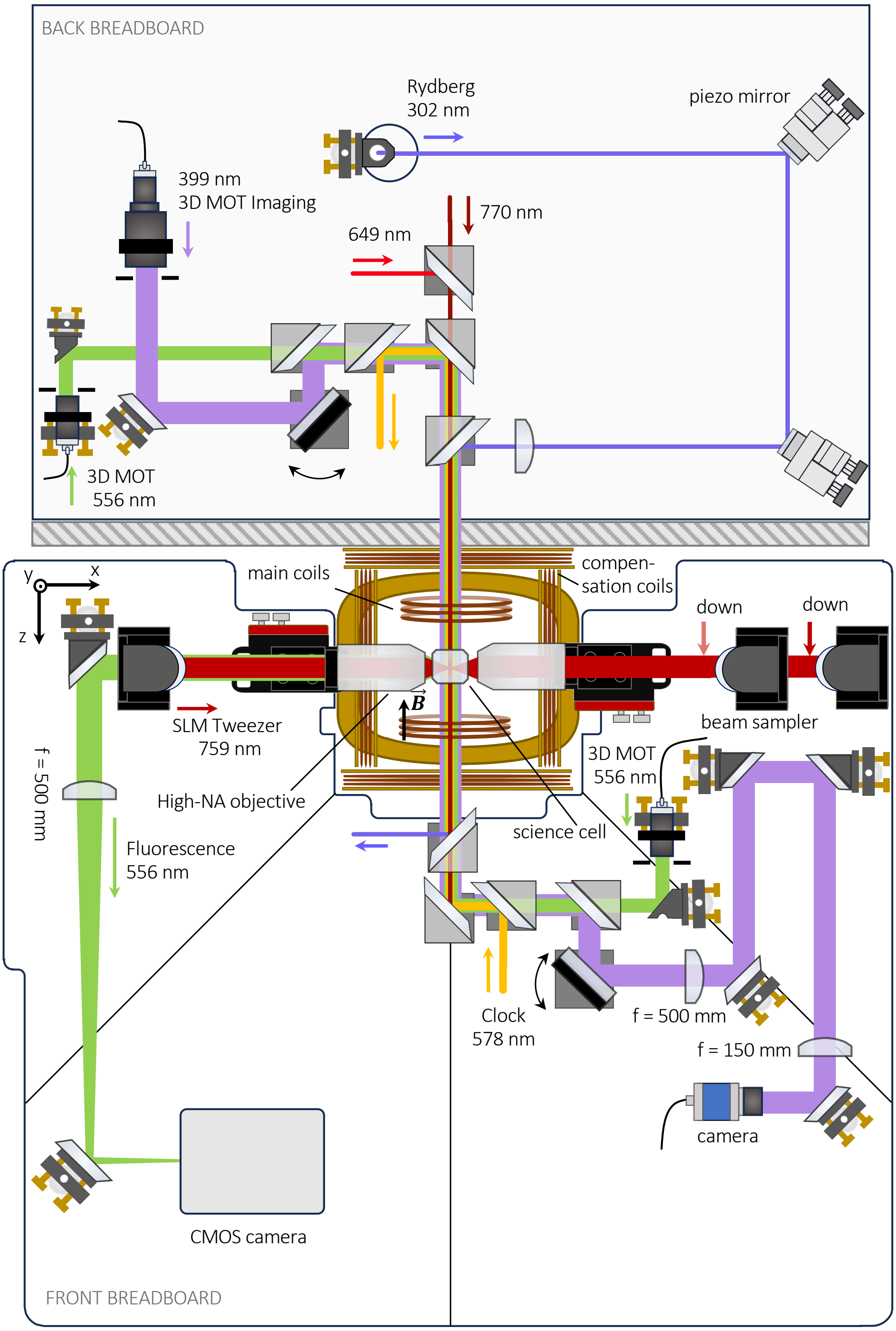

Figure 4.5 | Main experiment beam layout (breadboard). Schematic of the second level of the main experiment, where the atomic plane is located. The quantization axis is defined by the magnetic field ***B***, generated by the main coils. The SLM-tweezer beam propagates along the $x-$axis and is focused into the science cell by a high-NA objective. The beam is re-collimated after the science cell using an identical objective. A portion of the light is picked off by a beam sampler and redirected to the tweezer analysis branch on the ground level. Two counter-propagating 3D-MOT beams travel along the $z-$axis. The remaining laser beams are combined using custom-designed dichroic mirrors (see main text).

We combine all remaining laser systems using custom-manufactured dichroic mirrors. This includes setups at 301.5 nm for Rydberg excitation, 649 nm, 578 nm and 770 nm. The setup for auto-ionizing Rydberg atoms with a 369 nm laser is not shown here. This beam propagates along the y-plane and is launched from below the glass cell. For a detailed description of the implementation of this laser system see chapter 6.4 and Ref. [177].

Upper optical breadboard

During the course of this thesis, we installed two additional optical breadboards located above the science cell on each side of the vacuum system to gain more space for optical setups. Figure 4.6 illustrates the optical layout. The breadboards are mounted to the vertical breadboard using mounting brackets and are additionally supported with posts which are secured to the main breadboard.

As shown in Fig. 4.6a, the two diagonal 3D-MOT beams are launched from an optical fiber using a collimator (Schäfter+Kirchhoff, -M60-33). The 3D-MOT beams propagate through the glass cell in the xy-plane at an angle of 58° relative to the horizontal plane, as illustrated in Fig. 4.6b. The angle is given by geometrical constraints imposed by the objectives, compensation coils and the glass cell. We install counter-propagating 3D-MOT beams underneath the glass cell on the optical table.

The upper breadboard is designed to accommodate several additional laser wavelengths: This includes laser systems at 578 nm, 649 nm, 1388 nm and 1539 nm.

A 578 nm laser beam will allow for the preparation of clock state atoms in $^3\mathrm{P}_0$. The beam propagates diagonally through the glass cell and therefore is perpendicular to the quantization axis defined by the magnetic field $\boldsymbol{B}$, allowing arbitrary tuning of the polarization state.

Alternatively, a 1539 nm beam can be used to populate the $^3\mathrm{P}_0$ state by an optical pumping scheme via $^3\mathrm{D}_1$, as experimentally demonstrated in Ref. [133]. Work towards implementing a 1539 nm laser system at our experiment is presented in Ref. [177].

A 649 nm laser beam will be used for coupling the $^3\mathrm{P}_0$ nuclear spin states of $^{171}\mathrm{Yb}$ via Raman transitions. Details on this laser system can be found in Refs. [178] and [154].

The $^3\mathrm{P}_0$ clock state atoms can be transferred to the $^1\mathrm{S}_0$ ground state for imaging using a repumping scheme which utilizes the $^3\mathrm{P}_0 \leftrightarrow {}^3\mathrm{D}_1$ transition at 1388 nm. For details on the implementation of the 1388 nm laser system, see Ref. [179]. The respective optical systems can be easily integrated into the existing optical system using the designated dichroic mirrors illustrated in Fig. 4.5a.

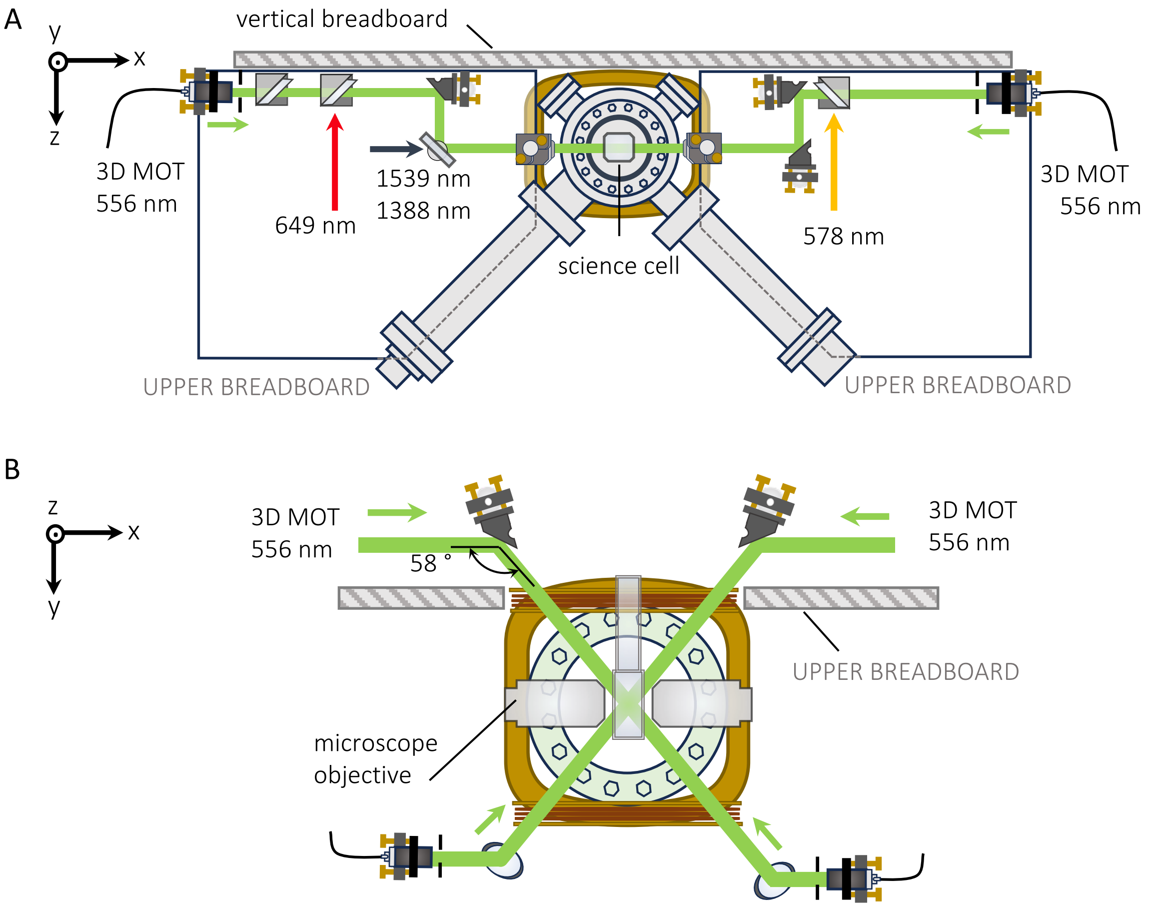

Figure 4.6 | **Main experiment beam layout (upper breadboard).** **(A)** Schematic of the third level of the main experiment. The two 3D-MOT beams exit a fiber on the upper breadboard and propagate diagonally in the xy-plane through the science cell. Additional input ports are available for laser beams at 578 nm, 649 nm, 1388 nm and 1539 nm at the respective dichroic mirrors. **(B)** Lateral view of the experiment, showcasing the 3D-MOT beam geometry. The counter-propagating diagonal 3D-MOT beams travel at an angle of 58° relative to the horizontal x-plane. The collimators for the counter-propagating beams are located on the optical table.

4.2.2 399 nm laser systems

The broad $^1S_0 \leftrightarrow ^1P_1$ transition in Yb ($\lambda = 399\,\mathrm{nm}$, $\Gamma = 29\,\mathrm{MHz}$) is used for the first stage laser cooling in a 2D-MOT as well as for absorption imaging of the 3D-MOT cloud. For these applications, we employ two separate frequency-doubled diode lasers. Here, we discuss the two laser systems.

Master laser setup

The 399 nm master laser provides light for absorption imaging of the 3D-MOT cloud and is used as a frequency reference for the 2D-MOT laser. The corresponding laser system has been built by K. Sponselee. A simplified schematic is shown in Fig. 4.7.

The laser system uses a frequency-doubled diode laser from Toptica with a maximum output power of 360 mW. The optical power can be tuned at a polarizing-beam-splitter (PBS) by adjusting a half-wave plate. A portion of the light is reflected at a PBS and is coupled into an optical fiber which is guided to the 2D-MOT laser system to serve as a frequency reference. We derive an error signal from a beat note of these two laser beams. We use an ultra-low-expansion (ULE) cavity from Stable Laser Systems as a frequency reference for the 399 nm master laser using the PDH locking method. To stabilize the frequency, we pick off some light at the fundamental wavelength (798 nm) of the laser and send it to the ULE cavity. We employ an electro-optical modulator (EOM) for imprinting sidebands onto the light. This allows us to tune the frequency of the laser over a wide range using a double-sideband modulation method, as described in Ref. [180]. The remaining 399 nm is used for absorption imaging of the 3D-MOT cloud. Light is reflected at a PBS and sent through an acousto-optic modulator (AOM) in double-pass configuration using a 150 mm lens and a quarter-wave plate. The AOM is driven by an in-house built digital radio-frequency source. The AOM allows us to shift the frequency to the $^1S_0 \leftrightarrow ^1P_1$ resonance. The double-pass configuration of the AOM minimizes leakage light to be coupled into the fiber. The fiber is guided to the main experiment (see Fig. 4.5).

An additional optical path has been built for the implementation of a pushing beam, which can be used to enhance the loading efficiency of the 3D-MOT. However, during the course of this thesis, a pushing beam has not been utilized. Further, the setup has the capability of providing light for fluorescence imaging of single atoms, which is not included in the schematic, as this remains a future extension to the work presented here.

2D-MOT setup

The 2D-MOT setup has been originally built in the first generation experiment and has mostly been left unchanged. The most recent description of this laser system can be found in Ref. [181]. Here, we summarize the key features of this 399 nm laser setup.

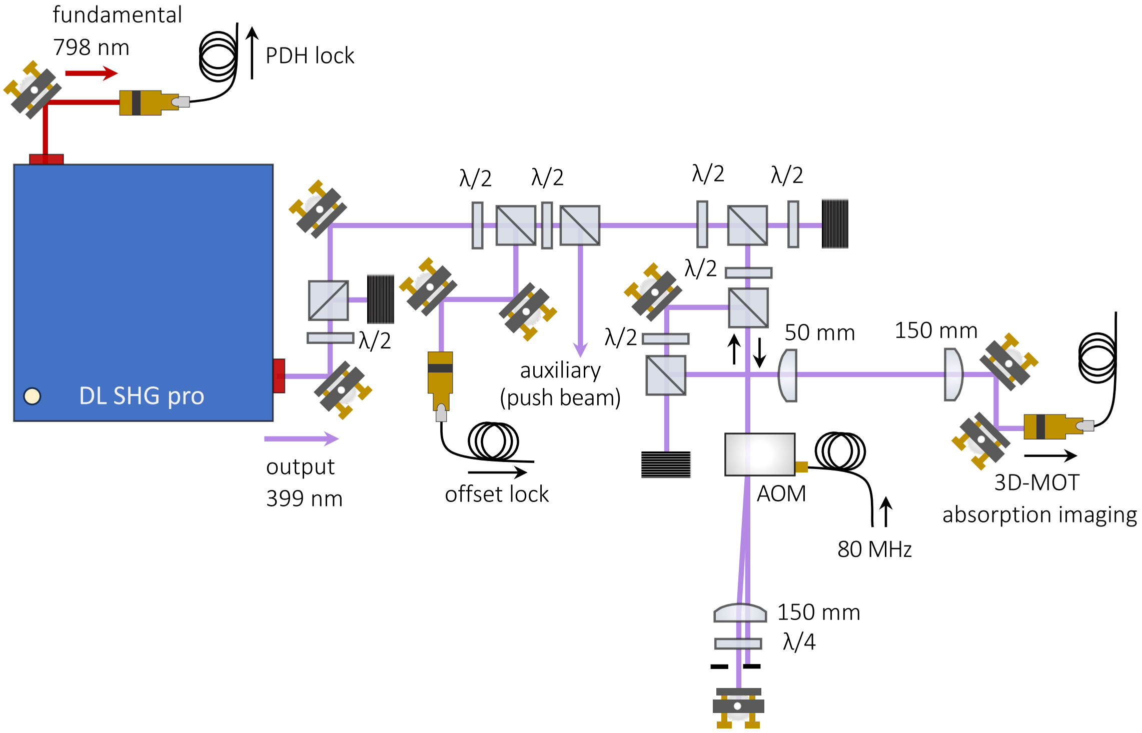

Figure 4.7 | 399 nm master laser system. Simplified schematic of the 399 nm master laser system. The frequency is stabilized to a ULE cavity via a PDH lock, using the fundamental mode. The power is tuned with a polarizing beam splitter (PBS) and a half-wave plate. Some light is picked off at a PBS and coupled into a fiber for an offset lock, which serves as a frequency reference for the 2D-MOT laser. A potential push beam can be implemented using the reflection at a PBS. Remaining laser light passes an AOM in double-pass configuration and is coupled into a fiber that is guided to the main experiment to be used for 3D-MOT absorption imaging.

The laser light for 2D-MOT laser cooling is generated by a frequency-double diode laser from Toptica (DLC TA-SHG pro) with a maximum output power of 1.9 W. We usually operate the laser at around 1 W to to preserve its lifetime, which is sufficient to saturate the transition. The 399 nm laser beam is guided to the 2D-MOT science cell in a free-space setup, as utilizing optical fibers is infeasible for high power applications at wavelengths in the near-UV range due to UV-induced solarization effects. For this reason, the laser heads is placed on a separate breadboard and raised by an aluminum frame such that the laser system is located in the horizontal plane of the 2D-MOT glass cell.

During the course of this thesis, we became aware of spatial drifts of the 2D-MOT beam, which affected the long-term stability of the 3D-MOT particle number. This instability stems from the fact that the elevated optical breadboard supporting the laser head is mechanically decoupled from the main experiment, resulting in a relative motion. For this reason, we implemented an active beam-pointing stabilization system (Aligna, TEM Messtechnik), which resolved this issue.

We stabilize the frequency of the 2D-MOT laser via an offset lock to the 399 nm master laser as described above.

4.2.3 556 nm laser system

We use the $^1S_0 \leftrightarrow {}^3P_1$ intercombination transition ($\lambda = 556\,\text{nm}$, $\Gamma = 2\pi\times 182\,\text{kHz}$) for narrow-line cooling in a 3D-MOT, single-atom preparation and fluorescence imaging of individually trapped Yb atoms. The 556 nm laser system presented in the following has been built by A. Ilin. The 556 nm delivery setup on the main experiment table has been built by the author.

556 nm laser system

A frequency-double diode laser from Toptica (TA-SHG pro) provides 1.7 W of laser light at 556 nm. Figure 4.8 shows a schematic of the 556 nm laser system. The optical power sent into the laser system can be tuned using a polarizing beam splitter and a half-wave plate. The beam height is adjusted to 50 mm using a periscope assembly.

A small portion of light is picked off at a PBS and sent to an ultra-low expansion (ULE) cavity via an optical fiber for stabilizing the laser frequency. Further, we stabilize the power of the light that is sent to the ULE cavity using an accousto-optical modulator (AOM) placed before the fiber.

The remaining light (~700 mW) is sent through a 200 MHz AOM in double-pass configuration. We drive the AOM with a MOGLabs XRF RF-source. While the narrow linewidth of $2\pi\times 182\,\text{kHz}$ allows for low Doppler temperatures (~5 µK), it leads to a reduced capture velocity in the 3D-MOT. In contrast, the 2D-MOT operates on a broad transition with a linewidth of $2\pi\times 29\,\text{MHz}$, resulting in a much higher MOT capture range. We therefore spectrally broaden the 3D-MOT beams during the MOT loading phase by applying a saw-tooth frequency modulation generated by a Keysight signal generator to the frequency modulation input of the MOGLabs XRF.

To tune the center frequency, a frequency offset provided by the experiment control system is added to the frequency modulation signal using a bias-T. We use a MOGLabs signal conditioning board in conjunction with the amplitude modulation input of the MOGLabs XRF to simultaneously utilize the AOM for power stabilization and control of the intensity. The corresponding photodiode signal is generated on the MOT delivery setup.

In order to perform a compression sequence on the 3D-MOT, we reduce the broadening and drive the frequency closer to resonance while ramping down the intensity to maintain operation below the saturation intensity. The compressed MOT allows to cool atoms to lower temperatures and results in a reduced size of the atomic cloud, which is imaged via absorption imaging on the blue $^1S_0 \leftrightarrow {}^1P_1$ transition.

Throughout the experiment sequence, the laser system provides laser light for fluorescence imaging as well as for generating a photo-association pulse to achieve single-occupancy of trapped atoms.

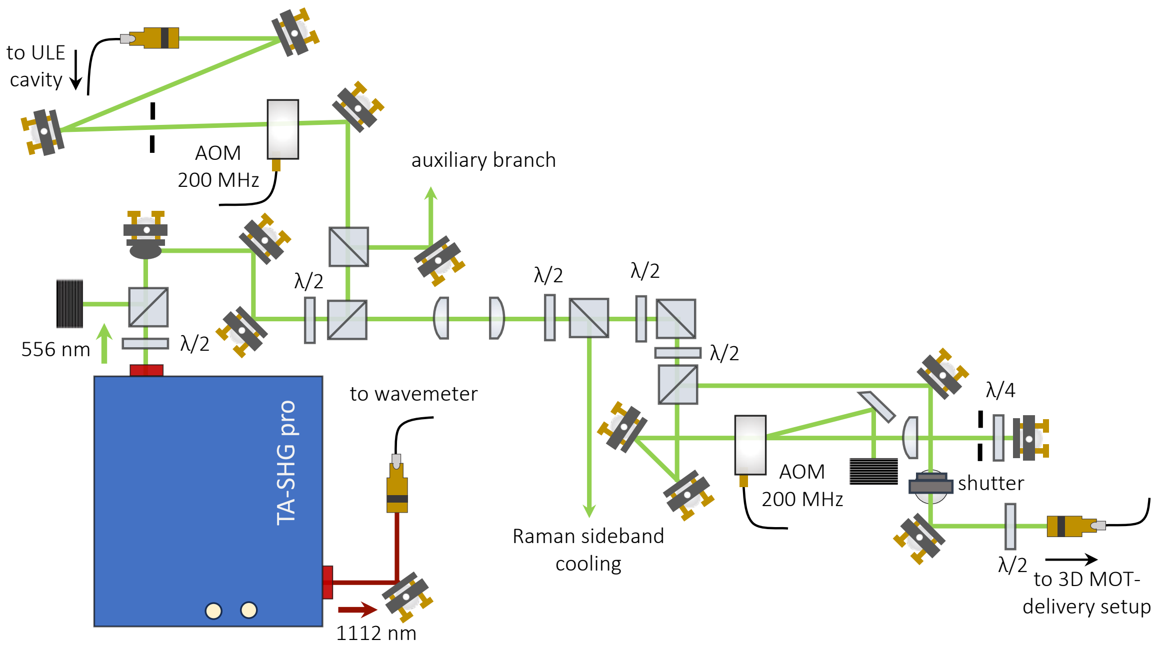

Figure 4.8 | 556 nm laser system. Schematic of the 556 nm laser system for 3D-MOT cooling, single-atom preparation and fluorescence imaging. The optical power is adjusted using a polarizing beam splitter (PBS) and a half-wave plate. The beam height is adjusted using a periscope assembly. A small portion of light is split off and sent to an ultra-low expansion (ULE) cavity for frequency stabilization. An acousto-optic modulator (AOM) is used for power stabilization. The majority of the light is sent through a double-pass AOM and coupled into a fiber that is guided to the 3D-MOT delivery setup on the main experiment table. The frequency is monitored at the fundamental wavelength of the laser.

In the second-generation experiment, the 556 nm laser system will be upgraded to be capable of providing light for implementing a Raman-sideband cooling scheme for cooling of trapped atoms to the motional ground state [125].

3D-MOT delivery setup

The MOT delivery setup is located on the main experiment table and serves the purpose of splitting the 556 nm beam into six individual 3D-MOT laser beams. Figure 4.9 shows the optical layout of the laser setup.

To accomplish this, the beam is first split into three optical paths at a polarizing beam splitter (PBS) for each pair of counter-propagating MOT beams. The power in each beam is carefully tuned by adjusting a half-wave. We divide each of the three laser beams one additional time using a PBS and half-wave plate. This scheme makes sure that we can tune the optical power of counter-propagating beams in an independent manner to achieve optimal beam balance. The resulting six beams are coupled into individual single-mode optical fibers and routed to the respective collimator at the main experiment. A detailed description of the 3D-MOT beam geometry is provided in Section 4.2.1.

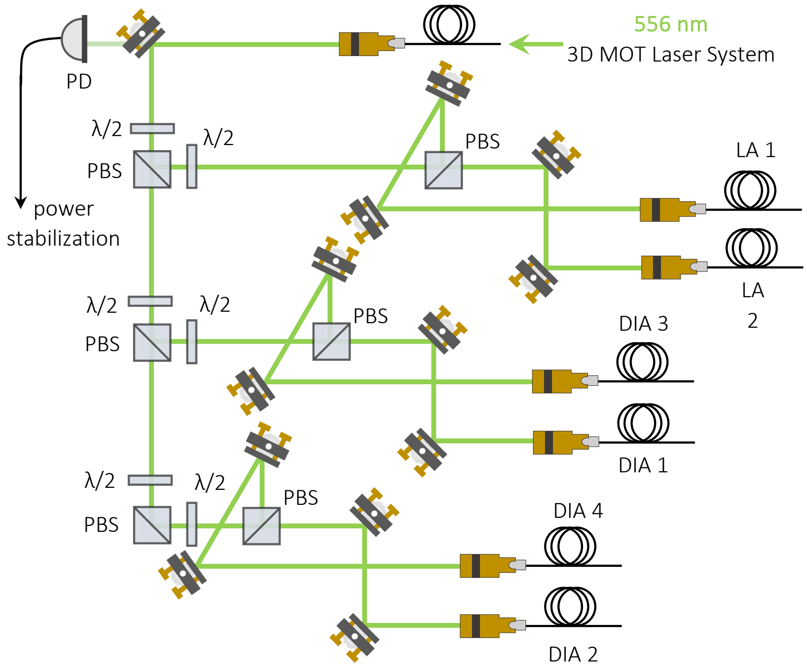

Figure 4.9 | 3D-MOT delivery setup. Schematic of a 556 nm laser setup for providing six 3D-MOT beams. The incoming beam is divided into three beams using polarizing beam splitters (PBS) and the power in each beam is tuned using a half-wave plate. The optical power is monitored for power stabilization using leakage light. Each of the three beams is divided again into a pair of beams, corresponding to counter-propagating 3D-MOT beams. The beams are labeled *LA* for 3D-MOT beams aligned with the long axis of the experiment and *DIA* for diagonally propagating 3D-MOT beams.

We label the 3D-MOT beams aligned with the quantization axis as *LA 1* and *LA 2* (denoting the *long axis* of the experiment, which runs along the length of the optical table). The 3D-MOT beams propagating diagonally in the xy-plane are labeled *DIA1* through *DIA4* (see Fig. 4.6B). To minimize the footprint of the optical setup, we employ $0\,^\circ$ mirrors in several location to deflect the beam at angles smaller than $< 20°$.

We use three-paddle manual polarization controllers for each fiber to obtain the required circular polarization state. The 3D-MOT is operated with up to 350 mW of total input optical power, with a typical fiber coupling efficiency of ∼50 % of each collimator.

Since the diagonal beams (*DIA*) have projections on all three dimensions, we use twice the optical power (~ 22 mW per beam) compared to the *LA* beams (~ 11 mW per beam).

Leakage light transmitted by one of the mirrors serves as a monitor signal for power stabilization. The photodiode signal is fed back into the MOGLabs signal conditioning board (see section above).

4.2.4 532 nm laser system

We generate optical tweezer arrays with 532 nm laser light using a pair of crossed acousto-optic deflectors (AODs). This wavelength offers 'magic' trapping conditions for the $^1S_0$ ground state and excited $^3P_1$ state in ^{174}Yb, which is used for narrow-line cooling as well as imaging. Here, we present a laser setup for providing laser light to the AODs. The laser system was built in collaboration between the author and T. Petersen.

Figure 4.10 shows a schematic of the 532 nm laser system. We use a CW solid state laser (Verdi V18, Coherent), which provides up to 18 W of optical power. The beam height is corrected to 50 mm right at the laser output using a periscope assembly consisting of two mirrors which reflect the beam in the vertical plane. A high-power polarizing beam splitter (PBS) is used to tune the optical power which goes into the laser system. The beam size is reduced with a 1:1.6 telescope and sent through an acousto-optic modulator (AOM). The AOM (3080-292, Gooch & Housego) is driven by a RF synthesizer (QRF, MOGlabs) at 80 MHz. The incident polarization is adjusted with a half-wave plate for optimal operation of the AOM.

The AOM is used for both fast switching and active power stabilization of the laser beam. The optical power is monitored on the site of the main experiment, i.e. after propagating through an optical fiber. The resulting photodiode signal and the setpoint specified in the experiment control software are fed into an analog PID controller (LB2005-S, Newport), which regulates the amplitude of the RF signal. This allows to account for most of the power fluctuations which are primarily caused by propagation through the fiber. The RF signal is amplified (LZY-22+, Mini-Circuits) before being fed into the AOM. The 0th diffraction order is picked off and redirected onto a beam trap. A slit aperture blocks higher AOM diffraction orders. Additionally, the laser beam can be mechanically blocked by a reflective mechanical shutter, which redirects the light onto a beam trap. The laser power before the optical fiber is monitored with a photodiode by measuring the power of the light transmitted by a mirror.

The resulting laser beam is launched into a polarization-maintaining (PM) fiber specially suited for high-power applications (LMA-10, NKT Photonics) using a collimator (Schäfter+Kirchhoff, 60FC-SMA-T-23-M11.5-01). We require the polarization state to remain stable as it is critical for the operation of the AODs. To achieve optimal coupling into the PM fiber, we make sure the light is linearly polarized by maximizing the transmission through a PBS using both a half- and quarter-wave plate. We fine-tune the orientation of the linearly polarized light with an additional half-wave plate to align the polarization direction of the input light to one of the fiber's axes. We accomplish this by measuring the polarization state at the fiber's output with a polarimeter (Schäfter + Kirchhoff, SK010PA).

Finally, the light is guided to the main experiment, where it is being utilized by the AODs. The laser system on the main experiment site is discussed in chapter 4.2.1. s

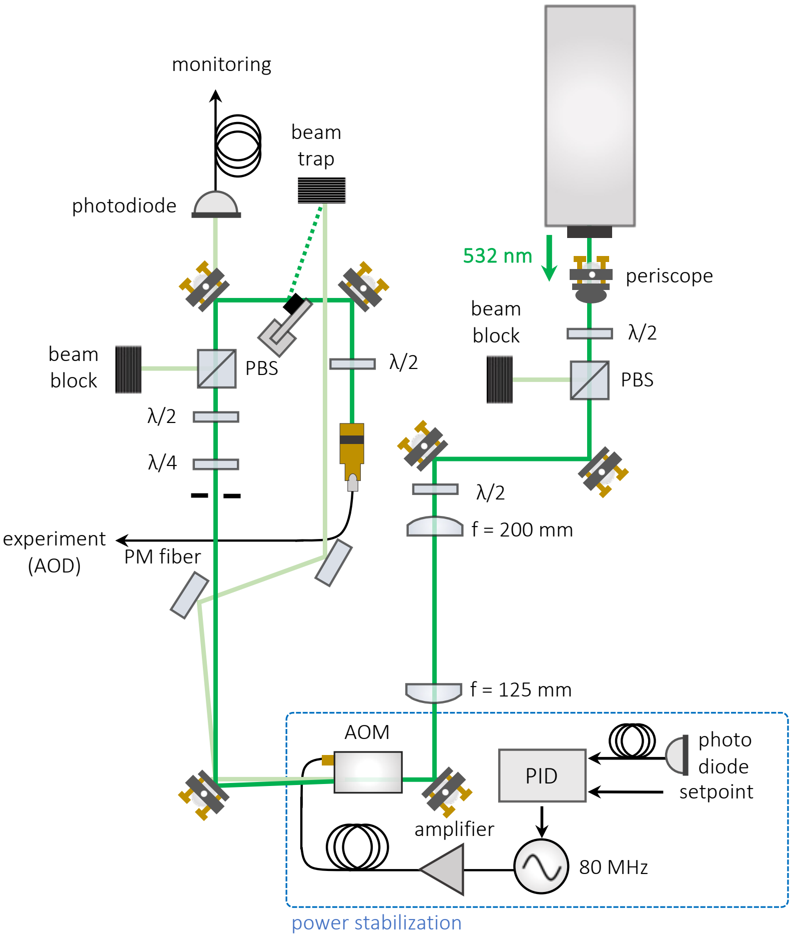

Figure 4.10 | AOD-tweezer laser system (532 nm). Schematic of the 532 nm laser system. The beam height is adjusted using a periscope assembly. The power can be tuned at a polarizing-beam splitter. The laser beam size is reduced using a telescope. A high-power AOM is used for switching and active power stabilization. The incident polarization state is tuned with a half-wave plate. The 0th AOM order is redirected to a beam block and the remaining AOM diffraction orders are blocked by a slit aperture. The laser beam is launched into a polarization-maintaining (PM) hollow-core photonic crystal fiber. Polarization adjustments for PM fiber coupling are made using a PBS and a combination of half-wave and quarter-wave plates. A reflective mechanical shutter is implemented to block and reflect the laser beam on a beam trap.

4.2.5 759 nm laser system

We employ SLM-generated optical tweezer potentials at 759 nm. At this trapping wavelength the polarizabilities for the ground state $^1S_0$ and excited clock state $^3P_0$ are equal, making it a ”magic” wavelength [182]. The magic trapping condition eliminates trap-depth dependent differential light shifts and therefore enables high-precision operation of the $^1S_0 \rightarrow {}^3P_0$ optical clock transition.

Here, we present a laser system for providing laser light at the magic wavelength to the SLM. The laser system was built by K. Sponselee. An upgrade to the setup was performed by T. Petersen and the author.

Figure 4.11 shows a schematic of the laser system. Laser light at 759 nm is generated by pumping a Ti:sapphire laser (MBR 110, Coherent). The pump laser emits light at 532 nm (Verdi V10, Coherent) with a maximum output power of 18 W. We achieve up to 4 W of optical power at 759 nm.

Right after the laser output, the beam height is corrected to 50 mm using a periscope setup consisting of two mirrors reflecting the beam in the vertical plane. We use a 1:1 telescope with $f_1 = f_2 = 50\,\mathrm{mm}$ to generate a focal point. The second lens f_2 is placed on a translation stage and moved along the optical axis by several mm to shift the focus to the location of an acousto-optic modulator (AOM) located further downstream the laser system. This ensures optimal operation of the AOM without the need for tailored beam shaping optics. A small portion of light is picked off at a polarizing beam splitter (PBS) and launched into an optical fiber to monitor the frequency of the light using a wavemeter. The remaining laser power is reflected by the PBS and diffracted by an AOM. We tune the polarization using a half-wave plate to optimize the AOM diffraction efficiency. The AOM is used for both fast switching and active power stabilization of the laser beam. The optical power is monitored on the site of the main experiment, i.e. after propagating through an optical fiber. The resulting photodiode signal and the setpoint specified in the experiment control software are fed into an analog PID controller (LB2005-S, Newport), which regulates the amplitude of the RF signal. This allows to account for most of the power fluctuations which are primarily caused by propagation through the fiber.

A reflective mechanical shutter provides an additional safety mechanism to divert and safely dump the laser light in a beam trap. The 0th AOM diffraction order is separated from the beam and diverted to the same beam trap. The beam size is expanded using a 1:2 telescope. The resulting laser beam is launched into a polarization-maintaining (PM) fiber (Schäfter+Kirchhoff) using an appropriate collimator (Schäfter+Kirchhoff). To achieve optimal coupling into the PM fiber, we to fine-tune the orientation of the linearly polarized light to align the polarization axis to the fiber’s axis. We accomplish this by measuring the polarization state at the fiber output with a polarimeter (Schäfter+Kirchhoff).

The light is guided to the main experiment, where it is utilized to generate arbitrary tweezer geometries using an SLM (see Fig. 4.4). The laser system on the main experiment site is discussed in chapter 4.2.1.

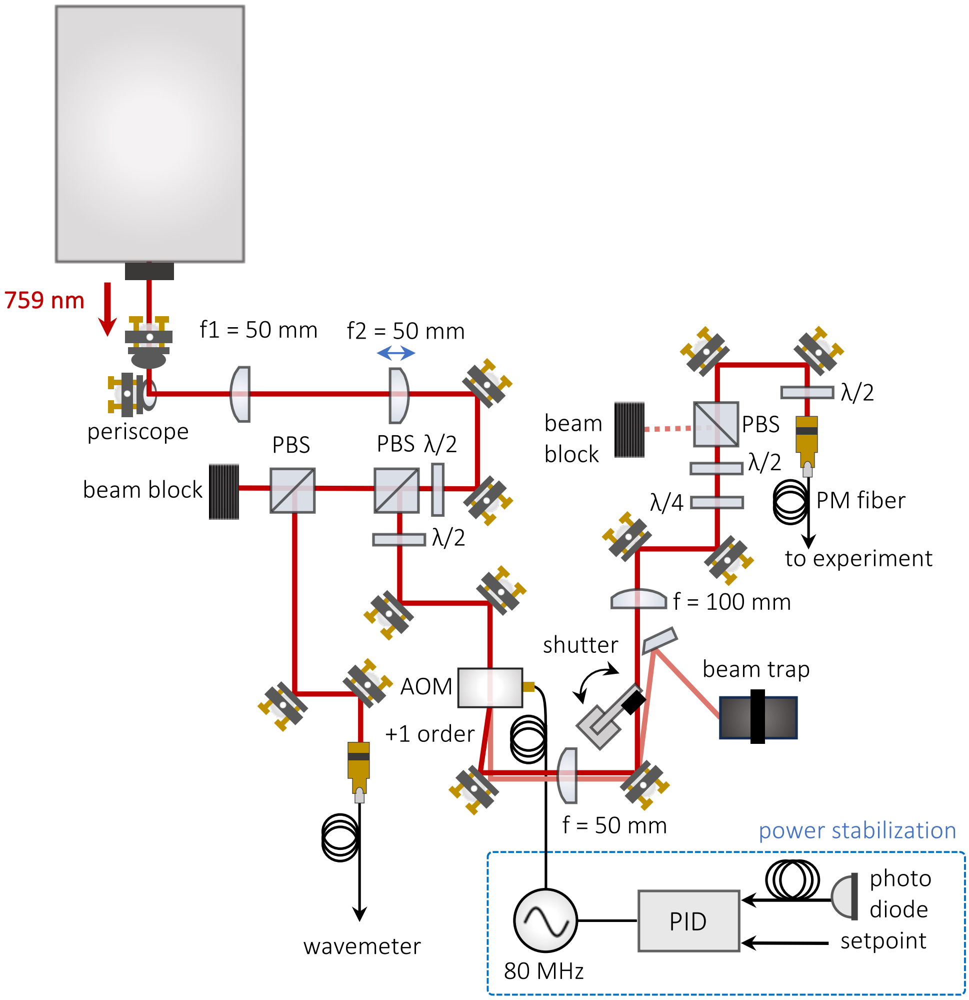

Figure 4.11 | SLM-tweezer laser system (759 nm). Schematic of the 759 nm laser system. The beam height is adjusted using a periscope assembly. A 1:1 telescope shifts the focal point to the location of an acousto-optic modulator (AOM) by translating the second lens (f2). A small portion of the light is picked off at a PBS and coupled into an optical fiber for frequency monitoring. The AOM is used for switching and intensity stabilization. The beam is expanded and coupled into a polarization-maintaining fiber and delivered to the experiment.

4.3 Summary and outlook

In this chapter we gave a detailed description of the optical layout of the main experiment adjacent to the science chamber.

We gave an overview of the individual laser systems used for 2D-/3D-MOT laser cooling, optical tweezer generation, atom imaging and manipulation. The experimental design incorporates twelve laser wavelengths, this includes 302 nm, 369 nm, 399 nm, 497 nm, 556 nm, 532 nm, 578 nm, 649 nm, 759 nm, 770 nm, 1388 nm and 1539 nm. A straightforward upgrade to the core experiment in the near future will bring new capabilities to the experimental apparatus presented here.

In particular, implementing the 578 nm laser system will enable the access to the metastable clock state of Yb. This will be a crucial step in realizing highly-anticipated quantum computing architectures which leverage the unique electronic structure of Yb. We designed the experiment to accommodate propagation both along the quantization axis of the experiment, as well as having projections on all three spatial dimensions with respect to the magnetic field axis.

The construction of the 302 nm and 369 nm laser setups for Rydberg excitation and Rydberg atom detection is subject to chapter 6 of this thesis. The implementation of Rydberg atoms is reserved for future studies, as it requires the ability to prepare atoms in the metastable clock state.

Additional laser systems targeting the 497 nm, 649 nm, 770 nm and 1539 nm transitions are currently under construction at the time of writing this thesis and their integration thus falls outside the scope of this thesis but will play an essential role in the future development of the experiment.

Chapter 5

Trapping and Imaging Individual ^{171}Yb Atoms in Optical Tweezers

Creating controllable arrays of individually trapped neutral atoms is at the forefront of quantum technology.

This chapter demonstrates the core capabilities of our optical tweezer platform utilizing alkaline earth-like atoms. We provide a detailed description of the experimental procedures employed to cool, trap and prepare individual fermionic ^{171}Yb atoms in an optical tweezer array operating at the magic wavelength of 759 nm.

The first part outlines the laser cooling procedure used to prepare a thermal atomic cloud in a 3D magneto-optical trap (MOT). By exploring the loading behavior of the 3D-MOT, we identify favorable parameters to maximize the loading rate. We conclude the MOT characterization with measurements of the atomic temperature and the MOT lifetime.

The second part of this chapter focuses on the main experimental results with individually trapped ^{171}Yb atoms. Following a concise overview of the apparatus and experimental sequence, we study the preparation of singly-trapped atom via light-assisted collisions. The probabilistic loading nature of the tweezer array is then characterized and prospects for enhanced loading are discussed. An in-depth analysis of the high-fidelity fluorescence imaging protocol is presented. We perform lifetime measurements of optically-trapped atoms and assess the temperature in a release-and-recapture experiment. The chapter concludes with a characterization of our tweezer platform with a measurement of the trap frequencies.

The experimental work presented in this chapter has been conducted together with T. Petersen. The data analysis has been carried out by the author in close cooperation with T. Petersen. The results have been discussed with C. Becker. Complementary work with ^{174}Yb can be found in Ref. [154].

5.1 3D-MOT

Atoms are loaded from a compressed narrow-line 3D magneto-optical trap (MOT) on the $^1S_0 \leftrightarrow {}^3P_1$ transition ($\Gamma = 182\,\mathrm{kHz}$) into optical tweezers. Here, we show measurements analyzing the performance of the ^{171}Yb 3D-MOT as a function of several experimental variables to determine parameters for optimal operation. This includes scanning the laser detuning, magnetic field gradient, MOT-beam intensity and compression parameters. In time-of-flight measurements, we determine the temperature of the 3D-MOT atoms and measure the lifetime of the compressed MOT cloud. Analogous work analyzing the bosonic ^{174}Yb 3D-MOT can be found in Ref. [154].

The data presented in this chapter has been measured and analyzed by T. Petersen and the author. The results have been discussed with C. Becker and the entire team.

Experimental Sequence

The loading process of the 3D-MOT can be divided in three stages. The experimental sequence for the 3D-MOT loading cycle is schematically depicted in Fig. 5.1.

In the initial loading stage, pre-cooled atoms from the 2D-MOT are transferred to the 3D-MOT science chamber through a differential pumping tube (see Sec. 4.1). We find that precise alignment of the 2D-MOT is required to achieve efficient transfer and loading into the 3D-MOT. Atoms are further cooled on the narrow-line 556 nm transition using six counter-propagating beams (see Sec. 4.2.1). We opt for a six beam MOT instead of a retro-reflected MOT beam configuration in which the optical elements altered the polarization state of the MOT light, preventing us from achieving a well-controlled polarization state at the position of the MOT. To set the correct polarization state, we use a polarimeter placed directly before to the science cell.

While the narrow linewidth of the 556 nm transition allows for low Doppler-temperatures of $4.4\,\mu\mathrm{K}$, it results in capturing only a narrow velocity class of atoms that experience a cooling force because of corresponding Doppler-shifts. For this reason, we spectrally broaden the 3D-MOT beams by applying a saw-tooth frequency modulation while loading the 3D-MOT. With the experimental method described in Sec. 4.2.3, we generate sidebands with fixed spacings. This frequency comb is characterized by its width given by the modulation depth and its center frequency. We make sure all present frequency components are red-detuned with respect to the resonance, as any blue-detuned light leads to heating of atoms out of the MOT. Additionally, we ensure that every sideband exceeds the saturation intensity of the green transition. Multi-frequency operation of the 3D-MOT allows us to increase the capture velocity of the atoms until the MOT cloud saturates. At this point, the temperature of the atoms is much higher than the Doppler temperature because of effectively broadening the transition. To further lower the temperature, the MOT cloud undergoes a compression stage. This process also

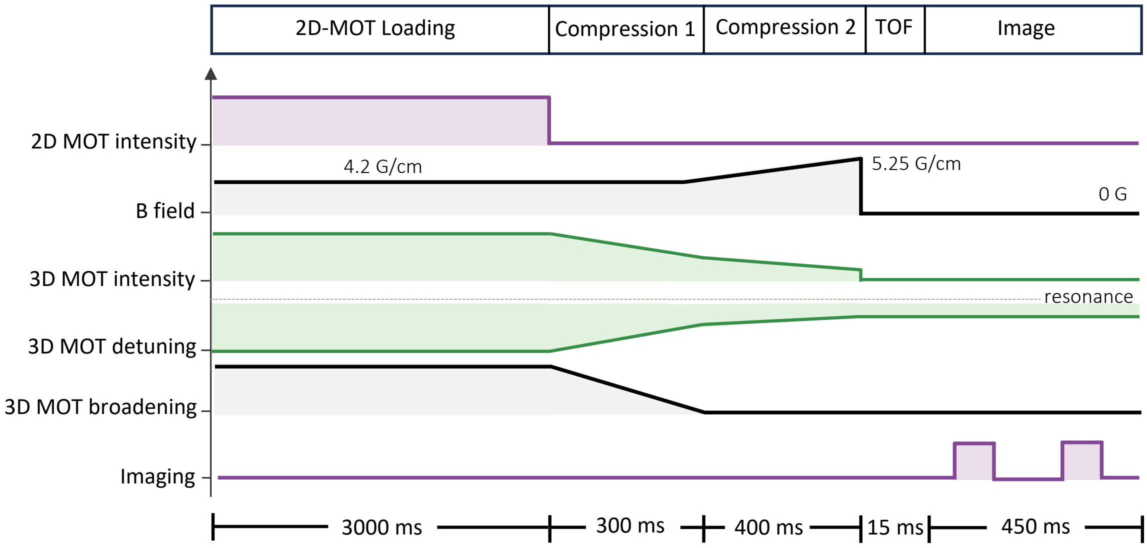

Figure 5.1 | Experimental 3D-MOT sequence. Illustration showing the experimental sequence for preparing a compressed 3D-MOT. The sequence is divided into five stages with different length (note, that the time axis is not to scale). After loading atoms from the 2D-MOT at 399 nm, the laser beam is switched off. The 556 nm 3D-MOT intensity is ramped down in the first compression stage and the frequency detuning is brought closer to resonance (indicated by the dashed line), while the spectral broadening is reduced. During the second compression stage, the magnetic field gradient is ramped up. After time-of-flight, we perform two 399 nm pulses for absorption imaging.

increases the density of the MOT, which later leads to an improved loading efficiency into tweezers. For compression, we reduce the width of the frequency comb and drive the center frequency closer towards resonance. Simultaneously, the intensity is ramped down to keep the intensity per sideband constant.

In a second compression stage, we switch to single-frequency operation of the MOT and drive the frequency towards a detuning of $\Delta = -0.22\,\text{MHz}$ (or - $1.2\,\Gamma$), while the magnetic field gradient is ramped up and the intensity continually decreased. After switching off the MOT-beams and allowing the cloud to expand during time-of-flight, we take an absorption and reference image using two subsequent 399 nm laser light pulses. From the expansion, we can deduce the temperature of the atoms in the 3D-MOT. With this experimental protocol, we achieve a 3D-MOT loading rate of 6×10^6 atoms in 3 s at temperatures of $\sim 14\,\mu\text{K}$. In the following, we explore how the 3D-MOT behaves when varying different experimental parameters.

To enable high tweezer experiment repetition rates, we require fast 3D-MOT loading. This ensures stable and efficient operation of the experimental protocol. In the following, we investigate the loading rate of the 3D-MOT. We explore different loading regimes by scanning relevant parameters during the 3D-MOT loading stage. We record the particle number, as well as the temperature of the atomic cloud.

3D-MOT Loading Parameters

We perform parameters scans of the loading phase (see Fig. 5.1). Two key parameters for this stage of cooling are the detuning and magnetic field gradient. The results are presented in Fig. 5.2. During this phase, 3D-MOT beams are spectrally broadened, where the detuning is given by the center frequency of the frequency comb. We load the 3D-MOT within 3 s and perform absorption imaging to determine the particle number. In a time-of-flight measurement we extract the temperature of the atomic cloud.

Figure 5.2a shows the particle number as function of the detuning and magnetic field gradient at loading. Consistent with our expectation, for small magnetic field gradients in the far red-detuned regime, the cooling force is reduced along with a decrease in trapping volume, preventing atoms from being trapped in the 3D-MOT.

Our measurement shows a well-defined region of enhanced 3D-MOT loading efficiency. Meanwhile, the temperature shown in Fig. 5.2b is mostly independent from the detuning and magnetic field gradient in the presented parameter regime.

Under these conditions, we identify optimal loading at a detuning of -7.76 MHz or $\sim$- $43\,\Gamma$ and at a magnetic field gradient of $4.2\,\text{G}\,\text{cm}^{-1}$. For these parameters we measure $(3.9\pm0.1)\times10^6$ atoms in 3 s with a temperature of $(21.05\pm0.54)\,\mu\text{K}$.

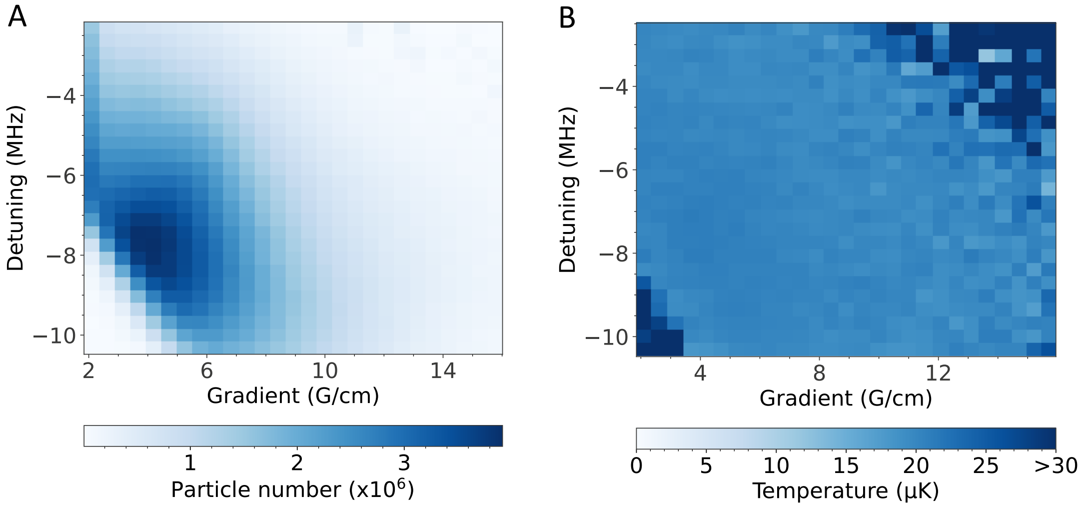

Figure 5.2 | Loading of the 3D-MOT. (A) Particle number and **(B)** temperature of the 3D-MOT as a function of the detuning from resonance and magnetic field gradient at the beginning of the loading cycle. The loading time is 3 s. During loading, the spectral width is 9 MHz with sideband spaced at 250 kHz. Data points are obtained by averaging over five experimental runs.

3D-MOT Spectral Broadening Parameters

During the first loading phase of the 3D-MOT, we spectrally broaden the cooling beams to increase the capture velocity range on the narrow intercombination transition. To explore the loading behavior, we perform two scans of different spectral broadening parameters.

In a first measurement, we vary both the width of the frequency comb and the detuning from resonance at a constant magnetic field gradient of 8.7 G cm^{-1} and sidebands spaced at 250 kHz. The detuning refers to the center frequency of the frequency comb. Figure 5.3a shows the recorded particle number and Fig. 5.3b the corresponding temperature measurement. We observe that increasing the spectral width of the frequency spectrum leads to an increase in particle number. For a comb width of 9 MHz and a center frequency detuning of -7.5 MHz, we achieve a maximum loading rate of $(4.24\pm0.08)\times10^6$ atoms at (22.7 ± 0.7) μK within 3 s.

This measurement is consistent with the expectation that a broader spectral frequency bandwidth ultimately leads to an increased capture velocity range, thereby improving the MOT loading efficiency. At a detuning closer to resonance, we observe regions with vanishing particle number. We attribute this to the presence of blue-detuned spectral components which induce heating and thus preventing the trapping of atoms. Whereas in the far red-detuned regime, a decreased spectral overlap with the Doppler-broadened atomic transition reduces cooling force and hinders trapping atoms in the MOT. Meanwhile, the temperature remains independent from the initial frequency comb width and detuning for relevant parameters. We observe increased temperatures in regions where the particle number vanishes, which prevents reliable temperature measurement and thus need to be treated as artifacts.

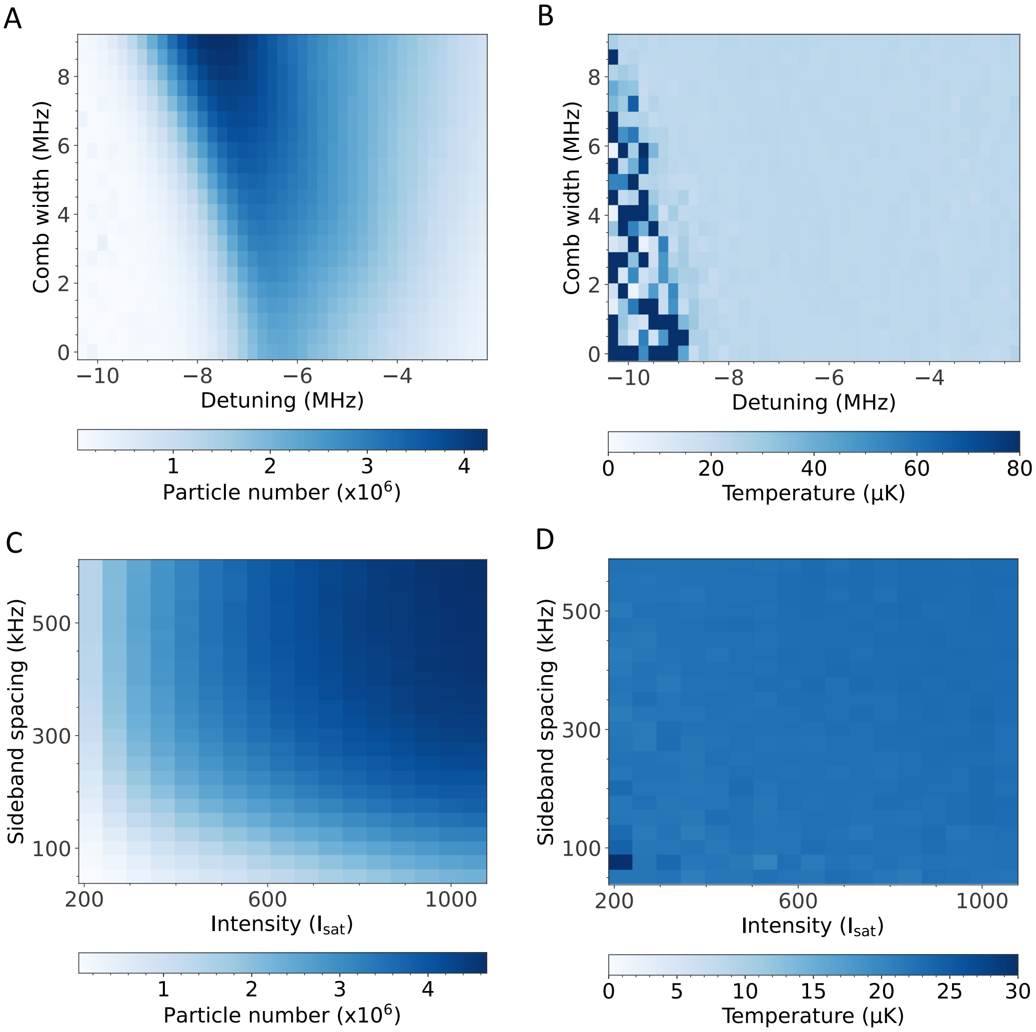

Figure 5.3 | 3D-MOT Spectral broadening. Particle number (left) and temperature (right) as a function of spectral broadening parameters during the 3D-MOT loading stage. The loading time is 3 s. Data points are obtained by averaging over five experimental runs. **(A, B)** Scan of the frequency comb and detuning of the center frequency from resonance. **(C, D)** Scan of the sideband spacing and total intensity of all 3D-MOT beams.

In a second measurement, we vary both the sideband spacing and the intensity of the MOT beams. Figure 5.3c shows the recorded particle number and Fig. 5.3d the corresponding temperature measurement.

We find that larger sideband spacings and a higher total MOT beam intensity lead to more efficient MOT loading. This is consistent with the interpretation, that increasing the sideband spacing results in a broader frequency comb, thus also increasing the capture velocity range. We assume that the available power is sufficient to operate in the power-broadened regime, ensuring that the individual spectral components have significant overlap.

We further observe that the particle number eventually saturates, suggesting that we reach sufficient spectral coverage within the investigated parameter space.

We find that the temperature is independent of the initial sideband spacing and intensity of the MOT beams. This measurement suggests that we require intensities of $\sim 950\,\mathrm{I_{sat}}$ for the loading rate to saturate, while operating the broadening at 600 kHz, yielding about $4.5\ \times 10^6$ atoms within 3 s.

Compression

To reach temperatures closer to the Doppler limit after the first loading stage, where the transition has been artificially broadened, the atomic cloud undergoes compression in two stages (see Fig. 5.1). Compressing the atomic cloud simultaneously increases the density of the MOT and makes efficient transfer of atoms into optical tweezers possible later on in this experiment.

In the first compression step, we reduce the spectral broadening, decrease the intensity of the cooling beams and bring the center frequency closer to resonance. In a second compression step, we ramp up the magnetic field, switch to a single-frequency MOT and reduce the detuning from resonance to its final value (see Fig. 5.1).

To explore optimal regions for MOT operation, we perform two scans of the final values in the second compression ramp.

In a first measurement, we vary both the final detuning and the end value of the magnetic field gradient. Figure 5.4a shows the recorded particle number and Fig. 5.4b the corresponding temperature measurement. We find a large parameter space for which sufficient atoms are trapped. We eventually observe atom loss when the final detuning is too close to resonance. We identify a magnetic field gradient of $5.25\,\mathrm{Gcm^{-1}}$ as a suitable value for 3D-MOT operation.

In a second measurement, we vary both the final detuning from resonance and the end value of the intensity ramp. Figure 5.4c shows the recorded particle number and Fig 5.4d the corresponding temperature measurement. Consistent with our expectations, we observe regions near resonance where the particle number vanishes, indicating heating effects. We find that reducing the intensity to minimal values (limited by the

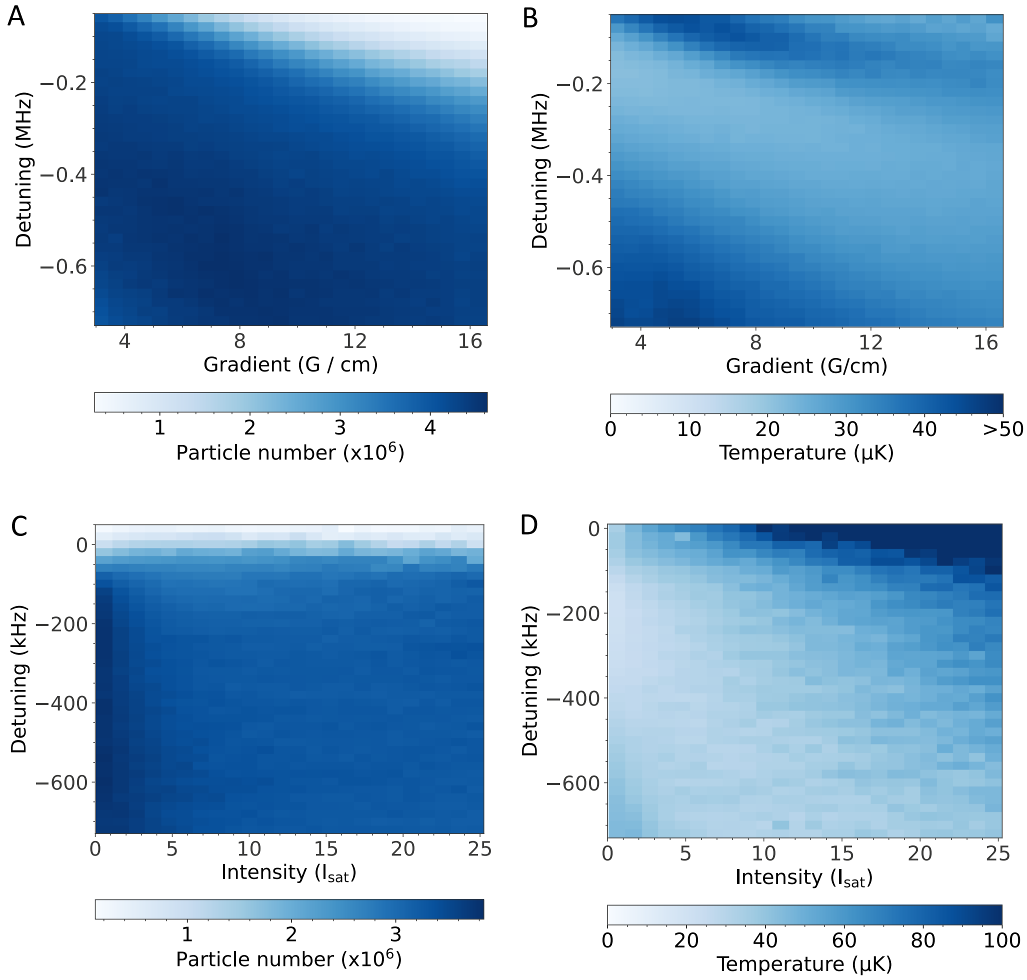

Figure 5.4 | **3D-MOT compression parameters.** Particle number (left) and temperature (right) as a function of final compression parameters of the 3D-MOT compression ramps. The loading time is 3 s. Data points are obtained by averaging over five experimental runs. **(A, B)** Scan of the detuning from resonance and magnetic field gradient. **(C, D)** Scan of the detuning and total intensity of all 3D-MOT beams.

power stabilization system), allows us to obtain the most atoms, while the temperature of the MOT is mostly independent from the intensity in the region of small intensities.

3D-MOT Loading Curve

We now investigate the loading behavior of the 3D-MOT. For this measurement, the MOT is loaded at a gradient of 8.7 G/cm, a total intensity of $\sim 1000\, I_{\text{sat}}$ and a detuning of $\sim 44\,\Gamma$. Spectral broadening is performed using a 9 MHz spectral comb containing sidebands spaced at 600 kHz. For MOT compression, we use a final gradient of 5.25 G/cm, a total intensity of $\sim 0.6\, I_{\text{sat}}$ and a detuning of $- \sim 1.3\,\Gamma$.

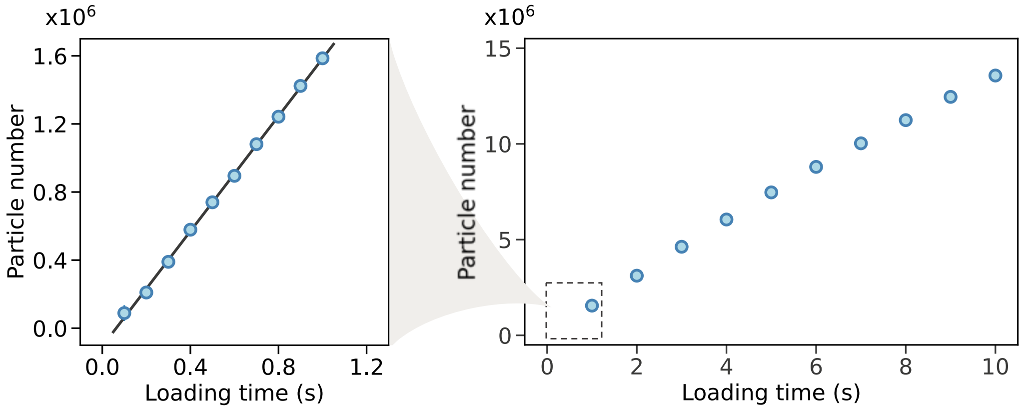

Figure 5.5 | 3D-MOT loading curve. 3D-MOT particle number as a function of loading time, shown for short (left) and long (right) time scales. Data points are obtained by averaging over five experimental runs. Error bars are smaller than the data markers. The data on the left is fitted with a linear function, suggesting a loading rate of $(1.69\pm0.02)\times10^6$ atoms/s.

The loading curve is presented in Fig. 5.5. The inset shows the loading on the time scale of 1 s. The plot on right side of Fig. 5.5 shows the loading behavior for up to 10 s for completeness. During standard operation, the anticipated high repetition experiments require only a small number of atoms. For conducting tweezer experiments this time scale is therefore most relevant. For such short loading periods, we find a linear relationship. A linear fit to the data yields a loading rate of about 1.7×10^6 atoms per second.

During daily operation, we find that the 3D-MOT particle number remains steady over a period of a few days. The loading rate primarily depends on the alignment of the 2D-MOT beams. Slow drifts in the 2D-MOT beams[1] cause the 3D-MOT particle number to decline and require maintenance on a weekly basis for optimal loading conditions. Additionally, we occasionally adjust the locking point of the 556 nm MOT laser because observe that over time the locking cavity causes a slow frequency drift. In the future, this effect can be mitigated by cavity drift compensation.

Temperature

To determine the temperature of the atoms in the compressed MOT, we allow the atomic cloud to expand ballistically after we switching off all cooling beams and the magnetic field. The MOT temperature is then derived from the rate of expansion.

To perform such time of flight measurements, we take an absorption image on the broad $^1S_0 \rightarrow ^1P_1$ transition and determine the size of the 3D-MOT cloud by fitting

---

[1] Since the 2D-MOT setup is operated entirely free-space and the beam propagates over a long distance, we observed large beam pointing fluctuations. This effect is exacerbated by mechanically unstable mounting components. We implemented an active beam stabilization system (Aligna, TEM Messtechnik) to mitigate most of the drifts. Residual beam pointing instability is cause by parts of the setup, which were not possible to stabilize and are free-running.

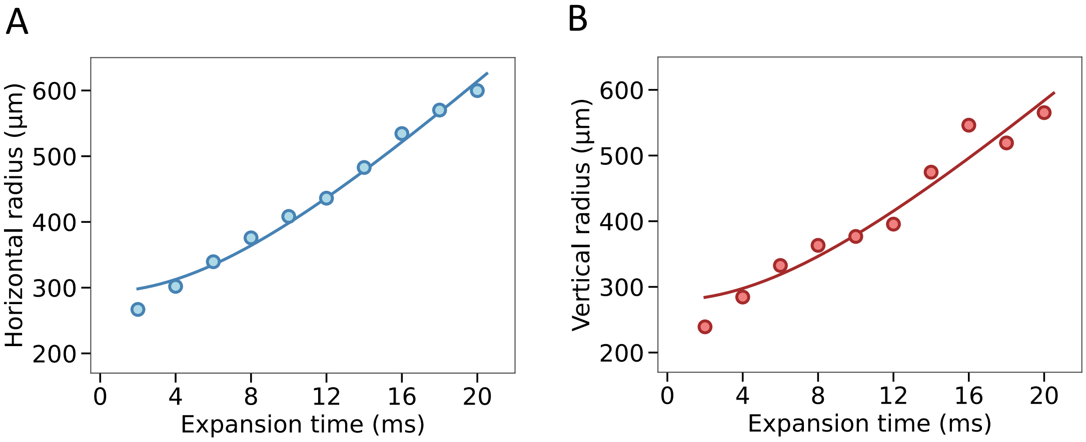

Figure 5.6 | **Time-of-flight (TOF) series.** Cloud width along the horizontal **(A)** and vertical **(B)** direction relative to the direction of gravity as a function of expansion time. The cloud diameter is given at the 1/e^2 level and extracted from absorption images using a Gaussian fit. Data points are obtained by averaging over five experimental runs. Error bars are smaller than the data markers. The solid lines indicate a fit to the data points (see main text for fit function). The extracted temperature along the horizontal/vertical axis are (14.9±0.6) µK and (13.5±1.3) µK, respectively.

a Gaussian function to the density distribution. Figure 5.6a and b show a typical time of flight measurement, where we record the width σ (1/e level) of the expanding atom cloud in the horizontal and vertical direction with respect to gravity for varying expansion times t, respectively. To extract the temperature T, we fit the data with the function

$$\sigma(t) = \sqrt{\sigma_0^2 + \frac{k_B T}{m} t^2}, \tag{5.1}$$

where σ is the cloud radius (1/e level) at expansion time t, σ_0 is the initial cloud radius at time $t = 0$, k_B is the Boltzmann constant and m the atomic mass. In this measurement, we obtain a MOT temperature of (14.9±0.6) µK along the horizontal axis and (13.5±1.3) µK along the vertical axis. Technical imperfections in the beam balance, alignment, polarization or magnetic field uniformity can contribute to a temperature mismatch between the two directions.

We find that at short time scales the presented data is not well described by the model. We therefore hypothesize that photon re-absorption in the high-density environment of a compressed MOT induces additional repulsive forces during ballistic expansion, leading to an overestimation of the temperature. This picture is consistent with the data, where the cloud is initially smaller that predicted by the model.

Reducing the density of the compressed MOT could suppress this effect and yield a more reliable temperature measurement. Under such conditions, temperatures approaching the theoretical Doppler limit of 4.4 μK may be achievable.

Lifetime

As a final characterization measurement, we investigate the lifetime of the compressed atom cloud after switching off all cooling beams and the magnetic field.

Figure 5.7 shows the survival fraction after a variable hold time. Because of the high densities after compression, we consider a two-atom loss model. Unlike in an uncompressed MOT, where we can assume one-body exponential decay through background gas collisions determined by the vacuum quality, the high density environment of a compressed atom cloud facilitates two-body losses through light-assisted collisions. Assuming two-body losses as the primary loss mechanism, the population N can be described by the differential equation [183]

$$\frac{dN}{dt} = -\frac{N}{\tau} - \beta N^2, \tag{5.2}$$

where τ is the $1/e$ lifetime and β is the loss rate. The analytical solution to this equation is given by

$$N(t) = \frac{N_0 \tau}{N_0 \beta (e^{\tau t} - 1) + \tau e^{\tau t}}, \tag{5.3}$$

with N_0 being the initial population. We find good agree between the fit and the data shown in Fig. 5.7 using eq. 5.2. We extract a lifetime of $\tau = (7.1 \pm 0.7)\,\mathrm{s}$ and a loss rate of $\beta = (0.211 \pm 0.006)\,1/\mathrm{s}$.

By repeating the same measurement with an uncompressed MOT, density-dependent losses can be eliminated, making it possible to determine the vacuum-limited lifetime, which is dominated by collisions with residual background gas. In this experiment, however, a TOF-measurement with an uncompressed MOT was not successful, as the expanding cloud became rapidly dilute, preventing a reliable measurement of the particle number.

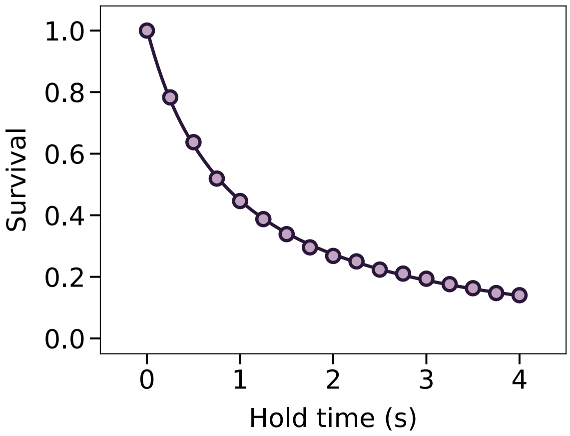

Figure 5.7 | Compressed MOT lifetime. Survival fraction of the compressed atom cloud as a function of hold time. The solid line is a fit, assuming a two-body loss model (see main etxt). We extract a 1/e lifetime of $\tau = (7.1 \pm 0.7)\,\mathrm{s}$.

5.2 Single atom preparation

In the previous section, we described the preparation of a laser-cooled ensemble of ^{171}Yb atoms in a three-dimensional magneto-optical trap. We now describe the procedure for initializing a tweezer experiment by loading single atoms into the tweezer traps. This is accomplished by spatially overlapping the optical tweezers with the 3D MOT, which operates on the intercombination line.

A key feature of tweezer-based experiments is their ability to isolate individual atoms within each trap. However, the initial loading process typically leads in multiple atoms being captured in a single tweezer. To achieve our goal of singly-occupied tweezer sites, pairwise loss is induced through light-assisted collisions, eventually leaving behind at most one atom per trap. Owning to the stochastic nature of this process, each tweezer is either empty or contains exactly one atom.

In the following, we discuss magic trapping and outline the experimental procedure for preparing a tweezer array filled with single ^{171}Yb atoms. In the second part of this section, we conduct first characterization measurements to investigate the single atom loading process into 759 nm tweezers enabled by light-assisted collisions.

5.2.1 Loading ^{171}Yb into optical tweezers

Figure 5.8 gives an overview of the beam geometry for optical tweezer trapping and imaging of individual atoms. We perform all characterization measurements by loading ^{171}Yb atoms into an 8×8 tweezer array generated by a spatial light modulator (SLM) operating. Throughout this work, we use a 759 nm laser beam to provide the trapping light for the tweezers. Optical tweezers at this wavelength benefit from a magic trapping condition for the clock transition $^1\mathrm{S}_0 \leftrightarrow {}^3\mathrm{P}_0$ [182]. In contrast, the widely employed tweezer wavelength 532 nm is magic for the imaging and cooling transition $^1\mathrm{S}_0 \leftrightarrow {}^3\mathrm{P}_1$ in ^{174}Yb. However, in ^{171}Yb this is not the case for any of the m_F states in the $F = 3/2$ hyperfine manifold of $^3\mathrm{P}_1$ because the non-zero nuclear spin leads to state mixing and modified polarizabilities. To overcome this drawback in the fermionic isotope, we can in fact tune the trapping potential by altering the polarization of the trap to obtain a magic trapping condition for transitions on the intercombination line as well [126]. The mechanism behind engineering equal trapping potentials by adjusting the polarization angle of the tweezer light field with respect to the quantization axis - referred to as the *magic angle* - is briefly discussed in the following.

Magic angle trapping

To fully exploit the narrow-line intercombination transition for cooling and imaging, it is critical to provide equal trap potentials for the ground ($^1\mathrm{S}_0$) and excited state ($^3\mathrm{P}_1$), thus eliminating trap-induced AC Stark shifts. In that case the transition

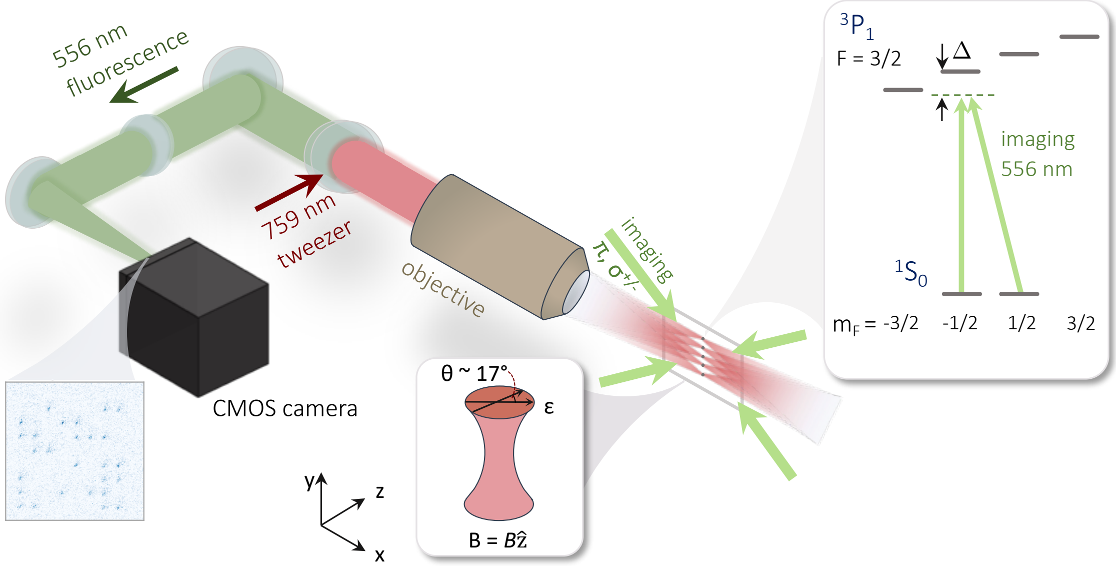

Figure 5.8 | Tweezer experiment beam layout. Simplified schematic of the experimental setup for performing tweezer experiment. An optical tweezer array at 759 nm is produced by an SLM and focused down with a microscope objective. Single atoms are imaged with 556 nm light, using all six 3D-MOT beams. We accomplish this via the $^1\text{S}_0 \rightarrow |^3\text{P}_1, F = 3/2, m_F = -1/2\rangle$ transition. The fluorescence is collected using the same microscope objective. The light is separated from the tweezer beam using a dichroic mirror and focused onto a CMOS camera for imaging. (Inset: Typical fluorescence image of an 8×8 tweezer array.) Magic trapping of ^{171}Yb atoms is achieved by setting the angle between the polarization of the trapping light ϵ and the magnetic field B to the magic angle of 17 °.

frequency is decoupled from the motional state of the atom in the trap and as a result is insensitive to slight variations in the trap depth and the position within the trap. The appropriate choice of the trapping wavelength can lead to magic conditions where the differential polarizability vanishes, such as at 759 nm for the ultra-narrow clock transition in ^{171}Yb.

We can simultaneously attain magic conditions at this trapping wavelength for the intercombination transition by setting the angle θ between the tweezer polarization and the magnetic field to a magic angle (see inset of Fig. 5.8). This technique has been demonstrated in both Yb [126, 146] and Sr [117, 184]. The magic angle approach relies on the interplay of the scalar, vector and tensor polarizabilities for the magnetic sublevels m_F of the excited (^{3}P$_1$) state $F = 3/2$ manifold, such that the differential light shift vanishes for the transition $^1\mathrm{S}_0 \leftrightarrow {}^3\mathrm{P}_1, F = 3/2$. The AC Stark shift ΔE for excited state is given by the expression [146]

$$\Delta E(^3\mathrm{P}_1, m_F) = -\frac{1}{4}\alpha_e(m_F, \theta) I,$$

where I is the laser intensity and $\alpha_e(m_F, \theta)$ is the polarizability of sublevels in the excited state:

$$\alpha_e(m_F, \theta) = \alpha_e^S - \alpha_e^T \frac{1 - 3\cos^2\theta}{4}(m_F^2 - 2). \tag{5.4}$$

Here, α_e^S and α_e^T are the scalar and tensor polarizabilities and θ is the angle between the quantization axis and the polarization direction of the light field. Note that since we use linearly polarized light, the contribution from the vector polarizability vanishes. The light shift on the ground state ^{1}S$_0$ is given by

$$\Delta E(^1\mathrm{S}_0) = -\frac{1}{4}\alpha_g^S I,$$

where α_g^S is the scalar polarizability in the ^{1}S$_0$ state. Because the ground state has angular momentum $J = 0$, the tensor polarizability vanishes. By tuning the angle θ in eq. (5.4), it is possible to achieve a magic condition such that $\Delta E(^3\mathrm{P}_1, F, m_F) = \Delta E(^1\mathrm{S}_0)$. In Ref. [126], a magic angle of 17° for the $^1\mathrm{S}_0 \leftrightarrow |^3\mathrm{P}_1, F' = 3/2, mF' = -1/2\rangle$ transition in ^{171}Yb has been demonstrated at a magnetic field of $B = 16\,\mathrm{G}$. In our experiment, we observe good agreement with this value. To control the polarization angle we use polarization optics (see Sec. 4.2.1). We measure the polarization angle directly before the microscope objective using a polarimeter[2].

Overview of the experimental sequence

Here we provide a general overview of the steps for conduction a tweezer experiment. A typical experimental sequence starts out by preparing a compressed 3D MOT, as described in the previous section. The sequence for executing a tweezer experiment run for the measurements shown in this work is illustrated in Fig. 5.8. The parameters

---

[2] Schäfter + Kirchhoff, SK010PA

specified here were obtained by optimizing each stage of the experimental cycle. The corresponding analysis is provided in the remainder of this chapter.

Our starting point is the preparation of a 3D MOT. To enable optimal overlap with the tweezer array, we tune the position of the compressed MOT cloud, by applying an external field generated by three compensation coil pairs for each spatial direction and moving the cloud to the focal point of the tweezers. This is necessary because the null point of the main magnetic field gradient differs from the position of the tweezer array[3]. We find that the MOT positioning is crucial for loading, as the extent of the cloud is roughly a few 100 μm.

In the next step, the MOT is extinguished. After waiting until the MOT is dissipated, we ramp up the magnetic field and then apply a 556 nm pulse to induce pairwise loss between atoms within a single trap, resulting in either zero or one atom per trap. This mechanism is explained in the next section. Afterwards we perform a cooling pulse with the same 556 nm beams. We then apply an imaging pulse to take a first fluorescence image, where we assess the initial filling of the traps. During imaging, we ramp up the tweezer depth. Depending on the performed experiment, the necessary operations such as rearrangement or qubit rotations can be executed afterwards. We take a second fluorescence to record the outcome of the experiment. Additional images can be performed in between experimental operations to enable mid-circuit measurements [126, 131].

---

[3] In our experiment, the two microscope objectives are located in between the magnetic field coils, leaving only a few mm of space between the objective and coils. This complicates the alignment of the objectives and prevented us from matching the position of the array with the null point of the magnetic field gradient.

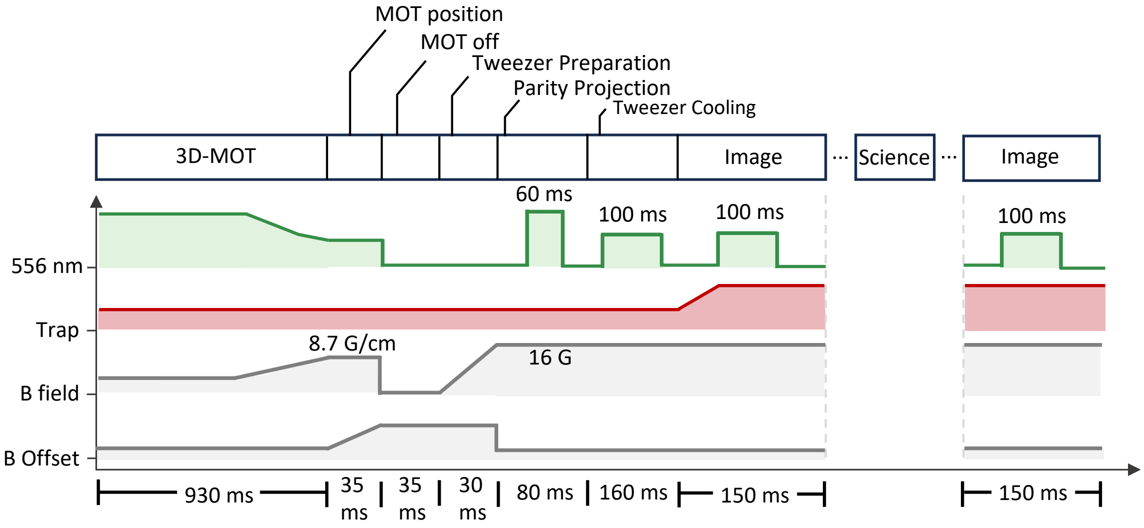

Figure 5.9 | Tweezer experiment sequence. Illustration showing a standard experimental sequence for performing tweezer experiments. After producing a 3D-MOT, the atomic cloud is moved to the tweezer array position by tuning the offset fields. The loading process into the tweezers is completed by extinguishing the MOT and waiting for the atomic cloud to dissipate. After ramping of the magnetic field, a parity projection pulse is applied to achieve single-atom occupation through pairwise loss, followed by a 556 nm cooling pulse. A fluorescence image allows to evaluate the occupation of tweezer array. A second image captures the outcome of a subsequent tweezer experiment protocol.

5.2.2 Parity Projection

A central step in operating a tweezer experiment is the isolation of individual atoms. This is accomplished by inducing light assisted collisions between the atoms captured by a single tweezer, leaving either a single or no atom per site.

When atoms are initially loaded into the traps, the loading process is stochastic and the loading probability with N atoms follows a Poissonian distribution. We can eliminate excess atoms by driving pairwise loss. Traps loaded with an even number of atoms would therefore result in an empty trap, whereas an uneven number of particles leaves a single atom behind, hence this process is also called parity projection (PP). In the limit of large particle numbers this yields a probability of 0.5 for a trap to be filled with an individual atom [65].

Pair-wise atom loss

A commonly employed technique for implementing such pair loss in tweezer experiments is through photo-association of atom pairs. This involves excitation to a two-atom molecular bound state, which upon decay, releases energy in the form of kinetic energy, resulting the pair to be expelled from the tweezer trap [118, 185, 186]. While the exact energy landscape of the molecular states involves sophisticated modeling, we can experimentally infer the likely presence of such resonances at which light assisted collisions occur based on changes in the loading probability, as discussed in the following.

To induce pairwise loss, we apply a 60 ms pulse driving the $^1\mathrm{S}_0 \leftrightarrow {}^3\mathrm{P}_1$ transition blue-detuned by 500 kHz ($\sim 2.7\,\Gamma$) from the $|^3\mathrm{P}_1, F = 3/2, m_F = 1/2\rangle$ resonance. We operate at a magnetic field of 16 G. Figure 5.10a shows the loading behavior of the tweezer array as a function of MOT loading time with (blue) and without (black) applying the parity projection pulse. The probability of detecting an occupied tweezer when omitting the PP pulse, becomes greater than 96.7 %. When driving the PP pulse, we observe that the occupation probability saturates at 0.5 for sufficient loading times and stabilizes at that value for longer loading times, suggesting stochastic loading and pair-wise loss. For longer loading times, the probability of 0.5 does not increase, which is an indication of single atom loading. From this measurement we also conclude that our experiment requires MOT loading times of ≈ 100 ms to sufficiently load an 8×8 tweezer array.

We further find that the loading probability is insensitive to the intensity (see Fig. 5.10b) as well as duration (see Fig. 5.10c) of the PP pulse in this measurement. We record the loss probability between the first and second fluorescence image. In practice, observing the loss probability is a useful measure for assessing the efficacy of the PP pulse, as an increased loss probability can indicate that excess atoms are removed by the fluorescence image pulse rather than the actual PP pulse. We find an average occupancy of (53.8 ± 1.3) % across the measured intensity range in units

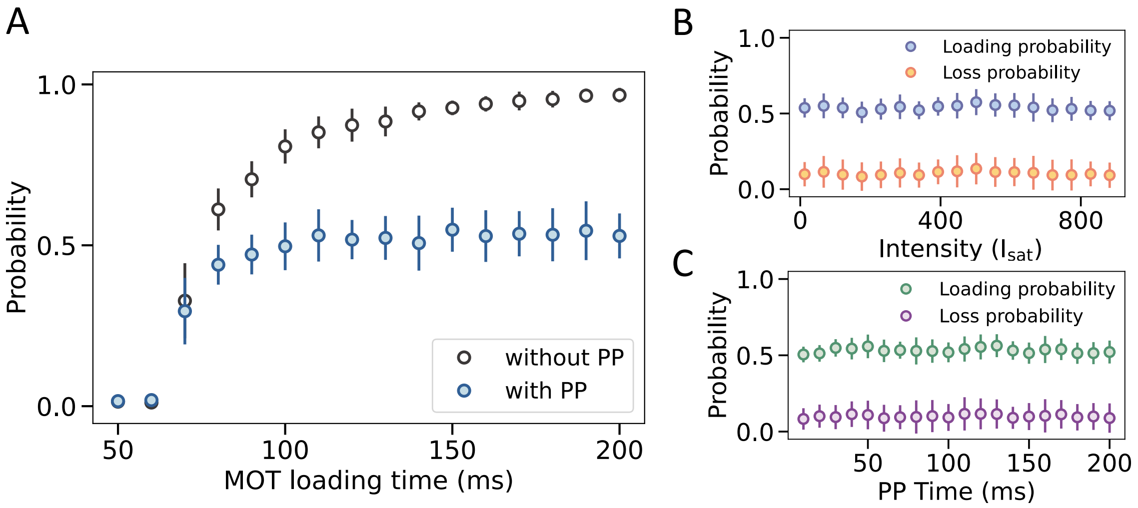

Figure 5.10 | Parity projection. Pair-wise loss measurement showing the tweezer loading probability. **(A)** Probability of finding an occupied tweezer as a function of MOT loading time with (blue circles) and without (black circles) applying a 60 ms parity projection (PP) pulse. **(B)** Loading probability and probability of loss after repeated measurement for varying PP pulse intensity and **(C)** pulse time.

of the saturation intensity ($I_{\mathrm{sat}} = 0.138\,\mathrm{mW/cm^2}$), whereas the loss probability is steady over the measured intensity range. When varying the pulse time, we measure an average loading probability of $(53.2 \pm 1.6)\,\%$, suggesting that PP pulse as short as 10 ms are sufficient to achieve full PP pulse efficiency.

Enhanced Loading

The reliable preparation of defect-free arrays is a key requirement in order to utilize optical tweezer platforms as quantum qubit registers. A common procedure is rearrangement of individual atoms into defect-free arrays using movable tweezers generated by acousto-optic modulators (AODs) [72, 187, 188]. While atom-by-atom assembly serves as an effective method for providing fully loaded arrays, it comes at the cost of limited scalability and requires complex sorting algorithms [72, 73, 75].

Careful engineering of light-assisted collisions has led to the development of enhanced loading schemes for both alkali [65, 189, 190] and alkaline earth atoms [118], thus overcoming the probabilistic loading efficiency limit of 50 %. This technique relies on optical shielding that occurs when exposing the atoms to near-resonant, blue-detuned light. Excitation to a repulsive molecular potential allows controlled energy transfer during two-body collisions, resulting in the loss of a single atom from the trap rather than loss of both atoms. This process increases the probability of retaining a single atom per trap, thereby increasing the overall loading efficiency.

Experiments with ^{171}Yb atoms in 532 nm tweezers reported efficiencies reaching 96 % [125] aided by blue-shielded collisions [189, 191]. Near-deterministic loaded has been also demonstrated with ^{171}Yb in 759 nm magic tweezers, achieving loading efficiencies of around 70 % [129] or even 80 % [126].

Here, we explore the prospect of overcoming probabilistic loading in our experiment by performing a scan of the PP pulse detuning.

To perform the measurement, we load atoms into an 8×8 array with ∼13 MHz deep tweezers (14 mW per tweezer). The total intensity of the 60 ms parity projection pulse is 447 $\mathrm{I_{sat}}$, where $\mathrm{I_{sat}} = 0.138\,\mathrm{mW/cm^2}$. We apply a 16 G magnetic field to split the m_F states of the $F = 3/2$ hyperfine level of $^3\mathrm{P}_1$. The selected experimental parameters were chosen to closely match established enhanced loading protocols.

Figure 5.11 shows the loading probability for a varying detuning of the parity projection pulse from the $^1\mathrm{S}_0 \leftrightarrow |^3\mathrm{P}_0, F = 3/2, m_F = -1/2\rangle$ resonance. We observe two distinct regions with non-zero single-atom loading probability.

The first plateau corresponds to the case where the addressing beam is blue-detuned with respect to the $m_F = -1/2$ resonance. The mean loading probability across this range is ≈ 54 %, with a maximum recorded loading fraction of (58.2 ± 7.9) %. The inset in Fig. 5.11 shows a typical single-shot fluorescence image at this detuning.

When crossing the resonance to the red-detuned side, we observe heating and all atoms are lost from the traps. We also can identify the $m_F = +1/2$ resonance and find a second plateau where the loading probability is slightly increased above 50 % as well.

While enhanced loading schemes in similar setups have demonstrated efficiencies of up to 80 % [126], we observe maximum loading fractions closer to 60 %. It has been suggested that the loading fraction correlates with the density of the reservoir [129]. Higher loading efficiencies may therefore be achievable under modified conditions.

The molecular dynamics leading to increased probabilities of one-atom loss depends on the intricate interplay between the trap characteristics, the involved motional states, cooling rates and pulse parameters to redistribute energy in a favorable way. Because of this, additional measurements are required to better understand the observed loading behavior in our experiment and to fully optimize the loading dynamics.

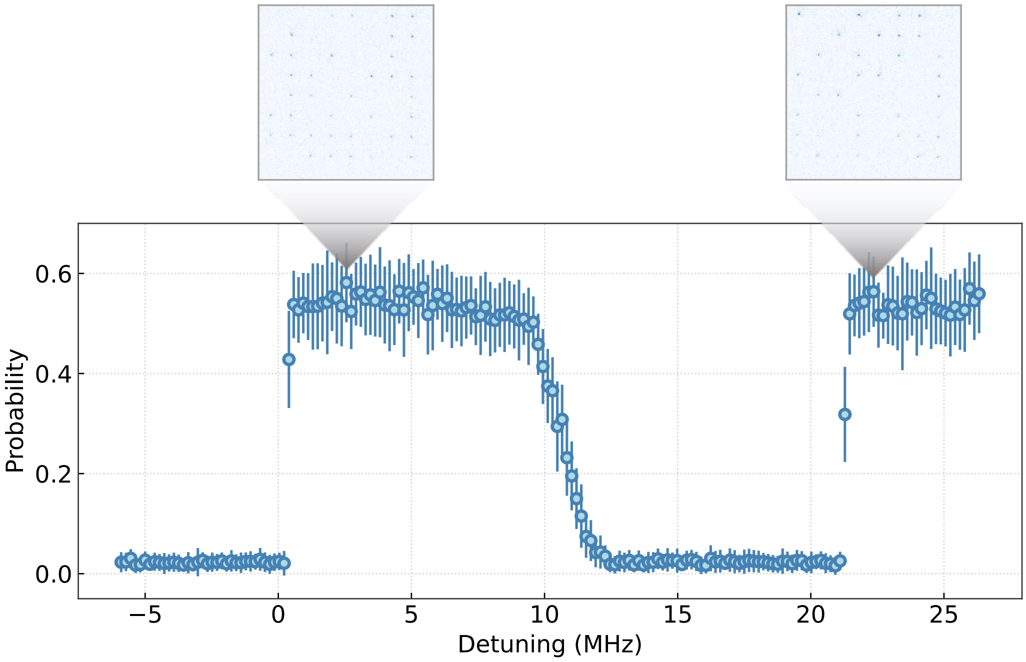

Figure 5.11 | **Single-atom loading fraction.** Loading probability as a function of parity projection pulse detuning from to the $|^3\mathrm{P}_1, F = 3/2, m_F = -1/2\rangle$ resonance. The measurement is performed at a magnetic field is 16 G and the total intensity of the parity projection pulse is 447 $\mathrm{I_{sat}}$. The pulse has a duration of 60 ms. Suitable regions of operation include two plateaus with $\approx 50\,\%$ loading probability. The insets show typical single shot fluorescence images at corresponding frequencies.

5.3 Single atom fluorescence imaging in 759 nm tweezers

The ability to detect single atoms with high accuracy is a core requirement in tweezer-based neutral atom experiments. To determine the presence of an individual atom within a tweezer trap, we perform a fluorescence image for qubit-readout.

Scattered photons are collected through the microscope objective and imaged onto a CMOS camera (Hamamatsu Orca Quest). We use the same six 3D-MOT cooling beams for imaging with polarization projection onto both the axial and radial direction of the tweezers. The imaging beam geometry is depicted in Fig. 5.8. After loading into tweezers in 35 ms and switching off the MOT beams, single-occupancy of the traps is obtained by a 60 ms parity projection pulse 800 kHz ($\sim 4.4\,\Gamma$) blue-detuned of the $^1\mathrm{S}_0 \rightarrow |^3\mathrm{P}_1, F = 3/2, m_F = +1/2\rangle$ resonance. Afterwards we apply an additional 100 ms tweezer cooling pulse. We acquire a fluorescence image at 100 ms exposure time. In the following, we explore the imaging properties of our ^{171}Yb tweezer system.

Photon statistics

A typical fluorescence image that we obtain is shown in Figure 5.12a. Single atoms are loaded stochastically into a 64-site (8×8) SLM-generated tweezer array spaced by 9.5 µm with 14 mW power per tweezer ($\sim$ 13 MHz trap depth).

In order to distinguish whether each site is occupied or empty, we define a mask containing each tweezer site and sum up the fluorescence counts within the area. Each mask is weighted with a point spread function (PSF), that is extracted from the average image (see Fig. 5.12b) of each individual tweezer site. At the end of each experiment, we take a reference image without any atoms that is then subtracted from the fluorescence in post processing to eliminate the effects of the imaging light.

By taking repeated images, we obtain a bimodal photon distribution, as illustrated in the histogram in Fig.5.12c. We collect this statistics by determining the photon count per site for each of the 64 sites for 60 measurements (3840 sites). The peak centered around zero photon counts is associated with an empty site (0 atoms), while the second peak can be attributed to the presence of a single atom.

The distribution is fitted with two Gaussian functions (solid line). The zero atom peak is expected to be Gaussian because the signal originates from stray light and thermal camera noise. The peak associated with the atomic signal is Possonian in nature because the statistics emerges from the independent and random emission of photons. However, we find that it is better described by a Gaussian. We believe this effect emerges due to variations in the tweezer depth across the array and thus scattering rates. The resulting peak is Gaussian as it is now the sum of many underlying Possonian events.

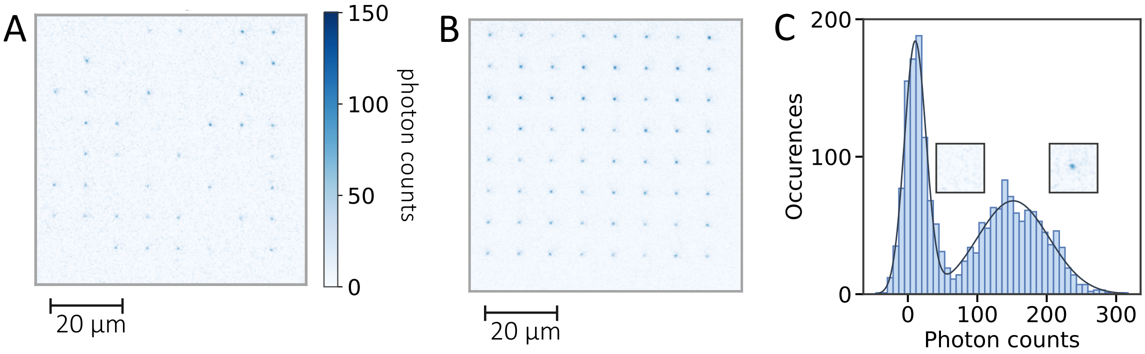

Figure 5.12 | Typical fluorescence images. (A) Single-shot fluorescence image of individual ^{171}Yb atoms loaded into an SLM-generated 8×8 tweezer array. The tweezers are spaced by 9.5 µm. **(B)** Averaged fluorescence image of the same tweezer array shown in (A). The image is obtained by averaging over 60 individual measurements. (C) Histogram of the photon count statistics obtained in 100 ms by 60 repetitions of a 8×8 array (1900 sites). The left peak is associated with an empty site, while the right peak corresponds to an occupied site. The insets show typical raw images of a vacancy and an atomic signal. The solid line is a fit with two Gaussian functions.

To identify the presence or absence of a site, we define a predetermined count threshold to classify the site into dark or bright. We discuss how we identify an appropriate threshold with the goal of minimizing the classification infidelity in the context of the imaging characterization in the following section.

Imaging fidelity

During qubit-readout there are several types of errors that can occur due to the imaging process which ultimately limit both the imaging classification fidelity and atom survival. This includes events where (1) an occupied site is classified as an empty site (false negative, $P_{b\to d}$), (2) a vacancy is identified an occupied site (false positive, $P_{d\to b}$), (3) the atom is lost during the imaging process ($P_{\mathrm{loss,d}}$) or (4) an empty site appears bright after imaging ($P_{\mathrm{loss,b}}$), where P_i is the probability of these events to occur. To minimize these quantities, we characterize our imaging procedure by exploring the influence of the imaging frequency and imaging intensity.

The result for the imaging classification infidelity $1-\mathcal{F}$ as a function of the imaging frequency and intensity is presented in Fig. 5.13a. In this context, the imaging fidelity $\mathcal{F}$ refers to the metric for how well we can discriminate the 0 from the 1 atom peak.

We prepare an 8×8 tweezer array loaded with ^{171}Yb atoms (14 mW per tweezer), following the previously presented protocol. We split the m_F states in the $^3\mathrm{P}_1, F=3/2$ hyperfine level with a 16 G magnetic field applied along the z-axis (see Fig. 5.8). The imaging beam detuning Δ is given relative to the $^1\mathrm{S}_0 \to |^3\mathrm{P}_1, F=3/2, m_F=-1/2\rangle$ transition. For each data point, we repeatedly take 60 fluorescence images in 100 ms from which the photon count statistics is obtained. The resulting histogram recorded at optimal imaging parameters which minimize the discrimination infidelity (denoted with a star symbol), is shown as an inset in Fig. 5.13a. We find $\mathcal{F}=0.99993$ at

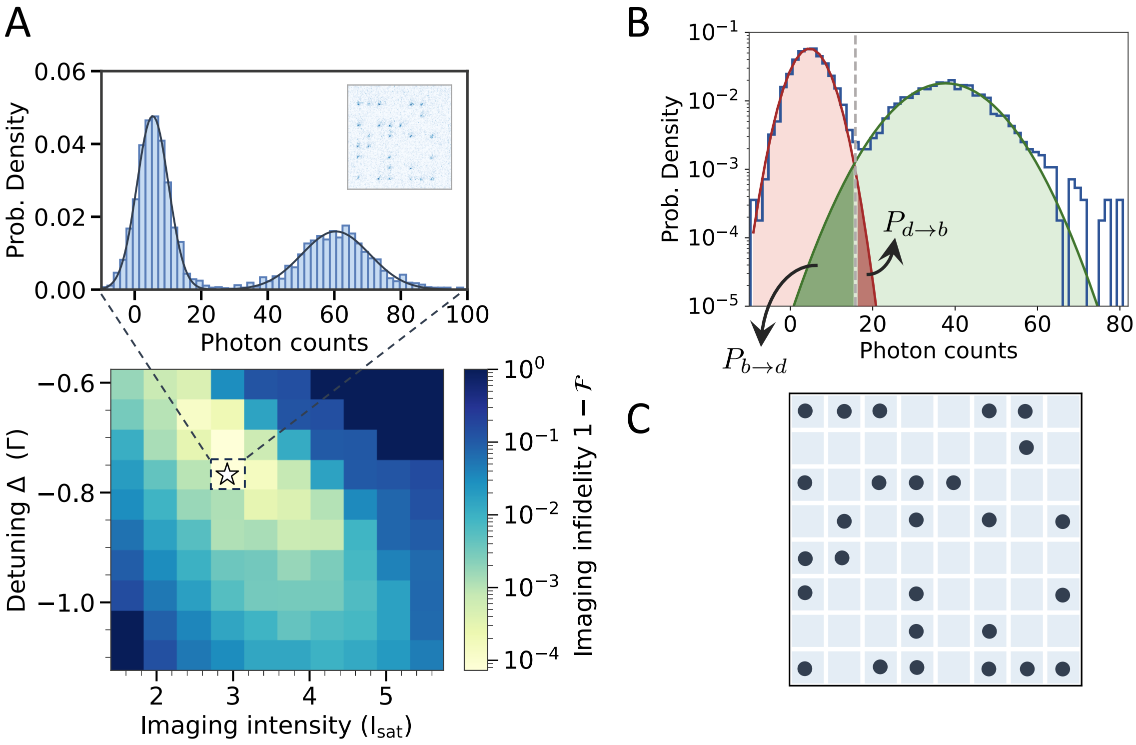

Figure 5.13 | Imaging fidelity of ^{171}Yb atoms in 759 nm tweezers. **(A)** Imaging infidelity as a function of the detuning from the $m_F = 1/2$ resonance ($\Gamma = 182\,\mathrm{kHz}$) and intensity of the imaging beams. The star denotes the parameter set with minimal imaging fidelity ($\mathcal{F} = 0.99993$, $\Delta = -0.8\,\Gamma$, $I = 2.9\,I_{\mathrm{sat}}$). Each data point is obtained by repeating the measurement 60 times. Inset: Corresponding histogram of the collected photon count statistics (8×8-array, 64 sites, 60 measurements) and a typical single-shot fluorescence image. The solid line a fit with two Gaussian functions. **(B)** Histogram of the photons counts with optimal imaging parameters (see main text). The detection threshold (dashed line) is determined for each histogram such that the overlap between the 0 (red) and 1 (green) atom peak is minimal. The two features are each fitted with a Gaussian function. Classification error probabilities (false negative and false positive) are denoted as $P_{b\to d}$ and $P_{d\to b}$, respectively. **(C)** Typical occupation matrix determined for each fluorescence image. The occupation is evaluated based on the classification threshold.

$\Delta = -0.8\,\Gamma$ and $I = 2.9\,I_{\mathrm{sat}}$, where $I_{\mathrm{sat}} = 0.138\,\mathrm{mW/cm^2}$ and $\Gamma/(2\pi) = 182\,\mathrm{kHz}$ is the saturation intensity and natural linewidth, respectively.

We determine a classification threshold, above which atoms are considered present and below which atoms are said to be absent. This process involves a Gaussian fit to both of the peaks, integrating over the fit functions and minimizing the area of overlap. A visual representation of this procedure is shown in Fig. 5.13b. The photon count threshold allows us to compute a corresponding occupation matrix based, which records the occupation for each fluorescence image (see Fig. 5.13c for a typical occupation matrix of the fluorescence image shown in the inset of Fig. 5.13a). We aim for imaging parameters, where the 0 and 1 atom peaks are well separated. This is necessitated by a higher photon count. While a longer exposure time allows more photons to be scattered, the downside is increased heating and a higher probability of the atom being lost after imaging. In future experiments we could reduce the exposure time to reduce atom loss, as sufficient photons are collected to discriminate vacancies from single atom signals, achieving ~ 150 photons in 100 ms. Recent demonstrations report on atom loss probabilities of 0.19 % and discrimination fidelities of 0.998 with imaging durations of 3.5 ms [126] in which approximately 20 photons per atom are detected. Another improvement is to decrease the noise background to improve the signal to noise ratio and in turn the discrimination fidelity.

Imaging loss

We now investigate the imaging loss between two consecutive fluorescence images as a function of the imaging beam detuning and intensity. The result of this measurement is shown in 5.14.

The parameter set at minimal observed imaging loss is indicated by a star symbol. We find that the imaging frequency at detuning $\Delta = -0.8\,\Gamma$ minimizes both the imaging loss and imaging classification infidelity. However, a reduced imaging beam intensity of $I = 2.1\,I_{\mathrm{sat}}$ ($I_{\mathrm{sat}} = 0.138\,\mathrm{mW/cm^2}$) is more desirable when minimizing the imaging loss is prioritized. This comes at the cost of a slightly decreased imaging fidelity of 0.996 compared to the optimal discrimination fidelity because less photons are scattered, resulting the peaks to be not as well resolved as for increasing intensities. This is reflected in the corresponding histogram, depicted as an inset in Fig. 5.14.

To further analyze the imaging-induced atom loss, we plot the histograms of the first and second fluorescence image in a two-dimensional histogram in Fig. 5.15 . The photon count threshold for both images is indicated by the orange lines and determined as outlined previously. This allows us to directly visualize the events $b \to b$, $d \to d$, $b \to d$ and $d \to b$, where b denotes a bright event and d a dark site. From this measurement we extract the probabilities $P_{b\to b} = 0.388$, $P_{d\to d} = 0.574$, $P_{b\to d} = 0.036$ and $P_{d\to b} = 0.002$. We attribute the dark to bright events to atoms which occupy trapped metastable states (${}^3\mathrm{P}_0$ or ${}^3\mathrm{P}_2$) during the first readout and are detected in the second readout upon decay.

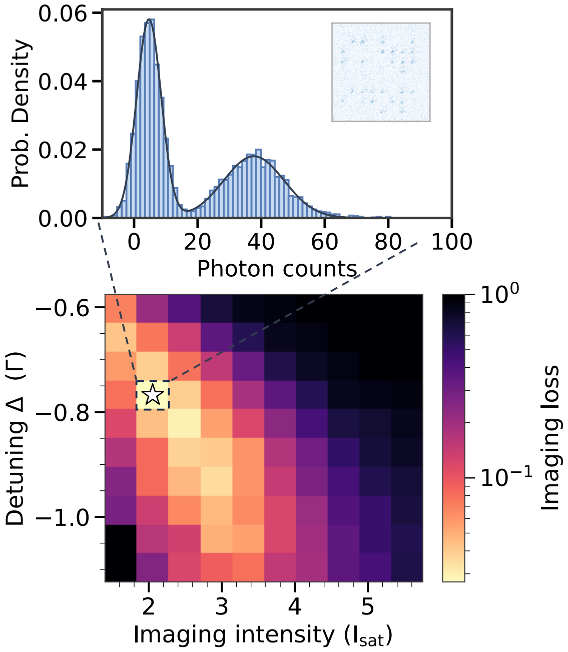

Figure 5.14 | Imaging loss of ^{171}Yb atoms in 759 nm tweezers. Atom loss as a function of the detuning from the $m_F = 1/2$ resonance ($\Gamma = 182\,$kHz) and intensity of the imaging beams. The star denotes the parameter set ($\Delta = -0.8\,\Gamma$, $I = 2.1\,I_{\mathrm{sat}}$) resulting in minimal atom loss probability (2.7 %). Each data point is obtained by repeating the measurement 60 times. Inset: Corresponding histogram of the collected photon count statistics (8×8-array, 64 sites, 60 measurements) and a typical single-shot fluorescence image. The solid line a fit with two Gaussian functions.

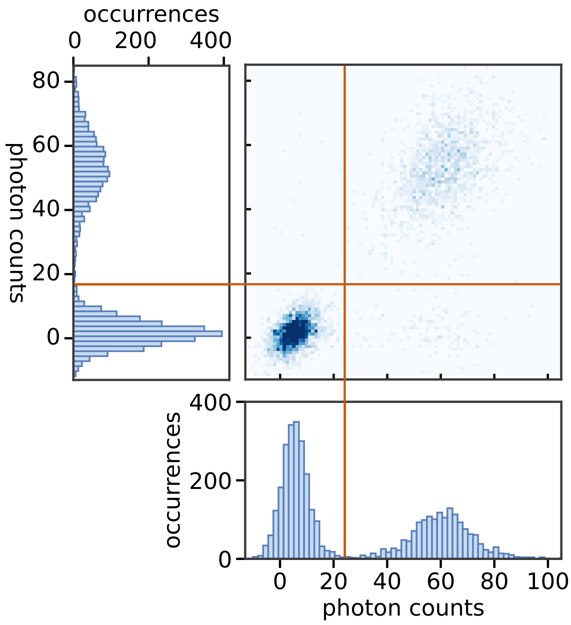

Figure 5.15 | Histograms of two consecutive images. Histogram from the first and second readout shown together in a two-dimensional histogram shown on the horizontal or vertical axis, respectively. The histograms are obtained by 60 measurements of a 8×8 tweezer array. The orange lines denote the discrimination thresholds of the first/second image. The measurements are performed with imaging parameters $\Delta = -0.8\,\Gamma$ and $I = 2.9\,I_{\mathrm{sat}}$ (see main text for details on the imaging procedure).

5.4 Lifetime of individually trapped atoms

A dominant error channel during qubit-readout is the loss of atoms from the traps. Fluorescence imaging inherently relies on photon scattering, which inevitably leads to heating through photon recoil and eventually atom loss from the traps. We address this issue by simultaneously cooling trapped atoms on the narrow-line green transition during imaging. This Doppler-cooling scheme is enabled by the magic trapping condition between the ground and excited state, as differences in the trapping potential cause changes in kinetic energy and therefore heating when driving the transition.

To characterize the atom loss in our setup, we study the lifetime of ^{171}Yb atoms in optical tweezers under different conditions. It allows us to determine on which time scale and at which rate atoms are lost from the traps. This knowledge is crucial for later experiments involving qubit operations and mid-circuit readout. We perform two measurements to assess the survival probability.

In a first measurement, we record the survival between two consecutive images after a variable wait time and keep the imaging beams turned off. The same measurement is then performed under continuous illumination from the imaging light during the wait time period.

5.4.1 Lifetime in optical tweezers

After loading atoms into a 8 × 8 tweezer array following the experiment protocol presented in the previous sections, we take a first image in 100 ms to assess the initial occupation within the array, following the classification procedure from Sec. 5.3. We then turn off all imaging beams and wait a variable amount of time before acquiring a second image, from which we can infer if atoms have been lost during the process.

We repeat this measurement to determine the survival probability, presented in Fig. 5.16. The lifetime measurement is performed in tweezers with two different trap depths: 12 mW/tweezer ($U_0 = 0.56\,\mathrm{mK}$) shown in Fig. 5.16a and 19 mW ($U_0 = 0.86\,\mathrm{mK}$) shown in Fig. 5.16b .

We attribute the loss dynamics during this measurement to two distinct physical mechanisms. First, we consider collisions with the background gas in the vacuum chamber, leading to exponential loss. The survival probability due to background collisions after time t reads

$$P_{\mathrm{coll}}(t) = e^{-t/\tau}, \tag{5.5}$$

where τ is the 1/e-lifetime.

The second loss channel is associated with the heating process in the harmonic trap.

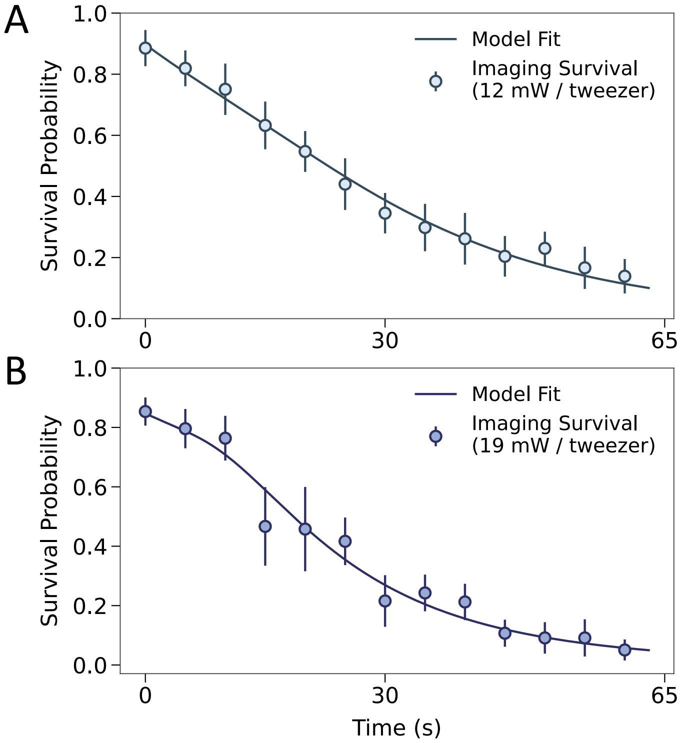

Figure 5.16 | Lifetime of ^{171}Yb in 759 nm tweezers. Survival probability of atoms in optical tweezers after repeated imaging as a function of hold time. During a variable hold time in between taking images, the imaging light is turned off. The measurement is performed with trap power **(A)** 12 mW (depth $U_0 = 0.56\,$mK) and **(B)** 19 mW (depth $U_0 = 0.89\,$mK) (bottom figure). Each data point is obtained by averaging over a 64-site stochastically filled array and repeating the measurement 15 times. We fit the data (solid line) using a model presented in the main text, yielding a 1/e-lifetime of $46 \pm 9\,$s or half-life of 26 s (top) and $70 \pm 65\,$s or a half-life of 22 s (bottom).

Using the heating term provided by Ref. [192], the survival probability due to heating reads

$$P_{\text{heat}}(t) = 1 - \exp\left(-\frac{U_0}{k_{\text{B}}(T+\alpha t)}\right)\left(1 + \frac{U_0}{k_{\text{B}}(T+\alpha t)} + \frac{U_0^2}{2k_{\text{B}}^2(T+\alpha t)^2}\right),$$

where U_0 is the trap depth, T the initial temperature and α the heating rate. The total survival probability is then given by

$$P_{\text{survival}} = P_0 \cdot P_{\text{coll}}(t) \cdot P_{\text{heat}}(t),$$

with P_0 being the survival probability at wait time $t = 0$. Fitting the data to this model, we can extract $\tau = 46 \pm 9\,\text{s}$ (or a half-life of 26 s) and $\alpha = 3.3 \pm 0.7\,\mu\text{K}$ in the more shallow traps at $U_0 = 0.56\,\text{mK}$. For the deeper traps at $U_0 = 0.89\,\text{mK}$, we find $\tau = 70 \pm 65\,\text{s}$ (or a half-life of 22 s) and $\alpha = 10 \pm 3\,\mu\text{K}$.

For small values of t, the contribution from collisional losses P_{coll} dominates over the heating-related term. However, in the experiment conducted here, the time scale over which collisions are relevant is limited to the first two data points, which likely contributes to large uncertainty in the extracted lifetime τ. We believe that the accuracy of τ provided by the model could be improved by collecting additional data at shorter times.

We further observe for both tweezer depths that the survival after taking two images back to back, i.e. at $t = 0$, is reduced. This suggests imaging-induced losses in the range of ∼ 10 - 15 % and could indicate unfavorable imaging parameters. Measuring the survival as a function of the number of consecutive images, would provide further insight.

5.4.2 Lifetime under constant illumination

To capture the additional effect of the imaging beams on the lifetime in tweezers, we repeat the above measurement but illuminate atoms with imaging light during the wait time period. The result is presented in Fig. 5.17. We perform this measurement in traps with different depths ($U_0 = 0.56,\text{mK}$, 0.72 mK, 0.86 mK).

We assume that atom loss can be attributed to collisions with residual background gas atoms while heating is counteracted by the cooling effect of the imaging beam. The data can therefore be modeled by exponential decay of the survival probability P_{coll} from eq. 5.5, yielding lifetimes (1/e-level) of $\tau = (1.03 \pm 0.04)\,\text{s}$, $\tau = (9.1 \pm 0.2)\,\text{s}$ and $(10.8 \pm 0.2)\,\text{s}$, respectively.

We find that the lifetime under illumination is shorter than without, suggesting that scattering green photons leads to additional heating and atom loss. It is therefore desirable to shorten the currently employed imaging time of 100 ms. Similar experiments work with imaging durations down to 3.5 ms [126].

Additional error source could potentially stem from pointing fluctuations in the tweezer beam or variations in the trap intensity caused by improper power stabilization,

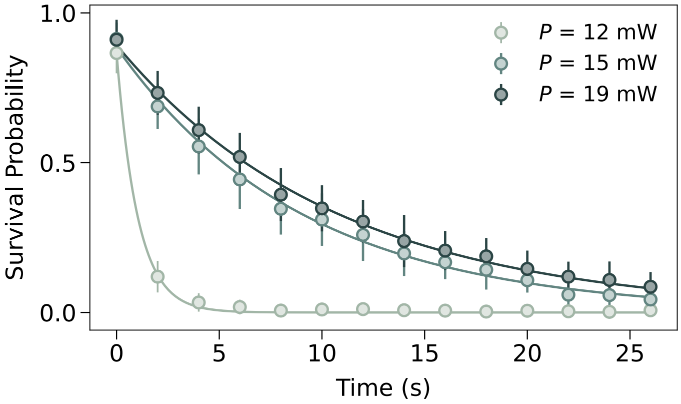

Figure 5.17 | Lifetime of ^{171}Yb under constant illumination. Survival probability of atoms in optical tweezers after repeated imaging as a function of hold time. Atoms are constantly illuminated with green imaging light in between image acquisition. The measurement is performed with trap powers 12 mW ($U_0 = 0.56$ mK, light green), 15 mW and ($U_0 = 0.72$ mK, green) 19 mW ($U_0 = 0.86$ mK, dark green). Each data point is obtained by averaging over a 64-site stochastically filled array and repeating the measurement 30 times. The data is fitted by an exponential decay (solid lines), yielding a 1/e-lifetime of $\tau = (1.03 \pm 0.04)$ s, $\tau = (9.1 \pm 0.2)$ s and (10.8 ± 0.2) s, respectively. .

leading to excess heating and expelling atoms from the traps. Further suppression of background gas collisions can be achieved by transitioning to a cryogenic environment [111, 193, 194].

5.5 Release-and-recapture measurement

To determine the temperature of the atoms in the tweezer traps, we perform a release-and-recapture experiment, following Ref. [195].

In this measurement we switch off the traps and allow the atoms to propagate according to their kinetic energy. When switching on the traps after a variable time-of-flight Δt, the initial velocity of the atoms in the traps is reflected in the probability to recapture the atoms. The same experiment is repeated many times from which the atomic temperature can be inferred.

Figure 5.18 shows the result of the release-and-recapture measurement, where we plot the probability of retaining an atom in the traps as a function of the release time from the traps, during which the trapping beams are turned off. The data is modeled using a classical Monte-Carlo simulation, yielding a best-fit temperature of 29 µK. The corresponding curve of the numerical simulation is shown as the solid line in Fig. 5.18 and well describes the recapture dynamics. The atom loss of $\approx 15\,\%$ at $\Delta t = 0$ is purely due to imaging. We attribute this significant loss to non-optimal imaging conditions (red-detuned by $\Delta = 0.7\,\Gamma$ from $|^3\mathrm{P}_1, F = 3/2, m_F = -1/2\rangle$, imaging beam intensity $I = 4.2\,I_{\mathrm{sat}}$). In particular, the elevated intensity of the imaging beams is most likely responsible for excess atom loss and the magnitude is in accordance to the measurement presented in Ch. 5.3, Fig. 5.14.

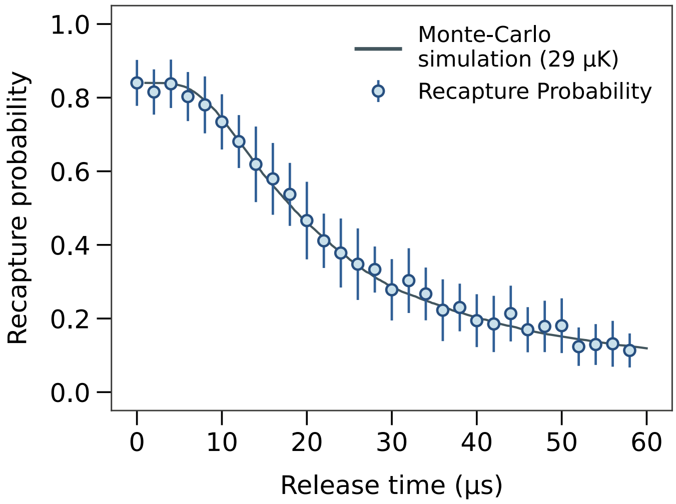

Figure 5.18 | Release-and-recapture measurement. Recapture probability of a single atom after releasing the atom from the traps by turning off the tweezer beam for a release time Δt. The solid line shows a classical Monte-Carlo simulation at 29 μK. Each data point is obtained by averaging over a 64-site stochastically filled array and repeating the measurement 15 times.

Reducing the intensity of the imaging beams to $2.1\,I_{\text{sat}}$ would most likely lead to an initial survival probability closer to ≈ 0.97.

A further reduction of the temperature down to the motional ground state of the tweezer traps is made possible with Raman sideband cooling schemes, which is currently being implemented in the experiment. Temperatures of 2.8 μK have been reported in Ref. [126].

5.6 Trapping frequencies

We finalize the characterization of our optical tweezer setup by probing the trapping potential and measuring the trapping frequencies based on the atomic response.

We assume a harmonic trapping potential, taking the form $m\omega_i r_i^2/2$. Within this approximation the radial (i.e. perpendicular to the tweezer axis) and axial (i.e. parallel to the tweezer axis) trap frequencies ω_r and ω_a are given by

$$\omega_r = \sqrt{\frac{4U_0}{m\omega_0^2}} \quad \text{and} \quad \omega_a = \sqrt{\frac{2U_0}{mz_\mathrm{R}^2}}, \tag{5.6}$$

where U_0 is the trap depth, m is the atomic mass, ω_0 is the Gaussian beam waist and z_R is the Rayleigh range.

In theory, the intensity profile of an optical tweezer closely resembles an Airy pattern due to diffraction caused by clipping of the beam at the finite aperture of the microscope objective. In reality, the actual beam shape lies between a Gaussian beam and an Airy disk. While in radial direction near peak intensity the beam can be well approximated by a simple Gaussian beam, the intensity distribution in axial direction provides weaker confinement compared to a Gaussian beam. For our further analysis, rather than using the Rayleigh range for a given spot size, we insert the measured values of the 1/e-level intensity level[4] into eq. 5.6 to account for the weaker confinement. This is possible because the assumption of a harmonic potential shape still holds true.

To experimentally infer the radial and axial trapping frequencies, we modulate the tweezer trap depth by 10 %. The goal is to induce parametric heating, resulting in atom loss when the modulation equals twice the trap frequency. We then measure the probability of retaining an atom as a function of the modulation frequency.

Figure 5.19 shows the results of the trap modulation measurement with atoms loaded in 14 mW tweezers. We can identify two modulation frequencies $f_{\mathrm{mod},i}$ where significant atom loss occurs. We attribute the dip in Fig. 5.19a to the axial trapping frequency ω_a and the resonance shown in 5.19b to the radial trapping frequency ω_r. From the fits to the data points (solid lines), we extract the following trap frequencies[5]:

$$\omega_\mathrm{a} = 2\pi \times 18.5(1)\,\mathrm{kHz} \quad \text{and} \quad \omega_\mathrm{r} = 2\pi \times 36.4(1)\,\mathrm{kHz}.$$

Applying Eq. 5.6, we calculate the expected trap frequencies to be:

$$\omega_\mathrm{a,calc} = 2\pi \times 9\,\mathrm{kHz} \quad \text{and} \quad \omega_\mathrm{r,calc} = 2\pi \times 80\,\mathrm{kHz}.$$

---

[4] The measurement is presented in Sec. 3.2.

[5] It should be noted, that the axial trapping frequency was determined from a single data set. Each data point represents an array-averaged value for the survival probability. The resonance feature associated with the axial trapping frequency was only identified during post-analysis, at which point acquiring supplementary data under identical conditions was no longer feasible.

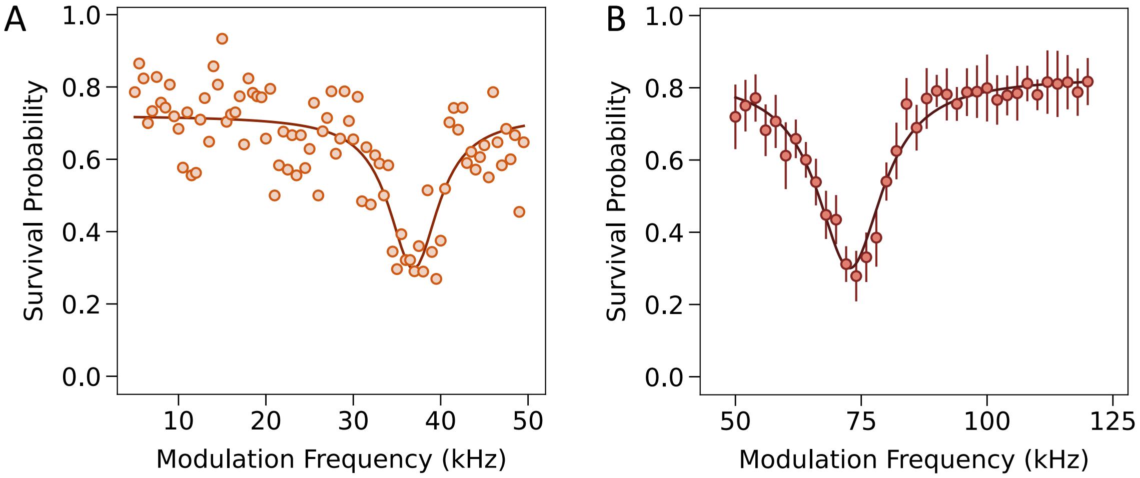

Figure 5.19 | Trap frequency measurement. Recapture probability as a function of trap depth modulation frequency. The tweezer beam intensity is modulated by 10 % for 100 ms to induce parametric heating. Solid lines represent fits to extract the **(A)** axial and **(B)** radial trapping frequencies, yielding $\omega_\mathrm{a} = 2\pi \times 18.5(1)$ kHz (orange) and $\omega_\mathrm{r} = 2\pi \times 36.4(1)$ kHz (red). The data points of the axial trapping frequency measurement (left) were obtained from a single experimental run using a 64-site array hence error bars are omitted. The data points for the radial trapping frequency (right) are obtained by averaging over 15 runs, with error bars denoting statistical uncertainties.

For this calculation, we use the following relation to determine the trap depth U_0:

$$U_0 = \frac{\alpha I_0}{2\epsilon_0 c},$$

where α is the polarizability at 759 nm [196] and I_0 is the peak intensity of each tweezer given by $I_0 = 2P/(\pi\omega_0^2)$, assuming power per tweezer of $P = 14\,\mathrm{mW}$ and a tweezer waist $\omega_0 = 730\,\mathrm{nm}$, which we determine in an independent measurement (see Sec. 3.2.1). This gives us an estimated calculated trap depth of $U_0/h = 14.5\,\mathrm{MHz}$.

The resonance associated with the axial trapping frequency (Fig. 5.19a) located at 37 MHz is at a multiple of the expected axial trap frequency of 9 kHz. We detect no atom loss around a modulation frequency of 18 kHz, which would be indicative of parametric heating.

Meanwhile, the resonance associated with the radial trapping frequency (Fig. 5.19b) appears to be at exactly the expected trapping frequency, i.e. $f_{\mathrm{mod},i} = \omega_i$ rather than at twice this frequency. No indication of atom loss was detected near a modulation frequency of ≈ 160 kHz. We speculate that the modulation might have been strong enough to result in trap shaking, which would lead to resonant excitation at ω_r.

Interestingly, we observe a similar effect in measurements with ^{174}Yb, where the atom loss seems to occurs at both the expected trapping frequencies ω_a and ω_r [154] suggesting a systematic origin. Additional experimental efforts are necessary to further investigate the trapping frequencies. Spectroscopic measurements of the trap depth for instance, could provide further insight by directly determining the actual value of U_0.

5.7 Summary and outlook

This chapter presented the current capabilities of our newly built optical tweezer apparatus employing ytterbium atoms. We demonstrated an approach for efficiently laser-cooling and loading single ^{171}Yb atoms into a two-dimensional optical tweezer array comprising up to 64 sites.

We achieved reliable operation of a 3D magneto-optical (MOT), with loading rates of 1.7×10^6 atoms/s and final temperatures around $15\,\mu$K.A more accurate temperature determination may yield temperatures closer to the theoretical Doppler-limit of $4.4\,\mu$K. A natural next step is the implementation of Raman sideband cooling to achieve motional ground-state preparation.

We consistently reach single-atom loading fractions of up to 58 % across the array using suitable pulse parameters for inducing parity projection. Similar experiments report on loading efficiencies of around 80 % [126, 129], indicating that further optimization is required.

Combining near-deterministic loading protocols with atom rearrangement techniques, is a compelling pathway toward fast and efficient preparation of large-scale defect-free arrays [72, 75, 131, 197]. A particularly effective method for atom-by-atom assembly utilizes pairs of crossed acousto-optical deflectors (AODs), which allows dynamic and precise tweezer beam steering. While we already employed AODs for trapping of ^{174}Yb, combining these two optical trapping procedures into a hybrid approach to rearrange ^{171}Yb atoms is a viable next step. Another promising avenue would be the implementation of more complex tweezer geometries as proposed in zone-based quantum computing proposals [14, 76, 102].

We demonstrated high-fidelity atom detection with classification fidelities of 99.993 %. The currently achieved minimal atom loss of $2 - 3\,\%$ can be improved by reducing the imaging time. This can be achieved by further technical improvements of the imaging system to reduce background counts and the implementation of motional ground state cooling.

At the time the experiments were conducted, the number of sites was limited by tweezer power. So far, only a fraction of the available laser power could be utilized in the experiment due to imperfect fiber coupling. With minor technical improvements, we expect a 30 % increase in laser power.

The excitation and trapping of atoms in the metastable $^3\mathrm{P}_0$ state represents a promising direction towards coherent qubit control and is under active construction at the time of writing this thesis.

The results presented in this chapter establish an excellent starting point for pursuing experiments aimed at precise control of individual neutral atoms, laying the groundworks for novel quantum processing or simulation applications with ^{171}Yb.

Chapter 6

Towards Ytterbium Rydberg Atoms

The capability of exciting atoms to Rydberg states is essential for inducing long-range interactions among single atoms trapped in optical tweezer arrays and is the key mechanism for generating entangled states and implementing quantum gate logic. Current experiments face several technical limitations regarding the Rydberg coupling strength and fidelity of entangling gate operations. This chapter describes the implementation of a Rydberg laser system, featuring several critical key requirements for overcoming prevalent technical challenges. These include the excitation uniformity across the array, efficient use of available laser power by means of beam shaping, control of frequency, amplitude and phase as well as the beam pointing stability. These improvements pave the way towards high-fidelity Rydberg excitation and detection of Yb atoms and facilitates the implementation of optimized gate protocols.

First, we review the basic properties of Rydberg atoms in the context of alkaline-earth atoms. We propose different beam shaping schemes tailored towards maximizing the Rydberg Rabi frequency. Next, the optical laser system for Rydberg excitation and Rydberg state detection is presented. Here, we analyze the resulting beam profiles and measure the laser pointing stability. Finally, we give an outlook on further improvements and discuss progress regarding laser phase noise and its suppression that has been made at our experiment in the form of proof of concept experiments.

The design process of the Rydberg laser setup was supported by C. Schellong. The Rydberg detection setup was built by F. Mrozek under co-supervision of the author.

6.1 Introduction to Rydberg physics

Engineering interactions between individual atoms trapped in an optical tweezer array relies on the excitation of Rydberg states. These highly-excited atoms exhibit large electric dipole moments that give rise to long-range interactions and facilitate two-atom entanglement. Rydberg-mediated blockade forms the basis for implementing conditional logic in quantum information processing [82]. Applications of Rydberg atoms range from quantum simulation of condensed matter models, nuclear and high

energy physics [198] to the implementation of variational algorithms for combinatorial optimization tasks [199].
This section reviews the basic principles of Rydberg physics in the context of neutral atom ytterbium arrays and the implementation of quantum gates. For more comprehensive discussions on Rydberg atoms and their relevance for neutral atom arrays, we refer the reader to [54, 56, 98, 100, 200].

6.1.1 Rydberg states

Rydberg atoms are atoms where the valence electron is in a highly excited orbital, characterized by a large principle quantum number $n \gg 1$. As a result, the Rydberg electron occupies orbitals with an increased distance r from the nucleus, leading to an electric dipole moment $\boldsymbol{d} = \mathrm{e}\boldsymbol{r}$ arising from the charge separation between the positively charged ion core and highly-excited Rydberg electron. We can develop a description of the Rydberg levels for atoms beyond hydrogen by introducing the quantum defect δ, which is a an empirical correction term accounting for shifts arising from the wavefunction overlap with the nucleus and inner-shell electrons. We can then define an effective principle quantum number as $n^* = n - \delta_{nlj}$. The Rydberg energy levels E_{nlj} are described by the principle, orbital angular momentum and total angular momentum quantum numbers denoted by n, j and l respectively. The electronic energy levels are given by the formula

$$E_{nlj} = \frac{R^*}{(n - \delta_{nlj})^2}, \tag{6.1}$$

where R^* is the effective Rydberg constant, n is the principle quantum number and δ_{nlj} is the quantum defect. The effective Rydberg constant is scaled by the effective mass and is defined as

$$R^* = \frac{R^{\infty}}{(1 + \frac{m_\mathrm{e}}{m})},$$

where $R^{\infty} = 109\,737.315\,685\,\mathrm{cm}^{-1}$ is the Rydberg constant, m the mass of the atom and m_e the electron mass.

Many key properties of Rydberg atoms exhibit universal scalings with the effective principal quantum number n^*. A summary of the most relevant scaling relations is given in table 6.1. The scalings are taken from Refs. [200, 201]. These atoms offer unique possibilities in view of the optical tweezer platform, as discussed in the following.

First, the **orbit size** $\langle r \rangle$ of the Rydberg electron scales as $(n^*)^2$, leading to wavefunctions with microscopic size extending into the µm length scale. Notably, for states with maximum angular momentum and magnetic quantum numbers l and m, that is $l_\mathrm{max} = n - 1$ and $|m| = l$, the Rydberg-electron wavefunction is localized in a nearly cicular orbit around the core, leading to the formation of long-lived **circular Rydberg states** [202].

Quantity	Notation	Scaling $(n^*)^x$
orbit size	$\langle n\rangle$	2
binding energy	E_{n^*}	-2
energy level spacing	$E_{(n^*+1)} - E_{n^*}$	-3
lifetime (BBR)	τ_{BBR}	2
lifetime (radiative)	τ_{r}	3
lifetime (total)	τ	2
dipole matrix element	$\langle g\vert d\vert nl\rangle$	$-3/2$
dipole matrix element	$\langle nl\vert d\vert nl+1\rangle$	2
polarizability	α	7

Table 6.1 | Scaling of Rydberg atom properties. Relevant properties of Rydberg atoms which scale with the principle quantum number n^* as $(n^*)^x$. The electric dipole operator is denoted as d and g is the ground state. The subscript BBR stands for black body radiation.

The **energy-level spacings** ΔE of neighboring Rydberg states decreases exponentially with $(n^*)^{-3}$ as they become more densely packed while approaching the ionization limit, resulting in Rydberg series.

The **Rydberg state lifetime** τ increases for higher n^* states as τ scales with $(n^*)^2$. The two decay channels contributing to the fundamentally limited lifetime τ are (1) decay via the radiative pathway τ_{r} which occurs due to spontaneous emission and (2) decay τ_{BBR} through stimulated emission to nearby energy levels caused by black body radiation (BBR) due to finite temperature. Lifetimes can be significantly improved by working in a cryogenic environment to mitigate BBR effects. The effective Rydberg state lifetime τ is then given by

$$\frac{1}{\tau} = \frac{1}{\tau_{\mathrm{r}}} + \frac{1}{\tau_{\mathrm{BBR}}}.$$

A lifetime of 65 µs has recently been experimentally demonstrated in ^{171}Yb with $n^* = 59$ [133]. The increased life time of higher-lying Rydberg states on the µs time scale therefore allows for Rydberg state manipulation in the MHz regime and is therefore well-suited for qubit operations.

While Rydberg atoms offer versatile properties, they can impose experimental challenges considering the strong scaling of its **polarizability** α as $(n^*)^7$, making them extremely sensitive to stray electric fields, which needs to be well-compensated in the experimental environment.

Lastly, Rydberg atoms exhibit large electric **dipole moments** as high-lying states are accessed. For transitions to neighboring Rydberg states the dipole moment matrix element $\langle nl|d|nl+1\rangle$ scales as $(n^*)^2$, therefore allowing atoms to interact via dipole-dipole interactions. The ability to switch interactions between atoms on and off, as well as tune the interaction strength is a central feature in Rydberg atom applications. This enables interactions between individually trapped Rydberg atoms on length scales in which optical tweezers can be optically resolved with typical spacings of around

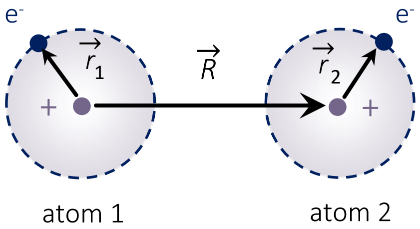

Figure 6.1 | Rydberg-Rydberg interactions. Schematic of two Rydberg atoms separated by R. The Rydberg-electron e^- orbits the positively charged ion core $(+)$ at distance r.

$3-5\,\mu\mathrm{m}$. While the interaction becomes increasingly larger for highly-excited states, the wavefunction overlap of the weakly-bound Rydberg electron with the atomic ground state is reduced with larger n^* as the respective dipole matrix element scales as $\langle g|d|nl\rangle \sim (n^*)^{-3/2}$, leading to a reduced coupling with the laser light field.

In the next section, we discuss the case where Rydberg atoms interact in more detail.

6.1.2 Rydberg interactions

The key feature of Rydberg atoms is their interaction with other Rydberg atoms mediated by the dipole-dipole interaction. In the following, we consider the simplest case of two Rydberg atoms denoted by subscripts $(1, 2)$ and separated by a distance R, as illustrated in Fig. 6.1. The position of the Rydberg-electron relative to the ion core is denoted by $\mathbf{r}_1$ and $\mathbf{r}_2$. The charge separation of the electron and the cation leads to an electric dipole moment $\mathbf{d} = -e\mathbf{r}$. In case of non-hydrogenic atoms, we assume that the wavefunction overlap of the Rydberg electron with the ion core is negligible for large $\mathbf{r}$ and that the ion core can be treated as a positive point charge. The dominant interaction is the electric dipole-dipole interaction and it is given to first order by

$$\hat{V}_{dd}(\mathbf{R}) = \frac{e^2}{4\pi\epsilon_0}\left(\frac{\vec{\mathbf{r}}_1\vec{\mathbf{r}}_2 - 3(\vec{\mathbf{r}}_1\cdot\hat{\mathbf{n}})(\vec{\mathbf{r}}_2\cdot\hat{\mathbf{n}})}{R^3}\right), \tag{6.2}$$

where $\hat{V}_{dd}$ is the dipole interaction operator, e the elementary charge, ϵ_0 the vacuum permittivity, $\vec{\mathbf{r}}_{1,2}$ is the relative displacement from the core, $\boldsymbol{R}$ is the vector connecting the atoms, $\hat{\mathbf{n}}$ is the unit vector along $\boldsymbol{R}$ and $R = |\boldsymbol{R}|$ is the interatomic distance. Here, we assume that the dipole-diopole is the dominant interaction between the Rydberg atoms as the interatomic distance R is larger than the spatial extent of the electronic wavefunction, which is given in tweezer experiments where the typical tweezer separation is a few μm.

The interaction dynamics depends on the specific initial Rydberg states of the atoms, as well as the R-dependent interaction strength. In the following we consider a model consisting of a pair of Rydberg atoms and discuss two interaction regimes.

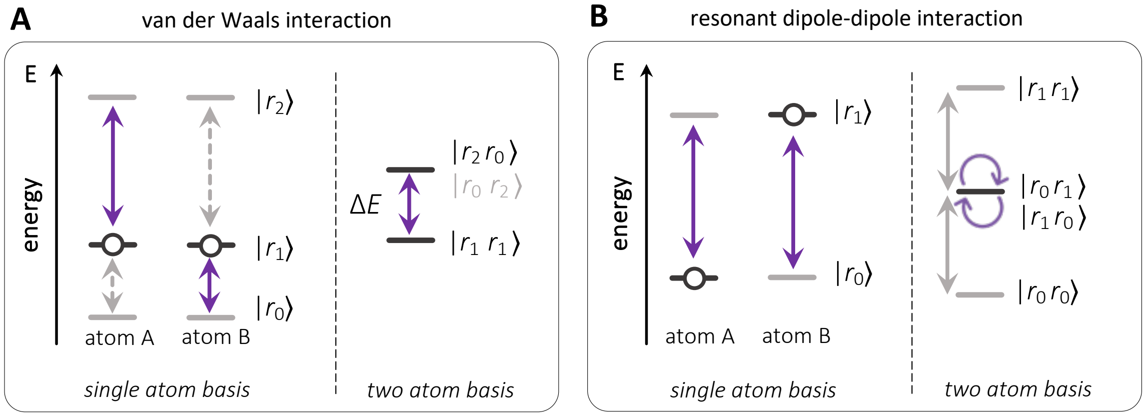

Figure 6.2 | Dipole-mediated Rydberg interactions. Level scheme of two interacting Rydberg atoms $i = \{A, B\}$ in the single and two atom basis. Rydberg levels $|nj\rangle$ are denoted as $\{|r_0\rangle, |r_1\rangle, |r_2\rangle\}$. (**A**) Illustration of van der Waals interactions. Both atoms are prepared in $|r_1\rangle$. The pair state $|r_{\mathrm{A}}r_{\mathrm{B}}\rangle$ $= |r_1 r_1\rangle$ is coupled to $|r_2 r_0\rangle$ or $|r_0 r_2\rangle$ (grey arrows) by the dipole-dipole operator via second order perturbation, resulting in an interaction shift V_{vdW}. (**B**) Illustration of resonant dipole-dipole interactions. Atoms are prepared in different states $|r_0\rangle$ and $|r_1\rangle$. The pair state $|r_0 r_1\rangle$ is degenerate and thus resonantly couples to $|r_1 r_0\rangle$.

Van der Waals interactions

In the first case, we assume that two Rydberg atoms denoted by A and B are both excited to the same single-atom Rydberg state $|nj\rangle = |r_1\rangle$, as pictured in Fig. 6.2a. Here, n represents the principle quantum number and j the total angular momentum of the Rydberg state. This scenario is typical for optical tweezer experiments which utilize a global Rydberg excitation laser beam and thus result in simultaneous occupation of the same state.

Treating the dipole-dipole interaction as a perturbation to the system, we find that the dipole matrix element $\langle r_1 r_1|\hat{V}_{\mathrm{dd}}|r_1 r_1\rangle$ in the two-particle basis $|r_A r_B\rangle = \{|r_1 r_1\rangle, |r_2 r_0\rangle\}$ vanishes in first order perturbation theory, as the electronic orbits are spherically symmetrical and therefore do not exhibit a permanent dipole moment. However, the off-diagonal dipole matrix elements are non-zero, suggesting coupling of states with opposite parity with a dipole coupling strength $\langle r_1 r_1|\hat{V}_{\mathrm{dd}}|r_2 r_1\rangle = V_0/R^3$. The initial pair state $|r_1 r_1\rangle$ is therefore coupled to the two-particle state $|r_2 r_0\rangle$ via $\hat{V}_{\mathrm{dd}}$ (see Fig. 6.2a) in a second order process, resulting in an energy shift ΔE which is called Förster defect.

In the limit of $\Delta E \gg V_0/R^3$, where the Rydberg interaction can be treated as a perturbation, the interaction is referred to as van der Waals interaction. In this regime, the interaction strength takes the form

$$V_{\mathrm{vdW}} = \frac{C_6}{R^6}, \tag{6.3}$$

where C_6 is the van-der-Waals coefficient and scales with n^{11}, while R is the interatomic distance. Due to the $1/R^6$ dependance, the van der Waals interaction dominates for larger inter-atomic distances.

Conversely, when the interaction becomes large compared to the energy shift, that is $\Delta E \ll V_0/R^3$, the energy difference between the initial and final two-particle states $|r_1 r_1\rangle$ and $|r_2 r_0\rangle$ become negligible and the pair states are coupled resonantly by $\hat{V}_{\mathrm{dd}}$. In this regime the dominating interaction is the resonant dipole-dipole interaction given by

$$V_{\mathrm{dd}} = \frac{C_3}{R^3}, \tag{6.4}$$

where $C_3 = V_0$ and scales with R^{-3}. It is possible to achieve the resonance condition $\Delta E = 0$ by applying an electric field to induce DC-Stark shifts, which tunes the pair states as depicted in Fig. 6.2a into degeneracy, such that $\Delta E = (E_{r_2} - E_{r_1}) + (E_{r_1} - E_{r_0}) = 0$. This is called a Förster-resonance which has been utilized in experiments to dynamically control the interaction [203, 204].

Resonant dipole-dipole interactions

While in the precious section we could treat the dipole-dipole interaction as a perturbation to the system, we now look at the case where this approximation breaks. In the limit where the energy difference between the pair states ΔE is small compared to the dipole-dipole coupling strength V, the interaction becomes resonant and real population transfer between states occurs.

This is true when two atoms initially occupy different Rydberg states $|r_0\rangle$ and $|r_1\rangle$ in the single particle picture, as illustrated in Fig. 6.2b. The energy difference between the two-particle states $|r_0 r_1\rangle$ and $|r_1 r_0\rangle$ is now $\Delta E = 0$ i.e. they are degenerate. The pair states are resonantly coupled by the dipole-dipole interaction with the interaction strength V_{dd} defined in eq. 6.4. The system will therefore undergo oscillations between the pair states with frequency $\sim R^{-3}$. Off-resonantly coupling to nearby pair states via the van der Waals interaction is indicated by grey arrows in the two-particle picture but highly suppressed since the resonant coupling dominates in this regime.

This 'flip flop' oscillation between the two degenerate pair states can be utilized to explore XY spin-1/2 models, by mapping Rydberg states onto spins and realizing an exchange interaction between them, mediated by the resonant dipole-dipole interaction. This enables optical tweezer systems with Rydberg atoms to explore quantum magnetism, transport phenomena in the XY model or the implementation of the Su-Schrieffer-Heeger (SHH) model.

6.1.3 Rydberg blockade

We now turn to the case in which we drive atoms coherently from the ground state to a Rydberg state. As discussed in the previous section, Rydberg atoms interact strongly with each other. This gives rise to the phenomena of Rydberg blockade, where simultaneous excitation of nearby atoms to a Rydberg state is suppressed. This effect plays a central role for many-body experiments and implementing quantum gates in neutral atom array systems. To understand how we can harness the blockade mechanism in our experiment, we first discuss how the blockade effect emerges in a system of two interacting Rydberg atoms. We then look at how the blockade mechanism facilitates the implementation of a CNOT gate. Finally, we discuss opportunities for Ytterbium Rydberg atom arrays.

Rydberg blockade radius

While Rydberg atoms can strongly interact with each other, as discussed in section 6.1.2, in some cases the Rydberg-mediated interaction can prevent other nearby atoms from being excited to a Rydberg state.

When coherently driving a pair of ground state atoms to a Rydberg state with single-atom Rabi frequency Ω, then the energy of the two-particle state $|rr\rangle$ is shifted due to the van der Waals interaction by an amount $V = C_6/R^6$, where C_6 is the van der Waals coefficient and R the interatomic distance. Figure 6.3a illustrates the energy of the pair states as a function of the interatomic separation R. In the regime where the Rydberg-mediated energy shift is larger than the coupling to the Rydberg state, i.e. $\hbar\Omega \ll C_6/R^6$, the doubly-excited state $|rr\rangle$ is shifted out of resonance and is now prohibited. The characteristic cross-over length scale, at which the Rydberg interaction becomes so strong that the excitation of the second atom is blockaded, is called the Rydberg blockade radius and is defined as

$$R_\mathrm{b} = \left(\frac{C_6}{\hbar\Omega}\right)^{1/6}. \tag{6.5}$$

For $R < R_\mathrm{b}$, indicated by the shaded region in Fig. 6.3a, the ground state $|gg\rangle$ is collectively coupled to the entangled state $|\psi\rangle = (|rg\rangle + |gr\rangle)/\sqrt{2}$. Further, the single-atom Rabi frequency is enhanced by a factor $\sqrt{2}$. The effect of Rydberg blockade can be generalized to an ensemble of N atoms, where the presence of a Rydberg atom prevents the excitation of atoms within the blockade volume, resulting in an entangled state which evolves with Rabi frequency $\sqrt{N}\Omega$.

For distances larger than the blockade radius R_b such that $\hbar\Omega \gg C_6/R^6$, the interaction shift falls off as $\sim R^6$ and both atoms are able to be excited to a Rydberg state.

Rydberg-based quantum gates

The capability of conditioning the excitation of one atom on the state of another atom through Rydberg blockade enables the implementation of conditional logic and has motivated numerous proposals for implementing quantum gates with Rydberg atoms

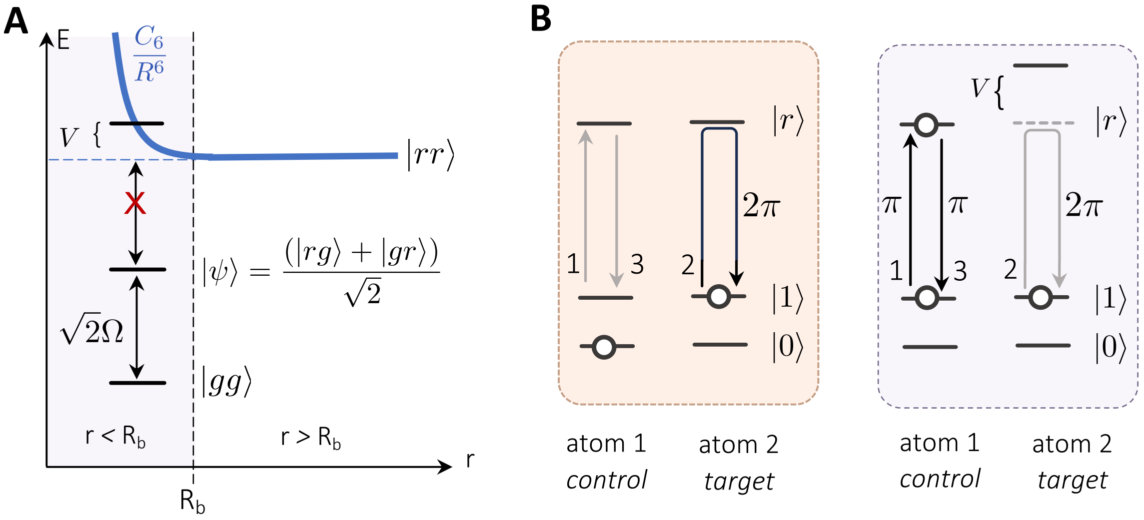

Figure 6.3 | Rydberg-blockade mechanism. (**A**) Energy diagram illustrating the Rydberg blockade mechanism. The energy of the pair states $|gg\rangle$, $|\psi\rangle$ and $|rr\rangle$ is shown as a function of the interatomic distance R. The van der Waals interaction (blue line) results in an energy shift V. Here, Ω denotes the single-particle Rabi frequency for the transition $|g\rangle \rightarrow |r\rangle$. The shaded area indicates the Rydberg blockade regime, where R_b is the blockade radius. For $R < R_\mathrm{b}$ the Rydberg-induced energy shift prevents excitation to $|rr\rangle$ and results in the entangled state $|\psi\rangle = (|rg\rangle + |gr\rangle)/\sqrt{2}$. (**B**) Controlled phase C_Z gate. Depicted is the pulse sequence (1-3) for implementing a C_Z gate, utilizing the Rydberg blockade mechanism. (1) A π pulse is applied to the control atom and couples $|1\rangle$ to Rydberg state $|r\rangle$. (2) A 2π pulse is performed on the target atom, driving $|1\rangle \rightarrow |r\rangle$. (3) A second π pulse on $|r\rangle \rightarrow |1\rangle$ of the control atom. When the control atom is in $|0\rangle$, pulses (1) and (3) are ineffective, while the target atom picks up a phase $\Delta\phi = \pi$ (left). Coupling the control atom to $|r\rangle$ (right), prevents double-excitation through Rydberg blockade.

[82, 83]. Additionally, the combination of single-qubit operations with two-qubit gates provides the foundation for universal quantum computing [205].

We now look at how a Rydberg-based controlled-Z (C_Z) gate can be realized in a system of two neutral atoms to generate a CNOT gate based on the seminal proposal published in [82] . The corresponding pulse sequence consists of three pulses and is illustrated in Fig. 6.3c. Here, we identify one atom as the target and the other as the control atom. Qubits $|0\rangle$ and $|1\rangle$ are encoded in the internal electronic states of the atoms. The protocol starts out by applying a π pulse $|1\rangle \to |r\rangle$ on the control atom, followed by a 2π pulse $|1\rangle \to |r\rangle \to |1\rangle$ on the target atom and a final π pulse $|r\rangle \to |1\rangle$ on the control atom.

When the atoms start out in state $|01\rangle$ (see left side of Fig. 6.3c), the control atom remains in $|0\rangle$, as only $|1\rangle$ couples to $|r\rangle$. Performing a subsequent 2π pulse on the target atom introduces a phase to the pair state $\Delta\phi = \pi$ or $e^{i\pi} = -1$.
Conversely, when the initial state is $|11\rangle$ (see right side of Fig. 6.3c), the first π pulse on the control atom drives the Rydberg transition and thereby induces an interaction shift V on the doubly-excited two-particle state $|rr\rangle$. In the regime where $V \gg \Omega$, Rydberg blockade prevents the target atom from excitation to $|r\rangle$ during the second pulse. A final π pulse returns the control atom to $|1\rangle$.
Fore the initial state $|10\rangle$, pulse (2) is off-resonant, while pulses (1) and (3) drive a 2π-rotation on the control atom and the pair $e^{i\pi} = -1$. In the case of both atoms initialized in $|0\rangle$, the state remains unchanged.

Combining this protocols for a C_Z gate with two Hadamard gates allows for the implementation of a controlled-NOT gate or CNOT gate. The fidelity of two-qubit gates operations is ultimately limited by the finite Rydberg state lifetime and remains a main challenge. In state-of-the art experiments, Rydberg-based two-qubit entangling gates have reached fidelities of $\mathcal{F} = 99.5\,\%$ [107], therefore establishing neutral atom arrays as a highly promising quantum computing platform.

6.1.4 Alkaline-earth Rydberg atoms

The recent advances in neutral atom array technology has generated growing interest in alkaline-earth like atoms such as Strontium (Sr) and Ytterbium (Yb). So far, we explored the general properties of Rydberg atoms. Here we consider Rydberg atoms with two valence electrons.

Divalent Rydberg atoms

While Rydberg atoms share many common key properties, the exact energy levels and dipole matrix elements depend on the specific electronic structure of the underlying atom. As discussed in section 6.1.1, introducing a quantum defect δ accounts for screening effects of the Coulomb potential by the inner electrons in non-hydrogenic Rydberg atoms. Alkali atoms such as Rb or Cs can be treated particularly well in

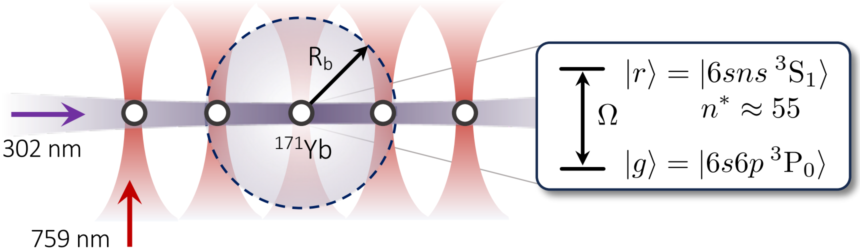

Figure 6.4 | Ytterbium Rydberg atoms in optical tweezers. (**A**) Schematics of the beam layout for Rydberg excitation in a tweezer array. The metastable state $^3P_0 = |g\rangle$ in ^{171}Yb is coupled to a Rydberg state $|r\rangle$ of the $^3S_1$ Rydberg series with strength Ω. The Rydberg blockade radius is denoted by R_b.

the context of quantum defect theory, as they have a single valence electron. As a result, the energy levels and dipole matrix elements can be calculated and its Rydberg spectra are well understood.

The situation is more complex for atoms with two valence electrons, giving rise with to a singlet-triplet Rydberg series structure. In this two-electron system, the inner core electron can be excited to a low-lying Rydberg state, leading to double excitation. In particular, Yb suffers from this effect as it has a high density of such low-lying states due to its relatively high mass. The ground state of Yb is described by the electronic structure $4f^{14}6s^2$, featuring a closed f-shell. However inner-core excitations result in electronic configuration such as $4f^{14}6pnl$. These states alter the structure of singly-excited Rydberg series, i.e Rydberg states of the form $4f^{14}6snl$, and are called perturber states.

For alkaline earth (-like) atoms with no nuclear spin ($I = 0$) such as ^{174}Yb and ^{88}Sr, single channel quantum defect theory can be applied and is a sufficient approximation[206]. A channel refers to a particular angular momentum configuration of the electron-ion-core system. This has lead to an improved understanding of the Rydberg energy and potential landscape of alkaline earth atoms with vanishing nuclear spin [207]. However, atoms with non-zero nuclear spin, such as ^{171}Yb with $I = 1/2$, hyperfine coupling leads to mixing of Rydberg series is described in the context of multi-channel quantum defect theory (MQDT) [208]. A detailed understanding of the Rydberg series energy structure is necessary for employing the nuclear spins of ^{171}Yb as qubits. Recently, MQDT has been employed to compute Förster defects of a $F = 1/2$ hyperfine Rydberg state in ^{171}Yb to find an improved entangling gate fidelity of $\mathcal{F} = 0.994\,\%$ [209].

Further, the presence of a second valence electron in the ion core enables opportunities for in-situ probing and imaging of alkaline earth Rydberg atoms through isolated core excitations (ICE), where the fluorescence is collected to detect Rydberg atoms [210].

Trapping alkaline earth atoms in optical tweezers

At our experiment we aim at utilizing Yb Rydberg atoms trapped in optical tweezer arrays. Figure 6.3 shows a simplified schematic of the anticipated Rydberg tweezer setup.
Unlike alkali atoms, alkaline-earth(-like) Rydberg atoms can be trapped in optical tweezer potentials. The ponderomotive potential of the nearly-free Rydberg atom results in a repulsive force and therefore anti-trapping of alkali Rydberg atoms. Due to the two-electron structure, the Yb^+ ion core has notable polarizability at trapping wavelengths, which generates an attractive net force and allows trapping of Yb Rydberg atoms [142]. This works for sufficiently high n, where the overlap of the Rydberg electron wavefunction with the tweezer beam is minimized and the repulsive effect is reduced.

The optical tweezer potentials are generated by a 759 nm laser beam. At this wavelength a magic trapping condition exists for which the polarizabilities of the ground and $^3\mathrm{P}_0$ clock state of Yb are identical, thus eliminating trap induced light shifts. The existence of a potential triple magic wavelength which additionally traps a Rydberg state magically, has been proposed [211].

The metastable $^3\mathrm{P}_0$ state, denoted by $|g\rangle$ in this schematic, conveniently serves as a second ground state due to its metastable nature and lifetime on the order of $\sim 10\,\mathrm{s}$, which exceeds typical time scales of such experiments. From $^3\mathrm{P}_0$, Rydberg states are accessible with a single photon transition by addressing the array with a global 302 nm laser beam and Rabi frequency Ω (see inset of Fig. 6.3).

There exist several possible methods to prepare atoms in the $^3\mathrm{P}_0$ state. One approach is to coherently transfer population to the metastable state via the $^1\mathrm{S}_0 \rightarrow {}^3\mathrm{P}_0$ transition using an ultra-narrow clock laser. Alternatively, optical pumping schemes utilizing a two-photon process (556 nm and 1539 nm) via $^3\mathrm{D}_1$ can be applied to initialize atoms in $^3\mathrm{P}_0$, as demonstrated in [133].

Recent proposals identify the $F = 1/2$ and $F = 3/2$ manifold of the $^3\mathrm{S}_1$ Rydberg series with $n^* \approx 55$ in Yb as an ideal candidate for Rydberg-based entangling gate operations due to its unperturbed structure [124, 133, 209].

In the next chapters, we describe the work towards the Rydberg laser system for enabling high-fidelity Rydberg excitations in ytterbium.

6.2 Elliptical beam shaping

A major challenge in implementing high-fidelity entangling operations is mitigating several noise sources. In particular, spatial intensity variations of the excitation beam leads to non-uniform excitation probability and thus diminishes the excitation fidelity. Additionally, achieving a high Rabi frequency is crucial to combat decoherence processes.

In order to achieve high degrees of uniformity while maximizing the available laser power across a two-dimensional array, we carefully choose our beam shaping optics to produce a beam with an elliptical Gaussian intensity profile. While it is more effective to utilize beams with top-hat intensity profiles, commercially available optics lack in adequate options for applications in the UV range. Further, for achieving high excitation fidelities, it is crucial to illuminate the atoms homogeneously across the array. Therefore, to minimize intensity fluctuations experienced by atoms at different array positions during global excitation, we determine an estimate for the elliptical Gaussian beam parameters in order to optimally illuminate the array. This framework is applicable to all global excitation beams.

6.2.1 2D elliptical Gaussian

To determine an estimate of the optimal beam parameters, we first establish a condition for achieving a uniform excitation fidelity across a two-dimensional array of a given size.

We consider the intensity profile of an elliptical Gaussian beam propagating along the axis z, given by

$$I(x,y,z) = I_0\left(\frac{w_{0x}}{w_x(z)}\right)\left(\frac{w_{0y}}{w_y(z)}\right)\exp\left(-2\left[\frac{x^2}{w_x^2(z)}+\frac{y^2}{w_y^2(z)}\right]\right), \tag{6.6}$$

where I_0 denotes the peak intensity, w_{0i} the beam waist and $w_i(z)$ the spot size for $i=(x,y)$. The peak intensity I_0 is calculated using

$$I_0 = \frac{2P}{\pi w_{0x} w_{0y}}, \tag{6.7}$$

where P is the total power. In case of a circular Gaussian beam where $w_{0x}=w_{0y}=w_0$, this expression simplifies to the intensity profile

$$I(r,z) = I_0\left(\frac{w_0}{w(z)}\right)^2\exp\left(-\frac{2r^2}{w(z)^2}\right), \tag{6.8}$$

where r is the radial distance from the center.

To derive a condition for the excitation uniformity across an atom array illuminated by a Gaussian beam, we consider driving a transition between a ground $|g\rangle$ and excited $|e\rangle$ state of an atom. On resonance, the excitation probability p_e for pulse time t is given by

$$p_\mathrm{e}(t) = \sin^2\left(\Omega t\right), \tag{6.9}$$

where Ω is the Rabi frequency. When driving Rabi oscillations in the presence of two neighboring atoms between a ground $|g\rangle$ and Rydberg state $|r\rangle$ in the strongly interacting regime, the single-photon Rabi frequency Ω is further enhanced by a factor $\sqrt{2}$ and the probability of finding an atom in the excited state $|r\rangle$ on resonance is modified to

$$p_{\mathrm{r}}(t) = \frac{1}{2}\sin^2\left(\sqrt{2}\Omega t\right). \tag{6.10}$$

Since the Rabi frequency depends on the intensity of the driving laser, an atom located at the periphery of the array will be exposed to intensity I' and excitation probability p_e' due to the Gaussian envelope of the intensity profile.

We can determine the fraction $F = p_e'/p_e$ to assess the maximum decline in excitation probability across the array, where p_e' denotes an atom at the periphery. Assuming ideal population transfer into $|e\rangle$ at $t = \pi/2$, i.e. $p_e(\pi/2) = 1$ and using $t = n\pi/(2\Omega)$, $n \in \mathbb{N}$, we can write

$$\frac{p_e'(t = \pi/2)}{p_e(t = \pi/2)} = \sin^2\left(\frac{\pi}{2}\frac{\Omega'}{\Omega}\right) = F, \tag{6.11}$$

where F is the excitation probability fidelity. Solving for the ratio between both Rabi frequencies Ω and Ω', we end up with

$$\left(\frac{\Omega'}{\Omega}\right)^2 = \frac{4}{\pi^2}\arcsin^2(\sqrt{F}), \tag{6.12}$$

Based on current state-of-the-art excitation fidelities, we set $F = 1 - 10^{-3}$. Since the Rabi frequency and intensity scale as $\Omega^2 \sim I_0$, we can impose a condition on the relative intensity drop across the array, leaving us with

$$I' \approx 0.960\, I_0, \tag{6.13}$$

suggesting that the uniformity in intensity is required to be about 4 % across the entire array in order to achieve an excitation fidelity of $F = 1 - 10^{-3}$. Note that the resulting scaling relation is identical for excitation to Rydberg states using the excitation probability p_r defined in eq. 6.10.

Optimal elliptical beam parameters

Next, we want to find an estimate for the optimal elliptical beam parameters $w_{0\mathrm{x}}$ and $w_{0\mathrm{y}}$, given the array dimensions. This involves maximizing the peak intensity, while satisfying the condition on the relative intensity decline in eq. 6.13. The beam geometry is illustrated in Fig. 6.5a. A two-dimensional optical tweezer array traps atoms along the y-axis. A global excitation beam, here the Rydberg laser beam, illuminates the array perpendicularly to the array and propagates along the z-axis.

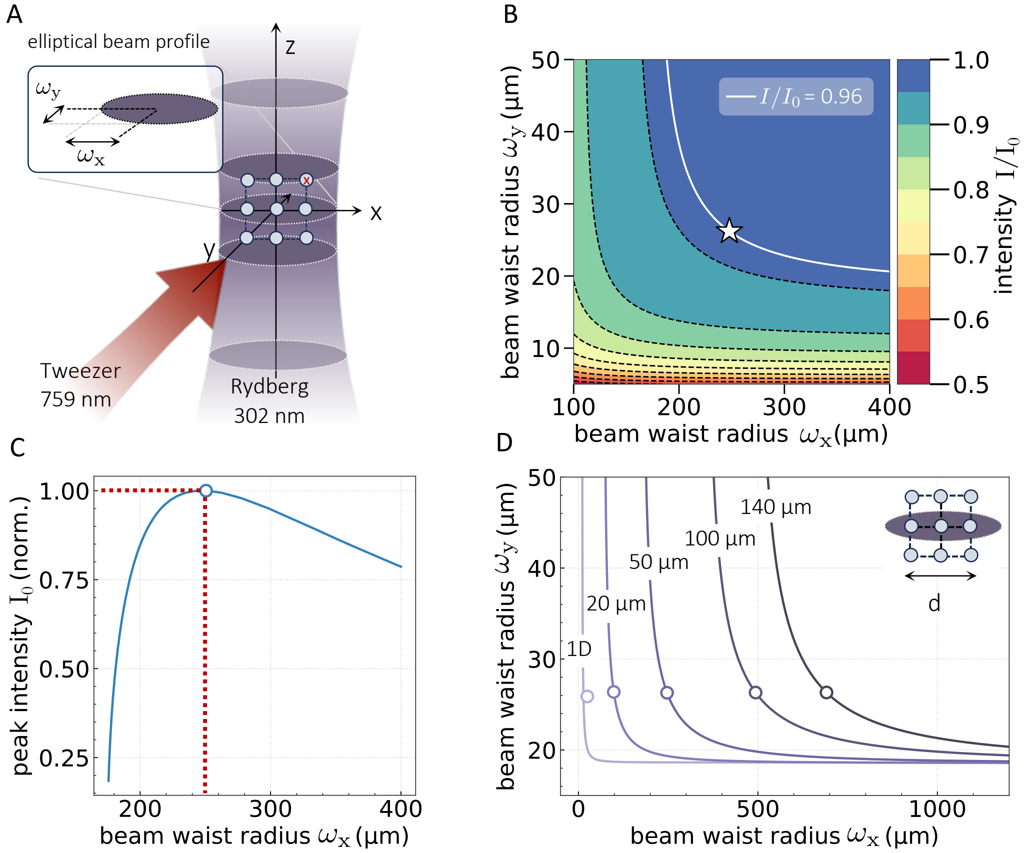

Figure 6.5 | Elliptical beam shaping. (**A**) Schematic of the beam geometry. Optical tweezers propagate along y, generating a 2D tweezer array. The global Rydberg beam propagates along z. The inset shows the elliptical Gaussian beam profile with beam waist radii $w_{0\mathrm{x}}$ and $w_{0\mathrm{y}}$. The red 'x' indicates the atom position furthest away from the center. (**B**) Relative intensity drop I/I_0 over a (50 x 50) µm 2D array. The plot shows the intensity drop across the array as a function of the elliptical beam waist radii $w_{0\mathrm{x}}$, $w_{0\mathrm{y}}$. The white solid line indicates beam parameters for which $I/I_0 = 0.96$ (see main text). The star marks parameters with maximum peak intensity I_0 . (**C**) Normalized peak intensity as a function of the beam waist w_x for $I/I_0 = 0.96$. The circle indicates the maximum peak intensity. (**D**) Elliptical beam parameters (w_x, w_y) satisfying $I/I_0 = 0.96$ (see main text). Calculation is perfomed for 2D arrays of size d, as specified in the inset. The 1D array extends 200 µm along z. Circles indicate the points of maximum peak intensity (see table).

To achieve uniform excitation up to 10^{-3} across the entire 2D array, we consider the atom position most distant from the excitation beam's center indicated by the red 'x' in the schematic (Fig. 6.5a). For the uniformity condition to be satisfied (eq. 6.13), the beam's intensity $I(x, y, z)$ at the corresponding coordinates can deviate up to $I/I_0 = 0.04$. We calculate the ratio I/I_0 at the perimeter of the array for a standard array size of (50x50) µm, corresponding to the maximum intensity drop across the array. To account for the axial confinement of the atoms due to the tweezer potential along y, we assume atoms are located within the Rayleigh range of an equivalent Gaussian beam ($z_\mathrm{R} \approx 2\,\mu\mathrm{m}$). We plot the relative intensity drop I/I_0 for different elliptical beam waist radii $w_{0\mathrm{x}}$ and $w_{0\mathrm{y}}$ and identify the beam parameters with $I/I_0 = 0.96$, indicated by a white solid line. Elliptical beams with parameters below this line deliver higher peak intensities, however the decline in intensity at the array edge exceeds the anticipated excitation uniformity. Conversely, larger beams located above the line offer high degrees of uniformity but are a suboptimal choice in view of the peak intensity and thus Rabi frequency.

To find the optimal beam parameters on this curve which maximize the achievable Rabi frequency, we compute the corresponding peak intensity according to eq. 6.7 and plot it against the beam waist radius $w_{0\mathrm{x}}$, as shown in Fig. 6.5c. The corresponding beam waist along the y-axis is determined from Fig. 6.5b. We can identify the maximum at $w_{0\mathrm{x}} = 247\,\mu\mathrm{m}$ and $w_{0\mathrm{y}} = 26\,\mu\mathrm{m}$, indicated by the star in Fig. 6.5b. Using existing experimental data [133] for the achieved Rabi frequency on the $^3\mathrm{P}_0$ to $6\mathrm{s}75\mathrm{s}^3\mathrm{S}_1$ transition, suggest a Rabi frequency of $\Omega \approx 2\pi \times 0.8\,\mathrm{MHz}$ with this beam size. To determine the optimal elliptical shaping for different array sizes with length and width d, we plot the level where the intensity drops to $I/I_0 = 0.96$ across the array for various 2D array geometries in Fig. 6.5d. The 1D array considered here extends along the z axis and includes the entire field of view (200 µm). We can identify the elliptical beam waist radii (w_x, w_y) where the peak intensity is maximized according to eq. 6.7 (marked as circles in Fig. 6.5d). The specific values for the different array dimensions are listed in table 6.2.

Array size d	waist w_x (µm)	waist w_y (µm)	Rabi frequency Ω (norm.)
1D - 200 µm	25	26	$5.44\ \Omega_\mathrm{FOV}$
(20 x 20) µm	98	26	$2.65\ \Omega_\mathrm{FOV}$
(50 x 50) µm	247	26	$1.62\ \Omega_\mathrm{FOV}$
(100 x 100) µm	493	26	$1.18\ \Omega_\mathrm{FOV}$
(140 x 140) µm	691	26	$1\Omega_\mathrm{FOV}$

Table 6.2 | Optimal elliptical beam waist radii. Calculated elliptical beam parameters (w_x, w_y) for different array sizes which ensure an intensity uniformity $(1 - 10^{-3})$, while maximizing the peak intensity. The 1D array extends over 200 µm. The expected Rabi frequency is given in units of the predicted Rabi frequency Ω_FOV for the (140 x 140) µm array which fills out the entire field of view (200 µm) of our objective.

6.3 Rydberg laser system (301.5 nm)

The Rydberg laser system incorporates several technical enhancements that can improve the excitation of ytterbium atoms to Rydberg states in future experiments. First the laser system is presented. We then show how spatial filtering of the Rydberg excitation beam can significantly improve its beam quality, alleviating the need for using an UV optical fiber, which can be challenging to manufacture and imposes power constraints. Further, we operate an acousto-optic modulator (AOM) in a double-pass configuration using a method specifically tailored towards polarization dependent crystalline quartz AOMs, allowing for phase modulation without sacrificing pointing stability. Lastly, we investigate the mechanical stability of our setup and present the implementation of an active beam stabilization system.

6.3.1 Optical layout

The optical layout of the Rydberg laser system is depicted in Fig. 6.6. We use a frequency quadrupled diode laser from Toptica Photonics AG[1] with an output power of 380 mW. The setup extends over two levels of our experiment and features two possible branches (see Fig. 6.7a and 6.7b). The beam can be brought to the atoms either along the quantization axis or perpendicularly to it, thus making it possible to address σ^+/σ^- or π transitions, respectively. Switching between these two operational modes is done via a flip mirror and involves only the exchange of several components (photodiode for power stabilization, piezo mirror and detector for active beam pointing stabilization).The laser is locked to a high-finesse cavity (Stable Laser Systems) by a PDH lock.

To reduce the exposure to UV light during alignment and to shield the experiment from stray light, the laser output is enclosed. During alignment procedures, the power can be adjusted appropriately using polarization optics (see Fig. 6.6), allowing the laser to run on its optimal settings while dumping excess power. During standard operation, the waveplates and two polarizing beam splitters (PBS) ensure a high purity of linear polarization.

For power stabilization we use a 110 MHz AOM (Gooch & Housego I-M110-3C10BB-3-GH27). The AOM is operated below its optimal RF power, allowing most of the light to pass without being diffracted and to be utilized in the experiment. Stabilization of the laser power of the unmodulated beam is achieved by regulating diffraction into the 1st order, while leaving enough overhead to flatten out any power fluctuations present in the zeroth order. Light is picked off with a nano-textured beam sampler and focused on a photodiode (Thorlabs PDA10A2) later on in the beam path (see Fig. 6.6b).

---

[1] Topitica Photonics TA-FHG pro

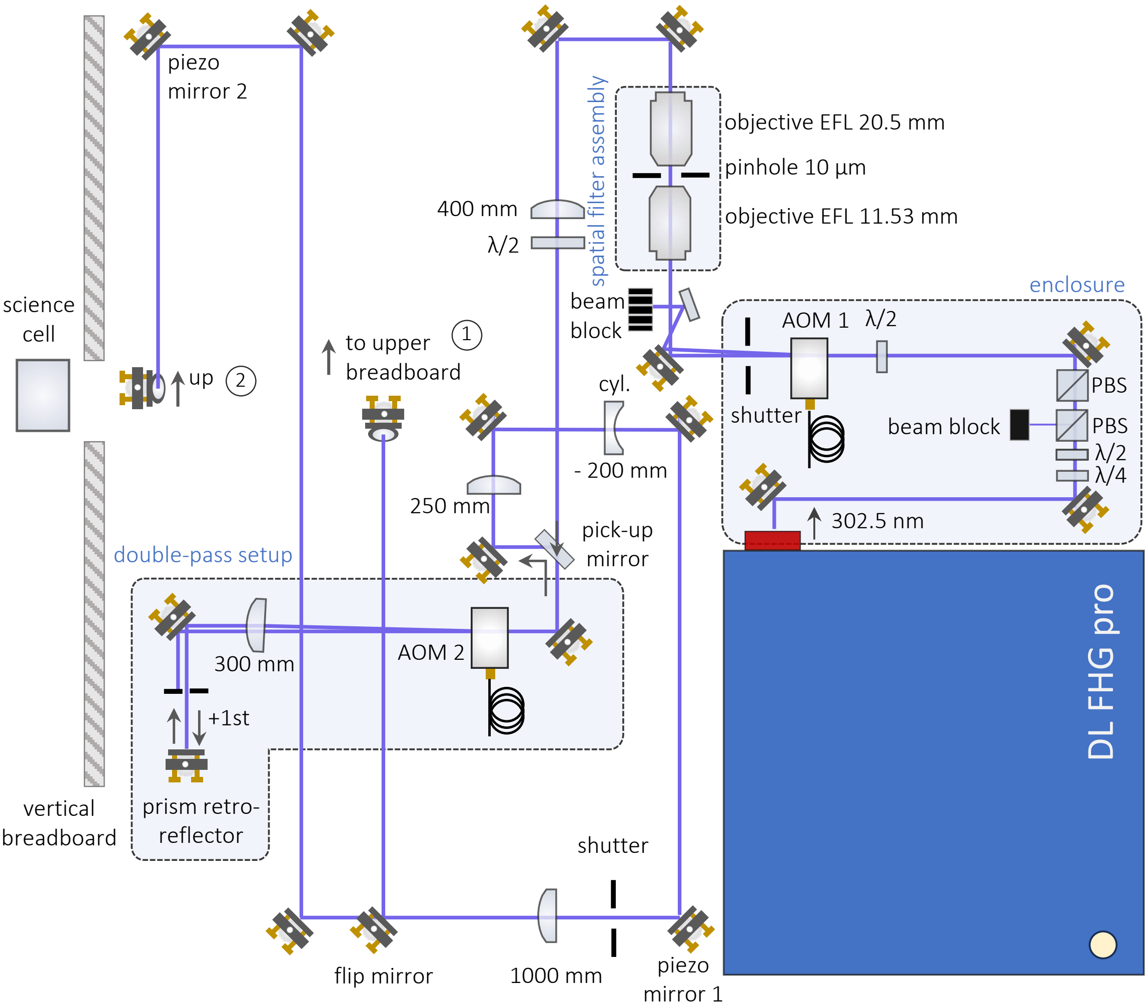

Figure 6.6 | Rydberg laser system on the optical table. Schematic layout of the Rydberg laser system. Rydberg excitation is accomplished using a 301.5 nm laser. The power is stabilized with an acousto-optic modulator (AOM 1). Spatial filtering is performed with two microscope objectives and a 10 µm pinhole. Pulses are generated with AOM 2 in double-pass configuration using a retro-reflector. A cylindrical lens telescope creates an elliptical Gaussian beam. The beam can propagate along two different paths (denoted 1, 2) for addressing different transitions using a flip mirror. Piezo mirror mounts perform active beam stabilization.

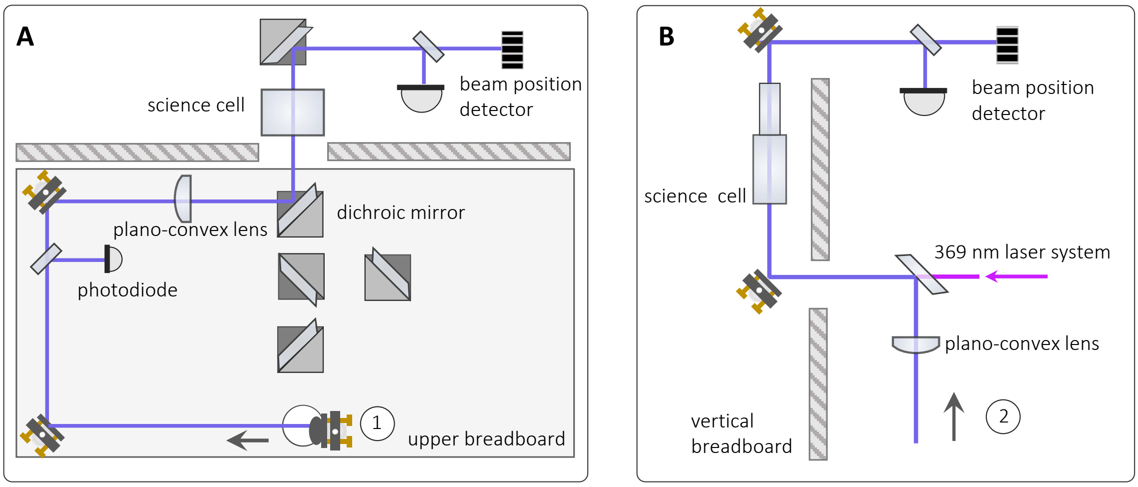

Figure 6.7 | Rydberg beam delivery. Schematic layout of two Rydberg setup branches for beam delivering from different directions. The beam position is measured for active beam stabilization. **A.** Laser system on a second level breadboard. Light is picked off with a beam sampler for power stabilization. The beam is focused down onto the atoms. **B.** Laser system shown in the vertical plane. The beam is focused down and combined with the 369 nm laser on a dichroic mirror.

To improve the beam quality of the laser beam, we remove spatial noise by utilizing a spatial filter setup. The assembly consists of two microscope objectives (Newport U-13X-LC, Thorlabs LMU-10X-UVB) and a molybdenum pinhole (Newport 910PH-5) with a diameter of 10 µm.

For generating pulses and to modulate both the phase and amplitude, we send the beam through a 200 MHz AOM (Gooch & Housego 3200-1210) with ≈ 10 ns rise time. The AOM is placed in the focal plane of a telescope with a spot radius ≈ 40 µm. To eliminate pointing instability arising from the angle-dependance on the modulation frequency, we operate the AOM in a double-pass configuration, while maintaining the polarization state, making it applicable to crystal quartz UV AOMs. We use a prism retro-reflector (Thorlabs HR1015-F01) to achieve vertical spatial separation of the incoming and reflected beam. The back-reflected beam is redirected by a half-inch rectangular mirror, which was manufactured in-house. A fast shutter is used to block unwanted back-reflexions from the surface of the AOM crystal. We characterize the double-pass configuration in section 6.3.3.

After exiting the double-pass, the beam is re-collimated with a plano-convex lens. We implement a cylindrical telescope to shape the beam profile into an elliptical Gaussian beam. A cylindrical lens telescope is used to achieve the desired elliptical beam parameters at the position of the array (see section 6.2).

The light is sent to the atoms via two possible paths allowing us to drive either σ or π transitions. A flip mirror redirects the beam upwards to a breadboard (path 1, see Fig. 6.6), which is shown in Fig. 6.7a. Light is picked up by a beam sampler and focused onto a photo diode to be used as a feedback signal for power stabilization. After the science cell, the alignment of the beam is measured with a position and angle sensitive detector used for active beam stabilization (TEM Messtechnik Aligna®).

Fig. 6.7b illustrates path 2 and shows the experiment from a vertical perspective. Here the beam is delivered to the atoms from beneath the science cell. Before reaching the atoms, the Rydberg laser is combined with the 369 nm laser system using a dichroic mirror. The detector for active beam stabilization can be placed after the light passes the glass cell through a differential pumping tube connecting 3D and 2D science cells. For alignment, a backwards propagating pilot beam can be used.

We now go in detail about subparts of the system.

6.3.2 Spatial filter

To ensure uniform excitation across the array when attempting global excitations with high fidelity, a homogeneous intensity profile of the excitation beam is required. Unfortunately, the output beam profile from our FHG laser shows significant distortions and consequently has a degraded beam quality[2], which results in a diminished excitation fidelity. Figure 6.8a shows the intensity profile of the Rydberg laser beam, taken approximately 1 m from the laser source output. Cross sections along the x and y direction are plotted as well.

We opt for a spatial filtering technique to improve the beam quality. Figure 6.8c illustrates the principle of a spatial filter. The beam is tightly focused to a spot by a microscope objective with effective focal length EFL = 11.53 mm (Newport U-13X-LC). In the picture of Fourier optics a perfectly collimated beam consists of plane waves, i.e. parallel k-vectors, however any imperfections contribute to a higher spread in k-vectors. In the focal plane or Fourier plane, those higher spatial frequencies are located further away from the center of the spot, as spatial frequency and spatial domain are conjugates. The separation is larger the higher the NA of the optics used and the better performing the spatial filter becomes. Placing a pinhole with an appropriate size in the focal plane blocks the noise and transmits only those spatial components that correspond to a point source.

As an approximation for selecting an appropriate pinhole size, as the minimal pinhole radius we use the radius r of the central spot of the Airy disk for a diffraction-limited spot given by

$$r = 1.22 \times \frac{\lambda f}{2D},$$

where λ is the wavelength of the laser beam, f the effective focal length of the microscope objective and D the entrance pupil of the microscope. Since sizing down would result in diffraction at the pinhole, it is recommended to size up when choosing the right pinhole diameter.

---

[2] The manufacturer attributes the shape of the spatial beam profile to spatial walk-off effects which are more prominent at UV wavelengths within the nonlinear crystal used for frequency-doubling.

Figure 6.8d shows a model of the spatial filter assembly used in this experiment. After passing a pinhole with diameter 10 µm (Newport 910PH-10), the beam is re-collimated using a microscope objective with EFL = 20.5 mm (Thorlabs LMU-10X-UVB). As precise alignment is required, the objectives can be each translated along X, Y and Z and tilted in the X and Y direction. To facilitate the alignment of the beam through the pinhole, the focusing objective and the pinhole are mounted in a joint positioner (Newport 910A). The objective used for collimation is mounted with a separate positioner (Newport LP-05A).

Figure 6.8b shows a normalized image and the transverse intensity profiles of the beam after sending it through the spatial filter and re-collimation. We fit a Gaussian function to the data and find good agreement. We extract the beam radii $w_{0,x} = (360.1 \pm 1.4)\,\mu\mathrm{m}$ and $w_{0,y} = (294.96 \pm 0.93)\,\mu\mathrm{m}$ for the x and y transverse intensity profiles, respectively.

Since alignment of the spatial filter can be demanding, we follow the alignment procedure down below. We find that the most difficult part is to get a detectable amount of light transmitted through the pinhole.

Alignment procedure

1. Begin with a beam that is parallel to the optical table by using two alignment screens or apertures to establish an optical axis.
2. Mount the objective into the positioner and make sure the objective is well centered within the mount. Place an alignment disk with a ≈ 1 mm through hole at the position of the pinhole. It can be useful to first mount the objective further away, since a diverging beam is more easily detectable after a pinhole.
3. Place the assembly into the beam and use the built-in aperture and alignment disk to position the objective as well as possible by hand.
4. After mounting the assembly onto the optical table, proceed to make fine adjustments using the knobs. Tune the angle knobs to align the beam through the alignment screen onto the optical axis and adjust the X, Y translation knobs to center the beam using the alignment disk.
5. Iterate step 4 until optimal alignment is achieved. Using the built-in aperture might be useful to adjust the beam size during different alignment steps.
6. Exchange the alignment disk for a pinhole. Carefully adjust the X, Y translation if there is no light visible yet after the pinhole. Repeat step 4 if no signal can be obtained.
7. Once light is transmitted, optimize the transmission of the beam through the pinhole by adjusting the X, Y and especially Z translation along the optical axis.

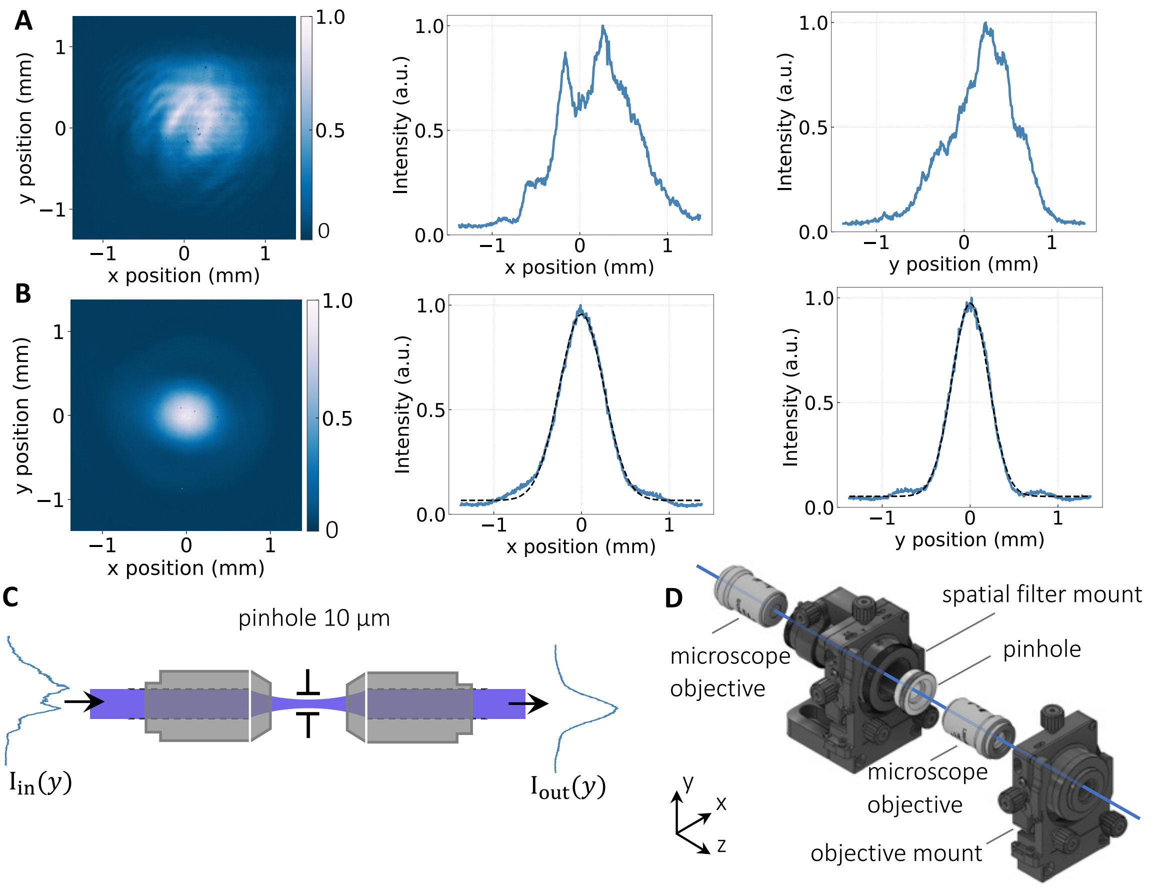

Figure 6.8 | Rydberg laser intensity profile. Image of the Rydberg laser beam before (**A**) and after (**B**) spatial filtering. The colorbar denotes the normalized intensity counts. Shown are the transverse intensity profiles along the horizontal (x) and vertical (y) direction. (**C**) Spatial filtering of the incoming beam (left) is achieved with a microscope objective and a 10 µm diameter pinhole. In the focal plane, spatial noise in the power spectral density is removed by the pinhole, leading to an improved intensity profile (right). The laser beam is re-collimated with a second microscope objective. (**D**) CAD model of the spatial filter assembly. The microscope objectives and pinhole are mounted in 5-axis positioners for precise alignment. Image created using CAD parts courtesy of Newport Corporation and Thorlabs, Inc. See main text for product part numbers.

6.3.3 UV AOM double-pass configuration

A common challenge in AOM applications is the dependence of the diffraction angle on the modulation frequency. To ensure stable beam pointing during phase and frequency modulation of the Rydberg pulse, we allow the beam to pass the AOM twice in a double-pass configuration, acquiring a frequency shift of $+2\Delta f$. While a double-pass setup is a standard procedure, which involves a quarter-waveplate ($\lambda/4$) and a polarizing beamsplitter to separate the incident and the back-reflected beam [212], this method is incompatible with UV laser systems as the only option for AOMs use crystalline quartz as an active medium. These types of AOMs are sensitive to the

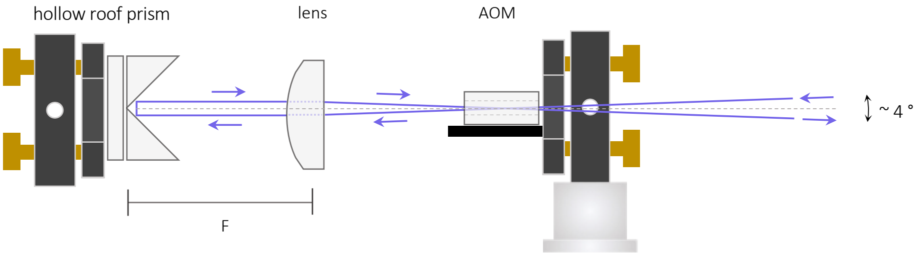

Figure 6.9 | **UV AOM double-pass configuration.** Schematic illustration of the AOM double-pass configuration viewed in the vertical plane. The beam is focused into the AOM with a proceeding lens and re-collimated after the AOM. The beam is sent through the AOM with a vertical tilt of a few degrees relative to the normal propagation axis (dashed line), leading to a vertical displacement when retro-reflected by a hollow roof prism. After passing the AOM a second time, the beam is separated from the incident beam.

polarization state of the incident light[3], requiring the polarization to remain unchanged throughout the double-pass setup.

Figure 6.9 illustrates an optical setup which works with crystalline quartz AOMs by spatially separating the back-reflected beam using a prism retro-reflector. The approach shown here is inspired by UV setups used in ion trapping systems [213, 214].

We tilt the incoming beam in the vertical plane by $\approx 2^\circ$ relative to the optical axis which is depicted by the dashed line. We accomplish this by using a mirror prior to the AOM (not shown here), making sure that no clipping at the aperture of the AOM occurs. Note, that the AOM is placed in the focal plane of a lens with focal length f = 400 mm (see Fig. 6.6) and is focused to a small spot of approximately 40 µm radius, which is not shown in this schematic for simplicity. A $f = 300$ mm lens is used for re-collimation, resulting in the beam to propagate parallel to the optical axis again but with a separation of several mm. We block the remaining light from the other diffraction orders with an aperture.

Mechanical Setup

Placing a retro-reflector (Thorlabs HR1015-F01) consisting of two prisms arranged at a 90° angle in the back focal plane of the telescope ensures 180° reflection regardless of the incident angle. Aligning the center of the retro-reflector to the optical axis, results the beam to be vertically displaced when retro-reflected before traveling back through the lens and focused into the AOM. The retro-reflector is placed in a mirror mount and can be translated along the vertical direction and the optical axis using a manual translation stage.

When propagating through the AOM a second time, the beam is diffracted by the same angle in the horizontal plane given by the Bragg condition. Traveling now in

---

[3] Crystalline quartz AOMs require a polarization 90° relative to its mounting base for optimal operation.

reverse, the beam returns to the initial position only translated vertically by several mm, allowing us to isolate the outgoing beam with a 1/2 inch rectangular mirror, while the incoming beam propagates above the straight edge of the pick-off mirror. With this method we achieve a double-pass diffraction efficiency of about 50 %. However, the efficiency of the double-pass AOM setup is reduced by the poor reflectivity of the retro-reflector surfaces [4]of merely $\approx 90\,\%$ at the employed wavelength. Replacing the retro-reflector with highly reflective prism pair offers a straightforward improvement to the setup, which could result in double-pass AOM efficiencies of $> 60\,\%$.

Frequency scan

To assess the beam pointing stability of the double-pass setup across different frequencies, we perform a frequency scan and measure the beam displacement. Figure 6.10a shows the vertical displacement of the beam centroid as a function of the applied RF frequency. The displacement is measured relative to the position corresponding to the AOM center frequency (200 MHz). For this measurement, a mirror is placed before the science cell to redirect the beam onto a CMOS camera and to image the focal plane. Figure 6.10b shows an illustration of the setup. The AOM in double-pass configuration is located on the lower level of our experiment and is shown in Fig. 6.6. While AOM diffraction occurs in the horizontal plane, the measured beam movement measured on the CMOS camera appears inverted, since the beam travels across two levels. Scanning the frequency over a 20 MHz range, we observe a linear relationship between the frequency and beam displacement. A linear fit to data the yields a slope of $a = (-1.19 \pm 0.08)\,\mu\text{m/MHz}$. Movement in the horizontal plane over this frequency scan is negligible when scanning the AOM frequency.

Compared to a single-pass setup, the lateral beam displacement in the focal plane during frequency scanning is significantly minimized. Assuming a 1st order separation angle of $\theta = 10.6\,\text{mrad}$ at the driving frequency $\nu = 200\,\text{MHz}$ according to $\theta(\nu) = \lambda\nu/v$, where v is the speed of sound in crystalline quartz, we can estimate a beam displacement $d/\text{MHz} = f\tan(\theta) \approx 22.8\,\mu\text{m/MHz}$, where f is the focal length of the focusing lens and in this case is $f = 400\,\text{mm}$.
Further improvements to minimize the frequency dependance of the beam pointing is possible by optimizing the alignment of the double pass. In particular, alignment of the retro-reflector is critical.
These results constitutes a starting point for implementing frequency chirp pulses to induce a controlled phase shift, enabling novel optimized two-qubit gate designs.

6.3.4 Rydberg beam shaping

The Rydberg setup allows for different beam profiles depending on the specific array geometry. For two-dimensional arrays, we implement a cylindrical lens telescope to

---

[4] The surfaces of the retro-reflector are coated with a UV enhanced aluminum coating.

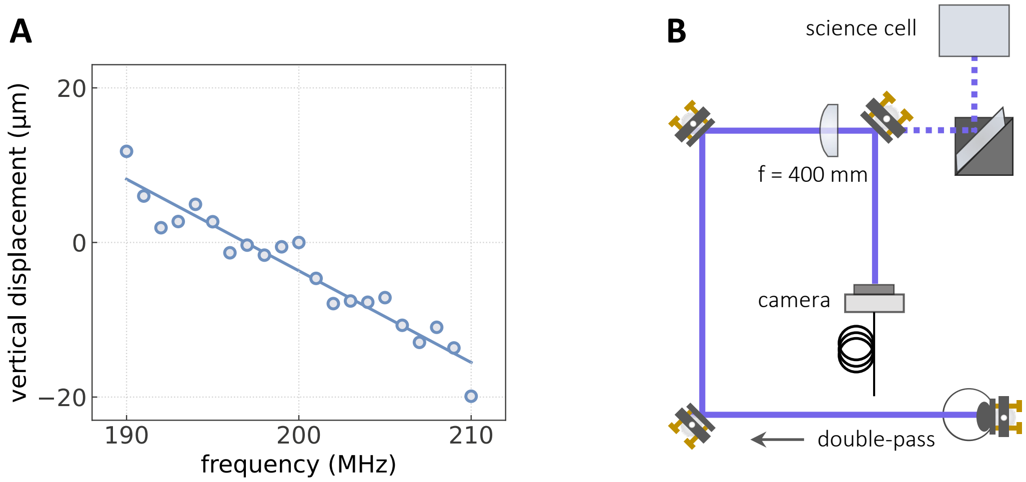

Figure 6.10 | Beam displacement during double-pass AOM frequency scan. Beam centroid displacement from the center frequency position (200 MHz) in the vertical (**A**) direction as a function of AOM RF driving frequency. The beam movement is captured in the focal plane of an elliptical beam as shown in (**C**). The solid lines indicate linear fits to the data.

optimally utilize the available laser power, while providing high degrees of intensity uniform (96 %). One-dimensional arrays are addressed with a circular Rydberg beam. The beam sizes are obtained from considerations presented in section 6.2.

Elliptical beam profile

First, we consider the case of two-dimensional arrays and target an array size of (20x20) µm. Based on the Rydberg beam shaping analysis presented in Ch. 6.2, we aim at an elliptical beam with size ω_x = (26) µm and ω_x = 98 µm (see Tab. 6.2).

Figure 6.11 shows the analysis of the resulting Rydberg beam in the focal plane. To achieve an elliptical Gaussian beam profile we employ a cylindrical telescope. Fig. 6.11a schematically illustrates the beam shaping telescope. We use a plano-concave cylindrical lens (f = -250 mm) to expand the incident beam along the horizontal axis (x), relative to the mounting plane (indicated by the light purple shaded area). The cylindrical lens is mounted in a rotation mount in order to match the cylindrical lens axis to the horizontal axis. Meanwhile the beam size is unaffected along the vertical axis (y). We use a Keplerian telescope with f_1 = 1000 mm and f_2 = 500 mm to reduce the horizontal beam size and assume the incident beam is collimated along this axis. In the horizontal plane, the first lens of the Keplerian telescope f_1 serves the purpose of collimating the expanding beam. This allows us to then focus the beam tightly along this dimension using f_2. Figure 6.11b shows an image of the resulting Rydberg beam in the focal plane. With this setup we achieve the beam waists radii ω_x = (30.8±0.2) µm and ω_y = (112.1±1.5) µm. We extract the beam size from Gaussian fits to the cross sections of the intensity profile, shown in Fig. 6.11c and d. The beam is about 15% larger in both directions than the anticipated beam size. We consider

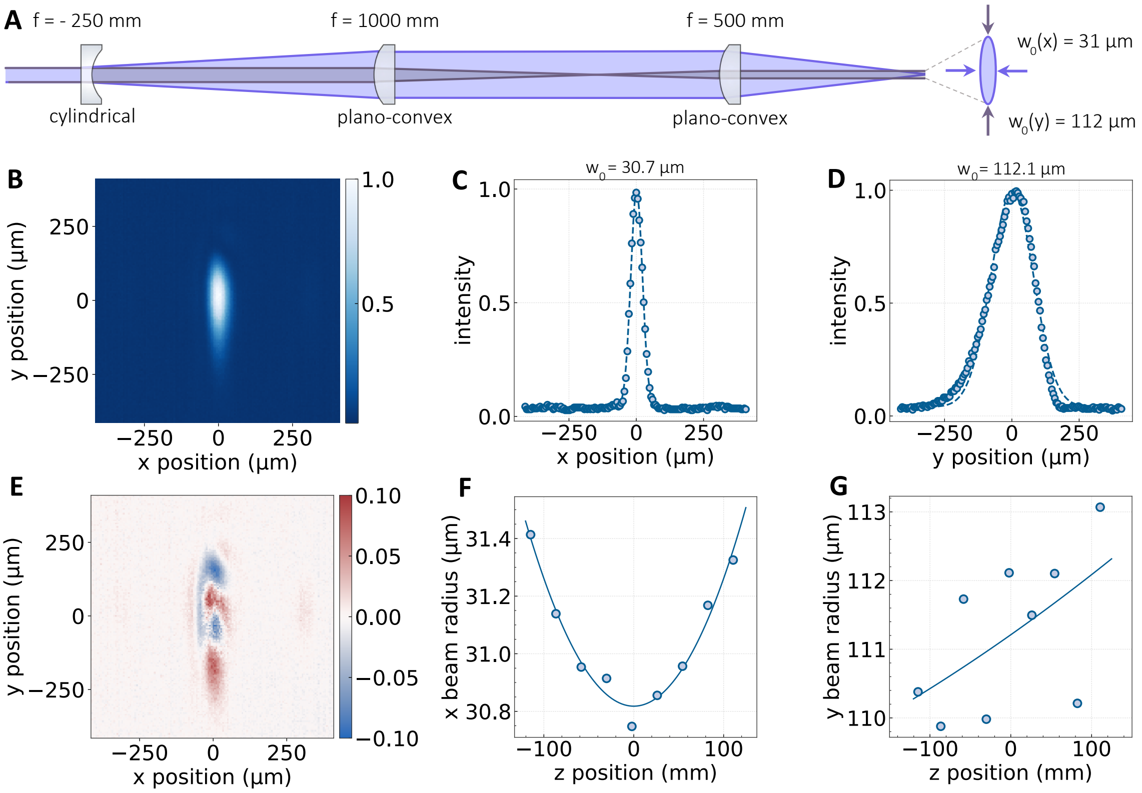

Figure 6.11 | Elliptical Rydberg beam shaping. (**A**) Schematics of the cylindrical beam shaping optics. An elliptical Gaussian beam profile is produced by using a plano-concave cylindrical lens. The beam is expanded along the horizontal axis by the plano-concave cylindrical lens, indicated by light purple shaded area, while the beam remains unaffected along the vertical axis (dark purple). A Keplerian telescope reduces the beam size in the vertical plane, while in the horizontal plane the first lens collimates and the second for focuses the beam to a small spot size. (**B**) Image of the elliptical Rydberg beam in the focal plane. The intensity is normalized to 1. (**C**)/ (**D**) ross sections of the intensity profile along the horizontal x/vertical$y$ axis, respectively. Dashed lines indicate Gaussian fits to the data. The extracted beam waist radii are $21.3\,\mu\mathrm{m}$ and $77.5\,\mu\mathrm{m}$, respectively. (**E**) Residuals of a 2D Gaussian fit to the measured beam image in (B). (**F**)/(**G**) Beam radii along the horizontal (F) and vertical axis (G) as a function of the position along the optical axis. The solid line is a fit to the data (see main text).

this result sufficient for first attempts of Rydberg excitation, since the influence of relative movement of the Rydberg beam and the tweezer array has not been taken into account by the model described in chapter 6.2.

Additionally, we compute the residuals of a 2D Gaussian fit to the beam intensity profile, shown in 6.11e. Overall, we find good qualitative agreement, however the beam shows slight skewness, which is also visible in the cross section along y in Fig 6.11d. We attribute this effect to suboptimal alignment of the cylindrical lens telescope.

Lastly, we measure the beam size along the optical axis z. The separate beam shaping along the vertical and horizontal directions result in two distinct focal planes, as the cylindrical lens refracts light only along one axis. Ideally we want the two focal planes along x and y to be located at the same position along the optical axis z. This ensures that atoms are exposed to a uniform wavefront curvature which obviates phase difference across the array. The behavior of the Rydberg beam along z is shown in Fig. 6.11f and g for the horizontal and vertical beam radius, respectively. We fit the data with $w(z) = \omega_0\sqrt{1+(\frac{z}{z_\mathrm{R}})^2}$, where ω_0 is the beam waist and z_R the Rayleigh range. While we can distinctly identify the position beam waist in the horizontal plane (Fig. 6.11f), while the focal point of the vertical axis is located well outside of the measured region. Adjustments to the length of the Keplerian telescope can be made in order to fine tune the focal plane position along z in the vertical direction and match it to the focus of the horizontal axis of the beam.

An alternative to this beam shaping setup is using a single cylindrical lens to produce an elliptical beam profile. However, this method restricts the achievable aspect ratio in the focal plane. While a larger input beam results in a smaller waist ω_x for a given focal length of the cylindrical lens, the waist size ω_y, which corresponds to the input size, may not be compatible with the desired beam parameters. A cylindrical lens telescope offers more flexibility for achieving a specific elliptical aspect ratio, however it comes at the expense of a higher number of required optical elements and added complexity. The setup can be modified easily to accommodate different elliptical Rydberg beam sizes.

Circular beam profile

We now consider the case of addressing a 1D array of atoms with a global Rydberg laser beam. We target a circular beam profile with beam waist radius $\omega_0 = 26\,\mu\mathrm{m}$ (see table 6.2), which ensures uniform excitation across a 1D line of atoms along the entire FOV of our objective (see chapter 6.2).

Figure 6.12 shows the analysis of the resulting circular Rydberg beam in the focal plane. Switching from the previously presented setup where the beam is shaped into an elliptical intensity profile, requires to exchange a plano-convex lens and remove the cylindrical lens (f = -250 mm).

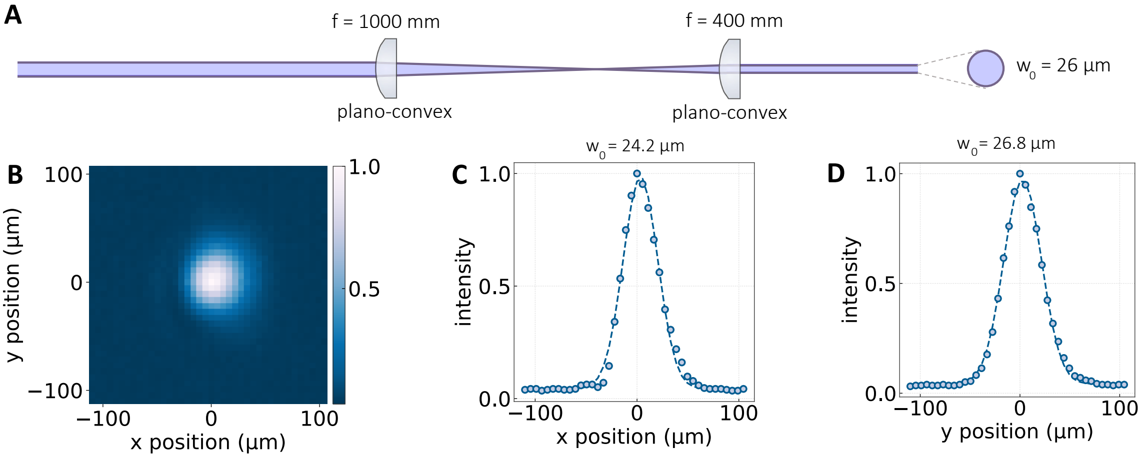

Figure 6.12 | Circular Rydberg beam shaping. (**A**) Schematics of the Rydberg beam shaping optics. A Keplerian telescope with $f_1 = 1000\,\mathrm{mm}$ and $f_2 = 400\,\mathrm{mm}$ reduces the spot size of the Rydberg beam. (**B**) Image of the Rydberg beam in the focal plane. (**C**)/(**D**) Cross sections of the intensity profile along the horizontal x/vertical$y$ axis, respectively. Dashed lines indicate Gaussian fits to the data.

The beam shaping optics is schematically shown in Fig. 6.12a. We employ a Keplerian telescope with $f_1 = 1000\,\mathrm{mm}$ and $f_2 = 400\,\mathrm{mm}$ to reduce the beam waist radius to $\approx 26\,\mu\mathrm{m}$. A image of the resulting Rydberg beam in the focal plane is presented in Fig. 6.12b. The intensity is normalized to 1. The cross sections of the intensity profile along x and y are shown in Fig. 6.12c and d, respectively. We extract beam waist radii $\omega_\mathrm{x} = (24.2 \pm 0.5)\,\mu\mathrm{m}$ and $\omega_\mathrm{x} = (26.8 \pm 0.3)\,\mu\mathrm{m}$ from a Gaussian fit to the data. We believe that the circularity of the beam can be improved by optimizing the alignment of the telescope.

6.4 Autoionization laser system (369 nm)

A crucial ability is to verify whether atoms have been successfully excited to a Rydberg state. This can be achieved through auto-ionization of Rydberg atoms, where the optically active Yb^{+} ion core is addressed with a 369 nm laser, resulting the ion to be expelled from the trapping potential due to its charge. Rydberg atoms can be identified in a subsequent fluorescence image as vacancies, providing a direct but destructive method for identifying Rydberg atoms. Additionally, removing Rydberg atoms from the array, enables state readout of hyperfine qubits.

This section describes the optical setup of a 369 nm laser system enabling Rydberg atom detection and qubit readout.

Rydberg atom detection scheme

Figure 6.13a shows the relevant level scheme for implementing Rydberg atom detection via auto-ionization in $^{171}\mathrm{Yb}$. The inset illustrates the electronic configuration of the two valence electrons. We define the $^{3}\mathrm{P}_{0}$ metastable nuclear spin states as our qubit basis with $|0\rangle = |m_F = +1/2\rangle$ and $|1\rangle = |m_F = -1/2\rangle$. Assuming atoms are initialized in $^{3}\mathrm{P}_{0}\ |1\rangle$, excitation to the $^{3}\mathrm{S}_{1}$ Rydberg state series with principle quantum number $n \approx$ 60 is performed via the 301 nm single-photon transition (see sec. 6.3). Alternatively, Rydberg states can be accessed by excitation from the ground state in a two-photon transition via the $^{3}\mathrm{P}_{1}$ state as shown in [128]. As proposed in [124], the $F = 3/2$ Rydberg state of the $^{3}\mathrm{S}_{1}$ series are favorable for implementing entangling gates as they are isolated from perturbations. By driving a σ^{+} transition coupling $^{3}\mathrm{P}_{0}\ |m_F = 1/2\rangle$ with the Rydberg states $6sns\ ^{3}\mathrm{S}_{1}|m_{F'} = 3/2\rangle$ ensures state-selectivity of the $|1\rangle$ nuclear qubit and suppresses Rydberg coupling of $|0\rangle$. Using a 369 nm laser to target the $6\mathrm{s}\rightarrow 6\mathrm{p}_{1/2}ns$ inner-core transition in Yb^{+} which lies above the ionization limit, resulting in autoionization of the atom and expulsion from the tweezer trap due to its charge. When applied locally, the 369 nm beam can potentially be used to off-resonantly to induce a light shift to the Rydberg states and thus tune the $^{3}\mathrm{P}_{0}$ to Rydberg transition out of resonance, opening up the possibility of local control of entangling operations [145]. Following this scheme, Rydberg atoms can be identified as losses in a subsequent fluorescence image. This enables verification of successful Rydberg excitation or can aid in identifying accidental Rydberg excitations and thus can is a tool to mitigate computational errors in post-selection of data.

State-selective qubit read-out

The capability of auto-ionizing atoms opens up the possibility of state-selectively reading out the qubit state population in $^{3}\mathrm{P}_{0}$. Figure 6.13b shows the relevant electronic levels for implementing a qubit readout scheme. Assuming all population in $|1\rangle$ has been excited to a Rydberg state and auto-ionized according to Fig. 6.13a, the

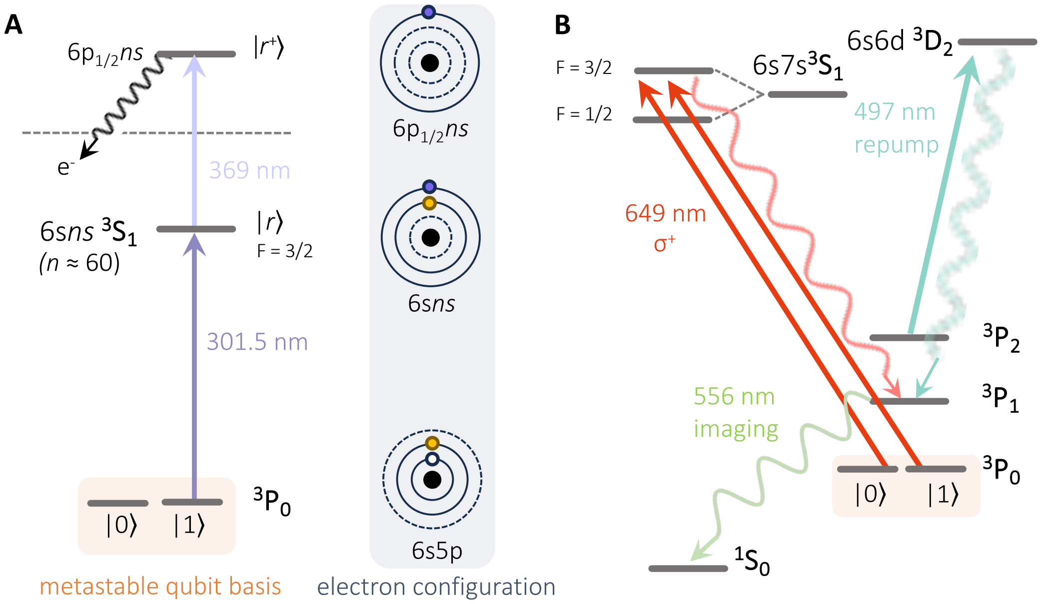

Figure 6.13 | Rydberg Atom Detection and Qubit Readout Scheme in ^{171}Yb. (**A**) Level diagram illustrating the detection scheme of Rydberg atoms via autoionization. Qubits can be encoded in the $^3P_0$ nuclear spins as $|0\rangle = |m_F = +1/2\rangle$ and $|1\rangle = |m_F = -1/2\rangle$, forming a computational basis. Excitation from $^3P_0$ to the $^3S_1$ Rydberg series is accomplished with a 302 nm laser. Driving an ion core transition with 369 nm, results in autoionization, as the ionization limit is exceeded (dashed line). The inset shows the electronic configuration of the two valence electrons. (**B**) Level diagram of a state-selective qubit readout scheme. Atoms remaining in $|0\rangle$ after autoionization are transferred to $^3P_1$ via optical pumping of $^3S_1$ using 649 nm, which are imaged when decaying back to the ground state. Atoms decaying into $^3P_2$ are repumped with a 497 nm laser via $^3D_2$.

remaining population in $|0\rangle$ can be transferred via the $6s7s^3S_1$ state with a 649 nm laser tuned to the F = 3/2 transition back into the ^3P manifold. Decay via $^3P_1$ into the ground state allows atoms to be imaged on the green 556 nm transition. Atoms scattering in $^2P_2$ are repumped on the $^3D_2$ transition at 497 nm. Alternatively, repumping via $^3S_1$ with 770 nm is possible and has been performed successfully in [133], however a major drawback is decay into the computational basis. State-selective qubit readout according to this protocol constitutes a non-destructive method which can be performed mid-circut, enabling detection of errors through leakage into the ground and qubit reloading.

369 nm laser system

The laser system presented in this chapter is conceptualized by the author. The optical layout is refined, built and characterized by Frederik Mrozek under co-supervision of the author. Further details on this setup can be found in [177].

The optical setup used for autoionization of Rydberg atoms is shown in Fig. 6.14. The laser system is mounted onto an external optical breadboard and enclosed for additional UV laser safety purposes. A diode laser[5] produces 20 mW output power. Figure 6.15 shows images of the beam at different positions along its propagation axis as measured from the laser source. Due to the divergent behavior of the produced laser beam, we opt for a fiber-based setup, to produce a well defined Gaussian mode. The light is divided into two branches at a polarizing beam splitter (PBS). A small portion of light (several tens of μW) is couled[6] into a single-mode fiber[7] and used for a wavemeter[8] frequency lock with 10 MHz accuracy. A plano-concave lens ($f = 100$ mm) slightly improves the coupling efficiency to $\approx 70\,\%$, as this presumably offers a better mode match. The electronic PID output signal is fed back into the laser controller. Light transmitted through the PBS propagates through a crystalline quartz accousto-optical modulator (AOM)[9]. The polarization[10] is adjusted prior to the AOM using a $\lambda/2$ waveplate, as the diffraction efficiency of crystalline quartz AOMs is sensitive to the incoming polarization state. We achieve a $\approx 70\,\%$ AOM diffraction efficiency. Because the diode laser produces a non-collimated beam with a beam waist at a distance of ≈ 700 mm from the output, we place the AOM at this position to ensure the beam wavefront is as flat as possible for optimal AOM performance. The AOM serves both the purpose of tuning the frequency and generating short pulses, as well as switching of the beam. The $+1$ AOM diffraction order is coupled[11] into a polarization-maintaining (PM) optical fiber[12] and transported to the main experiment. We match the linear polarization orientation to the principal axis of the PM fiber using a $\lambda/2$ waveplate. To mitigate potential solarization effects of the fiber at 369 nm, we keep the optical fiber as short as possible (1 m). We achieve a fiber coupling efficiency of $\approx 50\ \%$. Light in the remaining orders is picked off with a d-shaped mirror and dumped at a beam trap. A mechanical shutter hinders potential stray light from escaping the enclosure during cycle off-time. The light exits the PM fiber through a fiber collimator[13], which is used to focus the beam down to a beam waist radius of $w_0 = 120\,\mu$m onto the atoms at an approximate distance of 600 mm, which is compatible with the design of our experiment. The laser is combined with the Rydberg excitation beam at a dichroic mirror (see Fig. 6.7b), before it reaches the atoms.

---

[5] Toptica DL pro

[6] Schäfter+Kirchhoff, 60FC-SF-4-A6.2S-01

[7] in-house manufactured single-mode optical fiber (8 m length)

[8] High Finesse, WS Ultimate 10

[9] Gooch & Housego, I-M110-3C10T-3-GH72

[10] linear vertical polarization relative to the mounting plate.

[11] Schäfter+Kirchhoff, 60FC-SF-4-M6.2S-01

[12] Schäfter+Kirchhoff, PMC-360Si-1-18E-100

[13] Schäfter+Kirchhoff, 60FC-SF-4-M6.2S-01

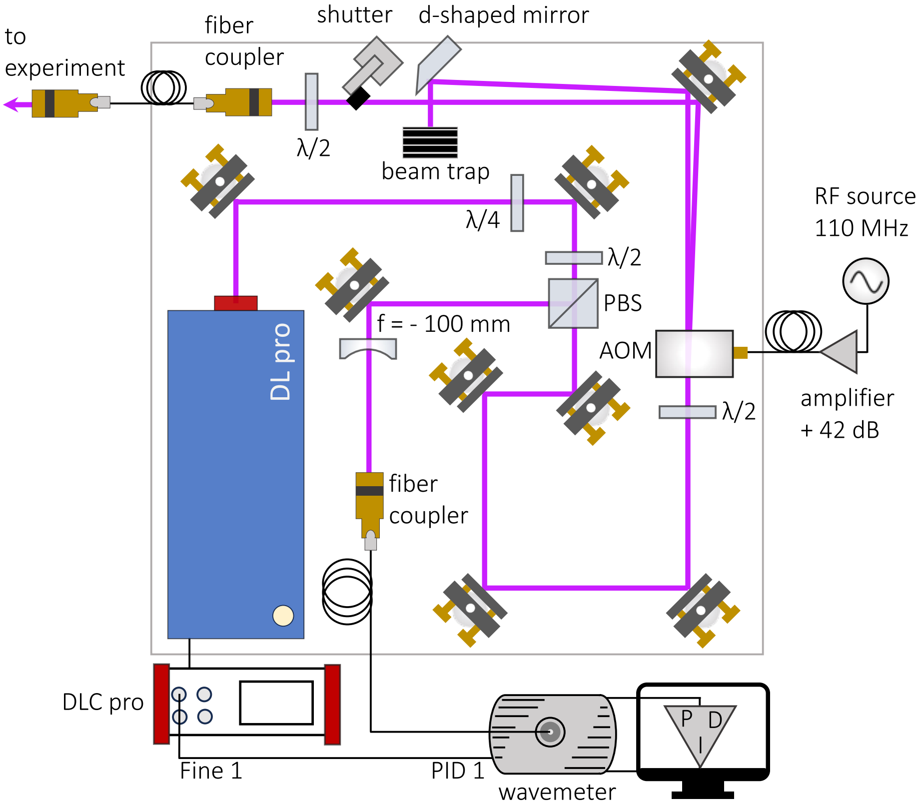

Figure 6.14 | Autoionization Laser Setup (369 nm). Schematic layout of the 369 nm laser system for detecting Rydberg atoms through auto-ionization. The setup is assembled onto an optical bread board. A small amount of light is split off by a polarizing beam splitter (PBS) and coupled into a fiber used for the wavemeter frequency lock. The electronic PID output signal from the wavemeter is fed back into the laser controller. The beam passes an AOM, allowing for frequency shifting and fast pulsing. A shutter ensures additional protection from stray light. The light is delivered to the experiment through a polarization-maintaining fiber.

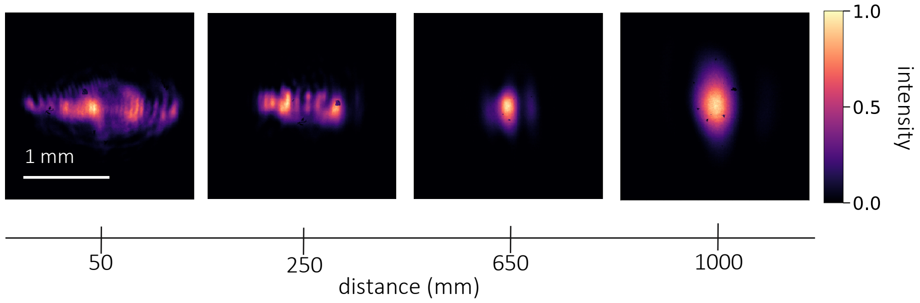

Figure 6.15 | 369 nm laser beam intensity profile. Image of the 369 nm diode laser beam measured at different distances from the output. The intensity is normalized.

6.5 Summary and outlook

This chapter demonstrated the work towards building an optical setup for achieving high fidelity entangled Bell-states in our Yb Rydberg optical tweezer platform. We computed optimal elliptical beam parameters for maximizing the available laser power and providing sufficient intensity uniformity. We successfully employed a beam shaping telescope for Rydberg beams tailored towards the underlying array geometries, both for two-dimensional arrays and one-dimensional lines of trapped atoms. We presented a setup for enabling the detection of Rydberg atoms by means of auto-ionization.

Further technical improvements to current neutral atom array systems are essential for realizing fault-tolerant quantum processors and digital quantum simulators. In particular, minimizing noise sources in these experimental platforms is crucial. Analysis of several different noise sources and their impact on Rydberg-based operations has been performed by C. Schellong [215] in the context of this work. Considered noise sources include laser-induced phase noise, intensity noise, finite temperature effects and beam pointing fluctuations. This represents an important step towards mitigating sources of decoherence.

Attempts at reducing laser-induced noise, include the implementation of active cancellation of laser servo noise schemes as published in [216]. Implementing this method at our experiment in the context of the work performed by P. Herbig [217], enabled a 20 dB suppression of the Pound-Drever-Hall lock induced servo bump.

The work presented in this chapter therefore lays the ground work for implementing Rydberg atoms at our experiment, featuring several technical improvements to existing state-of-the-art techniques.

Bibliography

[1] Jonathan P. Dowling and Gerard J. Milburn. “Quantum technology: the second quantum revolution”, Philosophical Transactions of the Royal Society of London. Series A: Mathematical, Physical and Engineering Sciences **361**, 1655–1674 (2003). Ed. by A. G. J. MacFarlane (cited on page 1).

[2] C S Adams, J D Pritchard, and J P Shaffer. “Rydberg atom quantum technologies”, Journal of Physics B: Atomic, Molecular and Optical Physics **53**, 012002 (2019) (cited on page 1).

[3] Jianwei Wang, Fabio Sciarrino, Anthony Laing, and Mark G. Thompson. “Integrated photonic quantum technologies”, Nature Photonics **14**, 273–284 (2019) (cited on page 1).

[4] Manuel Erhard, Mario Krenn, and Anton Zeilinger. “Advances in high-dimensional quantum entanglement”, Nature Reviews Physics **2**, 365–381 (2020) (cited on page 1).

[5] L. I. R. Gil, R. Mukherjee, E. M. Bridge, M. P. A. Jones, and T. Pohl. “Spin Squeezing in a Rydberg Lattice Clock”, Physical Review Letters **112**, 103601 (2014) (cited on page 1).

[6] E. M. Kessler, P. Kómár, M. Bishof, L. Jiang, A. S. Sørensen, J. Ye, and M. D. Lukin. “Heisenberg-Limited Atom Clocks Based on Entangled Qubits”, Physical Review Letters **112**, 190403 (2014) (cited on page 1).

[7] C. L. Degen, F. Reinhard, and P. Cappellaro. “Quantum sensing”, Reviews of Modern Physics **89**, 035002 (2017) (cited on page 1).

[8] Nabeel Aslam, Hengyun Zhou, Elana K. Urbach, Matthew J. Turner, Ronald L. Walsworth, Mikhail D. Lukin, and Hongkun Park. “Quantum sensors for biomedical applications”, Nature Reviews Physics **5**, 157–169 (2023) (cited on page 1).

[9] Nicolas Gisin and Rob Thew. “Quantum communication”, Nature Photonics **1**, 165–171 (2007) (cited on page 1).

[10] M. K. Bhaskar, R. Riedinger, B. Machielse, D. S. Levonian, C. T. Nguyen, E. N. Knall, H. Park, D. Englund, M. Lončar, D. D. Sukachev, et al. “Experimental demonstration of memory-enhanced quantum communication”, Nature **580**, 60–64 (2020) (cited on page 1).

[11] C. Monroe. “Quantum information processing with atoms and photons”, Nature **416**, 238–246 (2002) (cited on page 1).

[12] G Wendin. “Quantum information processing with superconducting circuits: a review”, Reports on Progress in Physics **80**, 106001 (2017) (cited on page 1).

[13] Fulvio Flamini, Nicolò Spagnolo, and Fabio Sciarrino. “Photonic quantum information processing: a review”, Reports on Progress in Physics **82**, 016001 (2018) (cited on page 1).

[14] Dolev Bluvstein, Harry Levine, Giulia Semeghini, Tout T. Wang, Sepehr Ebadi, Marcin Kalinowski, Alexander Keesling, Nishad Maskara, Hannes Pichler, Markus Greiner, et al. “A quantum processor based on coherent transport of entangled atom arrays”, Nature **604**, 451–456 (2022) (cited on pages 1, 90).

[15] Francesco Bova, Avi Goldfarb, and Roger G. Melko. “Commercial applications of quantum computing”, EPJ Quantum Technology **8**, (2021) (cited on page 1).

[16] Yulin Wu, Wan-Su Bao, Sirui Cao, Fusheng Chen, Ming-Cheng Chen, Xiawei Chen, Tung-Hsun Chung, Hui Deng, Yajie Du, Daojin Fan, et al. “Strong Quantum Computational Advantage Using a Superconducting Quantum Processor”, Physical Review Letters **127**, 180501 (2021) (cited on pages 1, 2).

[17] Youngseok Kim, Andrew Eddins, Sajant Anand, Ken Xuan Wei, Ewout van den Berg, Sami Rosenblatt, Hasan Nayfeh, Yantao Wu, Michael Zaletel, Kristan Temme, et al. “Evidence for the utility of quantum computing before fault tolerance”, Nature **618**, 500–505 (2023) (cited on page 1).

[18] Florian Schäfer, Takeshi Fukuhara, Seiji Sugawa, Yosuke Takasu, and Yoshiro Takahashi. “Tools for quantum simulation with ultracold atoms in optical lattices”, Nature Reviews Physics **2**, 411–425 (2020) (cited on page 1).

[19] Guido Pagano, Aniruddha Bapat, Patrick Becker, Katherine S. Collins, Arinjoy De, Paul W. Hess, Harvey B. Kaplan, Antonis Kyprianidis, Wen Lin Tan, Christopher Baldwin, et al. “Quantum approximate optimization of the long-range Ising model with a trapped-ion quantum simulator”, Proceedings of the National Academy of Sciences **117**, 25396–25401 (2020) (cited on page 1).

[20] C. Monroe, W. C. Campbell, L.-M. Duan, Z.-X. Gong, A. V. Gorshkov, P. W. Hess, R. Islam, K. Kim, N. M. Linke, G. Pagano, et al. “Programmable quantum simulations of spin systems with trapped ions”, Reviews of Modern Physics **93**, 025001 (2021) (cited on page 1).

[21] Andrew J. Daley, Immanuel Bloch, Christian Kokail, Stuart Flannigan, Natalie Pearson, Matthias Troyer, and Peter Zoller. “Practical quantum advantage in quantum simulation”, Nature **607**, 667–676 (2022) (cited on page 1).

[22] John Preskill. “Quantum Computing in the NISQ era and beyond”, Quantum **2**, 79 (2018) (cited on page 1).

[23] T. D. Ladd, F. Jelezko, R. Laflamme, Y. Nakamura, C. Monroe, and J. L. O’Brien. “Quantum computers”, Nature **464**, 45–53 (2010) (cited on page 1).

[24] Han-Sen Zhong, Hui Wang, Yu-Hao Deng, Ming-Cheng Chen, Li-Chao Peng, Yi-Han Luo, Jian Qin, Dian Wu, Xing Ding, Yi Hu, et al. "Quantum computational advantage using photons", Science **370**, 1460–1463 (2020) (cited on page 1).

[25] M. Cerezo, Andrew Arrasmith, Ryan Babbush, Simon C. Benjamin, Suguru Endo, Keisuke Fujii, Jarrod R. McClean, Kosuke Mitarai, Xiao Yuan, Lukasz Cincio, et al. "Variational quantum algorithms", Nature Reviews Physics **3**, 625–644 (2021) (cited on page 1).

[26] Lars S. Madsen, Fabian Laudenbach, Mohsen Falamarzi. Askarani, Fabien Rortais, Trevor Vincent, Jacob F. F. Bulmer, Filippo M. Miatto, Leonhard Neuhaus, Lukas G. Helt, Matthew J. Collins, et al. "Quantum computational advantage with a programmable photonic processor", Nature **606**, 75–81 (2022) (cited on page 1).

[27] Nicolas Gisin, Grégoire Ribordy, Wolfgang Tittel, and Hugo Zbinden. "Quantum cryptography", Reviews of Modern Physics **74**, 145–195 (2002) (cited on page 1).

[28] S. Pirandola, U. L. Andersen, L. Banchi, M. Berta, D. Bunandar, R. Colbeck, D. Englund, T. Gehring, C. Lupo, C. Ottaviani, et al. "Advances in quantum cryptography", Advances in Optics and Photonics **12**, 1012 (2020) (cited on page 1).

[29] Christian W. Bauer, Zohreh Davoudi, A. Baha Balantekin, Tanmoy Bhattacharya, Marcela Carena, Wibe A. de Jong, Patrick Draper, Aida El-Khadra, Nate Gemelke, Masanori Hanada, et al. "Quantum Simulation for High-Energy Physics", PRX Quantum **4**, 027001 (2023) (cited on page 1).

[30] Alberto Di Meglio, Karl Jansen, Ivano Tavernelli, Constantia Alexandrou, Srinivasan Arunachalam, Christian W. Bauer, Kerstin Borras, Stefano Carrazza, Arianna Crippa, Vincent Croft, et al. "Quantum Computing for High-Energy Physics: State of the Art and Challenges", PRX Quantum **5**, 037001 (2024) (cited on page 1).

[31] Nathalie P. de Leon, Kohei M. Itoh, Dohun Kim, Karan K. Mehta, Tracy E. Northup, Hanhee Paik, B. S. Palmer, N. Samarth, Sorawis Sangtawesin, and D. W. Steuerman. "Materials challenges and opportunities for quantum computing hardware", Science **372**, (2021) (cited on page 1).

[32] Sam McArdle, Suguru Endo, Alán Aspuru-Guzik, Simon C. Benjamin, and Xiao Yuan. "Quantum computational chemistry", Reviews of Modern Physics **92**, 015003 (2020) (cited on page 1).

[33] Jules Tilly, Hongxiang Chen, Shuxiang Cao, Dario Picozzi, Kanav Setia, Ying Li, Edward Grant, Leonard Wossnig, Ivan Rungger, George H. Booth, et al. "The Variational Quantum Eigensolver: A review of methods and best practices", Physics Reports **986**, 1–128 (2022) (cited on page 1).

[34] Y. Cao, J. Romero, and A. Aspuru-Guzik. "Potential of quantum computing for drug discovery", IBM Journal of Research and Development **62**, 6:1–6:20 (2018) (cited on page 1).

[35] Nick S. Blunt, Joan Camps, Ophelia Crawford, Róbert Izsák, Sebastian Leontica, Arjun Mirani, Alexandra E. Moylett, Sam A. Scivier, Christoph Sünderhauf, Patrick Schopf, et al. "Perspective on the Current State-of-the-Art of Quantum Computing for Drug Discovery Applications", Journal of Chemical Theory and Computation **18**, 7001–7023 (2022) (cited on page 1).

[36] Lixing Wang, S. K. Kowk, and W. H. Ip. "Design of an improved quantum-inspired evolutionary algorithm for a transportation problem in logistics systems", Journal of Intelligent Manufacturing **23**, 2227–2236 (2011) (cited on page 1).

[37] Román Orús, Samuel Mugel, and Enrique Lizaso. "Quantum computing for finance: Overview and prospects", Reviews in Physics **4**, 100028 (2019) (cited on page 1).

[38] Daniel J. Egger, Claudio Gambella, Jakub Marecek, Scott McFaddin, Martin Mevissen, Rudy Raymond, Andrea Simonetto, Stefan Woerner, and Elena Yndurain. "Quantum Computing for Finance: State-of-the-Art and Future Prospects", IEEE Transactions on Quantum Engineering **1**, 1–24 (2020) (cited on page 1).

[39] Jonathan Wurtz, Pedro L. S. Lopes, Christoph Gorgulla, Nathan Gemelke, Alexander Keesling, and Shengtao Wang. "Industry applications of neutral-atom quantum computing solving independent set problems", arXiv:2205.08500, (2022) (cited on page 1).

[40] Dylan Herman, Cody Googin, Xiaoyuan Liu, Alexey Galda, Ilya Safro, Yue Sun, Marco Pistoia, and Yuri Alexeev. "A Survey of Quantum Computing for Finance", arXiv:2201.02773, (2022) (cited on page 1).

[41] M. Cerezo, Guillaume Verdon, Hsin-Yuan Huang, Lukasz Cincio, and Patrick J. Coles. "Challenges and opportunities in quantum machine learning", Nature Computational Science **2**, 567–576 (2022) (cited on page 1).

[42] Peter W. Shor. "Polynomial-Time Algorithms for Prime Factorization and Discrete Logarithms on a Quantum Computer", SIAM Journal on Computing **26**, 1484–1509 (1997) (cited on page 1).

[43] Lov K. Grover. "Quantum Mechanics Helps in Searching for a Needle in a Haystack", Physical Review Letters **79**, 325–328 (1997) (cited on page 1).

[44] Paul Benioff. "The computer as a physical system: A microscopic quantum mechanical Hamiltonian model of computers as represented by Turing machines", Journal of Statistical Physics **22**, 563–591 (1980) (cited on page 1).

[45] Paul Benioff. "Quantum mechanical hamiltonian models of turing machines", Journal of Statistical Physics **29**, 515–546 (1982) (cited on page 1).

[46] David Deutsch. "Quantum theory, the church-turing principle and the universal quantumcomputer", Proceedings of the Royal Society A, (1985) (cited on page 1).

[47] Richard Jozsa David Deutsch. “Rapid solution of problems by quantum computation.”, Proceedings of the Royal Society A **439**, 553–558 (1992) (cited on page 1).

[48] David P. DiVincenzo. “Topics in Quantum Computers”, arXiv:cond-mat/9612126, (1996) (cited on page 1).

[49] Yuri Manin. *Computable and Uncomputable (in Russian)*. Sovetskoye Radio, 1980 (cited on page 1).

[50] Richard P. Feynman. “Simulating physics with computers”, International Journal of Theoretical Physics **21**, 467–488 (1982) (cited on page 1).

[51] Iulia Buluta and Franco Nori. “Quantum Simulators”, Science **326**, 108–111 (2009) (cited on page 1).

[52] Immanuel Bloch, Jean Dalibard, and Sylvain Nascimbène. “Quantum simulations with ultracold quantum gases”, Nature Physics **8**, 267–276 (2012) (cited on page 1).

[53] I. M. Georgescu, S. Ashhab, and Franco Nori. “Quantum simulation”, Reviews of Modern Physics **86**, 153–185 (2014) (cited on page 1).

[54] M. Saffman, T. G. Walker, and K. Mølmer. “Quantum information with Rydberg atoms”, Reviews of Modern Physics **82**, 2313–2363 (2010) (cited on pages 2, 92).

[55] Iulia Buluta, Sahel Ashhab, and Franco Nori. “Natural and artificial atoms for quantum computation”, Reports on Progress in Physics **74**, 104401 (2011) (cited on page 2).

[56] Loïc Henriet, Lucas Beguin, Adrien Signoles, Thierry Lahaye, Antoine Browaeys, Georges-Olivier Reymond, and Christophe Jurczak. “Quantum computing with neutral atoms”, Quantum **4**, 327 (2020) (cited on pages 2, 92).

[57] T. M. Graham, Y. Song, J. Scott, C. Poole, L. Phuttitarn, K. Jooya, P. Eichler, X. Jiang, A. Marra, B. Grinkemeyer, et al. “Multi-qubit entanglement and algorithms on a neutral-atom quantum computer”, Nature **604**, 457–462 (2022) (cited on page 2).

[58] Karen Wintersperger, Florian Dommert, Thomas Ehmer, Andrey Hoursanov, Johannes Klepsch, Wolfgang Mauerer, Georg Reuber, Thomas Strohm, Ming Yin, and Sebastian Luber. “Neutral atom quantum computing hardware: performance and end-user perspective”, EPJ Quantum Technology **10**, (2023) (cited on page 2).

[59] Colin D. Bruzewicz, John Chiaverini, Robert McConnell, and Jeremy M. Sage. “Trapped-ion quantum computing: Progress and challenges”, Applied Physics Reviews **6**, (2019) (cited on page 2).

[60] Morten Kjaergaard, Mollie E. Schwartz, Jochen Braumüller, Philip Krantz, Joel I.-J. Wang, Simon Gustavsson, and William D. Oliver. “Superconducting Qubits: Current State of Play”, Annual Review of Condensed Matter Physics **11**, 369–395 (2020) (cited on page 2).

[61] J. P. Gaebler, T. R. Tan, Y. Lin, Y. Wan, R. Bowler, A. C. Keith, S. Glancy, K. Coakley, E. Knill, D. Leibfried, et al. “High-Fidelity Universal Gate Set forBe9+Ion Qubits”, Physical Review Letters **117**, 060505 (2016) (cited on page 2).

[62] Rui Li, Kentaro Kubo, Yinghao Ho, Zhiguang Yan, Yasunobu Nakamura, and Hayato Goto. “Realization of High-Fidelity CZ Gate Based on a Double-Transmon Coupler”, Physical Review X **14**, 041050 (2024) (cited on page 2).

[63] Frank Arute, Kunal Arya, Ryan Babbush, Dave Bacon, Joseph C. Bardin, Rami Barends, Rupak Biswas, Sergio Boixo, Fernando G. S. L. Brandao, David A. Buell, et al. “Quantum supremacy using a programmable superconducting processor”, Nature **574**, 505–510 (2019) (cited on page 2).

[64] Z. Hu and H. J. Kimble. “Observation of a single atom in a magneto-optical trap”, Optics Letters **19**, 1888 (1994) (cited on page 2).

[65] Nicolas Schlosser, Georges Reymond, Igor Protsenko, and Philippe Grangier. “Sub-poissonian loading of single atoms in a microscopic dipole trap”, Nature **411**, 1024–1027 (2001) (cited on pages 2, 7, 20, 74, 75).

[66] Stefan Kuhr, Wolfgang Alt, Dominik Schrader, Martin Müller, Victor Gomer, and Dieter Meschede. “Deterministic Delivery of a Single Atom”, Science **293**, 278–280 (2001) (cited on pages 2, 7).

[67] W. S. Bakr, A. Peng, M. E. Tai, R. Ma, J. Simon, J. I. Gillen, S. Fölling, L. Pollet, and M. Greiner. “Probing the Superfluid–to–Mott Insulator Transition at the Single-Atom Level”, Science **329**, 547–550 (2010) (cited on page 2).

[68] Jacob F. Sherson, Christof Weitenberg, Manuel Endres, Marc Cheneau, Immanuel Bloch, and Stefan Kuhr. “Single-atom-resolved fluorescence imaging of an atomic Mott insulator”, Nature **467**, 68–72 (2010) (cited on page 2).

[69] Silvia Bergamini, Benoît Darquié, Matthew Jones, Lionel Jacubowiez, Antoine Browaeys, and Philippe Grangier. “Holographic generation of microtrap arrays for single atoms by use of a programmable phase modulator”, Journal of the Optical Society of America B **21**, 1889 (2004) (cited on pages 2, 19).

[70] F. Nogrette, H. Labuhn, S. Ravets, D. Barredo, L. Béguin, A. Vernier, T. Lahaye, and A. Browaeys. “Single-Atom Trapping in Holographic 2D Arrays of Microtraps with Arbitrary Geometries”, Physical Review X **4**, 021034 (2014) (cited on pages 2, 19, 23, 27, 34).

[71] Hyosub Kim, Woojun Lee, Han-gyeol Lee, Hanlae Jo, Yunheung Song, and Jaewook Ahn. “In situ single-atom array synthesis using dynamic holographic optical tweezers”, Nature Communications **7**, (2016) (cited on page 2).

[72] Manuel Endres, Hannes Bernien, Alexander Keesling, Harry Levine, Eric R. Anschuetz, Alexandre Krajenbrink, Crystal Senko, Vladan Vuletic, Markus Greiner, and Mikhail D. Lukin. “Atom-by-atom assembly of defect-free one-dimensional cold atom arrays”, Science **354**, 1024–1027 (2016) (cited on pages 2, 19, 75, 90).

[73] Daniel Barredo, Sylvain de Léséleuc, Vincent Lienhard, Thierry Lahaye, and Antoine Browaeys. "An atom-by-atom assembler of defect-free arbitrary two-dimensional atomic arrays", Science **354**, 1021–1023 (2016) (cited on pages 2, 75).

[74] Malte Schlosser, Daniel Ohl de Mello, Dominik Schäffner, Tilman Preuschoff, Lars Kohfahl, and Gerhard Birkl. "Assembled arrays of Rydberg-interacting atoms", Journal of Physics B: Atomic, Molecular and Optical Physics **53**, 144001 (2020) (cited on page 2).

[75] Kai-Niklas Schymik, Vincent Lienhard, Daniel Barredo, Pascal Scholl, Hannah Williams, Antoine Browaeys, and Thierry Lahaye. "Enhanced atom-by-atom assembly of arbitrary tweezer arrays", Physical Review A **102**, 063107 (2020) (cited on pages 2, 75, 90).

[76] Hannah J. Manetsch, Gyohei Nomura, Elie Bataille, Kon H. Leung, Xudong Lv, and Manuel Endres. "A tweezer array with 6100 highly coherent atomic qubits", arXiv:2403.12021, (2024) (cited on pages 2, 3, 19, 90).

[77] Bichen Zhang, Pai Peng, Aditya Paul, and Jeff D. Thompson. "Scaled local gate controller for optically addressed qubits", Optica **11**, 227 (2024) (cited on page 2).

[78] Yiyi Li, Yicheng Bao, Michael Peper, Chenyuan Li, and Jeff D. Thompson. "Fast, continuous and coherent atom replacement in a neutral atom qubit array", arXiv:2506.15633, (2025) (cited on pages 2, 3).

[79] J. A. Muniz, D. Crow, H. Kim, J. M. Kindem, W. B. Cairncross, A. Ryou, T. C. Bohdanowicz, C. -A. Chen, Y. Ji, A. M. W. Jones, et al. "Repeated ancilla reuse for logical computation on a neutral atom quantum computer", arXiv:2506.09936, (2025) (cited on page 2).

[80] W. R. Anderson, J. R. Veale, and T. F. Gallagher. "Resonant Dipole-Dipole Energy Transfer in a Nearly Frozen Rydberg Gas", Physical Review Letters **80**, 249–252 (1998) (cited on page 2).

[81] I. Mourachko, D. Comparat, F. de Tomasi, A. Fioretti, P. Nosbaum, V. M. Akulin, and P. Pillet. "Many-Body Effects in a Frozen Rydberg Gas", Physical Review Letters **80**, 253–256 (1998) (cited on page 2).

[82] D. Jaksch, J. I. Cirac, P. Zoller, S. L. Rolston, R. Côté, and M. D. Lukin. "Fast Quantum Gates for Neutral Atoms", Physical Review Letters **85**, 2208–2211 (2000) (cited on pages 2, 91, 99).

[83] M. D. Lukin, M. Fleischhauer, R. Cote, L. M. Duan, D. Jaksch, J. I. Cirac, and P. Zoller. "Dipole Blockade and Quantum Information Processing in Mesoscopic Atomic Ensembles", Physical Review Letters **87**, 037901 (2001) (cited on pages 2, 99).

[84] E. Urban, T. A. Johnson, T. Henage, L. Isenhower, D. D. Yavuz, T. G. Walker, and M. Saffman. "Observation of Rydberg blockade between two atoms", Nature Physics **5**, 110–114 (2009) (cited on page 2).

[85] Alpha Gaëtan, Yevhen Miroshnychenko, Tatjana Wilk, Amodsen Chotia, Matthieu Viteau, Daniel Comparat, Pierre Pillet, Antoine Browaeys, and Philippe Grangier. "Observation of collective excitation of two individual atoms in the Rydberg blockade regime", Nature Physics **5**, 115–118 (2009) (cited on page 2).

[86] T. Wilk, A. Gaëtan, C. Evellin, J. Wolters, Y. Miroshnychenko, P. Grangier, and A. Browaeys. "Entanglement of Two Individual Neutral Atoms Using Rydberg Blockade", Physical Review Letters **104**, 010502 (2010) (cited on page 2).

[87] Hendrik Weimer, Markus Müller, Igor Lesanovsky, Peter Zoller, and Hans Peter Büchler. "A Rydberg quantum simulator", Nature Physics **6**, 382–388 (2010) (cited on page 2).

[88] Sepehr Ebadi, Tout T. Wang, Harry Levine, Alexander Keesling, Giulia Semeghini, Ahmed Omran, Dolev Bluvstein, Rhine Samajdar, Hannes Pichler, Wen Wei Ho, et al. "Quantum phases of matter on a 256-atom programmable quantum simulator", Nature **595**, 227–232 (2021) (cited on pages 2, 19).

[89] M. Morgado and S. Whitlock. "Quantum simulation and computing with Rydberg-interacting qubits", AVS Quantum Science **3**, (2021) (cited on pages 2, 3).

[90] Daniel Barredo, Henning Labuhn, Sylvain Ravets, Thierry Lahaye, Antoine Browaeys, and Charles S. Adams. "Coherent Excitation Transfer in a Spin Chain of Three Rydberg Atoms", Physical Review Letters **114**, 113002 (2015) (cited on page 3).

[91] Johannes Zeiher, Rick van Bijnen, Peter Schauß, Sebastian Hild, Jae-yoon Choi, Thomas Pohl, Immanuel Bloch, and Christian Gross. "Many-body interferometry of a Rydberg-dressed spin lattice", Nature Physics **12**, 1095–1099 (2016) (cited on page 3).

[92] Henning Labuhn, Daniel Barredo, Sylvain Ravets, Sylvain de Léséleuc, Tommaso Macrì, Thierry Lahaye, and Antoine Browaeys. "Tunable two-dimensional arrays of single Rydberg atoms for realizing quantum Ising models", Nature **534**, 667–670 (2016) (cited on page 3).

[93] Guillaume Bornet, Gabriel Emperauger, Cheng Chen, Bingtian Ye, Maxwell Block, Marcus Bintz, Jamie A. Boyd, Daniel Barredo, Tommaso Comparin, Fabio Mezzacapo, et al. "Scalable spin squeezing in a dipolar Rydberg atom array", Nature **621**, 728–733 (2023) (cited on page 3).

[94] Pascal Scholl, Michael Schuler, Hannah J. Williams, Alexander A. Eberharter, Daniel Barredo, Kai-Niklas Schymik, Vincent Lienhard, Louis-Paul Henry, Thomas C. Lang, Thierry Lahaye, et al. "Quantum simulation of 2D antiferromagnets with hundreds of Rydberg atoms", Nature **595**, 233–238 (2021) (cited on pages 3, 32).

[95] Alexander Keesling, Ahmed Omran, Harry Levine, Hannes Bernien, Hannes Pichler, Soonwon Choi, Rhine Samajdar, Sylvain Schwartz, Pietro Silvi, Subir Sachdev, et al. "Quantum Kibble–Zurek mechanism and critical dynamics on a programmable Rydberg simulator", Nature **568**, 207–211 (2019) (cited on page 3).

[96] G. Semeghini, H. Levine, A. Keesling, S. Ebadi, T. T. Wang, D. Bluvstein, R. Verresen, H. Pichler, M. Kalinowski, R. Samajdar, et al. "Probing topological spin liquids on a programmable quantum simulator", Science **374**, 1242–1247 (2021) (cited on pages 3, 32).

[97] Hannes Bernien, Sylvain Schwartz, Alexander Keesling, Harry Levine, Ahmed Omran, Hannes Pichler, Soonwon Choi, Alexander S. Zibrov, Manuel Endres, Markus Greiner, et al. "Probing many-body dynamics on a 51-atom quantum simulator", Nature **551**, 579–584 (2017) (cited on page 3).

[98] Antoine Browaeys and Thierry Lahaye. "Many-body physics with individually controlled Rydberg atoms", Nature Physics **16**, 132–142 (2020) (cited on pages 3, 92).

[99] L. Isenhower, E. Urban, X. L. Zhang, A. T. Gill, T. Henage, T. A. Johnson, T. G. Walker, and M. Saffman. "Demonstration of a Neutral Atom Controlled-NOT Quantum Gate", Physical Review Letters **104**, 010503 (2010) (cited on page 3).

[100] Xiaoling Wu, Xinhui Liang, Yaoqi Tian, Fan Yang, Cheng Chen, Yong-Chun Liu, Meng Khoon Tey, and Li You. "A concise review of Rydberg atom based quantum computation and quantum simulation", Chinese Physics B **30**, 020305 (2021) (cited on pages 3, 92).

[101] A. Omran, H. Levine, A. Keesling, G. Semeghini, T. T. Wang, S. Ebadi, H. Bernien, A. S. Zibrov, H. Pichler, S. Choi, et al. "Generation and manipulation of Schrödinger cat states in Rydberg atom arrays", Science **365**, 570–574 (2019) (cited on page 3).

[102] Dolev Bluvstein, Simon J. Evered, Alexandra A. Geim, Sophie H. Li, Hengyun Zhou, Tom Manovitz, Sepehr Ebadi, Madelyn Cain, Marcin Kalinowski, Dominik Hangleiter, et al. "Logical quantum processor based on reconfigurable atom arrays", Nature **626**, 58–65 (2023) (cited on pages 3, 19, 90).

[103] P. Huft, Y. Song, T. M. Graham, K. Jooya, S. Deshpande, C. Fang, M. Kats, and M. Saffman. "Simple, passive design for large optical trap arrays for single atoms", Physical Review A **105**, 063111 (2022) (cited on page 3).

[104] Lars Pause, Lukas Sturm, Marcel Mittenbühler, Stephan Amann, Tilman Preuschoff, Dominik Schäffner, Malte Schlosser, and Gerhard Birkl. "Supercharged two-dimensional tweezer array with more than 1000 atomic qubits", Optica **11**, 222 (2024) (cited on page 3).

[105] Renhao Tao, Maximilian Ammenwerth, Flavien Gyger, Immanuel Bloch, and Johannes Zeiher. "High-Fidelity Detection of Large-Scale Atom Arrays in an Optical Lattice", Physical Review Letters **133**, 013401 (2024) (cited on page 3).

[106] Neng-Chun Chiu, Elias C. Trapp, Jinen Guo, Mohamed H. Abobeih, Luke M. Stewart, Simon Hollerith, Pavel Stroganov, Marcin Kalinowski, Alexandra A. Geim, Simon J. Evered, et al. "Continuous operation of a coherent 3,000-qubit system", arXiv:2506.20660, (2025) (cited on page 3).

[107] Simon J. Evered, Dolev Bluvstein, Marcin Kalinowski, Sepehr Ebadi, Tom Manovitz, Hengyun Zhou, Sophie H. Li, Alexandra A. Geim, Tout T. Wang, Nishad Maskara, et al. "High-fidelity parallel entangling gates on a neutral-atom quantum computer", Nature **622**, 268–272 (2023) (cited on pages 3, 99).

[108] S. Ebadi, A. Keesling, M. Cain, T. T. Wang, H. Levine, D. Bluvstein, G. Semeghini, A. Omran, J.-G. Liu, R. Samajdar, et al. "Quantum optimization of maximum independent set using Rydberg atom arrays", Science **376**, 1209–1215 (2022) (cited on page 3).

[109] F B Dunning, T C Killian, S Yoshida, and J Burgdörfer. "Recent advances in Rydberg physics using alkaline-earth atoms", Journal of Physics B: Atomic, Molecular and Optical Physics **49**, 112003 (2016) (cited on page 3).

[110] T. L. Nguyen, J. M. Raimond, C. Sayrin, R. Cortiñas, T. Cantat-Moltrecht, F. Assemat, I. Dotsenko, S. Gleyzes, S. Haroche, G. Roux, et al. "Towards Quantum Simulation with Circular Rydberg Atoms", Physical Review X **8**, 011032 (2018) (cited on page 3).

[111] Sam R. Cohen and Jeff D. Thompson. "Quantum Computing with Circular Rydberg Atoms", PRX Quantum **2**, 030322 (2021) (cited on pages 3, 86).

[112] S. Haroche, M. Brune, and J. M. Raimond. "From cavity to circuit quantum electrodynamics", Nature Physics **16**, 243–246 (2020) (cited on page 3).

[113] Tamara Đorđević, Polnop Samutpraphoot, Paloma L. Ocola, Hannes Bernien, Brandon Grinkemeyer, Ivana Dimitrova, Vladan Vuletić, and Mikhail D. Lukin. "Entanglement transport and a nanophotonic interface for atoms in optical tweezers", Science **373**, 1511–1514 (2021) (cited on page 3).

[114] Brandon Grinkemeyer, Elmer Guardado-Sanchez, Ivana Dimitrova, Danilo Shchepanovich, G. Eirini Mandopoulou, Johannes Borregaard, Vladan Vuletić, and Mikhail D. Lukin. "Error-detected quantum operations with neutral atoms mediated by an optical cavity", Science **387**, 1301–1305 (2025) (cited on page 3).

[115] I. I. Beterov and M. Saffman. "Rydberg blockade, Förster resonances, and quantum state measurements with different atomic species", Physical Review A **92**, 042710 (2015) (cited on page 3).

[116] K. Singh, C. E. Bradley, S. Anand, V. Ramesh, R. White, and H. Bernien. "Mid-circuit correction of correlated phase errors using an array of spectator qubits", Science **380**, 1265–1269 (2023) (cited on page 3).

[117] M. A. Norcia, A. W. Young, and A. M. Kaufman. “Microscopic Control and Detection of Ultracold Strontium in Optical-Tweezer Arrays”, Physical Review X **8**, 041054 (2018) (cited on pages 3, 7, 71).

[118] Alexandre Cooper, Jacob P. Covey, Ivaylo S. Madjarov, Sergey G. Porsev, Marianna S. Safronova, and Manuel Endres. “Alkaline-Earth Atoms in Optical Tweezers”, Physical Review X **8**, 041055 (2018) (cited on pages 3, 7, 74, 75).

[119] Niamh Jackson, Ryan Hanley, Matthew Hill, Frédéric Leroux, Charles Adams, and Matthew Jones. “Number-resolved imaging of ^{88}Sr atoms in a long working distance optical tweezer”, SciPost Physics **8**, (2020) (cited on page 3).

[120] S. Saskin, J. T. Wilson, B. Grinkemeyer, and J. D. Thompson. “Narrow-Line Cooling and Imaging of Ytterbium Atoms in an Optical Tweezer Array”, Physical Review Letters **122**, 143002 (2019) (cited on pages 3, 11).

[121] Andrew D. Ludlow, Martin M. Boyd, Jun Ye, E. Peik, and P. O. Schmidt. “Optical atomic clocks”, Reviews of Modern Physics **87**, 637–701 (2015) (cited on pages 3, 8).

[122] Andrew J. Daley, Martin M. Boyd, Jun Ye, and Peter Zoller. “Quantum Computing with Alkaline-Earth-Metal Atoms”, Physical Review Letters **101**, 170504 (2008) (cited on page 3).

[123] A. V. Gorshkov, A. M. Rey, A. J. Daley, M. M. Boyd, J. Ye, P. Zoller, and M. D. Lukin. “Alkaline-Earth-Metal Atoms as Few-Qubit Quantum Registers”, Physical Review Letters **102**, 110503 (2009) (cited on page 3).

[124] Neville Chen, Lintao Li, William Huie, Mingkun Zhao, Ian Vetter, Chris H. Greene, and Jacob P. Covey. “Analyzing the Rydberg-based optical-metastable-ground architecture for Yb171 nuclear spins”, Physical Review A **105**, 052438 (2022) (cited on pages 3, 14, 15, 101, 118).

[125] Alec Jenkins, Joanna W. Lis, Aruku Senoo, William F. McGrew, and Adam M. Kaufman. “Ytterbium Nuclear-Spin Qubits in an Optical Tweezer Array”, Physical Review X **12**, 021027 (2022) (cited on pages 3, 11, 51, 75).

[126] Joanna W. Lis, Aruku Senoo, William F. McGrew, Felix Rönchen, Alec Jenkins, and Adam M. Kaufman. “Midcircuit Operations Using the omg Architecture in Neutral Atom Arrays”, Physical Review X **13**, 041035 (2023) (cited on pages 3, 11, 13, 16, 43, 69, 71, 72, 76, 81, 85, 87, 90).

[127] A. M. Kaufman, B. J. Lester, and C. A. Regal. “Cooling a Single Atom in an Optical Tweezer to Its Quantum Ground State”, Physical Review X **2**, 041014 (2012) (cited on page 3).

[128] Shuo Ma, Alex P. Burgers, Genyue Liu, Jack Wilson, Bichen Zhang, and Jeff D. Thompson. “Universal Gate Operations on Nuclear Spin Qubits in an Optical Tweezer Array of Yb171 Atoms”, Physical Review X **12**, 021028 (2022) (cited on pages 3, 118).

[129] William Huie, Lintao Li, Neville Chen, Xiye Hu, Zhubing Jia, Won Kyu Calvin Sun, and Jacob P. Covey. “Repetitive Readout and Real-Time Control of Nuclear Spin Qubits in 171Yb Atoms”, PRX Quantum **4**, 030337 (2023) (cited on pages 3, 76, 90).

[130] A. G. Radnaev, W. C. Chung, D. C. Cole, D. Mason, T. G. Ballance, M. J. Bedalov, D. A. Belknap, M. R. Berman, M. Blakely, I. L. Bloomfield, et al. “A universal neutral-atom quantum computer with individual optical addressing and non-destructive readout”, arXiv:2408.08288, (2024) (cited on page 3).

[131] M. A. Norcia, W. B. Cairncross, K. Barnes, P. Battaglino, A. Brown, M. O. Brown, K. Cassella, C.-A. Chen, R. Coxe, D. Crow, et al. “Midcircuit Qubit Measurement and Rearrangement in a Yb171 Atomic Array”, Physical Review X **13**, 041034 (2023) (cited on pages 3, 14, 72, 90).

[132] Yue Wu, Shimon Kolkowitz, Shruti Puri, and Jeff D. Thompson. “Erasure conversion for fault-tolerant quantum computing in alkaline earth Rydberg atom arrays”, Nature Communications **13**, (2022) (cited on pages 3, 16).

[133] Shuo Ma, Genyue Liu, Pai Peng, Bichen Zhang, Sven Jandura, Jahan Claes, Alex P. Burgers, Guido Pupillo, Shruti Puri, and Jeff D. Thompson. “High-fidelity gates and mid-circuit erasure conversion in an atomic qubit”, Nature **622**, 279–284 (2023) (cited on pages 3, 14, 16, 46, 93, 101, 105, 119).

[134] Pascal Scholl, Adam L. Shaw, Richard Bing-Shiun Tsai, Ran Finkelstein, Joonhee Choi, and Manuel Endres. “Erasure conversion in a high-fidelity Rydberg quantum simulator”, Nature **622**, 273–278 (2023) (cited on pages 3, 16).

[135] J. A. Muniz, M. Stone, D. T. Stack, M. Jaffe, J. M. Kindem, L. Wadleigh, E. Zalys-Geller, X. Zhang, C.-A. Chen, M. A. Norcia, et al. “High-Fidelity Universal Gates in the 171 Yb Ground-State Nuclear-Spin Qubit”, PRX Quantum **6**, 020334 (2025) (cited on page 3).

[136] A. Ashkin. “Acceleration and Trapping of Particles by Radiation Pressure”, Physical Review Letters **24**, 156–159 (1970) (cited on page 7).

[137] A. Ashkin, J. M. Dziedzic, J. E. Bjorkholm, and Steven Chu. “Observation of a single-beam gradient force optical trap for dielectric particles”, Optics Letters **11**, 288 (1986) (cited on page 7).

[138] Jack Wilson, Samuel Saskin, Yijian Meng, Shuo Ma, Rohit Dilip, Alex Burgers, and Jeff Thompson. “Trapped arrays of alkaline earth Rydberg atoms in optical tweezers”, (2019) (cited on page 7).

[139] Sergey G. Porsev, Andrei Derevianko, and E. N. Fortson. “Possibility of an optical clock using the61S0→63P0otransition in171,173Ybatoms held in an optical lattice”, Physical Review A **69**, 021403 (2004) (cited on pages 8, 11).

[140] Andrei Derevianko and Hidetoshi Katori. “Colloquium: Physics of optical lattice clocks”, Reviews of Modern Physics **83**, 331–347 (2011) (cited on page 8).

[141] Lintao Li, Xiye Hu, Zhubing Jia, William Huie, Won Kyu Calvin Sun, Aakash, Yuhao Dong, Narisak Hiri-O-Tuppa, and Jacob P. Covey. “Parallelized telecom quantum networking with a ytterbium-171 atom array”, arXiv:2502.17406, (2025) (cited on page 11).

[142] J. T. Wilson, S. Saskin, Y. Meng, S. Ma, R. Dilip, A. P. Burgers, and J. D. Thompson. “Trapping Alkaline Earth Rydberg Atoms Optical Tweezer Arrays”, Physical Review Letters **128**, 033201 (2022) (cited on pages 13, 101).

[143] G. Lochead, D. Boddy, D. P. Sadler, C. S. Adams, and M. P. A. Jones. “Number-resolved imaging of excited-state atoms using a scanning autoionization microscope”, Physical Review A **87**, 053409 (2013) (cited on page 13).

[144] Ivaylo S. Madjarov, Jacob P. Covey, Adam L. Shaw, Joonhee Choi, Anant Kale, Alexandre Cooper, Hannes Pichler, Vladimir Schkolnik, Jason R. Williams, and Manuel Endres. “High-fidelity entanglement and detection of alkaline-earth Rydberg atoms”, Nature Physics **16**, 857–861 (2020) (cited on page 13).

[145] Alex P. Burgers, Shuo Ma, Sam Saskin, Jack Wilson, Miguel A. Alarcón, Chris H. Greene, and Jeff D. Thompson. “Controlling Rydberg Excitations Using Ion-Core Transitions in Alkaline-Earth Atom-Tweezer Arrays”, PRX Quantum **3**, 020326 (2022) (cited on pages 13, 118).

[146] Ryuta Yamamoto, Jun Kobayashi, Takuma Kuno, Kohei Kato, and Yoshiro Takahashi. “An ytterbium quantum gas microscope with narrow-line laser cooling”, New Journal of Physics **18**, 023016 (2016) (cited on pages 13, 71).

[147] Aruku Senoo, Alexander Baumgärtner, Joanna W. Lis, Gaurav M. Vaidya, Zhongda Zeng, Giuliano Giudici, Hannes Pichler, and Adam M. Kaufman. “High-fidelity entanglement and coherent multi-qubit mapping in an atom array”, arXiv:2506.13632, (2025) (cited on page 13).

[148] Tim O. Höhn, Etienne Staub, Guillaume Brochier, Nelson Darkwah Oppong, and Monika Aidelsburger. “State-dependent potentials for the S01 and P03 clock states of neutral ytterbium atoms”, Physical Review A **108**, 053325 (2023) (cited on page 14).

[149] Michael A. Nielsen and Isaac L. Chuang. *Quantum Computation and Quantum Information.* Cambridge University Press, 2012 (cited on page 14).

[150] D. T. C. Allcock, W. C. Campbell, J. Chiaverini, I. L. Chuang, E. R. Hudson, I. D. Moore, A. Ransford, C. Roman, J. M. Sage, and D. J. Wineland. “omg blueprint for trapped ion quantum computing with metastable states”, Applied Physics Letters **119**, (2021) (cited on page 15).

[151] H.-X. Yang, J.-Y. Ma, Y.-K. Wu, Y. Wang, M.-M. Cao, W.-X. Guo, Y.-Y. Huang, L. Feng, Z.-C. Zhou, and L.-M. Duan. “Realizing coherently convertible dual-type qubits with the same ion species”, Nature Physics **18**, 1058–1061 (2022) (cited on page 15).

[152] Jonas Rauchfuß. “Generation of Arbitrary, Homogeneous Dipole Trap Geometries Using a Spatial Light Modulator”, Master Thesis, University of Hamburg, (2024) (cited on pages 18, 25, 32).

[153] A. M. Kaufman, B. J. Lester, C. M. Reynolds, M. L. Wall, M. Foss-Feig, K. R. A. Hazzard, A. M. Rey, and C. A. Regal. “Two-particle quantum interference in tunnel-coupled optical tweezers”, Science **345**, 306–309 (2014) (cited on page 19).

[154] Tobias Petersen. “A new experimental setup for quantum computing and quantum simulation with individual ytterbium atoms in optical tweezer.” PhD thesis. Universität Hamburg, 2025 (cited on pages 19, 36, 39–41, 46, 58, 59, 89).

[155] Dustin Stuart and Axel Kuhn. “Single-atom trapping and transport in DMD-controlled optical tweezers”, New Journal of Physics **20**, 023013 (2018) (cited on page 19).

[156] Daniel Ohl de Mello, Dominik Schäffner, Jan Werkmann, Tilman Preuschoff, Lars Kohfahl, Malte Schlosser, and Gerhard Birkl. “Defect-Free Assembly of 2D Clusters of More Than 100 Single-Atom Quantum Systems”, Physical Review Letters **122**, 203601 (2019) (cited on page 19).

[157] David L. Andrews. *Structured light and its applications*. Academic Press, 2008 (cited on page 20).

[158] Nadya Reingand and Wolfgang Osten. *Optical imaging and metrology*. Wiley-VCH, (2012) (cited on page 20).

[159] Yiqian Yang, Andrew Forbes, and Liangcai Cao. “A review of liquid crystal spatial light modulators: devices and applications”, Opto-Electronic Science **2**, 230026–230026 (2023) (cited on pages 20, 21).

[160] Adam M. Kaufman and Kang-Kuen Ni. “Quantum science with optical tweezer arrays of ultracold atoms and molecules”, Nature Physics **17**, 1324–1333 (2021) (cited on page 20).

[161] Daniel Barredo, Vincent Lienhard, Sylvain de Léséleuc, Thierry Lahaye, and Antoine Browaeys. “Synthetic three-dimensional atomic structures assembled atom by atom”, Nature **561**, 79–82 (2018) (cited on page 20).

[162] Henning Labuhn. “Rydberg excitation dynamics and correlations in arbitrary 2D arrays of single atoms.” PhD thesis. 2016 (cited on page 22).

[163] Y. T. Chew, M. Poitrinal, T. Tomita, S. Kitade, J. Mauricio, K. Ohmori, and S. de Léséleuc. “Ultraprecise holographic optical tweezer array”, Physical Review A **110**, 053518 (2024) (cited on pages 22, 23, 25, 27, 32).

[164] J. R. Fienup. “Phase retrieval algorithms: a comparison”, Applied Optics **21**, 2758 (1982) (cited on page 22).

[165] Donggyu Kim, Alexander Keesling, Ahmed Omran, Harry Levine, Hannes Bernien, Markus Greiner, Mikhail D. Lukin, and Dirk R. Englund. “Large-scale uniform optical focus array generation with a phase spatial light modulator”, Optics Letters **44**, 3178 (2019) (cited on pages 23, 27).

[166] Roberto Di Leonardo, Francesca Ianni, and Giancarlo Ruocco. “Computer generation of optimal holograms for optical trap arrays”, Optics Express **15**, 1913 (2007) (cited on pages 23, 24).

[167] Sylvain de Léséleuc. “Quantum simulation of spin models with assembled arrays of Rydberg atoms.” PhD thesis. 2018 (cited on pages 23, 24).

[168] Carina Hansen. “Generation of arbitrary optical patterns with high repetition rate forcontrolling individual atoms in 2D optical tweezer arrays”, Master Thesis, University of Hamburg, (2025) (cited on pages 27, 34).

[169] Ivaylo Sashkov Madjarov. “Entangling, controlling, and detecting individual strontium atoms in optical tweezer arrays.” PhD thesis. California Institute of Technology, 2021 (cited on page 30).

[170] F. Zernike and F. J. M. Stratton. “Diffraction Theory of the Knife-Edge Test and its Improved Form, The Phase-Contrast Method”, Monthly Notices of the Royal Astronomical Society **94**, 377–384 (1934) (cited on page 30).

[171] Zoe Z. Yan, Benjamin M. Spar, Max L. Prichard, Sungjae Chi, Hao-Tian Wei, Eduardo Ibarra-García-Padilla, Kaden R. A. Hazzard, and Waseem S. Bakr. “Two-Dimensional Programmable Tweezer Arrays of Fermions”, Physical Review Letters **129**, 123201 (2022) (cited on page 32).

[172] Vincent Lienhard, Sylvain de Léséleuc, Daniel Barredo, Thierry Lahaye, Antoine Browaeys, Michael Schuler, Louis-Paul Henry, and Andreas M. Läuchli. “Observing the Space- and Time-Dependent Growth of Correlations in Dynamically Tuned Synthetic Ising Models with Antiferromagnetic Interactions”, Physical Review X **8**, 021070 (2018) (cited on page 32).

[173] Ivo H. A. Knottnerus, Yu Chih Tseng, Alexander Urech, Robert J. C. Spreeuw, and Florian Schreck. “Parallel assembly of neutral atom arrays with an SLM using linear phase interpolation”, arXiv:2501.01391, (2025) (cited on page 34).

[174] Sören Dörscher. “Creation of ytterbium quantum gases with a compact 2D-/3D-MOT setup.” PhD thesis. 2013 (cited on pages 35, 36, 38).

[175] Sören Dörscher, Alexander Thobe, Bastian Hundt, André Kochanke, Rodolphe Le Targat, Patrick Windpassinger, Christoph Becker, and Klaus Sengstock. “Creation of quantum-degenerate gases of ytterbium in a compact 2D-/3D-magneto-optical trap setup”, Review of Scientific Instruments **84**, (2013) (cited on page 36).

[176] Jan Deppe. “Charakterisierung eines hochauflösenden Objektivs zur Erzeugung von Anordnungen optischer Mikrofallen”, Bachelor Thesis, University of Hamburg, (2022) (cited on page 41).

[177] Frederik Mrozek. “Construction and Characterization of two LaserSystems for realizing Rydberg Atom Qubits on anYtterbium Neutral Atom Quantum Computer”, Bachelor Thesis, University of Hamburg, (2025) (cited on pages 46, 119).

[178] Till Schacht. “Construction and Characterization of a 649 nm Laser System for Qubit Rotations on a Metastable Ytterbium State”, Bachelor Thesis, University of Hamburg, (2024) (cited on page 46).

[179] Ben Michaelis. “Construction and Characterization of a Laser System for Detecting Metastable Qubit States”, Bachelor Thesis, University of Hamburg, (2023) (cited on page 46).

[180] Benjamin Abeln. “Probing Interactions in Ytterbium Fermi Gases and Mixtures Using the Optical Clock Transition.” PhD thesis. University of Hamburg, 2021 (cited on page 48).

[181] Koen Sponselee. “Lattice Clock Experiments with Interacting Fermionic Quantum Gases.” PhD thesis. University of Hamburg, 2021 (cited on page 48).

[182] Z. Barber, J. Stalnaker, N. Lemke, N. Poli, C. Oates, T. Fortier, S. Diddams, L. Hollberg, C. Hoyt, A. Taichenachev, et al. “Optical Lattice Induced Light Shifts in an Yb Atomic Clock”, Physical Review Letters **100**, 103002 (2008) (cited on pages 55, 69).

[183] D. Sesko, T. Walker, C. Monroe, A. Gallagher, and C. Wieman. “Collisional losses from a light-force atom trap”, Physical Review Letters **63**, 961–964 (1989) (cited on page 68).

[184] Tetsuya Ido and Hidetoshi Katori. “Recoil-Free Spectroscopy of Neutral Sr Atoms in the Lamb-Dicke Regime”, Physical Review Letters **91**, 053001 (2003) (cited on page 71).

[185] Alan Gallagher and David E. Pritchard. “Exoergic collisions of cold Na-Na”, Physical Review Letters **63**, 957–960 (1989) (cited on page 74).

[186] Kevin M. Jones, Eite Tiesinga, Paul D. Lett, and Paul S. Julienne. “Ultracold photoassociation spectroscopy: Long-range molecules and atomic scattering”, Reviews of Modern Physics **78**, 483–535 (2006) (cited on page 74).

[187] Yevhen Miroshnychenko, Wolfgang Alt, Igor Dotsenko, Leonid Förster, Mkrtych Khudaverdyan, Dieter Meschede, Dominik Schrader, and Arno Rauschenbeutel. “An atom-sorting machine”, Nature **442**, 151–151 (2006) (cited on page 75).

[188] Jérôme Beugnon, Charles Tuchendler, Harold Marion, Alpha Gaëtan, Yevhen Miroshnychenko, Yvan R. P. Sortais, Andrew M. Lance, Matthew P. A. Jones, Gaétan Messin, Antoine Browaeys, et al. “Two-dimensional transport and transfer of a single atomic qubit in optical tweezers”, Nature Physics **3**, 696–699 (2007) (cited on page 75).

[189] T. Grünzweig, A. Hilliard, M. McGovern, and M. F. Andersen. “Near-deterministic preparation of a single atom in an optical microtrap”, Nature Physics **6**, 951–954 (2010) (cited on page 75).

[190] Brian J. Lester, Niclas Luick, Adam M. Kaufman, Collin M. Reynolds, and Cindy A. Regal. “Rapid Production of Uniformly Filled Arrays of Neutral Atoms”, Physical Review Letters **115**, 073003 (2015) (cited on page 75).

[191] M. O. Brown, T. Thiele, C. Kiehl, T.-W. Hsu, and C. A. Regal. “Gray-Molasses Optical-Tweezer Loading: Controlling Collisions for Scaling Atom-Array Assembly”, Physical Review X **9**, 011057 (2019) (cited on page 75).

[192] Lucas Beguin. “Measurement of the van der Waals interaction between two Rydberg atoms.” PhD thesis. 2013 (cited on page 85).

[193] Kai-Niklas Schymik, Sara Pancaldi, Florence Nogrette, Daniel Barredo, Julien Paris, Antoine Browaeys, and Thierry Lahaye. “Single Atoms with 6000-Second Trapping Lifetimes in Optical-Tweezer Arrays at Cryogenic Temperatures”, Physical Review Applied **16**, 034013 (2021) (cited on page 86).

[194] Grégoire Pichard, Desiree Lim, Étienne Bloch, Julien Vaneecloo, Lilian Bourachot, Gert-Jan Both, Guillaume Mériaux, Sylvain Dutartre, Richard Hostein, Julien Paris, et al. “Rearrangement of individual atoms in a 2000-site optical-tweezer array at cryogenic temperatures”, Physical Review Applied **22**, 024073 (2024) (cited on page 86).

[195] C. Tuchendler, A. M. Lance, A. Browaeys, Y. R. P. Sortais, and P. Grangier. “Energy distribution and cooling of a single atom in an optical tweezer”, Physical Review A **78**, 033425 (2008) (cited on page 86).

[196] V A Dzuba and A Derevianko. “Dynamic polarizabilities and related properties of clock states of the ytterbium atom”, Journal of Physics B: Atomic, Molecular and Optical Physics **43**, 074011 (2010) (cited on page 89).

[197] Daichi Okuno, Yuma Nakamura, Toshi Kusano, Yosuke Takasu, Nobuyuki Takei, Hideki Konishi, and Yoshiro Takahashi. “High-resolution Spectroscopy and Single-photon Rydberg Excitation of Reconfigurable Ytterbium Atom Tweezer Arrays Utilizing a Metastable State”, Journal of the Physical Society of Japan **91**, (2022) (cited on page 90).

[198] Ian C. Cloët, Matthew R. Dietrich, John Arrington, Alexei Bazavov, Michael Bishof, Adam Freese, Alexey V. Gorshkov, Anna Grassellino, Kawtar Hafidi, Zubin Jacob, et al. “Opportunities for Nuclear Physics & Quantum Information Science”, arXiv:1903.05453, (2019) (cited on page 92).

[199] Jarrod R McClean, Jonathan Romero, Ryan Babbush, and Alán Aspuru-Guzik. “The theory of variational hybrid quantum-classical algorithms”, New Journal of Physics **18**, 023023 (2016) (cited on page 92).

[200] Thomas F. Gallagher. *Rydberg atoms.* Digitally print. 1. pbk version. Cambridge monographs on atomic, molecular, and chemical physics 3. Cambridge: Cambridge Univ. Press, 2005. 495 pp. (cited on page 92).

[201] Peter Schauß. “High-resolution imaging of ordering in Rydberg many-body systems.” PhD thesis. Ludwig–Maximilians–Universität, München, 2014 (cited on page 92).

[202] Randall G. Hulet and Daniel Kleppner. “Rydberg Atoms in “Circular” States”, Physical Review Letters **51**, 1430–1433 (1983) (cited on page 92).

[203] K. A. Safinya, J. F. Delpech, F. Gounand, W. Sandner, and T. F. Gallagher. “Resonant Rydberg-Atom-Rydberg-Atom Collisions”, Physical Review Letters **47**, 405–408 (1981) (cited on page 96).

[204] Sylvain Ravets, Henning Labuhn, Daniel Barredo, Lucas Béguin, Thierry Lahaye, and Antoine Browaeys. “Coherent dipole–dipole coupling between two single Rydberg atoms at an electrically-tuned Förster resonance”, Nature Physics **10**, 914–917 (2014) (cited on page 96).

[205] Adriano Barenco, Charles H. Bennett, Richard Cleve, David P. DiVincenzo, Norman Margolus, Peter Shor, Tycho Sleator, John A. Smolin, and Harald Weinfurter. “Elementary gates for quantum computation”, Physical Review A **52**, 3457–3467 (1995) (cited on page 99).

[206] E.J. Robertson, N. Šibalić, R.M. Potvliege, and M.P.A. Jones. “ARC 3.0: An expanded Python toolbox for atomic physics calculations”, Computer Physics Communications **261**, 107814 (2021) (cited on page 100).

[207] C L Vaillant, M P A Jones, and R M Potvliege. “Multichannel quantum defect theory of strontium bound Rydberg states”, Journal of Physics B: Atomic, Molecular and Optical Physics **47**, 155001 (2014) (cited on page 100).

[208] F. Robicheaux, D. W. Booth, and M. Saffman. “Theory of long-range interactions for Rydberg states attached to hyperfine-split cores”, Physical Review A **97**, 022508 (2018) (cited on page 100).

[209] Michael Peper, Yiyi Li, Daniel Y. Knapp, Mila Bileska, Shuo Ma, Genyue Liu, Pai Peng, Bichen Zhang, Sebastian P. Horvath, Alex P. Burgers, et al. “Spectroscopy and modeling of ^{171}Yb Rydberg states for high-fidelity two-qubit gates”, arXiv:2406.01482, (2024) (cited on pages 100, 101).

[210] Henri Lehec, Xin Hua, Pierre Pillet, and Patrick Cheinet. “Isolated core excitation of high-orbital-quantum-number Rydberg states of ytterbium”, Physical Review A **103**, 022806 (2021) (cited on page 100).

[211] T Topcu and A Derevianko. “Possibility of triple magic trapping of clock and Rydberg states of divalent atoms in optical lattices”, Journal of Physics B: Atomic, Molecular and Optical Physics **49**, 144004 (2016) (cited on page 101).

[212] E. A. Donley, T. P. Heavner, F. Levi, M. O. Tataw, and S. R. Jefferts. “Double-pass acousto-optic modulator system”, Review of Scientific Instruments **76**, (2005) (cited on page 111).

[213] Mathieu Chanson. “Design of a stable AOM double-pass setup for trapped-ion laser systems”, Semester Thesis, TIQI-Group, ETH Zürich, (2012) (cited on page 112).

[214] Lukas Möller. “Set up of a double pass AOM system for an ion trap experiment”, Semester Thesis, TIQI-Group, ETH Zürich, (2018) (cited on page 112).

[215] Clara Schellong. “Error Analysis and Mitigation Strategies for High-Fidelity Rydberg Excitations”, Master Thesis, University of Hamburg, (2024) (cited on page 122).

[216] Lintao Li, William Huie, Neville Chen, Brian DeMarco, and Jacob P. Covey. “Active Cancellation of Servo-Induced Noise on Stabilized Lasers via Feedforward”, Physical Review Applied **18**, 064005 (2022) (cited on page 122).

[217] Philipp Herbig. “A Novel Method for the Suppression of Servo-Induced Laser Phase Noise”, Bachelor Thesis, University of Hamburg, (2023) (cited on page 122).

Danksagung

Die Entstehung dieser Doktorarbeit wäre ohne die vielfältige Unterstützung zahlreicher Personen undenkbar gewesen. Daher möchte ich an dieser Stelle meinen Dank an alle aussprechen, die zur Durchführung dieser Arbeit beigetragen haben.

Mein besonderer Dank gilt Prof. Klaus Sengstock, der mir die Möglichkeit gegeben hat, diese Arbeit in seiner Gruppe anzufertigen und der durch sein außergewöhnliches Engagement exzellente Voraussetzungen für das Forschungsprojekt geschaffen hat.

Ebenso danke ich Prof. Henning Moritz für die Übernahme des Zweitgutachtens meiner Dissertation sowie für seine Rolle als verlässlicher Zweitbetreuer.

Während meiner Doktorarbeit hatte ich das große Glück, mit vielen motivierten und zielstrebigen Menschen am Yb Projekt zusammenzuarbeiten und auch bei gemeinsamen Aktivitäten außerhalb des Instituts Zeit miteinander zu verbringen. Allen voran möchte ich hierbei Christoph Becker danken, der dieses herausfordernde Projekt geleitet hat und dem es dabei gelungen ist ein kollaboratives Arbeitsumfeld zu schaffen. Seine präzise und zugleich enthusiastische Arbeitsweise hat meine Herangehensweise an unterschiedlichste Probleme nachhaltig geprägt.

Mein größter Dank geht an meinen Mitdoktoranden Tobias Petersen. Ohne seine Zusammenarbeit über die letzten vier Jahre, wäre diese Arbeit nicht annähernd so erfolgreich verlaufen und viele Ergebnisse wären nicht zustande gekommen. Die vielen gemeinsamen Stunden im Labor und Büro haben nicht nur dazu geführt einen leeren Labortisch in ein funktionierendes (und remote steuerbares [14]) Experiment zu verwandeln, sondern haben dabei auch sehr viel Spaß gemacht. Seine Fähigkeit jedes noch zu anspruchsvolle Problem gelassen anzugehen, war jederzeit motivierend und hat sich vor allem dann als äußerst nützlich erwiesen, als es darum ging die finalen Messungen in kürzester Zeit aufzunehmen. Darüber hinaus konnte er mich für exotische Orchideenarten begeistern, was zu einer ganzen Ansammlung neuer Büro- und Hauspflanzen führte.

Für ihre wertvolle Unterstützung im Labor danke ich zudem unseren Postdocs Koen Sponselee, Alexander Ilin und zum Ende hin Felix Klein, die stets bereit waren ihre umfangreiche Labor-Expertise mit uns zu teilen und uns Doktoranden in schwierigen Zeiten daran erinnert haben, dass die meisten Probleme im Labor lösbar sind.

---

[14] Das Experiment ”remote” betreiben zu können, war von Tag eins an Tobias’ Vision, welche wir am Ende tatsächlich umsetzen konnten.

Ohne den tatkräftigen Einsatz zahlreicher weiterer Beteiligten, wäre die Bewältigung der vielen Baustellen im Labor kaum möglich gewesen. Hierbei möchte ich folgende Personen namentlich erwähnen, die mit ihrer Bachelor- oder Masterarbeit einen wichtigen Beitrag zum Voranschreiten des Projekts und damit dieser Arbeit geleistet haben: Jan Deppe, Anton Bölian, Jonas Rauchfuß, Oscar Murzewitz, Till Schacht, Philipp Herbig, Ben Michaelis, Clara Schellong, Carina Hansen und Frederik Mrozek. Besonders möchte ich Jonas danken, der uns bereits während seines Masterprojekts mit seinen exzellenten Codingfähigkeiten zur Seite stand und sich deshalb schnell zu unserem "Kundensupport" entwickelte. Des Weiteren möchte ich Jan für die Implementierung der Labscript-Experimentsteuersoftware danken, der dadurch unsere Messkampagnen um ein Vielfaches erleichtert hat. Clara möchte ich für ihre tatkräftige Mithilfe zum Design und Bau des Rydberg Lasersystems danken und Frederik für die Unterstützung beim 369 nm Lasersystem.

Den nachfolgenden Doktoranden Jonas und Clara wünsche ich viel Erfolg bei ihrer Doktorarbeit. Ich bin mir sicher, dass das Experiment bei ihnen in guten Händen ist und freue mich auf zukünftige Resultate. Für das Korrekturlesen und die vielen hilfreichen Anmerkungen zu meiner Dissertation möchte ich mich bei Christoph, Tobias, Jonas und Alex bedanken.

Für Diskussionen bezüglich des Themas Quantencomputing und die Kollaboration möchte ich mich bei Prof. Ludwig Mathey, Nicolas Heimann und Lukas Broers bedanken.

Meinen ehemaligen Studienkollegen und späteren Mitdoktoranden Jette Heyer und Jim Skulte sei gedankt für die vielen gemeinsamen Kaffeepausen und netten Gespräche am Institut wie auch darüber hinaus.

Mein Dank gilt ebenso dem administrativen und technischen Personal des Instituts, insbesondere Ellen Gloy, Kirstin Behnke, Loreen Tornier, dem CUI Office, Reinhardt Mielck und Finn Gloyer. Ebenso möchte ich meinen Dank an Stephan Fleig und den weiteren Kollegen der Standortwerkstatt Bahrenfeld aussprechen, die immer bemüht waren meine oftmals dringenden Aufträge in die Tat umzusetzen.

Abschließend danke ich meiner Familie, die mir in vielerlei Hinsicht Rückhalt gegeben und mich in allen Aspekten unterstützt hat.

Eidelsstattliche Versicherung

Hiermit versichere ich an Eides statt, die vorliegende Dissertationsschrift selbst verfasst und keine anderen als die angegebenen Hilfsmittel und Quellen benutzt zu haben.

Sofern im Zuge der Erstellung der vorliegenden Dissertationsschrift generative Künstliche Intelligenz (gKI) basierte elektronische Hilfsmittel verwendet wurden, versichere ich, dass meine eigene Leistung im Vordergrund stand und dass eine vollständige Dokumentation aller verwendeten Hilfsmittel gemäß der Guten wissenschaftlichen Praxis vorliegt. Ich trage die Verantwortung für eventuell durch die gKI generierte fehlerhafte oder verzerrte Inhalte, fehlerhafte Referenzen, Verstöße gegen das Datenschutz- und Urheberrecht oder Plagiate.

22.08.2025	Nejira Pintul
Datum	Unterschrift der Doktorandin / des Doktoranden